ANL-87-29

Reactor Analysis and Safety Division
Reactor Analysis and Safety Division
Reactor Analysis and Safety Division

Analysis of Proposed Gamma-Ray Detection System for the Monitoring of Core Water Inventory in a Pressurized Water Reactor

by Diane Melanie Markoff

Argonne National Laboratory, Argonne, Illinois 60439
operated by The University of Chicago
for the United States Department of Energy under Contract W-31-109-Eng-38

DISCLAIMER

Printed in the United States of America
Available from
National Technical Information Service
U. S. Department of Commerce
5285 Port Royal Road
Springfield, VA 22161

NTIS price codes
Printed copy: A06
Microfiche copy: A01

Distribution Category:
Light Water Reactor Technology (UC-78)

ANL-87-29

ANL--87-29

DE88 005785

ARGONNE NATIONAL LABORATORY
9700 South Cass Avenue
Argonne, Illinois 60439

ANALYSIS OF PROPOSED GAMMA-RAY DETECTION SYSTEM FOR THE MONITORING OF CORE WATER INVENTORY IN A PRESSURIZED WATER REACTOR

by

Diane Melanie Markoff

Reactor Analysis and Safety Division

December 1987

TABLE OF CONTENTS

TABLE OF CONTENTS (Cont'd)

ANALYSIS OF PROPOSED GAMMA-RAY DETECTION SYSTEM FOR THE MONITORING OF CORE WATER INVENTORY IN A PRESSURIZED WATER REACTOR

by

Diane Melanie Markoff

ABSTRACT

An initial study has been performed of the feasibility of employing an axial array of gamma detectors located outside the pressure vessel to monitor the coolant in a PWR. A one-dimensional transport analysis model is developed for the LOFT research reactor and for a mock-PWR geometry. The gamma detector response to coolant voiding in the core and downcomer has been determined for both geometries. The effects of various conditions (for example, time after shutdown, materials in the transport path, and the relative void fraction in different water regions) on the detector response are studied. The calculational results have been validated by a favorable comparison with LOFT experimental data. Within the limitations and approximations considered in the analysis, the results indicate that the gamma-ray detection scheme is able to unambiguously respond to changes in the coolant inventory within any vessel water region.

1. INTRODUCTION

The well-known incident at the Three Mile Island Unit II power plant exposed deficiencies in the monitoring and operation of a large-scale nuclear power reactor during transient conditions. Studies of the event [1,2] agree that improvement of the plant operator's capability to know the status of primary system variables, including the reactor coolant inventory, under abnormal operations is imperative for the safe production of nuclear power. This improvement is being achieved through extensive operator training, with the introduction of definitive methods of determining plant conditions, or through the modification of existing instruments and procedures, and by informatively conveying the data to the operators. A vital plant variable for which monitoring systems need further development is the coolant inventory in the reactor vessel. The means of determining reactor coolant conditions for a pressurized water reactor (PWR) forms the motivation of this study.

During 1979, at the time of the Three Mile Island Unit II incident, the methods of determining coolant conditions in the reactor vessel were indirect and interpretive. For example, the water level in the pressurizer was used as an indication of reactor coolant inventory. Under normal operating conditions, the amount of water and gas in the pressurizer is directly related to the reactor coolant system pressure and coolant inventory. However, under some conditions, the pressurizer level can give an erroneous indication of total coolant inventory [2]. In particular during the Three Mile Island incident, the leak was from a valve after the pressurizer, and voids in the core created a non-collapsed water-level. The core temperature and pressure readings were also relied upon to indicate coolant conditions. According to the President's Commission on Three Mile Island, although temperatures and pressures were known during the accident, there was "no direct indication that the combination of pressure and temperature meant that the cooling water was turning to steam" [1]. The report presented evidence that the misinterpretation of available plant data led to confusion and an incorrect understanding of coolant conditions in the core. A speculative analysis of several reactor detectors not normally used as a means to determine coolant conditions, was used to recreate the accident scenario of boiling and core uncovery [2]. The fact that this interpretive and speculative analysis was necessary to determine the coolant conditions in the core, is a clear indication of the

lack of direct coolant inventory monitoring, and the resulting confusion in the Three Mile Island control room is an indication that such a monitoring system is needed.

As a result of the reports that were issued on the Three Mile Island incident, the Nuclear Regulatory Commission (NRC) responded with a series of requirements for the safe operation of nuclear power plants. Among the requirements is the establishment of a system for the "unambiguous, easy-to-interpret, indication of inadequate core cooling (ICC)" [3]. This definitive method must be capable of warning of the approach to, and of indicating a positive recovery from, ICC conditions. The detection system must be able to uniquely indicate inadequate coolant as a result of various conditions, while phenomena other than ICC do not cause a positive indication. The system is to cover the range of operations from normal throughout a full loss of coolant event of complete core uncovery, with the capability of surviving the harsh environment of an accident scenario.

The NRC relaxed its initial requirements to allow more flexibility of using existing instrumentation and interpretive methods, along with secondary data to reduce misinterpretation and account for possible deficiencies. The Commission proposed a three-part detection system that would meet the necessary qualifications [4]. The approved coolant monitoring system is composed of in-core and core-exit thermocouples, improved subcooling-margin monitors and a coolant-inventory tracking system with a minimum range from the upper head to the bottom of the hot leg. The core-exit thermocouples can indicate that the core has boiled dry, and the subcooling-margin monitors indicate abnormal cooling conditions, but cannot provide information to determine how the conditions are changing. The reactor-coolant-inventory tracking detection provides early warning information on void formation in the reactor head.

Several detection system methods for tracking coolant inventory have been proposed. Both NRC-sponsored and independent research for the development of new techniques and devices, for the modification of existing reactor instrumentation, and for the analysis and testing of proposed methods have been performed. The proposed methods that are currently being reviewed (with some being considered for licensing) include ultrasonic techniques, the application of thermal devices, including thermocouples and gamma thermometers, differential pressure detection methods, interpretation of self-powered neutron detector (SPND) signal output, and an ex-core neutron detection system.

The ultrasonic waveguide technique is based on the generation of extensional and torsional waves in a magnetic rod. The propagation velocity of a wave excited by a torsional stress pulse is dependent upon the surrounding medium density and temperature. The extensional wave is unaffected by the medium density and is thus used for temperature corrections. Studies of the ultrasonic method for use as a coolant monitor were performed at the Oak Ridge National Laboratory [5,6]. The advantages of this technique are the availability of continuous readout of coolant level, average density, and fluid temperature along specific points in a vertical path through the reactor vessel. The sensor materials made of stainless steel, are rugged and were proven to be able to survive radiation environments, while the sensitive electronics can be placed in remote protected areas. However, several problems and deficiencies need to be addressed before authorization for commercial application. A major difficulty with the sensors is that the boiling action of two-phase flow can interfere with the proper functioning of the device. The simultaneous variation of temperature and density, especially with detector sensor shapes and density conditions beyond the existing theoretical expressions, can necessitate complicated pattern recognition algorithms. The slight signal distortions at high temperatures will have to be eliminated or made accountable.

The thermal devices focus mainly on the application of differential thermocouples. Several methods employing thermocouples have been studied. The first is the interpretation of core-exit thermocouples for determining core coolant conditions. As mentioned above, these temperature readings are approved as an integral part of the ICC detection system. The indirect indication of core uncovery is through the detection of steam that has been superheated by the fuel rods. Limitations of these temperature readings as an indication of inadequate cooling were found in several tests at the Loss of Fluid Test (LOFT) reactor, a scaled-down pressurized water reactor [7]. The first limitation was a delay in response of up to three minutes, between the initiation of core uncovery and the thermocouple indication. Drainage of water from the upper plenum coated the thermocouples, preventing response to vapor superheat. Another limitation sited by this report is the lower response of the core-exit thermocouples as compared to the core-cladding thermocouples. The heat transfer with surrounding structural material cools the steam below clad temperatures and thus does not give an accurate indication of core heat-up.

Another method of tracking coolant inventory employs differential thermocouples in an axial array within and above the core. This system was evaluated at the Oak Ridge National Laboratory (ORNL) [8] at the request of the NRC. Two temperature sensing devices are used, either K-type thermocouples or heated-resistance temperature detectors, with one sensor heated electronically and the other sensitive only to ambient temperatures. The resulting temperature difference, ΔT, between the two sensors gives a direct indication of the cooling capacity of the medium. The advantages of this method are the direct measurement of fluid conditions, the quick-response capabilities of thermocouples, and the inexpensive construction of the devices which include reactor compatible materials. The experimental analysis of the sensors revealed several problems with this technique. Non-reproducible readings were recorded under conditions of high void fraction and large flow velocity. Unshielded detectors were susceptible to cooling by water droplets originating from above the liquid-vapor interface. The electronic heaters are prone to failure at high temperatures.

Combustion Engineering Corporation (C-E) developed a differential thermocouple technique for inventory tracking above the core, which solved the problems revealed in the ORNL analysis [9]. The system measures differential temperatures to monitor fluid cooling capacity, absolute temperatures to monitor fluid cooling capacity, absolute temperatures to monitor fluid and local core heating, and heater temperatures to monitor, and adjust if necessary, the heater current to prevent failure. A splash shield was developed to protect the sensors from cooling due to entrained water droplets. The sensing devices are placed at several points in a separator tube which divides the surrounding two-phase medium into the liquid and gas phase in which the liquid forms a column with a distinct water level. The differential thermocouples are no longer in a two-phase mixture, but are now used to determine the water level of a stagnant liquid column. When the separator tube is strategically placed in the reactor vessel, the resulting measurement is an indication of the fraction of volume above the core that is occupied by liquid, and hence determines if the core is covered with an adequate amount of coolant. Uncovery below the core is monitored with core-exit and in-core thermocouples.

The Scandpower Corporation has developed a coolant monitoring system with gamma thermometers, absolute thermocouples, and differential thermocouples

each strategically placed within an instrument guide tube which axially spans the core, upper plenum, and upper vessel head [10,11]. The gamma thermometer, referred to as the Radcal design, consists of (from inner to outer radius) a cable pack of thermocouples and heaters, a stainless steel core rod, an annular argon gas chamber, and a jacket tube. The thermocouples contain two leads for temperature difference readings, and the heaters are used for installed calibration purposes. The device relies on uniform gamma heating of the instrument, and the difference in heat transfer between areas where the gas chamber is located and where the core rod is in contact with the jacket tube, which is in contact with the coolant. The result is a temperature gradient with axial heat flow from areas of poor heat transfer, where the gas chamber is located, to areas of good cooling conditions, where the core rod can transfer heat to the coolant. The measured ΔT is proportional to the gamma-ray production, which is related to the local fuel power.

Energizing the heater in the Radcal gamma thermometer converts the device to a "signature-of-uncovery sensor" [11]. For a well-defined water level, the signal from the gamma thermometer in this mode, undergoes a characteristic change or signature as the liquid-vapor interface decreases or increases. This is caused by changes in heat transfer characteristics along the sensor with respect to the thermocouple points of measurement (which are referenced as T_{hot} and T_{cold} under normal operation). Removal of the gas chamber and enabling the heater produces a differential thermocouple, (with no power monitoring capability), which operates by the method discussed above. In this application, the measured ΔT is compared with a pre-calculated reference value to determine if the defined water level is above or below the sensor, and is also converted to a measure of heat transfer characteristics. To measure collapsed coolant level, the Radcal differential thermocouples are placed in a separator tube similar to that described above for the C-E design. A second differential thermocouple sensor operates on the same principle, but contains the annular gas chamber to minimize effects from splashing.

Several features of the C-E and Scandpower differential thermocouple reactor coolant inventory monitoring systems take advantage of existing instrumentation which has been well studied both in and out of operating reactors. Installation of these systems includes the use of existing guide tubes, and vessel penetration points allocated for in-core instrumentation.

The methods meet the basic NRC-defined requirements for an ICC system. They do, however, rely on in-core temperature thermocouples which may give inaccurate indications of core heat-up and recovery [12]. The Scandpower system employs different types of thermo- couples which give a different response to the local fluid conditions, especially in the core. This may provide a beneficial redundancy in measurements. However, confusion could result under conditions where one or more device readings give different indications of local water density--for example, interpreting water-level indication from responses of unshielded differential thermocouples in high velocity flow or in prime conditions for existing water entrainment.

In a post-accident analysis of the Three Mile Island core-coolant conditions, the self-powered neutron detector (SPND) data was used as an indication of in-core temperatures and as a secondary inference of water-level [2]. Analysis of SPND response was conducted for several LOFT loss-of-coolant simulation tests [13,14]. The SPND signal response contains two components: contribution from the thermal neutron flux which produces a positive current, and from the γ-ray flux which produces a negative component current signal. With a decrease in core coolant density, the thermal neutron flux decreases and the gamma-ray flux increases producing a decrease in negative current, or an increase in the net signal amplitude. The loss-of-coolant tests showed a correlation between SPND response and fluid uncovery of the detector. Reproducibility of the output signal was demonstrated by showing nearly equal relative changes in signal amplitude for similar changes in core fluid density during two separate test events. Since the SPND signal is dependent upon changing neutron and gamma-ray fluxes, the response of each SPND during a normal reactor scram would be recorded and used as a comparison reference so that any differences would indicate coolant density changes.

In-core devices must be able to survive severe radiation and temperature environments throughout a loss-of-coolant event. The ICC systems must be able to conform to reactor vessel isolation requirements, and should not interfere with existing instrumentation, and procedures. To circumvent some of these problems, ex-core detection methods have been devised.

A method of coolant monitoring external to the reactor vessel developed by the Westinghouse Electric Corporation (Westinghouse), is based upon differential pressure measurements [15]. The technique involves a two-train system

each with the same three differential measurements ΔP. Each measurement is designed to specifically address the ICC system requirements set by the NRC. The first is a full range measurement from the top to the bottom of the reactor vessel, and determines, along with core-exit thermocouple readings, the extent of inadequate core cooling in order to define when ICC recovery procedures should be initiated. The second measurement spans the full vessel and is used when the reactor coolant pumps are on. When the system is at saturation pressure and voids begin forming in the coolant, this differential pressure will decrease, indicating the relative amount and trend of void content in the vessel. The third is the differential pressure measurement between the top of the vessel and the hot leg, to indicate voiding in the upper head area. The reference leg pressure measurements are compensated by temperature monitors and system pressure and temperature readings, to account for density changes.

This system is being installed in several reactors to satisfy NRC coolant monitoring requirements. Minor back-fitting difficulties and system operations have been overcome [15]. Although an ex-vessel method, this system still requires vessel penetration, and adaptation to refueling and maintenance procedures. Although differential pressure measurements have given positive indications of voiding in the vessel, especially in the upper head, the method is an indirect technique and requires some interpretation to determine coolant conditions.

Like the SPND data, the source-range neutron detector response during the Three Mile Island accident showed anomalous behavior which seemed to correspond with core uncovery [2]. An in-depth neutronics calculational study determined that core voiding behavior could account for the source-range detector data [16]. Analysis of LOFT power-range and intermediate-range neutron detector data obtained during loss-of-coolant simulations shows the existence of a relationship between the fluid inventory and the detector response [12].

As a result of the above evidence, the Pennsylvania State University (PSU), under NRC contract, developed and tested the concept of a "non-invasive liquid-level and density gauge" which detects high-energy neutrons that penetrate the reactor vessel wall [17]. The method employs a vertical string of epi-cadmium neutron detectors external to the vessel. Each detector views an

axial section of the core through the detection of epi-thermal neutrons which are most likely to have originated from within the vessel. This is based on the fact that most of the thermal and nearly thermal neutrons will be absorbed by the steel and only the higher energy neutrons from within the vessel can reach the detector. The low-energy neutrons at the detector are likely to have been scattered in from any direction and must be removed from the signal. Water-density variation or liquid-level variation in the reactor vessel affects the moderation of neutrons which will cause an increase in the high-energy neutron flux for a decrease in water density. Decreasing the core water content affects the reactivity, causing a decrease in the source of neutrons. The production of neutrons, photoneutrons, from the absorption of high-energy γ-rays in the deuterium found in water also produces a water-density-dependent source of neutrons. The result is a complicated interaction of effects which may increase or decrease the neutron flux as a function of water density.

Computational and experimental simulations show that changes in coolant density, or liquid level produce a specific detector response dependent upon the location of the changing coolant (core or downcomer) and the detector axial position. Specifically, one stage of experimental and analytical analysis was associated with the LOFT research reactor. Four fission chambers were installed in an instrument tube located outside of the pressure vessel [18]. The radial location of the instrument tube and the relative axial positions of the detectors are shown in Figure 1. In addition, time- and space-dependent calculations were performed for two specific LOFT experiments [18]. The first simulated experiment was a large-break loss-of-coolant event, L2-5, for which the PSU detectors were not yet installed. The neutron detector data were available for the second calculational simulation of the LP-02-6 test.

Some limitations exist with the neutron detection system. For large times after core shutdown (beyond the time-frame of LOFT tests), the neutron flux at the detector located outside the vessel decreases greatly. Questions have been raised concerning the capability of a system based on the detection of neutrons outside the vessel to indicate voiding in the upper plenum and upper head areas [19,20]. This method relies on the interpretation of detector response to determine whether the density is changing, the coolant

level is changing, or whether the variation is in the core or downcomer or both.

A new ex-core technique for reactor coolant monitoring has been proposed at Argonne National Laboratory (ANL) [20]. This method extends the ideas put forward in the neutron detection system, by applying the techniques of a γ-ray hodoscope, an array of detectors [21]. This concept is based on the detection of high-energy gamma-rays emitted from neutron capture in steel, primarily in the reactor vessel wall. The hodoscope detection scheme employs an axial array of collimated detectors located in or near the biological shield and positioned so that the overlap of detector response functions provides a monitoring system that continuously spans the entire length of the reactor vessel. The collimation is designed to minimize the signal from scattered γ-rays, so as to restrict the detector response to a designated vertical and horizontal range of the vessel. In the horizontal direction, the detectors are physically aimed and collimated for tangential viewing of the core and of the downcomer to reduce the contribution of core gamma-rays to the detector signal, and to provide a means to monitor the downcomer separately. A general schematic view of the γ-ray hodoscope monitoring system is provided in Figure 2. The proposed sodium-iodide scintillation detectors are to be shielded with a lead filter to eliminate low-energy contributions to the signal.

Since the γ-ray monitoring system relies on the detection of high-energy γ-rays as a result of neutron capture in the steel, the sensitivity to water density is through the low-energy neutron flux. The neutron population which reaches the core barrel and reactor pressure vessel is dependent upon the water density in the core and in the downcomer. The neutron-capture process in steel emits a number of γ-rays above 5 MeV, while the fission-product gamma-rays are primarily lower in energy. Thus, the restriction to very high-energy detection further reduces core γ-ray contributions to the detector signal.

The neutron population in the core changes in time as a function of decay power. In order to eliminate the effects from power variations, the detector responses are normalized using the lowest detector in the axial array. This detector is least affected by core voiding, but is equally affected by power decay. This method provides on-line, real-time normalization to remove any dependence on power decay.

The axial array of γ-ray detectors includes viewing of the upper-plenum and upper-head regions of the reactor vessel. In this vertical range, the detectors are horizontally aimed along the diameter of the vessel. For this region, the 2.23 MeV capture γ-rays emitted from the hydrogen in water may also be used as a signature for coolant detection. In this area above the core, the background core γ-ray flux is reduced, and a reduction in the detector energy threshold to include the hydrogen capture γ-rays would not compromise the detector signal.

This proposed γ-ray method for coolant monitoring satisfies many of the original requirements for a reactor-coolant-inventory tracking system. Wth the detectors monitoring the full range of the vessel, one direct indication of coolant conditions is employed for the full range of operation from normal operating conditions to complete core uncovery. This eliminates some interpretation and ambiguity of the combination methods discussed above. With the location of the detection system outside of the pressure vessel, there is no interference with normal and shutdown operations, and no need for vessel penetration. Radiation damage is greatly reduced for a detector located near the biological shield, ensuring the survivability of the system during a severe loss-of-coolant event, and reducing maintenance requirements. With an axial array of detectors, and the proposed system of back-up detectors, (four detectors in series) on-line calibration and monitoring for detector failure is available.

A fast-neutron hodoscope (horizontal and vertical array of fast-neutron and γ-ray detectors in tandem) detection scheme has been in use for diagnostics in fuel-motion surveillance monitoring in the Transient Reactor Test Facility (TREAT) [21]. Reactor experience and methodology for the proposed γ-ray hodoscope coolant inventory monitoring system is based on the diagnostics experience at TREAT. However, no direct light-water reactor (LWR), or more specifically pressurized water reactor (PWR), experience has been established. At the initiation of this study, only preliminary analysis on the applicability of the proposed γ-ray detection scheme had been performed.

As a result, this study was directed at the evaluation of the feasibility and applicability of a γ-ray detection scheme to monitor water level and density changes in the reactor vessel. The NRC requirement of an unambiguous method was addressed by considering the uniqueness of an indication of

inadequate cooling, and whether other conditions could produce a positive indication. A calculational approach was developed which would determine the response of a γ-ray detector to water changes, and the relative contributions from different sources (e.g. core or capture gamma-rays).

It was decided that a one-dimensional calculation would provide valuable information while minimizing cost. A coupled neutron and γ-ray transport-theory analytical model was developed. In the interest of comparing to known results, the LOFT research reactor, a scaled version of a pressurized water reactor, was chosen for the model to represent a PWR. The LOFT reactor performs simulations of loss-of-coolant events while monitoring reactor parameters including the coolant level in the core and downcomer [22]. Another advantage of the LOFT reactor is the ability to compare with available neutron detection results. The use of a coupled calculation allows for the simultaneous extraction of neutron data. Unfortunately, LOFT test data was not available for a test in which the PSU detectors were installed. Therefore, the L2-5 test was chosen as the basis for the model, with the LOFT intermediate-range neutron detector data for comparison.

2. THEORETICAL ANALYSIS

The system being studied comprises the LOFT research reactor with γ-ray detectors located radially at the instrument tube. (See Figure 1.) The LOFT reactor is a scaled down version of a commercial pressurized water reactor (PWR). The reactor was designed to emulate the thermal-hydraulic conditions of a PWR for analysis during simulated loss of coolant events [22]. LOFT has 4% uranium enriched, zircaloy clad fuel with an active height of 5.5 ft., is water moderated, and has a full thermal power rating of 50 MW. The system is designed to simulate various sized pipe breaks and other loss-of-coolant scenarios, with the option of manually triggering or delaying the emergency core cooling system.

The main goal of the study is to determine the response of a γ-ray detector to changing water conditions within the reactor pressure vessel during a transient. The main concern of the problem is determining the sources of γ-rays and the properties of the materials in the transport path, and how each is affected by water density and water level changes. In this section, a general overview of these concerns is presented, while details of the calculational model are provided in Section 3.

The sources of photons after shutdown are fission product gamma-rays, and gamma-rays produced from the capture of neutrons. As a consequence of the production of γ-rays from neutron interactions, the production and transport of neutrons must also be studied. The primary sources of neutrons after shutdown are delayed fission neutrons and the neutrons produced from the capture of γ-rays (photoneutrons).

The spectral distribution and strength of the fission product gamma-rays is determined by the composition of the fission products, which is dependent upon the power history of the fuel. The most probable energy of the emitted γ-rays is about 0.7 MeV [23]. This gamma-ray source will decrease exponentially in time as the fission products decay.

The production of γ-rays from neutrons is primarily from capture in the coolant and structural materials. The source contribution of photons from inelastic neutron scattering is secondary when compared to that from neutron capture. The source of γ-rays produced from the interaction of neutrons (henceforth referred to as n-γ interactions, or n-γ production) will depend

upon the neutron population and the material in the transport path. Capture of neutrons in hydrogen produces a single photon with energy of 2.23 MeV. In a PWR, low-energy neutron capture in the steel and structural materials of the vessel is prominent. The average number of γ-rays produced per capture may exceed 1; for example 1.7 photons are produced on the average per capture in iron.[23] The spectrum of emitted γ-rays is primarily of energies greater than 1 MeV (e.g. in iron, 72% of the emitted photons are of energies greater than 5 MeV) whereas the spectrum of the core fission product γ-rays is predominantly lower in energy. Thus, the detection of very-high-energy gamma-rays (E > 5 MeV) outside the pressure vessel in the γ-ray hodoscope scheme, serves to focus on the monitoring of photons emitted from the steel.

The strength of delayed neutrons is strongly time dependent in the first minutes after control-rod insertion, with the slope of the decay decreasing as time increases. This dependence is described by the point reactor kinetics equations [24].

$$\frac{dn}{dt} = \frac{\{\rho(t) - \beta\}}{\Lambda} n(t) + \sum_{i=1}^{6} \lambda_i C_i(t) \tag{2.1a}$$

$$\frac{dC_i}{dt} = \frac{\beta_i}{\Lambda} n(t) - \lambda_i C_i(t) \tag{2.1b}$$

where $n(t)$ is the neutron population at time t; $C_i(t)$ is the effective concentration of neutron precursors in group i at time t; $\rho(t)$ is the reactivity at time t given by

$$\rho(t) = \frac{\{k(t) - k_0\}}{k(t)} \tag{2.2}$$

with the effective multiplication factor as a function of time denoted by $k(t)$ and the initial value by k_0; λ_i is the decay constant of the ith precursor; β_i is the fraction of delayed neutrons in the ith precursor group, with the sum of all β_i given by β, the total fraction of delayed neutrons; and Λ is the mean generation time between the birth of a neutron and its subsequent

absorption-inducing fission. As can be seen from this coupled set of differential equations, the initial power will determine the initial neutron population at shutdown, and therefore acts as a scaling factor for the neutron source post-shutdown. Reactivity changes after shutdown must be considered because of its influence on the neutron population. The change in reactivity from control-rod insertion occurs over a very short time immediately after scram. Water coolant density changes in the core can affect the reactivity, and therefore the neutron population. The production of neutrons from sources other than fission may also alter the reactivity.

The photoneutron process, absorption of a photon with the subsequent emission of a neutron, is limited to high threshold energies. The two most common elements which undergo this process are beryllium, with a threshold energy of 1.67 MeV and deuterium, with a threshold energy of 2.23 MeV. The source of beryllium considered in this system is from the conversion by nuclear processes of boron and lithium, and therefore will be neglected. Thus the source of photoneutrons will be from the naturally occurring deuterium in the water. The density of deuterium is on the average 0.0159 atom% of natural hydrogen [25], and the largest microscopic cross section is approximately 2.4 mb for a photon of energy E ~ 4.5 MeV [26]. An estimate of the average number of neutrons emitted per photon in water is 2×10^{-8} [19]. Although the production of photoneutrons is small, it can become the primary source of neutrons after the delayed neutrons have decayed. The energy of the emitted photoneutron is given by the following relation [26]:

$$E_n = a + b \cos(\phi) \tag{2.3}$$

where E_n is the photoneutron energy; ϕ is the angle between the incident photon and the emitted neutron; and a and b are constants which are a function of the incident γ-ray energy, the mass of the target nucleus, and the interaction threshold energy. Assuming isotropic emission of the neutron, the cosine term will become zero when averaged over all angles. This leaves the following expression for the average energy of the photoneutron:

$$E_n(\text{avg}) = a = \frac{A-1}{A}\left(E_\gamma - Q - \frac{E_\gamma^2}{1862(A-1)}\right) \tag{2.4}$$

where E_γ is the incident γ-ray energy; A is the mass of the target nucleus (2.014 amu); and Q is the threshold energy (2.23 MeV). Substitution of the appropriate values and simplifying, gives:

$$E_n(\text{avg}) = 1/2\ (E_\gamma - 2.23) \tag{2.5}$$

to within 1% of the exact value.

The attenuation properties of the neutrons from the core to the pressure vessel wall, and of the γ-rays from the core to the detector are defined by the materials in the transport path. Between the LOFT core edge and the inner pressure vessel wall, there exists a total of 6 cm of water and 36 cm of stainless steel. The vessel wall itself is 10 cm of low-carbon steel. For the following discussion, iron, the primary component (68 wt.%) will be used to approximate the transport properties of steel.

In general, the attenuation of γ-rays by a material decreases for increasing energy, thus increasing the probability of penetration for very high-energy photons. The mass attenuation coefficient for 5 MeV γ-rays in water is $\mu = 0.0301\ \text{cm}^{-1}$, giving an effective mean free path of $\lambda \cong 33$ cm [26]. For lower energies, the mass attenuation coefficient is still relatively small: for γ-rays with E = 1 MeV, the effective mean free path, λ, is 14 cm. With only 6 cm of water between the LOFT core and the vessel wall, the water will only slightly affect the high-energy photon population at the detector. The steel, however, is much more dense than water and will have a greater effect on the photon flux. The mass attenuation coefficient for 5 MeV photons passing through steel is $\mu = 0.246\ \text{cm}^{-1}$, giving an effective mean free path of $\lambda \cong 4$ cm. The exponential law,

$$N = N_0\ e^{-\mu \Delta r} \tag{2.6}$$

where μ is the mass attenuation coefficient; Δr is the radial width of the material being traversed, N_0 is the initial number of particles, photons, and N, the number expected to be seen after traversing a distance Δr, is an approximation of the actual attenuation (having neglected details such as build-up factors). The equation gives an estimate of the percentage of γ-rays that will penetrate a material, or of the probability that a given photon of a

specified energy will penetrate the material. Substitution of the appropriate values for the LOFT pressure vessel (μ = 0.246 cm^{-1}, Δr = 10 cm), gives an attenuation for 5 MeV photons of 8%. The attenuation by the total amount of steel between the core and the detector (Δr = 46 cm) is a factor of 10^{+5}. This is the approximate attenuation by steel expected for core-born γ-rays, and the maximum possible attenuation due to the steel seen by a capture γ-ray produced outside the core.

The neutron attenuation process most relevant to the γ-ray detection scheme, is the absorption of neutrons which subsequently leads to the production of a photon. The microscopic cross section for gamma-ray emission from thermal neutron capture in iron is $\sigma_{(n,\gamma)}$ = 2.43 b [23], which gives a mean free path of $\lambda \cong 5$ cm. Thus, the LOFT vessel is approximately 2 mean free paths wide with respect to n-γ production. Using a similar form of Equation 2.6 (where the macroscopic cross section, Σ, is substituted for the mass attenuation coefficient, μ) and the values of $\Sigma_{(n,\gamma)}$ = 0.206 cm^{-1}, and Δr = 10 cm, gives an attenuation factor of 0.13. Thus, 87% of the thermal neutrons which enter the steel will be captured with the production of photons. Absorption of neutrons in the keV energy range is also possible, though the microscopic cross section is approximately 2 to 3 orders of magnitude smaller than that for thermal neutrons. Resonances for neutron capture also exist in the 100 keV energy range for isotopes which are components of steel.

The magnitude of the low-energy neutron capture process is dependent upon the neutron spectrum near the inner boundary of a steel region, and within the steel. Steel is a poor neutron moderator, requiring 407 collisions to reduce a neutron of energy 2 MeV (the average fission energy) to 1 eV (the thermal energy range), in contrast to water which requires only 16 collisions [27]. Thus, it is expected that the steel will not greatly thermalize incoming neutrons, leaving them to be either captured or scattered with small energy losses. Downscattering in the steel could only become significant for a relatively large high-energy neutron flux. Thus, the extent of thermal neutron capture in the steel will depend primarily upon the thermalizing capabilities of the water which precedes it. The water not only serves to produce low-energy neutrons, but will also absorb thermal neutrons. The thermal microscopic cross section for absorption is σ_a = 0.66 b, giving a mean free path of $\lambda \cong 45$ cm. The more likely process for thermal neutrons will be

scattering, with a cross section of σ_s = 103 b. Considering that the total amount of water between the LOFT core and the vessel is 6 cm, there will be more scattering than absorption in the water.

The essence of the γ-ray hodoscope water-monitoring scheme is the determination of a characteristic response to changes in water density and water level. A reduction of water density causes a reduction of the mass attenuation coefficient for γ-rays, and the macroscopic cross sections for neutrons. A reduction of μ would produce a decrease in the γ-ray attenuation caused by the water. As discussed above, the photons are not greatly affected by the water so that a decrease in water density would cause a minor change in the γ-ray population. A change in the water density will, however, affect the low-energy neutron population at the water/steel boundaries. A decrease in water density will reduce the moderating capability, and therefore decrease the thermal neutron population producing an expected decrease in the thermal neutron capture process for n-γ production. An increase in the resonance energy capture rate will be expected. The reduction of water density will also decrease the thermal neutron capture in the water, offsetting some of the loss of thermal neutron production from reduced moderation.

The ratio of steel (36 cm) to water (6 cm) between the core and the pressure vessel is very high. The LOFT reactor was designed to thermal-hydraulically respond to loss of coolant as a large-scale PWR would. To achieve this goal, several regions of steel as a core filler were included in the design as both a neutron reflector and a heat shield. Blocks of steel were again added as a vessel filler for heat transfer characteristics. The added steel fillers raise the relative amount of steel in the transport path to 86%. The effect of the relatively small amount of water is to inhibit the moderating capability outside of the core. With the large amount of thermal neutron capture and limited thermalization in the steel, the neutron spectrum may become peaked in an energy range above thermal. This would not be characteristic of the over-moderated system in a PWR.

The large amount of steel will affect the γ-ray detector response to water voiding. The voiding of water in the downcomer regions outside of the core may not have a large impact since the amount of water is small. The loss of thermalization may not be large since the spectrum is already biased in the epi-thermal energy range. Conversely, the reduction in the amount of steel

may decrease the capture γ-ray production, while increasing the probability of the photon to penetrate the steel and reach the detector. These effects will be considered in the study.

3. CALCULATIONAL METHOD AND ANALYSIS

The main purpose of the calculations is to determine the response of a γ-ray detector located some distance outside of the reactor pressure vessel to transient core conditions in which there is changing water content. The calculational model attempts to recreate the reactor conditions, accounting for as many relevant effects and details as is possible within the inherent limitations of the methods employed. Two advantages of a computational model are the opportunity to run computer experiments in which parameters can be varied over a wide range of potential physical conditions, and the ability to dissect the events into separate parts which can be studied individually. Both of these processes were done for several parameters and reactor conditions.

The calculations focused primarily on determining the γ-ray flux at a specified detector site for the Loss of Fluid Test (LOFT) research reactor during a simulated loss-of-coolant event. A one-dimensional, neutral particle transport code, ONEDANT (see Appendix Section A.2 for description), was used to calculate the γ-ray flux under various reactor conditions. The data input which comprises the computational model for the LOFT reactor, can be divided into three categories: the geometry, the source, and the cross sections.

3.1 Geometry

The cylindrical geometry option with particle transport in the radial (r-) direction was chosen to best describe the general reactor shape and detector location. (See Figure 1.) The mesh-interval volume is calculated using the cylindrical ring area ($\pi r^2_{right} - \pi r^2_{left}$) and assuming a 1-cm axial height. Inherent in one-dimensional calculation models is the assumption of an infinite reactor height with no leakage and scattering in to the mesh intervals equal to scattering out in the axial direction. Although scattering from sources above or below the calculational plane is neglected, some axial leakage for a finite system is accounted for with the buckling height correction which adds an absorption term to the calculations. The buckling was determined using the active core height of 5.5 ft. Effectively, it is the core mid-plane which is being modeled.

The detailed LOFT geometry model used in the calculations is presented in Figure 3. The geometrical configuration for the vessel internals was based on

Figure 4 (not drawn to scale) which shows the coolant flow paths. In the analysis, regions of similar flow were voided together. The core (CORE) and core bypass (H2OFLO) regions became the extended core region, and the two annular downcomer regions (labeled DNCMR and H2OFLO) voided together as the extended downcomer. The core is a homogenization of fuel, zircaloy cladding, and water. The homogenization is not a bad approximation for large distance transport problems, since the flux of interest is far from the core source. Source fluctuations within the core are dissipated along the transport path, and in the limit of very large distances, the core acts as a point source. Some heterogeneous effects more relevant for neutronics-type calculations are retained in the pin cell generated cross sections used in the source calculations. (See discussion below in Section 3.2.)

The detector site was chosen to be the first interval in the INSTRM region, as shown in Figure 3. This is located approximately at the instrumentation tube which houses the source range detectors and is where PSU placed their neutron detection system. (Refer to Figure 1.) The actual γ-ray detector would be shielded to minimize back scattering, but this was not taken into account in the model. Further details concerning the geometry configuration are discussed in the ONEDANT input description. (See Appendix Section A.3.)

To study the effects of steel and water in the transport path, another geometry model was developed. The LOFT reactor was designed to thermal hydraulically respond to transients as a commercial pressurized water reactor would. To achieve this goal, several regions of steel as a core filler were included in the design as both a neutron reflector and as a heat shield, and again added as a vessel filler for heat transfer characteristics. Therefore, the LOFT reactor contains a high ratio of steel (86%) in the transport path between the core and the reactor vessel. In a Three Mile Island II neutronic study [16], a homogenized downcomer, core barrel, water gaps, thermal shield and core liner was modeled with approximately 74% water and 26% steel. In another general pressurized water reactor study [28], approximately 83% water and 17% steel existed in the path between the core and the pressure vessel. It was the second, more extreme ratio, that was adapted into the LOFT geometry model. The mock-PWR model given in Figure 5 contains the 83% water in two regions, a small gap region and a larger downcomer region. The 17% steel is also divided into two regions, the core barrel and a filler or heat shield.

3.2 Source

There are three generated sources which are entered into the transport code to model particle generation in a reactor. They are the core neutron source, the core gamma-ray source, and the photoneutron source.

The core neutron source was generated with an eigenvalue (k) calculation for steady-state operation of the LOFT reactor. The k search option of the ONEDANT code was invoked with a non-poisoned core (no control rods, fission products or boron) and the five group EPRI-CELL generated cross sections. (See discussion below in Section 3.3.) The calculations produced a k_{eff} = 1.17. The flux, normalized to 50 MW operating power, was then converted to a volumetric source file, FIXSRC, by the utility program SOURCE. (See Appendix discussion Section A.4.3.) The source terms are generated with the following equation:

$$S_g(i) = \chi_g \sum_g \left(\nu\Sigma_f\right)_g \phi_g(i) \qquad (3.1)$$

where S_g is the volumetric neutron source in group g for interval i; $\phi_g(i)$ is the neutron flux for group g, interval i generated in the eigenvalue calculation $\left(\nu\Sigma_f\right)_g$ is the product for group g of the number of neutrons produced per fission, ν, and Σ_f, the macroscopic core fission cross section, which is taken directly from the ONEDANT output; χ_g is the fraction of fission neutrons which are emitted in group g, given in the ONEDANT cross section edit; and the sum is over all neutron groups. The neutron source is generated by a homogeneous core composition, but is spatially heterogeneous as a result of the transport properties in the k calculation.

For the post-shutdown neutron core source, the same eigenvalue calculation was carried out with the flux normalized to a new neutron power output. REKINS, a reactor kinetics program, (see Appendix discussion Section A.4.5), was run to calculate the decay of the neutron population after reactor shutdown. The calculations were performed for the insertion of the control rods from a fully withdrawn position and a shutdown k=.89. For a specific time t seconds after shutdown, the fraction of the original neutron flux provided by the REKINS output multiplied by the full power output of 50 MW, is the new power to which the generated flux is normalized. The generated spectrum is that of steady state operation, no poisons, and a supercritical eigenvalue.

An actual shutdown core would include rod poisons and have a subcritical eigenvalue. For the general transient studies, this discrepancy was neglected.

The core gamma-ray source for steady state (t=0 sec) operation and post shutdown decay was calculated by the isotope generation and depletion code ORIGEN. (For discussion see Appendix Section A.2.) The code provided the photon release rates from interactions with core materials, the fission process and the fission products, for each assembly exposed to a specified irradiation history. The total core volumetric photon release rate for each energy group was determined by summing the contribution from each assembly and dividing by the core volume. The result is an evenly distributed homogeneous core γ-ray source. The photon release rate for a given time, t, was then converted from the ORIGEN 12 group energy structure to the 20 group BUGLE energy structure (see discussion below in Section 3.3) using the mapping scheme in Figure 6, and then organized into a fixed source input file by the SOURCE program.

The photoneutron source was calculated in a two-step process similar to that for the core neutron source. First, the gamma flux in the regions containing water was calculated by ONEDANT. The resulting flux file was entered into the appropriate SOURCE program where the interaction rate for γ-ray absorption in deuterium which produces a neutron of a specified energy was calculated, and the volumetric neutron source was determined. The photoneutron energy was determined using Equation 2.5. The scheme for converting γ-ray group interaction rates to a neutron source with the appropriate energy interval is given in Figure 7.

3.3 Cross Sections

The coupled neutron and γ-ray (referred to as n-γ) cross section library, BUGLE, compiled at the Oak Ridge National Laboratory (ORNL), was the primary basis for the cross section datasets used in the calculations. BUGLE is a transport-coupled n-γ dataset library, accounting for radiative capture (n,γ) interactions within a material, but does not include γ-ray production from fission [29]. Because there is no fission production included, it is consistent to use the ORIGEN source with the BUGLE cross sections. The BUGLE library was generated for light water reactor shielding calculations. The

BUGLE package provides microscopic cross section datasets for a limited number of light water reactor materials in a 47 neutron group and 20 γ-ray group structure. These sets were collapsed from a fine group structure using a typical PWR model.

Steady-state eigenvalue calculations with the BUGLE cross sections, resulting in values of k near 0.4 failed to give a critical flux spectrum. This was the motivation for introducing the 5 neutron group EPRI-CELL generated cross section set. (See Appendix Section A.1.) The EPRI-CELL code generated LOFT specific cross sections based on the unit fuel cell compositions, which neglected control rod poisoning, provided in the code input. Eigenvalue calculations with the EPRI-CELL cross sections produced supercritical k values.

A comparison of the neutron macroscopic cross sections generated for the core regions by the two datasets showed that the BUGLE resonance absorption was high and scattering terms from the resonance groups to the thermal energies were low. Therefore, the neutrons in the BUGLE calculation were being absorbed and not thermalized as is necessary to sustain a critical reactor. Because the BUGLE library was generated for shielding calculations for a commercial PWR, the flux spectrum used in the collapsing scheme was that of a typical spectrum found outside the pressure vessel, which would not be representative of a research reactor core. Thus, while the cross sections are reasonable for transport purposes, they are not appropriate for core neutronics calculations. The EPRI-CELL cross sections are calculated specifically from the LOFT core configuration, and therefore are very appropriate for core eigenvalue calculations. Further consideration of the effects on the results of using each cross section dataset is given in the Discussion section, Section 5.1.2.

All of the neutron source calculations were performed with the EPRI-CELL cross sections. The EPRI-CELL code uses a pin cell model to calculate the flux spectrum which is used to collapse the fine group cross section data to the 5 broad group structure. Thus, although the core has been homogenized in the transport calculations, the use of the cross sections generated with a heterogeneous spectrum creates a reasonable representation of a heterogeneous core source.

In order for the BUGLE cross section set to be compatible with the 5 group neutron source, the COLLAPSE program was used to modify the neutron group structure, leaving the γ-ray structure intact. (See Appendix Section A.4.2.) The 47 neutron groups for each material were collapsed over various regions, with a straight flux weight scheme, using the fluxes generated by a BUGLE eigenvalue calculation. As discussed above, the generated flux spectrum from this calculation is not representative of the actual spectrum in and near the core. This, however, was the only viable means of reasonably generating a 67 group neutron flux spectrum for LOFT geometry, and is therefore, a limitation of the method. The approximation is not too extreme considering that the BUGLE cross sections are being used for particle transport calculations only; they are not used in source eigenvalue calculations. To minimize the impact of the collapsing process, which inherently alters the cross sections, several materials were collapsed over more than one region. Thus, for example, separate water cross sections for the core, downcomer and shield tank regions are produced. This serves to better preserve the interaction characteristics of a particular region. This new collapsed BUGLE dataset, referred to as COLLBUGL, was then transformed into an XS.ISO datafile by the COCANE program. (See Appendix Section A.4.1 for details.)

A flow chart diagram of the cross section dataset generation processes is provided in Figure 8.

3.4 L2-5 Simulation

The model of the L2-5 transient experiment followed the same general procedure described above with some modifications. The burn history in effective full power hours (EFPH) of operation at 50 MW for the peripheral (885 EFPH) and center (39 EFPH) fuel assemblies at the initiation of the test was used in the EPRI-CELL and ORIGEN calculations. An additional equivalent of 28 EFPH burn-up was acquired by the fuel during the test procedures [30]. This equivalent irradiation at 50 MW was used instead of the actual 50 hours of operation at powers between 0 and 36 MW.

The neutron core source was recalculated using a steady state power of 36 MW. The neutron decay data were recalculated using a SCRAM time and an addition of negative reactivity associated with the control rods being inserted from 1.4 meters (82% of the maximum insertion distance, or fully withdrawn position).

The core and downcomer region voiding as a function of experiment time was calculated from data provided by PSU. The data included their determination of the void fraction in the core and downcomer by mesh region corresponding to their two-dimensional model of LOFT. The void fraction was determined from LOFT liquid level transducer data and self-powered neutron detector response for the L2-5 transient [18]. The liquid level data, or "bubble plot data", has a low resolution of measurement, with the output designation for void fractions in one of three ranges: 0.0-0.2, 0.2-0.8, and 0.8-1.0. The SPND response is an interpretive guide to the water level during the event. As a result, the PSU data is speculative, and given for only specific times during the L2-5 test.

Data for the core is divided into an inner and outer region corresponding to the center and peripheral assemblies, for which the bubble plot data is provided. The void fractions of the axial regions in the inner core, outer core and the downcomer are volume averaged to provide an equivalent one-dimensional value. For consistency, only the area of the downcomer axially positioned along the active core height was used in the volume average. Thus, the upper and lower plenum voiding does not contribute to the averaged downcomer void fraction.

Figure 9 diagrams the flow of the calculations and the input/output relationship between the codes and programs used.

4. RESULTS

The results are described in five sub-sections. In Section 4.1, the sensitivity of the calculations to several parameters and the limits of applicability of the calculational methods are indicated. Section 4.2 defines the transport characteristics of the system model. The results of the homogeneous voiding studies provided in Section 4.3, quantify the effects of water voiding under various real and artificial conditions. The source decay behavior for post-shutdown times is discussed in Section 4.4. The last section, Section 4.5, presents the calculational results of the model simulation of the LOFT L2-5 transient event.

4.1 Sensitivity Studies

For several steps in the calculations, studies were performed to determine the sensitivity of a particular code or of the model in general, to various parameters and system configurations.

4.1.1 Calculational Parameters

Core neutron spectrum shape: The shape of the core neutron spectrum can be quantified with the ORIGEN code thermal, resonant, and fast input parameters THERM, RES, and FAST. The THERM parameter is a measure of how close to theoretical the actual thermal spectrum is. The RES and FAST parameters measure the strength of the resonant and fast (E>1MeV) flux, respectively, in comparison to the thermal flux. (For a detailed explanation of these terms, see Appendix Section A.2.) The spectrum parameters were calculated from EPRI-CELL results, using the methods described in the Appendix. The EPRI-CELL code was run for various conditions of pin cell geometry and burn-up over the core lifetime to establish a standard model input. The two calculated unit cell geometries, for the cold and hot conditions (see Input Description for EPRI-CELL Section A.1), produced a maximum difference in THERM, RES, and FAST of 1%. The addition of boron to the cell composition decreased the thermal parameter by 1% and increased the resonant and fast parameters by 4% and 3% respectively. Qualitatively, this is an expected shift toward the higher energies in the neutron spectrum produced by the addition of a thermal neutron absorber.

As a function of burn-up, the THERM parameter initially decreased to a minimum at 300-500 effective full power hours (EFPH) of operation and then increased with further burn-up. Both RES and FAST monotonically increased with increasing burn-up. (See Figure 10.) The maximum variation was 0.4% for THERM, 6% for RES, and 5% for FAST. Considering the above variations, the neutron spectrum, as represented by the factors THERM, RES, and FAST, is not sensitive to small changes in cell geometry or by fuel burn-up. Thus, the use of the "cold conditions" unit cell and 200 EFPH burn-up for calculations of the neutron spectrum parameters approximates the actual conditions over the life of the core to within 6%.

Core γ-ray source: An understanding of the core γ-ray source parameter dependences was gained through studies with the ORIGEN code. The ORIGEN output divides the photon release rate into three categories by type of emitter: light elements and structural materials, fission products, and heavy elements. A primary result of the calculations is that the fission product source dominates the photon release rate. The N-16 contribution to the mean energy 5.25 MeV group drops below 1% by approximately 10 seconds. Thus, calculations for the photon source are sensitive to only the content of fissionable isotopes through the dependence on the composition of the fission products. The source determination is independent of the structural content of the core.

Several runs of the code were performed with various extremes of the neutron spectrum parameters. It was found that these parameters affect the actinide and structural material photon release rates, and do not affect the fission product photon production. Therefore, to first order, the core γ-ray source is independent of the neutron spectrum in the core at shutdown, and during the transient.

Power history: The power history for the assembly affects the fission rate and therefore the photon release rate at shutdown. The decay rate and energy distribution of the photon source post shutdown are governed by the initial composition of fission products. The initial photon release rate at shutdown (t=0), will vary with the burn-up conditions, specifically the power level, the total duration of the irradiation period, and the calculational time intervals chosen to model the irradiation period. Under constant power irradiation for a specified burn period, which is the case for effective full

power hour calculations, the photon source is scaled linearly with reactor power, since the number of fission products is directly proportional to the fission rate. The calculational time intervals, or burn steps, will have a small effect on the results depending upon when the times are varied during the burn-up period. Early in the burn period, small time intervals are needed to establish an equilibrium for the fission products. Therefore, calculations performed with various time intervals early in the burn-up stage will differ to a greater extent than those calculations with changes in the later time periods.

The total photon release rate is a rapidly increasing function of irradiation time until 500 EFPH when the curve begins to level. (See Figure 11.) The fission product emitters of higher energy ($E \geq 2.2$MeV) γ-rays have an average lifetime on the order of the production rate, which is equal to the yield times the fission rate. Thus, it is seen in Figure 12, that the high-energy photon release rate after saturation is reached at about 50 EFPH, is approximately constant over the lifetime of the LOFT core, with a maximum 1% variation between two values. Thus, the core source photons above the photo-neutron threshold are independent of the core burn-up time chosen for the ORIGEN calculation.

4.1.2 Modeling Conditions

The transport and water voiding studies were performed for steady-state core sources. (See below, Sections 4.2 and 4.3.) Shutdown core conditions and voiding core coolant were studied to identify the effects on the neutron spectrum. The two configurations were simulated with ONEDANT eigenvalue calculations using the EPRI-CELL cross section dataset. The generated neutron flux values were then entered into the SOURCE programs to produce fixed source input for subsequent ONEDANT calculations. The fixed source ONEDANT calculations were used to study shutdown source effects on the neutron spectrum and γ-ray flux.

Shutdown poisons: To simulate shutdown control rod and boron poisoning, a large amount of boron (3015 ppm) was added to the core water coolant to produce a shutdown eigenvalue of k=0.90. When compared to the steady-state results, the neutron spectrum was unchanged at the pressure vessel (interval 95) and at the detector site (interval 156). At the core centerline (interval

1) and the core outside edge (interval 19) the fraction of epithermal neutrons ($E \geq 1.8eV$) increased slightly, and the fraction of low-energy neutrons ($E \leq 1.8eV$) decreased correspondingly. The maximum increase or decrease in the fraction of the total neutron population appearing in only one group, was an addition or loss of 2 percent. The resulting effect on the neutron and γ-ray flux is an increase of at most 1% for any one group at a specific interval.

Core water density feedback: The effect of changing water density on the eigenvalue was determined through a series of ONEDANT k searches for various conditions of core water voiding. The computed change in eigenvalue is dependent upon the amount of boron which exists in the coolant. Additional boron in the voiding water causes a smaller reduction in the eigenvalue since removal of water adds negative reactivity to the system, but also functions to remove a neutron control poison, adding possitive reactivity. In order to compensate for the artificially high amounts of boron in the core to simulate control rod poisons, a fixed amount of boron (1000ppm) was put into the core materials and 668ppm boron (approximate LOFT operating concentration) was placed in the coolant. The fixed amount of boron served to bring the reference initial k to approximately 1.0. The eigenvalue as a function of decreasing core water density is given in Figure 13. The value of k slowly decreases from the reference of 1.0 as initial density is decreased, then rapidly falls to .392 for a completely voided core. Thus, the estimated maximum effect of reactivity, is a reduction in the neutron source by 40%.

The neutron spectrum at the vessel and at the detector site is unchanged between the 100% core density and any of the reduced core density calculations. The spectrum however, is affected at the core centerline (interval 1) and at the core edge (interval 19). The result is a relative increase of high-energy neutrons primarily in the 7.1-821 keV energy range (energy Group 2), and a relative decrease in the lower energy groups. For the 40% core density case, the maximum difference appears at the core centerline with an increase in the fraction of total neutrons appearing in Group 2, from 34% to 45%. At the core edge, the increase for Group 2 is from 40% to 49%. The thermal neutrons decrease from 5% to 1% of the total number of neutrons at the core centerline and from 3% to 1% of the total at the core edge. For the extreme case of no core water, the fraction of Group 2 neutrons increases to about 75% of the total, and the thermal energy neutrons decrease to less than 0.1% of the total neutron population in the core.

The flux values from the eigenvalue calculations with depleted core conditions were used to generate neutron source terms for ONEDANT fixed source computations. These fixed source computations were performed with the corresponding core void conditions. Similarly, fixed source calculations with core void conditions were performed using an input neutron source generated from eigenvalue calculations with a full water density in the core.

The resulting neutron spectra and flux from the two fixed source calculations were compared to determine the propagated effects of the source terms generated with voided conditions. For a voided core at 20% of operating density, the neutron spectrum at the core edge, barrel edge and vessel edge was essentially the same for the two different fixed source calculations. The magnitude of the neutron flux increased about 4% for the fixed source calculation with the depleted core generated source terms. When the same comparison was performed for a completely voided core (0% density), a different relationship was found. The neutron spectra differed slightly between the full water and complete void source conditions in the core only and was the same at the barrel and vessel. For the depleted core source term calculation, the fraction of Group 2 neutrons increased at the core centerline, while the fraction of Group 1 neutrons increased at the core edge. The absolute magnitude of the flux decreased by as much as 20% at the core centerline, showed an increase in the high-energy neutron groups and a decrease for the low-energy groups at the core edge. Outside of the core, the absolute flux is approximately 5% less in the depleted core source term calculation.

The γ-ray flux at the detector site given by the two calculational methods were compared to determine how the effects of core voiding on the source term generation alters the response of the detector. The differences varied from an increase in γ-ray flux by 4% for the 40% core density condition, to a decrease of 2% for complete core voiding. Of the void conditions modeled, only the extreme case of no core water showed a decrease in flux for the method which includes core voiding in the source generation calculations.

Homogeneous voiding: A series of calculations was performed as a means of quantifying the error incurred by using a homogeneous voiding model to describe an active two-phase medium which can include violent boiling. The downcomer region of the LOFT model was divided into 20 mesh intervals of nearly equal volume. The first calculation assigned the first ten intervals

as 100% water density and the second ten intervals as 100% void. The second calculation alternately assigned two intervals to water, then to void, to create five water subregions and five air subregions. The third calculation alternately assigned each interval to water and to void. This model was designed to imitate bubbles in the downcomer region with an average water density of 50% over the entire region. The air region width, or effective bubble diameter is 2.5 cm, 0.52 cm, and 0.26 cm for the 1-, 5- and 10-bubble configuration, respectively. In the limit of an infinite number of bubble and water subregions, the homogeneous voiding conditions is attained. To determine any streaming affects due to the water region being the initial region after the barrel and air being the material prior to the vessel filler, the water and bubble order was reversed and the calculations repeated.

The detector site gamma-ray flux results for the bubble simulation is presented in Table 1, along with the values for 50% homogeneous voiding. The maximum discrepancy between the water region first and the air region first is 3% for 1-bubble and decreases for the 5- and 10-bubble calculations. All of the simulated bubble flux values are less than the homogeneous case. The minimum value occurs for the 1-water/1-bubble calculation giving a maximum 4% variation from homogeneous voiding. The fluxes increase as the number of bubbles increase for the water region first calculations. The largest bubble simulation flux values occur for the 1-bubble/1-water configuration giving a minimum variation with the homogeneous values of 2%. For the air first configuration, the fluxes tend to decrease with increasing numbers of bubble regions.

The high-energy and thermal energy groups (Group 1 and Group 5, respectively) were used for comparison with the homogeneous case to determine the effect of bubbles on neutron flux. As can be seen in Table 2, the neutron flux follows the same trends and qualitative behavior as described above for the high-energy γ-ray flux. The maximum variation between bubbles and homogeneous voiding for high-energy neutrons is 18%, and for thermal neutrons is 23%, both found in the 1-bubble/1-water configuration.

4.2 Transport Studies

The transport characteristics of the system model were studied with the one-dimensional transport code ONEDANT. (See Appendix Section A.3 for description.) The calculations were performed with various combinations of the steady-state neutron, gamma-ray, and photoneutron sources. The code was run for both a neutron or gamma-ray problem separately, and as a coupled n-γ calculation.

4.2.1 Loft Geometry

Flux: Sample values for the LOFT geometry n, γ, and n-γ flux calculations are provided in Tables 3 and 4. The discrepancy in neutron flux between the neutron only EPRI-CELL values and the collapsed BUGLE (COLLBUGL) generated values arise as a result of the characteristic differences of the two cross section sets. The COLLBUGL low-energy flux values are depressed at the core edge due to high resonance absorption and reduced downscattering in the core region. The flux differences between the γ-ray calculations arise from the addition of the (n,γ) interaction in the COLLBUGL computations. The neutron capture interaction in steel which produces predominantly high-energy photons, accounts for the total γ-ray flux in the neutron source only COLLBUGL computation. As can be seen from the flux table, at steady-state operation, the neutron-capture γ-ray source overwhelms the core γ-ray source at the detector site by 8 orders of magnitude.

At steady-state operation, the photoneutron source contribution has been determined to be completely negligible when compared to the core neutron source. The resulting gamma-ray flux from photoneutron n-γ reactions is approximately 7 orders of magnitude less than that produced by prompt and delayed neutron n-γ reactions, and therefore is insignificant. (See Table 5.) An estimate of the photoneutron source using ONEDANT generated γ-ray fluxes shows a neutron emitted per photon absorbed ratio of 0.5×10^{-8}, a factor of 4 disagreement with a previous publication [19] which used the value of 2.0×10^{-8}. Therefore, because of the relative magnitude, the photoneutron source contribution was neglected for the steady-state spectrum calculation studies.

Attenuation: Neutron attenuation is approximately 2 orders of magnitude from the core to the vessel. The γ-ray attenuation is 5 orders of

magnitude from the core to the pressure vessel and 7 orders of magnitude from the core to the detector. The effective photon attenuation, the sum of losses and production over the distance of the transport path, is approximately 2 orders of magnitude from the core to the vesssel, and 3 orders of magnitude from the core to the detector.

Neutron spectrum: The neutron spectrum behavior was determined for the LOFT geometry using the ONEDANT generated core neutron source in a transport calculation with the 5 group EPRI-CELL cross sections and with the 25 group collapsed BUGLE (COLLBUGL) cross sections separately. The first interval outside the core (19), the first core barrel interval (39), and the first vessel interval (95) were the primary points of interest for the neutron spectrum comparison study. The two calculations show a similar spectrum behavior with slight differences in the intermediate energy range. The EPRI-CELL calculations result in a higher attenuation of neutrons by a factor of approximately 2 in the upper energy range to 7 in the thermal group. Again, the discrepancy between the two calculations is a direct result of the different characteristics of the two cross section sets.

The neutron spectrum for LOFT is a relatively hard spectrum as can be seen in Figure 14, which charts the fraction of total neutrons as a function of energy group for each point of interest along the transport path. Looking primarily at the 25 group COLLBUGL data, the neutron spectrum peaks at the 7.1-821 keV energy range at all three locations. At the core edge, there is a relatively high number (24% in Group 1; E≥821 keV) of high-energy neutrons which are scattered and absorbed until they reach the vessel where they comprise only 3% of the total number of neutrons. The second and third energy groups, E=1.8eV to E=821keV, increase in the fraction of the total number of neutrons with a relatively small change in spectrum shape. The thermal neutrons begin as 1% of the neutron population at the core and are 2% of the total at the vessel. This behavior of highly-attenuated, high-energy neutrons, stability in the thermal group, and slight relative increases in the intermediate resonance region is a result of the high volume of steel in the neutron path which scatters high-energy neutrons and absorbs thermal neutrons.

Gamma-ray spectrum: The steady-state gamma-ray spectrum was examined for the propagation of both the core γ-ray source and the (n,γ) interaction production photons. The ONEDANT transport code was used with the BUGLE cross

sections and ORIGEN generated source terms for the core γ-ray source spectrum analysis. The neutron and γ-ray core sources and the COLLBUGL cross sections were entered into the transport code for the total gamma-ray production analysis. The core edge (interval 19), the vessel inner boundary (interval 95), and the detector site (interval 156), were chosen as points of study along the transport path.

At the core edge, the γ-ray spectrum above 1 MeV for both source calculations peaks in the 1.0-1.5 MeV energy range. The peak at the pressure vessel and the detector site, appear in the 2-3MeV group for the n-γ calculation and in the 3-4MeV group for the γ-ray only calculation. For the n-γ calculation, the very high energy ($E \geq 5$MeV) γ-rays comprise 2.3% of the total gamma-ray activity at the core edge, increase to 19.2% at the vessel, then decrease to 8.7% at the detector site. Considering only the attenuation of the core source, the high-energy γ-ray flux is .07% of the total at the core edge and increases to 1.2% and 1.8% at the vessel and detector respectively. The relative amount of γ-ray flux above the photoneutron threshold ($E \sim 2.0$MeV) is similar for the two calculations at the vessel and detector (~30%) although they initially differ at the core with 21.9% in the n-γ calculation and 7.8% in the γ-ray only calculation.

4.2.2 Mock-PWR Geometry Comparison

Flux and attenuation: The steady-state neutron and gamma-ray fluxes and spectra for the mock-PWR geometry were also studied. The neutron flux is presented in Table 6 and the γ-ray flux is given in Table 7. The neutron flux is attenuated between the core and the vessel by approximately 3 orders of magnitude, a factor of 10 more than for the LOFT geometry. The gamma-ray attenuation has been greatly reduced to 4 orders of magnitude from the core to the detector, as compared to a factor of 10^7 for LOFT. The effective gamma-ray attenuation, accounting for both loss and production, is a factor of 10^3, which is the same as for the LOFT calculations. The absolute γ-ray flux values at the detector are about a factor of 1.5 larger for the mock-PWR as compared to LOFT. Thus, although the amount of steel in the transport path has been drastically reduced in the PWR geometry, a greater fraction of the photons produced from n-γ interactions in the steel are reaching the detector. It also appears that although the LOFT geometry has a greater transport

distance over which n-γ interactions can occur, the steel acts as a large γ-ray sink which reduces its effective source strength.

Neutron spectrum: The neutron spectrum analysis for the mock-PWR geometry was performed for both the 5 group EPRI-CELL and 25 group COLLBUGL cross section datasets. The points of interest in the study were the same, with the first barrel interval at a new position, mesh interval 53, in the PWR geometry configuration. Unlike the results obtained with the LOFT geometry, the neutron spectra obtained in this case show the peak flux for the EPRI-CELL calculation in the 3rd energy group (1.8eV<E<7.1keV) at the barrel and vessel, but in the thermal group (E<1.1eV) for the COLLBUGL calculation. The EPRI-CELL spectrum shape does not change very much as the neutrons diffuse from the core to the vessel. In contrast, the COLLBUGL spectrum gradually becomes more thermal with relative decreases in the upper energy groups and a substantial relative increase, from 3% to 51%, in the thermal group. The spectrum from the COLLBUGL calculation is presented in Figure 15.

In comparing absolute magnitudes, the pressure vessel neutron flux from the LOFT geometry is greater than that of the mock-PWR model by nearly a factor of 10 in all groups of the EPRI-CELL calculation, and in all but the thermal group of the COLLBUGL calculation. The PWR geometry thermal group flux is approximately a factor of 2 greater than the corresponding LOFT geometry value.

Gamma-ray spectrum: The mock-PWR geometry gamma-ray spectrum study employed the same method as described above for the LOFT geometry analysis. The peak flux for the n-γ coupled calculation occurs in the 1.0-1.5 MeV range at the core and in the 2-3 MeV range elsewhere, which is nearly the same (except at the barrel), as for the LOFT geometry. In contrast, the peak flux behavior for the γ-ray only calculation differs between the two geometries. For the mock-PWR configuration, the maximum flux values appear in the 1.0-1.5 MeV group from the core to the vessel and in the 2-3 MeV group at the detector, whereas there is a gradual increase in peak flux energy from 1.0-1.5 MeV to 3-4 MeV for the LOFT geometry.

The fraction of high-energy photons at the detector site is less for the mock-PWR configuration. In the n-γ calculation, the fraction of very high-energy γ-rays (E≥3MeV) is approximately the same for the two geometries, but the fraction of photons above 2 MeV is 31% for the LOFT model and 22% for

the PWR model. Considering the transport of core γ-rays only, the fraction of photons in the E≥5MeV, E≥3MeV and E≥2MeV ranges was 1.8%, 25%, and 34% respectively in the LOFT calculation. The corresponding mock-PWR values are 0.07%, 15%, and 26%.

Although the geometry configuration for the two models is the same beyond the first vessel interval (95), the spectrum behavior between the vessel and detector site differs. In both the γ and n-γ calculations, the attenuation of photons below a specific energy, 3 MeV in the first and 8 MeV in the latter, is greater for the mock-PWR geometry.

4.3 Homogeneous Voiding Studies

The effects of changing water density on flux and spectrum behavior was studied for both the LOFT and mock-PWR models. The steady-state sources were used and kept constant for this analysis. The impact on photon attenuation of varying water density was determined using the γ-ray core source and the BUGLE cross section dataset. The effects on neutron attenuation and the more complex interaction of (n,γ) production and γ-ray attenuation were examined with the 25 group COLLBUGL cross section set and the core neutron and photon sources.

4.3.1 Flux and Attenuation: LOFT Geometry

Region voiding: Figure 16 presents the detector site γ-ray flux from the attenuation of core photons only, as a function of changing water density in various regions of the LOFT model. The increase in γ-ray flux for E≥5MeV from core voiding (from steady-state operating water density to 0% water density, or 100% void) is a factor of 1.1, the same as for downcomer voiding (100% density to 0% water density). The total water voiding calculation includes the voiding of the two narrow water regions H2OFLO and H2OGAP, (refer to Figure 3), and produced an increase in γ-ray flux above 5MeV of 1.2. For a γ-ray flux of energies above 3MeV, the factor increases were 1.01 for core voiding, 1.1 for downcomer voiding and 1.2 for total water voiding. From the figure and the increase-factors, it can be seen that changing water density has a small effect on gamma-ray attenuation.

The very high-energy (E≥5MeV) γ-ray flux variation with water density for the coupled calculations is presented in Figures 17 and 18. The flux

increases by a factor of 4.3 for complete core voiding and downcomer voiding separately, and by a factor of 22.5 for the complete voiding of the core and downcomer together. The extended core and downcomer include the H2OFLO and H2OGAP regions, respectively. The voiding of these combined regions produced an increase in flux by a factor of 4.8 for the extended core and of 5.2 for the extended downcomer, and the sum, or total voiding, showed an increase by a factor of 33.4. Nearly identical behavior was observed for the flux of photons with energies above 3MeV. Some small differences were seen when the flux was extended to include photons of energies down to 1MeV, with voiding in various combinations of regions producing increase-factors greater than, equal to, and less than those of the E≥3MeV responses. For the total water voiding, the increase in flux of energies above 1 MeV was a factor of 35.7.

Downcomer configurations: The downcomer condition of full water density below and complete void above a distinct waterline, which is below the core boil-off interface, was postulated for the time after the pumps were shutdown during the Three Mile Island II incident [16]. Also, the experimental data for the LOFT L2-5 test for times between approximately 10 and 20 seconds show the downcomer with a void fraction between 0.2 and 0.8 while the core is reported to have a void fraction greater than 0.8 [31]. In response to the above core and downcomer water configurations, a study was performed of core voiding under different extended downcomer (DNCMR and H2OGAP) void conditions. The extreme situation of no downcomer water and core voiding resulted in an increase in the high-energy (E≥5MeV) γ-ray flux by a factor of 5.2 from 100% core operating water density to 0% water density. The flux increase-factor with the downcomer at 10% density, or 90% void fraction, was 5.0, and for a downcomer density of 50%, the flux increase was a factor of 4.6. As stated above, the increase-factor for core voiding with 100% downcomer density was 4.3. Figure 19 presents the core voiding curves for each extended downcomer void fraction. The increase in downcomer void fraction slightly enhances the resulting core void flux changes.

Vessel thermal neutron behavior: As was shown above, the steady-state gamma-ray flux for the full coupled calculation is from (n,γ) interactions. Thus, the change in gamma-ray flux from core voiding for the COLLBUGL calculations will have some dependence upon the thermal neutron flux changes. The increase-factors for the thermal neutron group in the pressure vessel were

determined. Mesh interval number 105 was chosen for this study because it is located just beyond the midpoint distance of the vessel and is least affected by boundary conditions. Activity at the inner boundary of the vessel is greatly affected by the density of the H2OGAP water region there, and the outer boundary is affected by the void region which follows the vessel. For comparison, the thermal neutron flux differences were determined for both the EPRI-CELL cross section dataset and the COLLBUGL cross section dataset calculations. The COLLBUGL calculations are the same calculations which were used to extract the above γ-ray flux factors. A comparison of the increase-factors from 100% density to 0% density (100% void) is given in Table 8. As can be seen from the table, the high-energy γ-ray flux at the detector follows the change in thermal neutron flux in the pressure vessel. The EPRI-CELL values are generally higher when compared to those of the COLLBUGL calculations. Thus, if the relationship between thermal neutron and γ-ray flux changes which resulted in the COLLBUGL calculations, is extracted to the EPRI-CELL neutron only calculations, a slightly greater change in the γ-ray flux at the detector site would be reported in response to water density changes.

High-energy neutron response: For comparison between the γ-ray and fast neutron detection methods, the neutron flux above the PSU established cut-off energy of 1.8 eV was studied as a function of changing water density in several regions of the LOFT geometry. Like the γ-ray flux, the neutron flux changes were monotonically increasing functions of increasing void fraction. The change in flux from operating density to 0% water density is a factor of 3.7 for the core voiding, and a factor of 3.6 for the downcomer voiding. The flux increase-factors for complete extended core voiding, extended downcomer voiding, and total water voiding are 4.1, 4.8, and 25.8 respectively.

4.3.2 Flux and Attenuation: Mock-PWR Geometry Comparison

Region voiding: In order to estimate the transport effect of the steel to water ratio, the mock-PWR model was used in several void calculations. In this model geometry, there are three regions which contain water: CORE, H2OFLO, and DNCMR. (Refer to Figure 5.) The effect of water density changes on strictly photon attenuation for the mock-PWR geometry is presented in Figure 20. For the E≥5MeV flux, the increase-factor from 100% to 0% operating

water density for core voiding is 1.1, for downcomer voiding is 1.7, and for total water voiding is 2.7. The downcomer and total water increase-factors are slightly greater than for the LOFT geometry. For the coupled n-γ calculation, the high-energy γ-ray flux changes for several voiding conditions are presented in 21. The core, downcomer, and extended downcomer, (H2OFLO and DNCMR), show an increase in flux by a factor of 3.8, 3.6, and 36.7, respectively. The total voiding resulted in an increase by a factor of 183.5. The values for the flux of photons of energy 1MeV or greater varied from the very high-energy flux behavior. Factors of 3.3, 4.2, 47.6, and 239.0, were calculated for the core, downcomer, extended downcomer, and total water voiding, respectively. These factors show an extremely dissimilar behavior compared to the LOFT geometry calculations.

High-energy neutron response: As with the LOFT model, the epi-thermal neutron flux ($E \geq 1.8eV$) was studied as a function of changing water density in the mock-PWR model. For core voiding, the increase in flux from operating density to complete void was 3.1. The increase-factors for downcomer voiding and extended downcomer voiding (DNCMR and H2OFLO) were 66.5 and 1049.9 respectively. The change in neutron flux for complete water voiding was determined to be a factor of 3904.2, an increase by 2 orders of magnitude from the LOFT geometry model result.

Increase-factors: The series of above calculations include various combinations of voiding regions. An examination of the increase-factors reveals that for two regions, the product of the respective increase-factors is less than or approximately equal to the increase-factor from voiding of the combined regions. For example, the n-γ calculation for the LOFT geometry resulted with a flux, a factor of 4.3 larger than operating conditions for the core voiding alone and for the downcomer voiding alone. The product, 18.5, is less than the factor increase in flux for the core and downcomer voiding taken together (22.5). This suggests that there is a more complicated interaction than the common simplification of the multiplication of two exponential attenuation factors. This intricate dependence is consistent with the disproportionately large flux increases found in the PWR geometry total water voiding calculations.

4.3.3 Neutron and Gamma-Ray Spectra: LOFT and Mock-PWR Geometries

Voided core: An analysis of the neutron and gamma-ray spectra for two voiding conditions was performed in both the LOFT and mock-PWR geometry model. One analysis was for the core water at 20% normal density and the other for 10% downcomer density. The voided core produced an increase in the relative number of neutrons in energy group 2 ($7.1/keV \leq E \leq 821keV$) and a decrease in the other energy groups at the core edge for both the LOFT and PWR geometry models. The neutron spectrum at the core barrel and at the vessel for the reduced core water density calculation has been restored to the shape of the reference 100% density calculation, necessitating an increase in thermal neutrons between the core and the barrel. The gamma-ray spectrum for the same reduced core density calculation was unchanged in the LOFT geometry. In the PWR geometry, the initial distribution of γ-rays at the core edge was altered by an increase in the fraction of very high energy photons, $E \geq 3MeV$, from 11% to 13%. The attenuation of the high-energy photons as they diffuse from the core to the detector is the same for both the full core and voided core calculations.

Voided downcomer: The voided downcomer calculation did not change the neutron spectrum at the core and barrel. Both geometry models show a decrease in thermal and epi-thermal neutrons at the vessel edge in comparison with the reference calculation, with a corresponding increase in the high-energy neutron groups. Specifically, the LOFT geometry showed an increase in primarily group 2 ($7.1keV \leq E \leq 821keV$) neutrons with a decrease in groups 3, 4, and 5 ($E < 7.1keV$). The mock-PWR geometry, however, showed an increase in all groups except the thermal group which was 11% of the total as compared with 57% in the normal water density calculation. In each model, the density of the water regions next to the vessel was modified, thus reducing the amount of thermalization between the barrel and the vessel. The overall attenuation between the core and the vessel has been greatly reduced in the PWR model, by as much as a factor of 100 in the non-thermal groups and a factor of 5 in the thermal group. The decrease in attenuation for the LOFT downcomer void calculation was not as large. A maximum of a factor of 5 was found for the non-thermal groups and the increase in attenuation in the thermal group was by a factor of 3.

The photon spectrum at the core edge was essentially unaffected by the downcomer voiding. At the vessel, the LOFT geometry produced a depression of 2% in the fraction of high-energy photons (E≥2MeV), in contrast to the mock-PWR model which showed an increase of 3% when compared to the normal water density calculations. This difference arises from the large amount of steel in the LOFT model which absorbs a greater fraction of the γ-rays produced, and the fact that the removal of 90% of the total water within the vessel still leaves more water in the mock-PWR system. The detector site showed an increase in the high-energy fraction of 1% in the LOFT calculations. For the PWR geometry, the fraction of photons above 5MeV was unchanged, the fraction of photons above 3MeV increased by 1%, and the fraction of photons above 2MeV increased by 4%.

Vessel interaction rates: The interaction rate, the product of the energy dependent macroscopic cross section and the absolute flux $(\Sigma_{(n,\gamma)}\phi_n)$, defines the neutron capture production of γ-rays within a material. Inherent in this expression is the dependence of the n-γ production rate on the shape of the neutron spectrum and the magnitude of the neutron flux. The cross sections are larger for lower energies, favoring thermal neutron capture, but are significant at the higher resonant energies. As discussed above, both the neutron flux and the spectrum at the vessel is altered by the voiding of water. Therefore the interaction rate within the vessel is dependent upon the water density. The shape of the group flux (and thus the group interaction rate) as a function of position in the vessel is dependent upon the water density in the region preceding the vessel. The flux shape will change only when the H2OGAP region in the LOFT model and the DNCMR region in the mock-PWR model is voided.

The effect of water voiding on the interaction rate in the vessel is presented in Figure 22 for the LOFT geometry. The graph shows the epi-thermal (E>1.8eV) and nearly thermal (E<1.8eV) interaction rate as a function position (interval) in the vessel for two water conditions: normal operating density and 10% of normal density in all water regions. (The interval radial width is constant throughout the vessel.) The epi-thermal interaction rate for normal water density monotonically decreases, while the low-energy rate initially decreases to a minimum at interval 103 then increases to a value at the outer edge (interval 110) which is higher than that at the inner edge (interval 95).

The shape of the curves is altered for the 10% density (or 90% void) conditions. The magnitude of the interaction rates has increased as expected. The relative position of the epi-thermal curve with respect to the thermal energy curve has changed, showing an increase of high-energy neutron capture. The minimum point for the low-energy curve has moved toward the inner boundary (interval 100) and the maximum flux at the outer boundary is a factor of 13 larger than the minimum as compared to a factor of 7 for the 100% water density case. The interaction rate of the epi-thermal neutrons is greater than the low-energy rate at the inner vessel boundary for the voided configuration.

The increase in the thermal neutron capture rate after a specified penetration depth in the vessel shows that the downscattering of neutrons into the lower energy groups is significant, becoming greater than the absorption rate. Although the cross section for downscattering is two orders of magnitude smaller, the thermal flux drops below this amount approximately 6 cm into the steel for the normal water density case and within 3 cm for the reduced density case. The curves also show that the epi-thermal neutron capture is a significant contribution to the total interaction rate. For the normal water density case, the epi-thermal neutron capture is 43% of the integrated total interaction rate for the vessel, and is 50% of the total for voided conditions.

The above analysis was repeated for the mock-PWR geometry model with the interaction rates presented in Figure 23 for the 100% and 10% total water density conditions. As discussed in Section 4.2.2 the neutron spectrum is thermal so that the point in the vessel at which the thermal flux falls below the epi-thermal flux by two orders of magnitude is closer to the outer edge (interval 106) than for the LOFT geometry. This is not drastically altered in the 10% case which shows a minimum interaction rate for the thermal flux at interval 105. In this geometry, the thermal neutron capture dominates the interaction rate contributing 90% of the total interaction rate integrated over the vessel for the normal water density case and 66% of the total for the voided conditions. The increase in contribution from the epi-thermal interaction rate caused by water voiding is much greater for the mock-PWR geometry.

The corresponding γ-ray flux shapes in the pressure vessel of the LOFT geometry found in the n-γ coupled calculations, are given in Figure 24 for the

high-energy photons with energies above 5MeV. The two curves, one for total water, the other for 90% void, are similar, each having the maximum flux in the first vessel mesh interval, 95, and the minimum flux in mesh interval 105 and 102 for the total water and 10% density conditions respectively. These curves show the characteristic behavior of the sum of the epi-thermal and low-energy reaction rate curves described above.

4.4 Decay Calculations

Gamma-ray source: The high-energy (E≥2MeV) photon release rate is plotted in Figures 25 and 26, as a function of decay time for the square assembly during the first minute and during an extended decay time for the LOFT L2-5 transient event initial conditions. The expected exponential decay is evident over the 30 minutes after scram. For the first minute, the decay is very well approximated with a linear fit. More significantly, during those first 60 seconds, the release rate decreases by only 15%. Over the 30 minutes, the release rate decreases by 63% of the initial value. The very high-energy, E≥5.25MeV, photon release rate for the square assembly as a function of decay time is also presented in Figures 25 and 26. The first plot shows the decay curve for times t=0 to t=60 seconds, in which the flux decreases by only 12% of the initial value. The second figure is a semi-log plot of the decay for 30 minutes post-shutdown. The curve is nearly linear with an effective exponential decay constant of $\lambda \sim 4 \times 10^{-3}$. The release rate decreases by over 3 orders of magnitude during those 30 minutes. To first order, these decay curves qualitatively describe the post-shutdown detector response to core γ-ray sources. The transport properties have obviously been neglected here with the assumption that photons of all energies are absorbed and scattered at the same rate.

Neutron source: The core neutron decay rate for times t>0 after the initiation of the transient, has been determined for LOFT using the utility program REKINS. (See Appendix Section A.4 for discussion.) The total volumetric delayed neutron source from core fissions only, as a function of time post shutdown is illustrated in Figure 27. The curve was calculated using the initial steady-state total source normalized to 50MW, and the neutron fraction as a function of time generated by the REKINS program, assuming an insertion of reactivity from the control rods only. Sources other than from fission have not been included.

The post-shutdown neutron source from spontaneous fission and α-particle absorption (for example, (α,n) reactions in oxygen) was determined from the ORIGEN calculations. The neutron source is stated in particles per given amount of fuel, in this case, a fuel assembly. The constant total core neutron source over the 30 minute decay time is 8.21×10^4n/sec, giving a volumetric source term of 0.166n/cm^3/sec. At 30 minutes, the total core delayed neutron source is 5.44×10^2n/cm^3/sec, well above the ORIGEN neutron source contribution, which was subsequently neglected.

Source contributions: Using the decay curve and steady state neutron and gamma-ray flux relationships, estimates were made to determine the time at which negligible sources at t=0 seconds can no longer be ignored. The steady-state gamma-ray flux from core neutron n-γ production at the detector is approximately 7 orders of magnitude greater than the γ-ray flux at the detector site from the core fission product photon source only. A decrease in neutron flux of 10^7 occurs at about 13 minutes. The core source decay has been neglected because the decrease for E$\geq$2MeV photons is less than an order of magnitude over the 30 minute decay time.

The photoneutron source flux at steady-state is approximately 8 orders of magnitude less than the flux from core neutrons. Thus, at 16 minutes post-shutdown, the core neutron flux will be comparable to the steady-state photoneutron source. However, the photoneutron source will also decay with the n-γ production rate, but will not drop below that produced by the core γ-ray source. Considering a γ-ray flux of about 10^{12} γ/cm^2 sec at t=0 from the core fission product photon source only, a deuterium number density N~10^{-6} atoms/b-cm, and the maximum photoneutron production cross section of $\sigma(\alpha,n)$=2.4mb, the generated photoneutron source is on the order of 10^4 n/cm^3-sec. The core delayed neutron source decays to this level at approximately 25 minutes.

For 20 minutes post-shutdown, the relative contributions to the neutron and gamma-ray flux at various points in the system are presented in Table 9. From the table, it can be seen that the photoneutron flux is 1% or less of the total neutron flux in the core and at the vessel. The core γ-ray source dominates the photon flux at the core edge. As the photons are transported through the system, the core γ-rays are absorbed and scattered, and progressively contribute less to the total flux. As more steel is encountered by the neutrons along the transport path, the n-γ production increases until it

becomes the major source of photons at the detector. Specifically, at the detector site, the core sources contribute 4% to the very high energy, E≥5MeV, γ-ray flux, 35% to the E≥3MeV flux, and 14% to the E≥1MeV flux.

The above analysis was repeated for 30 minutes post-shutdown, with the relative flux contributions presented in Table 10. The photoneutron source becomes the primary contributor to the core neutron flux and constitutes approximately half of the vessel flux. The corresponding γ-ray flux from the photoneutrons significantly contribute, by 9%, to only the very high energy (E≥5MeV) flux at the detector site. The core neutron n-γ production also significantly contributes to only the E≥5MeV flux at the detector site (8%) giving a total neutron capture contribution of less than 20%. The core γ-ray source is the only contributor to the flux at all points for photons of energy E≥3MeV. At this time, the γ-ray flux from the fission product photon source dominates throughout the system.

4.5 L2-5 Experiment Simulation

Sources: The ORIGEN code was run with neutron spectrum input parameters THERM=0.576, RES=0.396, and FAST=3.135, for a total irradiation time of 913 EFPH for the square and triangle fuel assemblies, and 67 EFPH for the center assembly. The decay times were chosen to correspond with the void data-points derived from the PSU information. The tables for the photon release rates after shutdown for the center, square, and triangle fuel assemblies under L2-5 transient conditions are given in the appendix as Tables 11, 12, and 13, respectively.

The steady-state core neutron flux was calculated with a ONEDANT eigenvalue calculation and normalized to a total power of 36 MW. After processing the neutron flux through the SOURCE programs, the volumetric neutron source was determined to be 9.34×10^{14} n/cm^3/sec, resulting in a ONEDANT calculated total source of 2.75×10^{18} n/sec/axial cm. (This can also be considered as the total source for a core with 1 cm axial height.)

A normal shutdown decay curve was calculated for the L2-5 event. The neutron and gamma-ray decay sources were calculated as described above. The transient decay curves were calculated for both the high-energy gamma-ray and epi-thermal energy neutron fluxes at the detector site.

Voiding: As explained in Section 3.4, the void data for each time data-point is a homogenization of the void fraction data provided by PSU. The calculated volume fractions used as input for ONEDANT are given in Table 14. A pictoral representation of water voiding during the transient is given in Figure 28, which presents the core inner and outer regions, and the downcomer region void fractions as a function of time.

Gamma-ray detector response: The very high-energy γ-ray flux located at the detector site was calculated as a function of experiment time and is presented with the computed normal shutdown results in Figure 29. The figure gives the calculated flux under voiding conditions conditions for discrete times, along with a computer generated fit of the data points. It can be seen from the graph that the experiment simulation curve deviates from normal shutdown flux values during four distinct time periods: 0-55 sec, 174-225 sec, 235-460 sec, and 611-750 sec.

Figure 30 focuses on the initial core voiding results over the first 0-60 seconds. During this time, the core and downcomer were modeled as completely voided beginning at 15 seconds and remain so until core reflood begins at approximately 36 seconds. The maximum deviation from normal shutdown during this interval occurs at 21 seconds with an increase in flux by a factor of 33.7.

The second deviation, beginning at 174 sec and returning nearly to normal at 225 sec, is small, as can be seen in Figure 31. The maximum increase in flux appearing at 182 seconds is by a factor of 1.5 over the normal decay results. During this time interval, the outer core maintains a 3% void fraction while the inner core increases to a maximum 18% void fraction at 182 seconds, and then drops to a 9% void fraction at 225 seconds. The downcomer follows the same pattern with a maximum void fraction of 16% at 182 seconds, and a return to 0% void at 225 seconds.

The third time period also depicted in Figure 32, shows a major deviation from the normal shutdown curve. The absolute flux during this time interval rises to an initial peak at 300 seconds, appears to decrease with the next data point at 331 seconds, increases to a major peak at 380 seconds, and finally decreases to normal at 460 seconds. Although the absolute flux rises and falls, the deviation from normal shutdown values increases monotonically to a maximum of 15.5 at 380 sec. A quick glance at Figure 28 reveals that the

inner core region and the downcomer curves both rapidly rise to an initial large void fraction at about 300 seconds, level off, then rapidly rise again to their maximum void fractions of 88% and 100% respectively. The decrease in absolute flux at 331 seconds is a result of constant void fractions and a decrease in source terms from natural decay.

Figure 32 presents the last deviation which begins at 611 seconds and ends with the return to normal decay values at 750 seconds, the last data-point. The deviation is small, with a maximum increase in flux by a factor of 1.8 at 676 seconds. During this time period, the outer core region remains at 0% void. The inner core region and the downcomer region both increase in void fraction to a maximum of 35% and 44% respectively at 676 seconds, and return to 0% void at 750 seconds.

Neutron detector response: For comparison purposes, the epi-thermal ($E \geq 1.8eV$) neutron flux at the detector site was also determined for the L2-5 Experiment, and is presented in Figure 33 in a similar format as the γ-ray results, with a computer fit of the discrete calculational data points. In general, the neutron flux behavior is similar to that of the γ-ray flux discussed above, with peak deviations from normal shutdown being either the same or smaller. Specifically, the first deviation interval of 0-55 seconds showed a maximum increase-factor of 25.8. The second time period resulted in a peak deviation from normal shutdown of 1.5 at 182 seconds. The third interval showed the same two apparent peaks as with the γ-ray flux, but the difference between the voided condition and the normal decay was a factor of 13.3 at 380 seconds. The final deviation interval resulted with an increase by a factor of 1.8 at 676 seconds.

A graphic illustration of the deviation from normal shutdown decay values is presented in Figure 34. The L2-5 experiment fluxes were normalized by dividing with the corresponding decay curve flux values. The result is a graph of the increase-factors for both the high-energy gamma-ray and neutron flux as a function of experiment decay time.

The LOFT intermediate range detector is an ion chamber compensated for γ-ray flux, located in an excore instrumentation tube and positioned axially at the core mid-plane [12]. The instrument tube is similar to the one used for the PSU neutron detectors, and forms the basis of the geometry model detector site position. Detailed data on detector operating characteristics were not

available. Therefore, for simplicity, an infinite detector cross section for neutrons of energy E≤0.1eV, the upper limit for thermal energy Group 5, and a zero cross section for neutrons above this energy limit was assumed. The following normalizing equation was used for the detector response:

$$V_{norm} = \omega + 0.0496 \, \ell n \, (\phi)$$

where ϕ is the thermal neutron flux and ω is a normalizing constant to coordinate the simulated detector response at t=0 to the normalized experimental value [18]. The constant was calculated as ω=-0.3065. The simulated detector response along with the normalized experimental detector data are given in Figure 35.

5. DISCUSSION

This section assimilates the calculational results and discusses various aspects of the γ-ray detection system and the calculational model. Section 5.1 provides a detailed review and explanation of the LOFT L2-5 Simulation results along with a comparison with the available neutron experimental and calculational results. Section 5.2 presents an estimate of expected detector operating characteristics. Section 5.3 discusses the calculational model, its applicability and limitations. Section 5.4 presents a comparison between the LOFT and mock-PWR geometry model results, and a discussion of extending the implied results to a full sized PWR. Section 5.5 compares the estimated response of the epi-thermal neutron detection system and the high-energy γ-ray detection method.

5.1 L2-5 Simulation

The LOFT large-break loss-of-coolant test, L2-5, was computationally simulated to show how a γ-ray detector located at the instrument tube would respond to coolant voiding conditions in the pressure vessel. A review of the expected detector response is presented below. The distinct advantage of using the LOFT reactor as the basis of the model, is the ability to compare the calculated results to actual experimental data from the test. This was done to validate the simulation model, the calculational process, and the assumptions therein. A detailed review and comparison of the actual and simulated intermediate-range detector data is provided in Section 5.1.2.

5.1.1 Gamma-Ray Detector Response

A comparison of the core regions and downcomer region voiding as a function of time (Figure 28) and the γ-ray flux at the detector as a function of time (Figure 29), reveals that the γ-ray flux closely follows the voiding conditions. When voiding in the core or downcomer occurs, there exists a corresponding deviation of the detector-site γ-ray flux from normal shutdown conditions. The normalized detector flux (Figure 34) shows two large peaks with a similar shape as the voiding curves, including the double peak between 240 and 400 seconds, discussed in Sect. 4.5. The two smaller peaks in the γ-ray flux response curve correspond to voiding of 30% or less in any one

region. For these regions, the flux increase above normal is less than a factor of 2.

As expected, the L2-5 transient simulation increase-factors are consistent with the steady-state voiding studies. Within the time-frame of the experiment, less than 800 seconds, the γ-ray flux at the detector is dominated by n-γ production. Thus, the difference between the steady-state studies and the transient simulation is the inclusion of a neutron decay factor, which merely scales the flux results. The maximum increase in flux during the initial core uncovery is a factor of 33, which is the same as that found for the total water voiding case. The second major peak showed an increase by a factor of 15. At this time, the core has approximately an 85% void fraction, and the downcomer is approximately at 95% void. Referring to the series of core voiding calculations under various downcomer conditions, the increase in flux for 100% downcomer void fraction and 80% core void fraction is a factor of about 15 over the 100% water density case.

5.1.2 Validation of Simulation Model

The experimental data for the intermediate-range neutron detector is available for comparison with the simulation results. Figure 35 presents the curves for both the simulated and experimental neutron detector response as a function of experiment time. The calculated intermediate-detector response showed an overall similar behavior as the experimental data, with some discrepancies in the 250-400 second range. It should be emphasized that the data for the voiding conditions in the simulation are speculative, and available for only discrete time points, which can introduce or smoothen some peaks and valleys.

Initial core voiding begins immediately after shutdown in the first seconds of the test. The simulated curve does not drop as low as the experimental curve in the first 10 seconds, but closely follows the detector data within about 30 seconds, just before core reflood begins. The sharp decrease in neutron flux seen by the detector is a result of the decrease in the neutron source in response to the large quick insertion of negative reactivity from both control-rod poisoning and from loss of moderating coolant. The simulation accounts for only the decrease in neutron source from normal shutdown approximated by a linear ramp insertion of negative reactivity calculated

by the REKINS code. The simulation shows an increase from the non-voided, normal shutdown conditions because of the increase in transport of neutrons as a result of the loss of water. The effect of increased transport is seen in the experimental curve with a nearly identical shape several seconds after the simulation when the negative reactivity effects no longer dominate the neutron population.

Data-points for times between 54 seconds and 127 seconds were not available and the vessel was assumed to be completely covered under normal coolant densities. The two curves are the same during this time interval except for a dip by the detector at around 80 seconds. This shows that the calculation of normal shutdown decay at times after insertion of reactivity simulates the actual decay reasonably well.

The simulated response begins to diverge from the experimental data at 200 seconds. At this time, the core and downcomer have begun to void for the second time. The intermediate-range detector response has begun to increase while the simulation seemingly continues to follow the normal decay. The PSU void data shows a 20% void fraction for the inner core and some regions of the downcomer [18]. However, the homogenized void fraction becomes only 4% for the core and 9% for the downcomer region. (Volume fractions for the core and downcomer are presented for reference in Table 14.) It is not until 255 seconds when the homogenized core is about 15% voided, and the downcomer over 20% voided that the simulation shows a substantial increase. Thus, the detector is responding to the 20% voiding in the central region of the core while the simulation loses this detail as a result of the one-dimensional necessity of homogenizing the data.

The simulation continues to increase with the continued increase in void fraction in the core and downcomer, while the experimental curve steadily decreases with a slope slightly larger than for normal shutdown. Comparing with Figure 28, the simulated curve seems to follow the trends of the void data. The discrepancy between the two responses can again be explained as a result of the homogenization of the void data and the absence of reactivity effects. The central region of the inner core begins to void first, with the outer core and areas above and below the core mid-plane voiding later. The detector sees mostly the core mid-plane area and is less affected by the voiding in other areas; thus additional voiding in areas above or below the

central area would not cause the same increase in response. In contrast, all axial areas of the core are treated equally in the homogenization, so that increased voiding in the upper or lower core areas has the same impact on the simulated response as voiding in the central area. A complicated interplay between a response to transport effects from voiding of the regions above and below the primary detector viewing area, and from shielding effects of the downcomer, along with a reduction in the neutron source term from core coolant voiding, could result with no further increase in detector response for increased voiding. This interplay cannot be simulated for a one-dimensional model with very discrete data.

Core reflood begins at around 400 seconds, with both curves showing an increase in slope, thus, a greater decrease in response. At 435 seconds, both curves exhibit a small dip, and return to follow the same response curve. Again, the simulated curve follows the correct normal shutdown decay response, and nearly identical response to the 10-30% voiding in the inner core and downcomer regions. The voiding at this time is in the upper core region and not in the direct viewing path of the detector. The simulation has produced an effective void fraction (less than the actual value for the voiding region) of the core which is consistent with the response of the detector located a distance axially away from the actual voiding area. This shows the influence of detector mid-plane position on its response to voiding in the upper and lower core areas. The flux at around 640 seconds begins to drop below the sensitivity of the intermediate-range detector, causing a flat detector response in contrast to the continuing decrease of the simulation curve.

5.2 Detector System Operation Characteristics

The voiding calculations showed, with the change in flux expected at the detector site, that the γ-ray system is capable of responding to voiding conditions in the pressure vessel. Details qualifying the response and possible operating characteristics of the detector are direct byproducts of the computer study. The calculations are able to artificially determine the contributions to the detector signal (Section 5.2.1), and the response sensitivity to different voiding conditions, either real or contrived (Section 5.2.3). The response for different energy limits, or thresholds, was also determined (Section 5.2.2). These characteristics of the γ-ray system are discussed below.

5.2.1 Component Contributions to the Signal

The proposed gamma-ray detection method emphasizes the detection of capture γ-rays which are a signature for changing water density. The core-generated fission product γ-rays were thus considered a minor contribution to the detector signal. The proposed method, as discussed in the Introduction (Section 1), employs tangential viewing of the core to maximize the signal from the capture γ-rays from the steel, thereby minimizing the core γ-ray flux contribution. As a result of the capability to artificially break down the source terms within the calculations, the contribution to the detector signal of each of the two primary sources of γ-rays has been determined. The calculations were performed for radial viewing of the core and thus form an upper limit of the core γ-ray contribution to the signal from a tangential viewing configuration.

The relative contribution of the two components of the γ-ray flux signal at the detector varies with time, detector threshold energy and void fraction. As discussed in Section 4.2.1, at steady-state, the capture γ-ray source is the predominate contribution to the detector signal. Results from Section 4.4, specifically Tables 9 and 10, showed that the relative contribution from core fission-product γ-rays increases with time as the n-γ production decreases with the delayed neutron decay. This occurs as a result of the large neutron decay constant and the relatively unchanged core photon source. In general, the contribution to the signal from core γ-rays increases for the lower detector threshold energies, since the fission product photons are primarily lower in energy. This does not become important until the core γ-rays are a significant fraction of the detector signal.

At 30 minutes post-shutdown, a major source of neutrons is from the production of photoneutrons. (Refer to Table 10.) The core neutron source will continue to decay at a greater rate than the photoneutron source which decays with the core photons. Thus, the n-γ production will continue to decrease to the level of that produced by photoneutrons alone. The trend here suggests that after a given time post-shutdown, the n-γ contribution to the signal will become a small fraction of the total flux at the detector (~16% for $E \geq 5$MeV), which decreases with decreasing energy threshold (less than 0.01% for the $E \geq 1$MeV case).

The detector characteristics can therefore be divided into two extreme time regions; times shortly after shutdown when the detector response is dominated by the core-neutron n-γ production, and times long after shutdown (t>30minutes) when the signal behavior is determined by the core γ-rays. The intermediate time between these two regions is characterized by the contributions from both sources. The detector response is then complicated by the different operating characteristics and behavior of the two sources.

As the void fraction changes, the source contribution to the signal is altered. The fraction of the detector signal from capture γ-rays will increase for decreasing water density, or increasing void fraction. This occurs because n-γ production is affected by water changes through the transport of neutrons which is more sensitive than photon transport. (See Section 4.3.1.) This effect will not be important during the two extreme time regions described above, but will determine the detector behavior during the transition time in which both sources contribute to the changing signal as a function of void fraction.

5.2.2 Voiding Response Sensitivity

The sensitivity of the system to water density changes in the core and downcomer is dependent upon the conditions under which the voiding occurs. These conditions include the time after shutdown and the distribution of water in the vessel.

As discussed in the above subsection, the time after shutdown will determine the primary source contribution to the detector signal. The voiding responses characterized by the increase-factors, differ under the two extreme cases when either the n-γ production or the core fission product photons dominate the flux. (Refer to Results Section 4.3.1.) The transport of neutrons is more sensitive to water density than is the transport of γ-rays, so that the voiding response is larger for the conditions when the n-γ production dominates the signal.

From the many figures which present the change in flux as a function of void fraction, it can be seen that the response is not a linear function of water density. In general, the response is nearly linear for small void fractions (densities near to normal) and increases for increasing void fraction, or decreasing density. Thus, the voiding response is dependent upon the density range in which the change occurs.

The water density in neighboring regions will alter the voiding response. As discussed in Section 4.3.2, the increase-factors do not indicate a simple exponential transport attenuation relationship between the voiding of two regions separately and simultaneously. A specific example was given in Section 4.3.1 (refer to Figure 19) in which the γ-ray detector response to core voiding was enhanced by increasing the downcomer void fraction. These results indicate that subsequent water regions act as a shield, obstructing the transport effect on the neutron flux and spectral distribution caused by voiding. This occurs as a result of the water moderating the neutrons. The neutron spectrum exiting the shielding water region is more thermal than that which exited the voided region, and more closely resembles the original normal density spectrum. Thus, the interaction rate in following steel regions is similar to the non-voided condition. Removal of the shielding water reduces the moderation and maintains the hardened spectrum created by the original voided region, allowing subsequent production of γ-rays in steel to be more characteristic of voided conditions.

A quantitative measurement of the sensitivity to water voiding can be estimated. The increase-factors quoted in the results, Section 4, are ratios measuring the overall increase in flux as a result of extreme voiding conditions. This describes a change in flux for 100% or unit change in density averaged over the complete density range. The following refinement will be made to describe the voiding sensitivity. Define the

$$\text{voiding sensitivity ratio} = \frac{\Delta\phi/\phi_0}{\Delta\rho/\rho_0} \tag{5.1}$$

where $\Delta\rho=\rho-\rho_0$, the change in density from a specified initial density ρ_0, and $\Delta\phi=\phi-\phi_0$, the corresponding change in flux from ϕ_0 at density ρ_0 to ϕ at density ρ, as the relative change in flux for a relative change in density. The density range from 0% to 10% void, or 100% to 90% density, will be used for the reference change in density. This region was chosen because the reactivity effects are at a minimum within this density region, and the smallest estimate is determined with the sensitivity increasing for other density ranges. Thus, ρ_0 is the density at normal operating conditions with the resulting flux ϕ_0, and ρ is 90% of operating density, giving $\Delta\rho=-0.10$, or $\Delta\rho=-$

10%. In general, these sensitivity ratios will be negative for an increasing flux in response to a decreasing density.

The voiding sensitivity ratios for a γ-ray flux of energy E≥5MeV at the detector site for various voiding regions in both the LOFT and mock-PWR geometry is presented in Table 15. The ratios are presented for the two extreme cases of core neutron n-γ production and core photon source contributions to the detector flux. The sensitivity ratios for n-γ production are greater than the corresponding core γ-ray source only ratios. In general, the response sensitivity to the core γ-ray source shows a relative change in flux which is less than the change in density, and the n-γ production response shows a greater change in flux for a given change in density.

The change in density from 100% to 90% normal operating conditions is a critical voiding range because as discussed in Section 1, the water monitoring system requirements include the capability of providing an early warning and detection of initial voiding. A 10% change in homogeneous water density corresponds to the reduction in collapsed water volume by 10%, and thus a 10% decrease in water level. For the active (LOFT) core height of 5.5ft., a 10% change in density corresponds to a drop in water level by one-half of a foot. Multiplying the values in Table 15 by 10% gives the percentage change in flux for an equivalent decrease in water level of 0.5ft. The result is an increase in detector signal of approximately 10% for this level change in the core when n-γ production dominates. The sensitivity then increases for the downcomer and total water voiding. The core γ-ray source produces only an increase of 0.5% for 10% core voiding. These detection sensitivities are likely to be statistically significant, depending upon the signal-to-background ratios and other specific detector operating characteristics.

5.2.3 Threshold Energy

The detector system threshold energy settings will be determined by maximizing the advantages of each case and minimizing compromises. A very important parameter is the background contribution to the signal which will be affected by the threshold setting, and will favor the case where the signal-to-background ratio is greatest. This determination, however, depends upon the specific detector device and its working environment, and is therefore beyond this study. The calculations were able to determine how the threshold

setting altered a general detector response to voiding. As discussed in Section 5.2.1, the source contribution to the detector changes for the different threshold energies, and this difference will be discussed here with respect to detector performance.

The flux changes with water density were studied for three detector energy ranges of E≥5MeV, E≥3MeV, and E≥1MeV. The direct effect of energy threshold on the flux is to increase the magnitude for a decrease in energy cut-off. Thus, ignoring the background and detector non-linearities, decreasing the threshold will increase the count rate and therefore the signal. However, above the count rate that provides adequate statistics, this may not be an advantage, and in fact could be a disadvantage if the detector becomes saturated. The changes in flux magnitudes are relevant for long times after shutdown when the count rates are reduced.

The first extreme case to be studied is for times just after shutdown when the core neutron n-γ production dominates the detected gamma flux. At this time, the flux is sufficiently large for all energies so that any differences in magnitude are not relevant to detector performance. The energy range responses to region voiding differed between the LOFT and mock-PWR geometries. For the LOFT geometry, (see Section 4.3.1) the E≥5MeV and the E≥3MeV responses to changing water density were nearly identical, while those for the E≥1MeV case were similar. The shielding effects, discussed above, are increased for the lower energies, between 1 and 3 MeV, resulting in slightly larger increase-factors for combined region voiding. For example, the increase for the coupled calculation 5MeV threshold was a factor of 33, while the increase for the 1MeV threshold was 36, a 10% enhancement. The detector response for each of the three threshold settings for total water region voiding is presented in Figure 36. As can be seen in the figure, the response curves are very similar in shape.

The mock-PWR model resulted in a different response behavior for the three energy thresholds. The 3MeV threshold differed from the E≥5MeV response with smaller flux changes, ranging from 10% to 18% less for the same voiding conditions, while in general, the 1MeV threshold showed a greater detector response to voiding. Again, shielding effects are seen for the 1-3MeV energy range, even more so than in the LOFT geometry. For example, the increase in flux for the total PWR water voiding was by a factor of 184 (5.5 times that of

LOFT) for the 5MeV threshold and a factor of 239 (6.6 times that of LOFT) for the 1MeV threshold.

The comparisons discussed above for times short after shutdown when n-γ production dominates the photon flux at the detector site and the flux is large, show that the 1MeV case maximizes both the response and flux. However, the response enhancement is not large and the 5MeV threshold would be sufficient. It is likely that the background flux is larger for the lower energy cut-off, but the decrease in signal-to-background ratio may not be significant. The question of saturating the detector will also have to be considered, in which case the 5MeV cut-off would be favored.

The core photon source was also studied to determine how the response characteristics vary with energy threshold. For times long after shutdown when the core photon source dominates, the magnitude of the flux has decreased dramatically from the steady-state values. At this time, the flux, and thus the count rate is relevant to determining the detector performance, and must be considered in the choice of threshold setting. Similar to the core neutron source n-γ production case, the LOFT geometry responses to voiding were the same for the three energy limits. The flux increases by an order of magnitude from the 5 to the 3MeV cut-off, and then increases by a factor of 2 from the 3 to 1MeV cut-off. In this case, lowering the threshold gives the advantage of increased count rate with no effect on voiding response. Again, the mock-PWR geometry showed different responses for the three different energy thresholds. As the lower energy limit decreased from 5 to 1 MeV, the change in flux increased in response to voiding water conditions. For example, the increase-factors for the total water voiding condition were 2.7, 3.1, and 3.7 for the 5MeV, 3MeV, and 1MeV threshold energy, respectively. The absolute flux also increased by an order of magnitude for each decrease in energy cut-off. For this case, reducing the energy threshold to 1MeV clearly gives a two-fold advantage of increased flux and voiding response.

For times when both source contributions are important, the threshold energy can alter the contribution of each source, which will effect the detector response to voiding. The voiding response is larger for conditions where the n-γ production is significant. Thus, for a 5MeV energy threshold, the voiding response will be larger than that for the 3MeV or 1MeV case. However, at the times after shutdown when this is a significant difference,

the increase in flux from the 5MeV cut-off to the lower energies is also significant. Therefore, there is a trade-off between increased flux and decreased voiding sensitivity.

The above conclusions suggest that varying the threshold energy as a function of time would maximize flux and voiding sensitivity over the operating range of the system. For times just after shutdown, a 5MeV threshold would provide both sufficient sensitivity and counting statistics. For times long after shutdown, a 1MeV would maximize the flux rate and voiding response. During the range of time when both sources are significant a more detailed analysis (perhaps onsite calibration) would be required to determine the optimum threshold energy.

5.3 Model Characteristics and Limitations

In order to properly evaluate the results, an understanding of the limitations, and assumptions that constitute the calculational model and methods must be understood. Several tests were performed to evaluate the limitations and approximations of the model in order to identify systematic errors, and to determine the extent to which the results can be applied beyond the calculational model.

5.3.1 One-Dimension

The computations were performed as a one-dimensional transport problem which creates inherent calculational limitations. Contributions to the detector flux from above or below the transport plane (axial position) are not considered. The total source, either neutron or gamma-ray, is calculated from a volumetric source term multiplied by the mesh volume of 1cm axial height. Thus, the source of a piece of the core with a 1cm axial height is transported in a 1cm axial strip. The assumption is that this strip is part of an infinite z system so that any streaming of particles into the axial strip is equal to the number of particles leaving to enter the fictitious neighboring strip. For a finite system, the calculations can be applied to approximate the mid-plane of the core, assuming a collimation on the detector equivalent to a 1cm height at the core source. Thus, the calculations can be considered for a collimated detector located mid-core in a semi-infinite system. Another interpretation is arrived at if the source, and thus the flux at the detector,

is multiplied by the active fuel height, then the calculations are effectively propagating the whole core source, with only the buckling term to account for any finite characteristics. In effect, this is a detector with a window which is axially the same height as the core.

The calculations are based on an active fuel height of 5.5ft. The response of a detector aimed anywhere outside the core axial height, for example, the upper and lower plenum regions, was not modeled. The response of a detector aimed at the downcomer within the active fuel height region can be approximated with the downcomer voiding results. The error incurred would involve the difference in the transport path, either materials or distance, between the actual detector path and the centerline path assumed in the calculations. For LOFT, the angle off centerline necessary to tangentially focus on the downcomer is approximately 20°, and the increase in transport path is approximately 7% of the centerline distance. Employing basic geometry considerations, the increase in the transport path through the downcomer is greater than a factor of 3 times the downcomer radial width. This may not be significant if a comparison between the LOFT and mock-PWR models is considered. For an increase in downcomer radial width by a factor of 4 from the LOFT geometry to the mock-PWR geometry, the downcomer voiding increase-factor for $E \geq 5MeV$ γ-ray flux changed from 4.3 to 3.6. Indirect effects of core voiding on the response of a detector aimed at the downcomer, cannot be modeled with this method. The above argument would apply to the condition of downcomer voiding only.

Another major limitation of the one-dimensional calculation is the inability to model changing water-level. A one-dimensional configuration allows only homogeneous voiding conditions, and cannot account for the scattering effects of void above and water below a given axial position, nor can it model the different detector responses with different detector positions relative to that waterline. An attempt was made to quantify the differences between homogeneous voiding and changing water-level within a one-dimensional model. Assuming that a detector was aimed along a transport path which included a distinct water-level within its axial range, then the detector would crudely see the response of a specific percent of void above and a corresponding percentage of water below the waterline. For example, if the waterline was exactly at the midpoint of the axial range of site, the

detector response could be approximated by taking 50% of the response of the completely voided case, and add to it 50% of the response of the full water case. This approximation completely neglects any interaction between the two regions of void and water. The high-energy γ-ray flux calculations for several volume densities, along with the corresponding homogeneous values are given in Table 16. All of the split waterline flux values are larger then the homogeneous case, by at most a factor of 1.5.

As a consequence of the inability for a one-dimensional calculation to model a distinct waterline, the shielding effects of the downcomer cannot be determined exactly. A homogeneous approximation was made to quantify the effect of downcomer liquid shielding the detectors from voiding the core. The results of homogeneous core voiding for various static downcomer densities is discussed in Section 4.3.1 and presented in Figure 19. The relative increase of the flux between full core and completely voided core for the downcomer densities increases for decreasing downcomer density with the maximum increase of 21%. (Compare the increase-factor of 4.3 for a full downcomer to 5.2 for a voided downcomer.) As can be seen in the figure, the basic shape of the core voiding curve is the same for each case, with the absolute flux increasing for a decrease in downcomer water density, or increasing void fraction. The flux increases linearly from 100% to 0% downcomer density for any specific core void condition. The increase ranges from a factor of 5 to a factor of 6 from 100% core density to 0% core density. This flux increase is comparable to the relative flux increase from core voiding alone.

For a distinct downcomer waterline, homogenization of the total volume into an equivalent water density, overestimates the flux for a detector located below the waterline and underestimates the flux for a detector aimed above the waterline. This is most easily seen by glancing at Figure 19 which shows that of the nonintersecting curves, the topmost is for 100% downcomer density and the bottom curve is for 100% void with the homogeneous density curves in between. The maximum error is a factor of 6 in flux.

5.3.2 Cross Sections

The cross sections are an important aspect of the calculational model because they determine the particle interaction rates. Throughout the calculational studies, both the BUGLE and the EPRI-CELL cross section datasets

were used to quantify the characteristics of each set, and to understand any differences between them.

An important difference between the two cross section sets is the eigenvalue produced by employing one or the other in a ONEDANT search calculation. As stated in the Calculational Methods Section 3.3, search calculations with the BUGLE, and thus COLLBUGL, cross sections, produced an eigenvalue of k=0.44. Under the same geometry conditions, the EPRI-CELL cross sections produced a k=1.17. A comparison of the EPRI-CELL 5 group dataset and the collapsed 5 neutron group cross sections of the COLLBUGL data showed that the COLLBUGL resonance region absorption was high, and that scattering down from energy Group 3 (1.855eV<E<721eV) was excessively small. This is caused by high resonance absorption and self-scattering cross sections of the uranium. The EPRI-CELL cross sections were specifically collapsed with a hard neutron spectrum produced by the under-moderated, slightly higher uranium enriched core of the LOFT reactor. The code is designed to carefully model the resonance behavior of the actinides with the emphasis placed on the neutron generation chain reaction. These cross sections show a much higher percentage of neutrons scattering down to the thermal range, and thus are able to sustain a critical chain reaction. In contrast, the BUGLE cross sections were generated with the intent for use in transport calculations so that the property of the actinides as a resonant neutron absorber is emphasized.

The water cross sections also show some differences between the two datasets which results in the production of different neutron spectra upon exiting a water region. The out-scattering from the upper energy groups is greater in the COLLBUGL calculations, and the high-energy absorption is greater in the EPRI-CELL case. As a result, a greater thermal neutron flux is found in the COLLBUGL calculations, with a corresponding higher upper-energy neutron flux in the same geometry configuration with the EPRI-CELL cross sections. (See Results Section 4.2.1.)

Both cross section sets produce a hard spectrum (peak in the Group 2 energy range 1.85keV<E<821keV), with the LOFT geometry, but with the mock-PWR geometry, the COLLBUGL cross sections produce a thermal spectrum while the EPRI-CELL spectrum is nearly unchanged. (Refer to Section 4.2.2.) An understanding of the steel cross section behavior along with the above water cross section differences explains why this occurs. The thermal neutron absorption

in steel is 31% greater in the COLLBUGL dataset when compared to EPRI-CELL. The increase in thermal neutrons produced by the COLLBULGL cross sections are subsequently lost at a greater rate than those entering the steel in the EPRI-CELL calculations. Thus, the large amount of steel assures that the outgoing spectrum is dominated by fast neutrons. In the mock-PWR geometry with COLLBUGL cross sections, the large a mount of water allows for neutron moderation, while the small amount of steel does not alter the spectrum. However, with the reduced down-scattering and high absorption characteristics of the EPRI-CELL water cross sections, the spectrum is never moderated, and remains peaked in the resonance region as it was in the core.

The increase-factors presented in Table 8 for the EPRI-CELL and COLLBUGL cross sections are similar, showing that the relative effect of the different cross section sets on the calculated results for the detector response is small. A comparison of results for the mock-PWR geometry show that there is a less than 10% difference between the relative neutron flux changes (increase-factors) for the EPRI-CELL and COLLBUGL cross section datasets.

From the above discussion of the cross section data characteristics, it can be seen that the EPRI-CELL cross sections are appropriate for use in the neutron core flux generation calculations for source term determination, while the COLLBUGL cross sections are better suited for the transport calculations. Also it has been shown that although the cross section datasets produce different neutron spectra, nearly the same relative changes in flux are produced in response to water voiding. Thus, the use of either set of cross sections is not critical to the calculational results.

5.3.3 Homogeneous Voiding

The changing water inventory in the core and downcomer regions was simulated by homogeneous voiding. The dispersed bubbles calculations attempted to quantify the error of neglecting the real scenario of bubbling in the core. The maximum variance between the simulated bubbles and homogeneous voiding was 4% for the $E \geq 5MeV$ γ-ray flux, and 18% and 23% for the fast and thermal neutron fluxes respectively. This difference is not severe when compared to gamma-ray flux changes of 180% and neutron flux changes of 172% for homogeneous voiding of 50% density from full water conditions. The

differences in flux results between the water first and the air first region configuration can best be explained by noticing that although the amount of material (volume times number density) encountered by the particles is the same in both cases, the actual total transport path traversed in water or void will differ for the two configurations. In order to achieve equal volume mesh regions in a cylindrical geometry, the radial mesh width must decrease for increasing radius. Thus, the water first configuration contains a larger radial transport path for water than the bubble first configuration. This allows more absorptions in the water region, and produces a reduced flux at the detector site. Thus, the water first geometry always results in a smaller detector flux when compared to the void region first. The flux difference decreases for an increasing number of bubbles which effectively reduces the difference in the total radial transport path between the water and void regions.

The above reasoning can be extended to explain the difference in flux results between the bubble configuration and the homogeneous voiding condition. In the first, the transport path is approximately half the total downcomer width for either the water or void combined regions. In the latter, the transport distance is the full width, however, the number density of the material has been reduced. The effect is to compare a calculation of half the transport distance for full density and zero density with a calculation of full transport width at half the material number density. In the second situation the approximate exponential attenuation factor is

$$e^{-(1/2\ N\sigma_a)(r_w)} \tag{5.2}$$

while the attenuation factor for the first situation of bubbles is

$$e^{-(N\sigma_a)(1/2\ r_w)} \times \varepsilon \tag{5.3}$$

where r_w is the radial width, N is the number density, σ_a is the microscopic cross section for water, and ε is a non-zero attenuation factor for the total void regions. The situation of 10 bubbles best approximates the assumption of equal radial transport paths for the water and void regions, and shows a 3% decrease in flux when compared with the homogeneous voiding case. The increase in leakage in a void region could account for part of this decrease.

5.3.4 Steady-State Conditions

The REKINS code provided the scaling factor to adjust the neutron flux to represent shutdown source conditions. This scaling factor was applied to a steady-state neutron flux spectrum. The effect of neglecting some characteristics of shutdown conditions will be to change the core neutron flux shape. Thus, a study of the result of neglecting shutdown poisons is reduced to determining their effects on the core neutron spectrum.

The addition of boron to simulate shutdown poisons in the core changed the neutron spectrum, but not dramatically. An expected reduction of the fraction of thermal neutrons with a corresponding increase in the fraction of high-energy neutrons occurred, but the basic spectrum shape was not altered. The heterogeneous fuel cell neutron spectrum, as measured by the three spectrum parameters, changed by at most 4%. The transport code neutron spectrum for a homogeneous core, as discussed in Section 4.2.1, is a hard spectrum, with the peak number of neutrons in the second energy group, and only 2% of the total neutron population in the thermal group at the core edge. Thus, a 20% reduction in the fraction of thermal neutrons from 5% to 4% of the total at the core centerline does not significantly alter the spectrum shape. Outside the core, the exact unpoisoned spectrum is achieved before the vessel is reached. The result of neglecting shutdown poisons is a maximum 1% error in flux.

Neglecting the poison materials does not alter the high-energy core γ-ray source. The control rod poison materials are silver (Ag), indium (In), and cadmium (Cd). The photons emitted from these isotopes, including their neutron capture products, are predominantly of energies less than 2 MeV. Any of the photons above this energy are emitted less than one percent of the time. The core γ-ray source was shown in Section 4.1.1, to be independent of the neutron spectrum parameters. Thus, changes in the neutron spectrum from poisons will not affect the photon release rate.

The source terms for the voiding calculations were generated with the steady-state conditions and normal operating water densities. As discussed earlier (Section 2, Section 4.1), the reactivity of the core is affected by changes in coolant density, which will alter the neutron source population. The change in transport properties will also affect the resulting source neutron spectrum within the core. The result of neglecting core reactivity

feedback from voiding in the source term generation calculation was studied by determining its effect on the detector response.

Referring to the results of Section 4.1.2, a comparison of the full core density and the depleted core density eigenvalue computations showed a substantial shift of the core neutron population toward the higher energy groups, while the excore neutron spectrum was nearly unchanged. However, when the depleted-core-generated fixed source calculations were compared to the steady-state fixed source density calculations, the neutron spectra were nearly the same. The absolute neutron flux outside the core increased for void conditions other than the extreme case of 0% density in which the flux values decreased. From these relationships, it can be seen that the transport characteristics of the system, and not the source distribution, determines the neutron spectrum. Therefore, except for the completely voided condition, neglecting core voiding for source generation does not alter the resulting neutron spectrum in the transport calculations, but creates flux values which are too small by about 4%. The complete void condition is overestimated with the steady-state calculation by at most 5% outside the core.

5.3.5 Summary of Limitations

The limitations of the one-dimensional configuration must be taken into account when the results are interpreted, and an extraction to an axial array of detectors is made. The calculations are best suited for non-localized, nearly uniform density changes within a water region. Extrapolation to water-level response must be done with caution. The effect of the cross sections also cannot be quantified, but as discussed above, the two datasets are able to reasonably recreate the particle interactions.

The remaining limitations and assumptions discussed in this section were quantified. The homogeneous voiding model gave an error in flux which is at most 4% too large; shutdown poisons affected the flux by at most 1%; neglect of core voiding feedback on the neutron source produces flux values which are 4% too small for non-zero densities, and 5% too large for zero density. Assuming an additive relationship to these errors, the calculations are at most 10% in error. Transport calculations, regardless of the accuracy of the input data, are not completely exact, with the error in flux increasing with the distance from the source. With this consideration, errors incurred from the above summarized conditions are not significant.

The primary motive for the calculations is to determine relative flux effects as a result of changing system configurations. Thus, the reliance on the absolute flux is minimized with the normalization and flux comparison process. Within the limitations of one-dimension, and the accuracy of the cross sections, the calculational model and process should give a reasonable estimate of the relative effects on the flux due to changing water density.

5.4 LOFT and Mock-PWR Geometry Comparison

As suggested in Section 2, and confirmed in the results, the large amount of steel in the LOFT geometry plays a major role in defining the γ-ray detector response to water voiding. The steel-to-water ratio configuration is not typical of a commercial PWR which motivated the creation of the mock-PWR geometry model in an attempt to quantify the extent of the effects caused by steel and to correct the detector response results for an extraction to commercial power reactor operation. The mock-PWR geometry, as described in Section 3.1, is essentially the LOFT geometry with the region between the core and pressure vessel replaced with material so that the steel-to-water ratio closely resembles a commercial PWR.

The flux and spectrum behavior in the two geometries can be explained by the difference in transport properties of the water and steel. The neutron attenuation increases and the γ-ray attenuation decreases for the mock-PWR geometry as a result of the large amount of water, which is a good neutron moderator and absorber which is relatively transparent to photons, and the reduction of steel which drastically decreases the γ-ray attenuation.

Both the attenuation properties and neutron spectra can be quantified by comparing the number of mean free paths (mfp), $\lambda=1/\Sigma$ for neutrons and $\lambda=1/\mu$ for photons, of a particular material in the radial transport direction. The neutron spectral distribution of the LOFT geometry is a relatively hard energy spectrum in contrast to the thermal spectrum in the mock-PWR geometry. Neutron moderation occurs in the mock-PWR geometry water with 4 mfp of scattering from fast to thermal energies, ($E \leq 1.8eV$). However, with the LOFT geometry, the total equivalent of only 0.7 scattering mean free paths of water exists between the core and the pressure vessel, thus less moderation is expected. Using the exponential attenuation law (Equation 2.6) with $\Sigma\Delta r$ as the exponent and substituting $1/\lambda=\Sigma$ and $mfp=\Delta r/\lambda$, the number of mean free

paths, on the average only 2% of the high-energy neutrons reach the vessel in the mock-PWR model, whereas 50% survive in the LOFT model. For the γ-ray production and attenuation, the number of mean free paths in steel for thermal neutron absorption has decreased by a factor of 3, but the mean free path for gamma-ray attenuation in both the steel and water decreases by about a factor of 2.5, leaving the effective γ-ray attenuation as a result of n-γ production and material attenuation the same in both geometries as sited in Section 4.2.2.

As a consequence of the different attenuation and spectral distribution properties, the interaction rates for the two geometries behave differently under voiding conditions, resulting in dissimilar detector responses. For the n-γ coupled calculations at steady state, the γ-ray detector response to core voiding decreased from a voiding sensitivity ratio of magnitude 1.01 for the LOFT geometry to a ratio of magnitude 0.76 in the mock-PWR geometry. (Refer to Table 15.) The larger downcomer region following the voided core results in a larger shielding effect, reducing the relatively harder spectrum leaving the core to more thermal energies at the vessel. The change in flux and neutron spectrum is then seen primarily at the steel region located just beyond the core but in the mock-PWR geometry,the thickness has been decreased, thereby reducing the expected increase in n-γ production.

Combined region voiding, especially the case of total water voiding, resulted in a larger detector response in the mock-PWR geometry. As can be seen in Table 15, for the n-γ production source, the absolute value, or magnitude of the sensitivity ratio increases for the mock-PWR geometry under extended downcomer and total region voiding conditions. The total region voiding response can be explained with Figures 22 and 23, and the results of Section 4.3.3. The increase in interaction rates for 100% to 10% density for the mock-PWR geometry, results in a large relative increase in epi-thermal capture rates. In contrast, the LOFT spectrum is peaked in the epi-thermal range under normal operating conditions, so that a spectrum energy shift form voiding does not greatly alter the relative contribution of fast neutron captures. The mock-PWR geometry system is able to take advantage of the large increase in fast neutrons due to decreased moderation as a result of voiding.

The core γ-ray source response to voiding is the same in the two geometries for core voiding and is greater in the mock-PWR system for all other

region voiding conditions. The detector response to core source photons under voiding conditions is a result of attenuation through the material in the transport path. Therefore, changing core water densities in both geometries equally effects the transport properties (since the core is the same in the two models) while voiding a water region in the mock-PWR geometry removes a greater amount of material in the transport path than voiding of a region in the LOFT geometry.

With the relationships discussed above for the LOFT and mock-PWR geometries, a qualitative extraction of the detector response results to a commercial PWR can be made. For times just after shutdown when the n-γ production dominates, there is a complicated interaction between increased transport of high-energy neutrons, increased transport and decreased production of thermal neutrons, a hardening of the neutron spectrum, and changing source terms due to reactivity effects from core voiding. These interactions may be different for a large scale PWR for several reasons. The core spectrum is thermal in the PWR in contrast to the hard spectrum of the LOFT research reactor. This may increase the change in core voiding response with a greater change in the neutron spectrum. For a large-scale PWR, the volume of the core is relatively larger than the LOFT core with a relatively shorter transport distance between the core and the vessel. This is based on a scale increase of 2.8 for the core volume, 1.2 for the radial thickness of the vessel, and 0.25 for the radial transport distance between the core edge and the vessel inner boundary to roughly achieve the dimensions of a Three Mile Island reactor model [16]. The relative decrease in downcomer thickness may reduce the shielding effects calculated with the mock-PWR geometry, allowing increased core voiding sensitivity. The voiding response for the core and downcomer regions voiding separately have been calculated as nearly equal in both the LOFT and mock-PWR models. The increase in the ratio of core water volume to downcomer water volume would likely result in a characteristic response for core voiding which is different than that of the downcomer.

During the time frame long after shutdown when the core fission product photon source dominates the detector flux, an extension to a commercial PWR is more straightforward. The detector response to voiding will be related to the amount of water voiding and will be relatively insensitive to specific reactor operating characteristics. Therefore, for a larger water volume in the PWR, it is expected that the γ-ray detector response will be enhanced.

5.5 Fast Neutron and High-Energy Gamma-Ray Detection System Comparison

As a consequence of the γ-ray detector response computations being an n-γ coupled calculation, the fast neutron flux is readily available to establish a comparison between the predicted behavior of the γ-ray detector and the fast neutron detector systems. This comparison does not consider detector type, configuration, efficiencies or any specific operating characteristic. Background flux at the detector site was also neglected. The extent of the comparison is for two general detectors, one for neutrons of energies greater than 1.8eV, the other for γ-rays of energy 5MeV and above or 1MeV and above, whose response is measured by the normalized predicted flux changes, or the voiding sensitivity ratio (Equation 5.1).

The steady-state voiding studies showed that the response of the neutron detector is the same or less than that of the gamma-ray response in the LOFT model (Section 4.3.1), while the fast neutron flux voiding response was generally larger in the mock-PWR geometry (Section 4.3). At times during and just after steady state, the prompt and delayed neutron flux is the dominant source for both neutrons and γ-rays, the latter through n-γ production. In both geometries, the high-energy neutrons increase more than the thermal neutrons for a given change in density. In the LOFT geometry, approximately half of the γ-ray production is from the epi-thermal neutron capture in contrast to the mock-PWR geometry where the definite majority of the capture interaction rate is from thermal neutrons. In the LOFT geometry, the increase in epi-thermal flux is similar to the increase in the (n,γ) interaction rate in the vessel, but the attenuation of high-energy neutrons between the vessel and the detector increases relatively for the voided condition, thereby reducing the neutron detector response to the change in density. In contrast, the overmoderated mock-PWR system shows a substantial increase in the high-energy neutron flux while the thermal neutron dominated interaction rate increases by a smaller amount.

The only exception to this relationship of the greater neutron response in the PWR model is for core voiding at full power. The neutron detector response is slightly less than the γ-ray response because of the shielding effects from the downcomer. The epi-thermal neutron population is easily thermalized by the subsequent water region, directly reducing the potential increase in detector signal from core voiding. The γ-ray system is not as

susceptible to this shielding effect. The increase in epi-thermal neutron population will increase the high-energy capture rate in the steel region following the core. Once the increased fraction of epi-thermal neutrons has been captured, the transport of the resulting photon through water is less likely to result in a reduced signal as compared to the case where the high-energy neutrons must diffuse to the detector. The remaining fraction of high-energy neutrons that are not captured are likely to be thermalized in subsequent water regions where they can then contribute to the γ-ray signal through thermal neutron capture.

In general, the fast-neutron flux at the detector is less than the high-energy γ-ray flux for the same voiding conditions. This difference increases substantially with time after shutdown because of the rapidly decaying neutron source. The depressed neutron flux may be a characteristic particular to the LOFT system in which water exists between the vessel and the detector, in contrast to the air which exists between the vessel and the biological shield in a commercial PWR. Nevertheless, the flux trends show that the neutron flux will decrease with time until it reaches the photoneutron source level which will be less than the core γ-ray source. The detector flux at operating density and the normalized voiding response ratios are presented in Table 17 for both the neutron and γ-ray systems at steady-state and at 30 minutes post-shutdown. By 30 minutes, the fast-neutron detection system depends upon the photoneutron behavior for changing density. With a decrease in water density, the photoneutron source will decrease while the transport properties will enhance the epi-thermal neutron population. Thus it is seen that the fast-neutron voiding sensitivity ratio is less for 30 minutes post shutdown. The γ-ray system 30 minutes after shutdown, is independent of the complicated neutron behavior, and strictly increases for decreasing water density. Thus, although the response to voiding may not be as large relatively, for the γ-ray system, the larger flux rates and likely better counting statistics, along with a simply defined response may prove the γ-ray system a more faithful monitor of water level for times long after shutdown, and just as useful as the neutron monitor at full power.

6. CONCLUSIONS

Within the applicability of the methods, the model, and the calculations, this study has shown that the proposed ex-vessel γ-ray detection system is able to respond to and indicate voiding changes located in the core and in the downcomer. The calculational studies show that the detector flux increases exponentially (nearly linear in semi-log plots) with increasing void fraction within a water region. The loss-of-coolant simulation showed that the γ-ray signal promptly and faithfully follows density changes within the vessel, deviating from normal shutdown values when voiding occurs and returning to normal when water densities do so.

There are inherent limitations and approximations in the calculational model which can restrict the applicability of the results. However, the qualitative behavior indicated by the results are reasonable. To a great extent, the relative changes in flux are not sensitive to model parameters and assumptions used to simulate the reactor. The two model approximations of a one-dimensional calculation and minimum reactivity effects are likely to have the largest impact on the quantitative measurements. While the inclusion of a more accurate representation of these effects would better define the voiding response, it is expected that the overall behavior of the γ-ray system will not be altered and will continue to indicate the system's capability to respond to changes in water density and water-level.

The calculational method has been validated with experimental data, which upon comparison, showed that the simulation is able to account for the general behavior of neutrons and gamma-rays at the detector site during a loss-of-coolant event. The computational simulation of the LOFT L2-5 loss-of-coolant transient event was able to reproduce the intermediate-source-range detector response within the limits and capability of a one-dimensional, time-independent model. Although there are deficiencies in the input void data and the model assumptions, the major features of the response are well represented. The ability of the neutron data from the n-γ coupled calculation to follow experimental data gives confidence in the predicted behavior of the γ-ray detector.

The γ-ray hodoscope detection scheme shows great promise in the fulfillment of the requirements issued by the NRC for an inadequate-core-coolant

inventory monitor. The calculations for a non-collimated detector located axially mid-core, qualitatively indicate that a series of collimated detectors will respond to local water density and water-level changes. The method of detecting void content in the vessel is dependent upon the coolant density effects on particle transport and production, which is independent of the phenomenon causing the voiding conditions. The normalization technique would provide the measurement of relative change in signal for indications of voiding. Tangential viewing of the downcomer would provide further guidance in determining the core and downcomer voiding conditions separately, reducing the dependence upon deconvoluting shielding effects on the detector response.

This study has demonstrated that the γ-ray detector response is measurable, unique and predictable for all times after shutdown and during the loss-of-coolant event. The response characteristics may change during the first hour after shutdown, but this change is dependent upon a predictable and reproducible neutron and fission product decay rates. The γ-ray response for times just after shutdown coincide with the neutron behavior as a function of water density. For times long after shutdown, the core γ-ray source provides a substantial signal strength with a simple measurable sensitivity to water transport effects.

An advantage of the γ-ray system over the neutron detection technique for coolant monitoring indicated by this analysis is the behavior at times long after shutdown. The available flux for the γ-ray system is much larger than the fast neutron flux. The water density dependence of the neutron detection method is complicated by the effects on photoneutron production which defines the neutron source strength, and the increased transport of neutrons. The core fission product photon source strength is essentially independent of water density effects, so that the γ-ray level sensing is based strictly on the relationship that reducing the material in the transport path decreases attenuation.

Some operating characteristics of the γ-ray detection method have been studied, but further detailed calculations and experimental analysis need to be done to qualify the information. The analysis has demonstrated that the core γ-ray source is negligible until the delayed neutrons have decayed, at which time this source becomes an important contributor to the detector signal. This suggests that radial viewing of the core would not greatly alter

the response to n-γ production at times just after shutdown, and would later enhance the response to core γ-rays. The background signal strength and specific detector operating properties, such as efficiency, have all been neglected in this study. These environment and detector dependent characteristics may alter the voiding response sensitivity and will need to be determined.

Further analysis work should now be performed to refine the results cited in this study. Reactivity effects on the neutron source strength and subsequent effects on the capture rate need to be refined to better estimate the γ-ray response to voiding at times just after shutdown. These effects include the reduction in reactivity, and thus source strength, as a result of loss of coolant. For completeness, the solution to the time-dependent transport equation should be considered, which would address the complex condition of changing reactivity during shutdown and core voiding. The model should be extended to a commercial PWR to clarify the response under the correct water volume ratios in the transport path. A more detailed analysis of times between approximately 15 and 45 minutes would better define the detector behavior when both n-γ production and core γ-ray sources contribute to the signal. All of these proposed studies would provide beneficial information even if performed for a one-dimensional system.

The major next step in the calculational analysis is to extend the model to two-dimensions. This would remove many of the limitations of the one-dimensional model, including the loss of scattering effects, and of accurate downcomer shielding behavior. The second computational dimension would provide the capability of determining the differences in the detector response between a falling, or rising, distinct water-level and changing homogeneous voiding. The second dimension would also provide the response of a detector aimed at the upper head to determine the system's capability of fulfilling the NRC requirement of tracking coolant between the top of the vessel and the hot leg. The response of the detector aimed at the lower plenum could also be determined to calculate its sensitivity to water changes thereby establishing the reliability of using it for power normalization. This analysis would provide the detector behavior at various axial positions along the vessel to discern the relationships of all of the responses and how they can coordinate as a system to indicate coolant voiding changes in the pressure vessel.

ACKNOWLEDGEMENTS

This project was carried out at the Argonne National Laboratory in the Reactor Analysis and Safety Division, under the DOE sponsored Nuclear Science, Engineering, Health Physics, and Radiation Waste Management Fellowship administered by the Oak Ridge Associated Universities. I have greatly appreciated the opportunity and support which both institutions have provided, with thanks to the staff at ORAU, in the Department of Educational Programs at Argonne, and in the RAS Division office for handling all the paper-work and the numerous questions and complications that arose.

There are several people associated with EG&G and the LOFT reactor who provided useful information: P. Prassinos (now at LLNL), J. P. Adams, and W. Carpenter.

Thanks is due to my committee, Professors S. Kaplan, L. Grossman, and S. Prussin for taking the time to read through the manuscript and providing their comments. Special thanks is owed to my thesis advisor, Professor Prussin, for the hours on the phone and in person that was spent discussing numerous details and ideas, and for his attempts at keeping me on the right track.

Thanks to my research supervisor, Dr. A. DeVolpi, for his initiating my involvment in this research topic and for his continued support and guidance throughout the project.

This project put me many times at the door of various offices. I would like to express my gratitude for the helpful open door policy that was prevalent in the Applied Physics Division. Specifically, there was one individual for each of the major codes that I worked with who generously gave their time to share their experiences and provide useful advise. For EPRI-CELL discussions, thanks goes to J Deen. Help with ORIGEN and the basic initiation to the philosophy of large-scale reactor codes came from the enlightening discussions with D. Malloy. I have a great appreciation for the many times that C. Adams was able to see through my errors and provide invaluable advise with ONEDANT. Above all, I am indebted to R. Lell for his never tiring interest and generosity in providing insight and advise, in helping me to work through and understand complications, for making available the various programs and routines which reside in the unofficial AP code libraries, and in general, for easing my way around the world of reactor codes and cross section decks.

Thanks goes to K. Jenicek for typing and editing assistance, and to B. Korelc for her time spent with the last minute editing crisis. Figures 1, 2, 3 and 5 were drawn by T. Lucitt, who also provided some good advise with other figures and layout, along with occasional 'comic' relief.

I also wish to express my gratitude for the unending encouragement given by my parents, from always too far away; and for the many ways that my friends, both those from close by and those from 2200 miles, helped me out with their distractions from this project.

REFERENCES

1. J. G. Kemeny et al., "Report of the President's Commission on the Accident at Three Mile Island" (Oct. 30, 1979).

2. "Analysis of Three Mile Island-Unit 2 Accident," Nuclear Safety Analysis Center, EPRI, NSAC-1 (July 1979).

3. "Clarification of TMI Action Plan Requirements," Nuclear Regulatory Commission, NUREG-0737 (Nov. 1980).

4. A. L. Hon, N. N. Kondic, and L. E. Phillips, "Summary of NRC Requirements and Its Research Studies on Reactor Water-Level Measurement," First Proceedings of Nuclear Thermal Hydraulics, ANS (Nov. 1983).

5. W. B. Dress, "A Torsional Ultrasonic Technique for LWR Liquid Level Measurement," NUREG/CR-3113, ORNL/TM-8585 (Jan. 1983).

6. W. B. Dress and G. N. Miller, "An Ultrasonic Level and Temperature Sensor for Power Reactor Applications," First Proceedings of Thermal Hydraulics, ANS (Nov. 1983).

7. J. P. Adams and G. E. McCreery, "Limitations of Detecting Inadequate Core Cooling With Core Exit Thermocouples," EGG-M-0084 (June 1984).

8. J. E. Hardy et al., "Evaluation of Thermal Devices for Detecting In-vessel Coolant Levels in PWRs," NUREG/CR-2673, ORNL/TM-8306 (1982).

9. C. H. Neuschaefer, "A Reactor Vessel Level Monitoring System, An Aid to the Operators in Assessing an Approach to Inadequate Core Cooling," IEE Trans. on Nuclear Science, Vol. NS29 (Feb. 1982).

10. D. L. Pomeroy and J. P. Waring, "Advances in Gamma Thermometers Used As Inadequate Core Cooling Monitors," First Proceedings of Nuclear Thermal Hydraulics (Nov. 1983).

11. D. L. Bell et al., "Testing and Implementation of a Radcal Based Reactor Vessel Monitoring System for Inadequate Core Cooling Determination," Proceedings Symposium New Technology in Nuclear Power Plant Instrumentation and Control (Nov. 1984).

12. J. P. Adams, V. E. Flitton, and L. D. Goodrich, EG&G, unpublished information (1979).

13. J. P. Adams and V. T. Berta, "Monitoring Reactor Vessel Liquid Level With a Vertical String of SPNDs," First Proceedings of Nuclear Thermal Hydraulics (Nov. 1983).

14. J. P. Adams, "Monitoring PWR Reactor Vessel Liquid Level With SPNDs During LOCAs," Proceedings of the Topical Meeting on Advances in Reactor Physics and Core Thermal Hydraulics, ANS, NUREG/CP-0034 (Sept. 1982).

15. R. S. Kalita et al., "Installation and Startup Experience of Westinghouse Reactor Vessel Level Instrumentation," First Proceedings of Nuclear Thermal Hydraulics (Nov. 1983).

16. D. J. Malloy and Y. I. Chang, "Neutronic Analysis of the Three Mile Island Unit-2 Ex-Core Detector Response," Argonne National Laboratory, ANL-81-75 (1981).

17. A. J. Barrata et al., "Feasibility Study on the Development of a Non-Invasive Liquid Level Gauge for Nuclear Power Reactors," NUREG/CR-3290 (May 1983).

18. M. L. Gundy, "Application of the Adiabatic Spatially Dependent Reactor Kinetics Method to Voided Pressurized Water Reactors," Thesis Pennsylvania State University (1984).

19. "Reactor Water Level Measurement Using Ex-Vessel Neutron Detectors," Nuclear Safety Analysis Center, EPRI, NSAC-42 (Dec. 1981).

20. A. DeVolpi, "Water-Level and Fuel-Failure External Monitoring," Proceedings of Symposium New Technology in Nuclear Power Plant Instrumentation and Control (Nov. 1984).

21. A. DeVolpi, et al., "Fast-Neutron Hodoscope at TREAT: Methods for Quantitative Determination of Fuel Dispersal," Nuclear Technology, Vol. 56 (Jan. 1982).

22. D. L. Reeder, "LOFT System and Test Description (5.5-ft. Nuclear Core 1 LOCES)," NUREG/CR-0247, TREE-1208 (July 1978).

23. T. Rockwell, editor, Reactor Shielding and Design Manual 1st Edition, D. Van Nostrand Co. (1956).

24. J. J. Duderstadt and L. J. Hamilton, Nuclear Reactor Analysis, John Wiley and Sons (1976).

25. C. M. Lederer et al., "Table of Isotopes," 6th Edition, John Wiley and Sons (1967).

26. Reactor Physics Constants, 2nd Edition, US Atomic Energy Commission, ANL-5800 (1963).

27. J. R. Lamarsh, Introduction to Nuclear Reactor Theory, Addison-Wesley Publishing Co. (1972).

28. J. M. Dumas, unpublished information (1984).

29. R. W. Roussin, "BUGLE 80: Coupled 47 Neutron, 20 Gamma-Ray, P_3, Cross Section Library for LWR Shielding Calculations," RSIC, DLC-75 (June 1980).

30. W. Carpenter, EG&G, private communication (1985).

31. P. D. Bayless and J. M. Divine, "Experiment Data Report for LOFT Large Break Loss-of-Coolant Experiment L2-5," EG&G Idaho, NUREG/CR-2826, EGG-2210 (Aug. 1982).

LIST OF FIGURES

LIST OF FIGURES (Cont'd)

General Configuration of LOFT Reactor

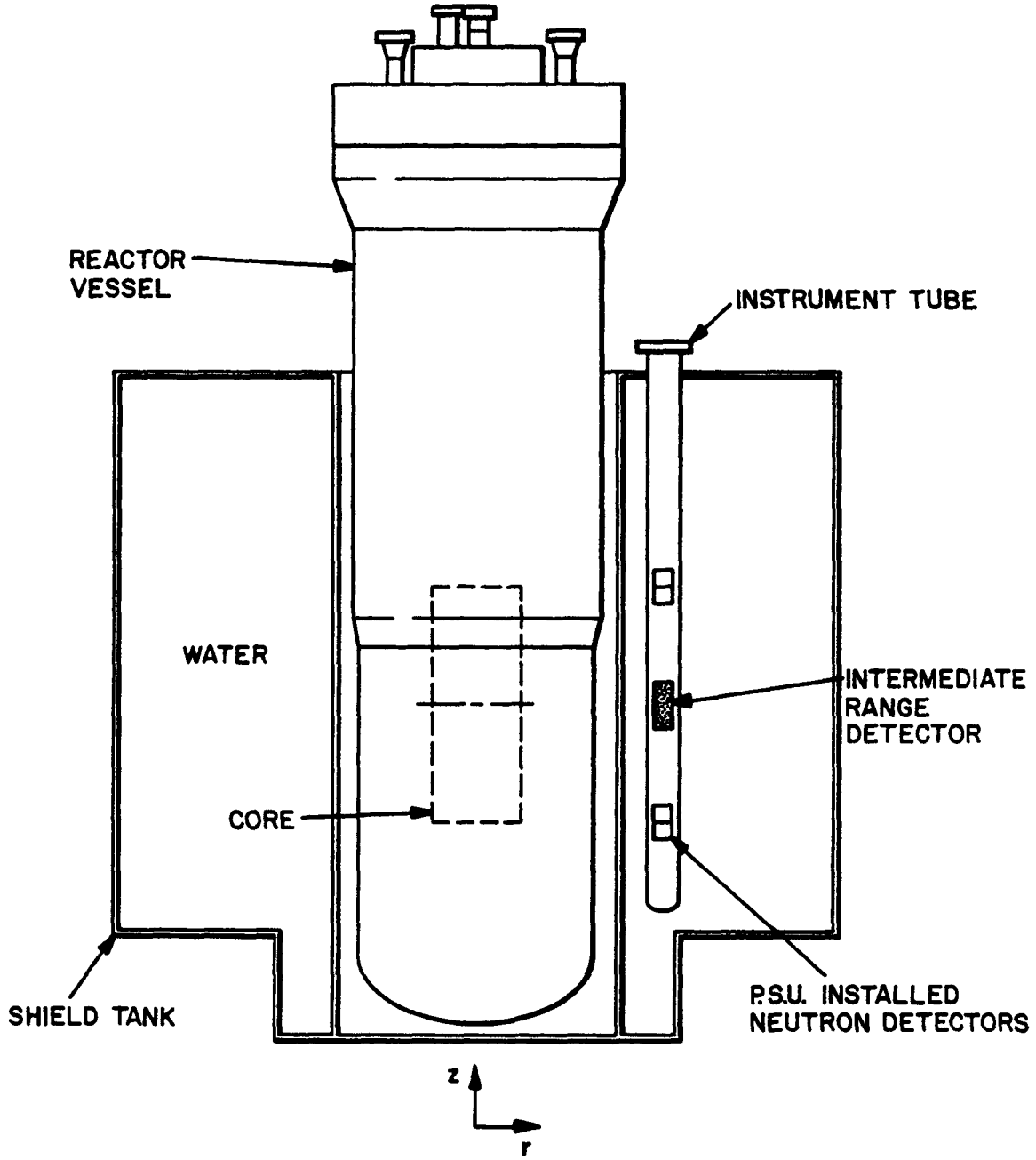

Figure 1

Gamma-Ray Hodoscope Detection Concept for Coolant Inventory Monitoring

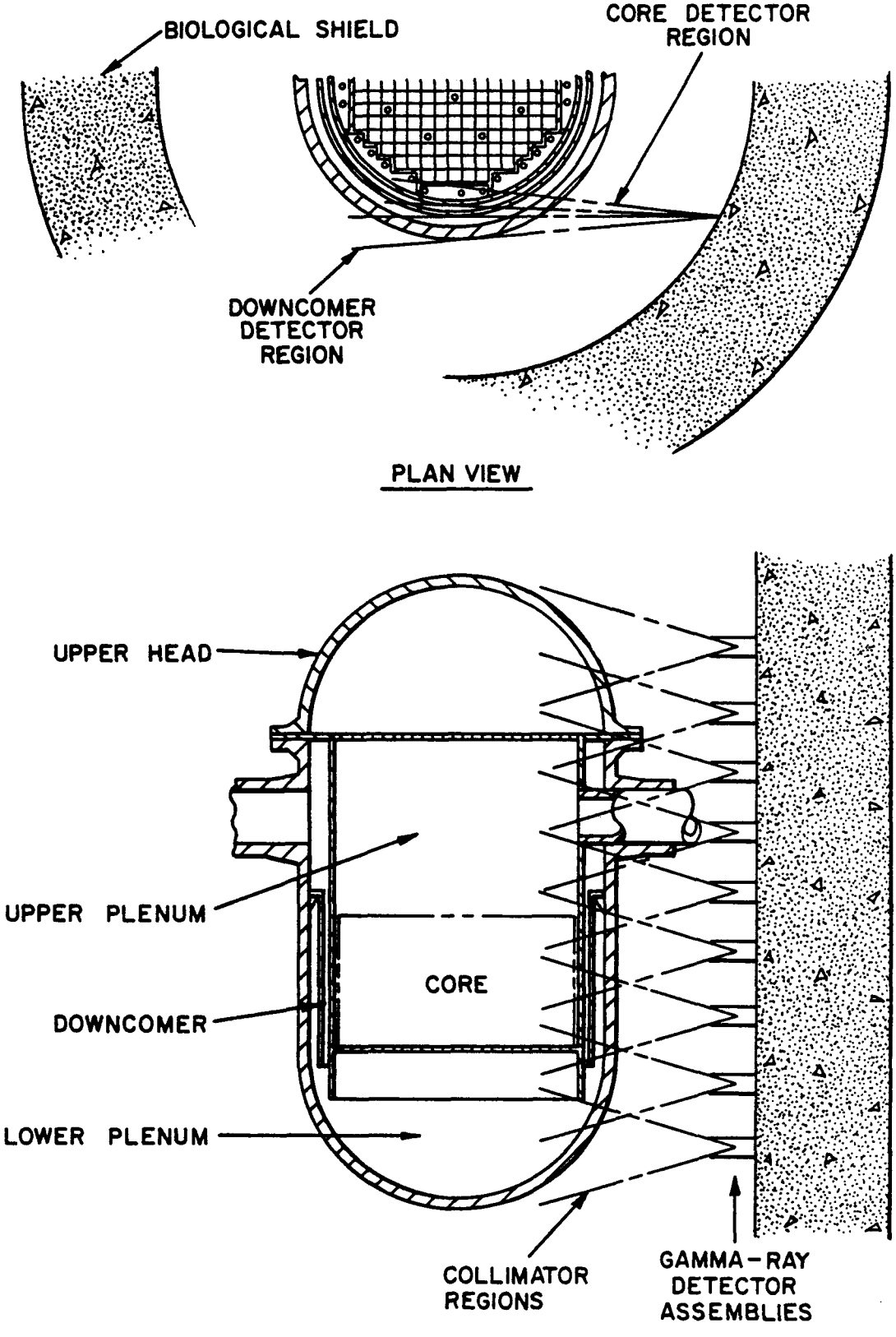

Figure 2

One-Dimensional Geometry Model for LOFT Reactor

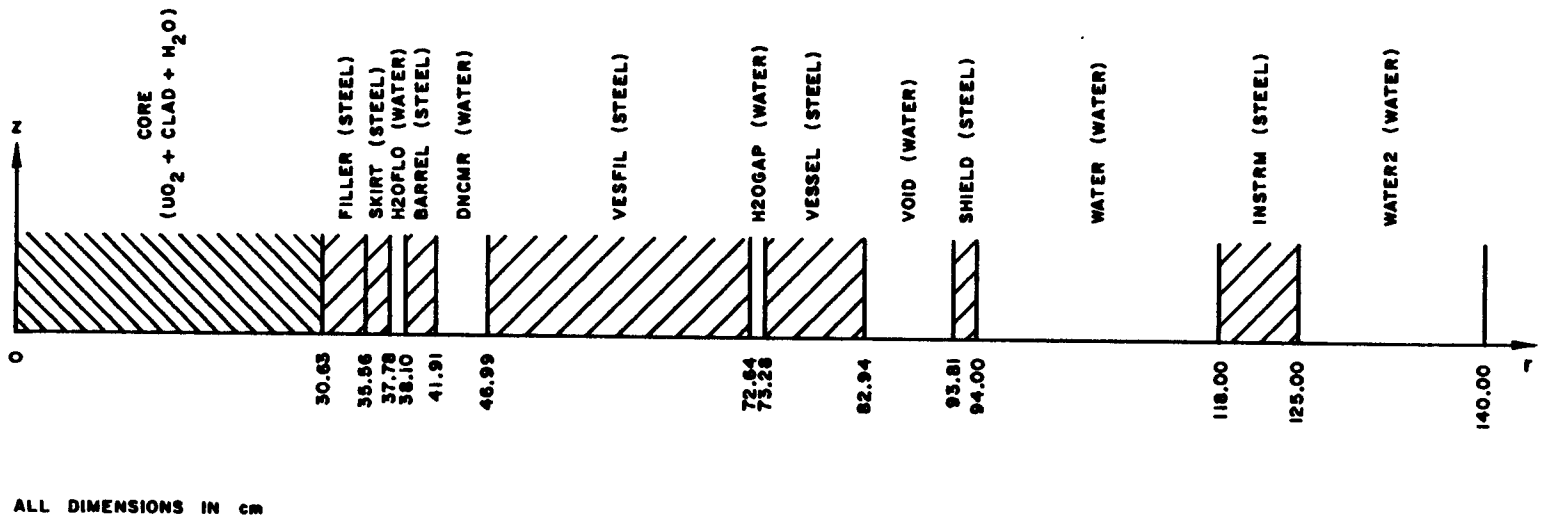

Figure 3

Internal Configuration of LOFT Pressure Vessel[22]
(Not to Scale)

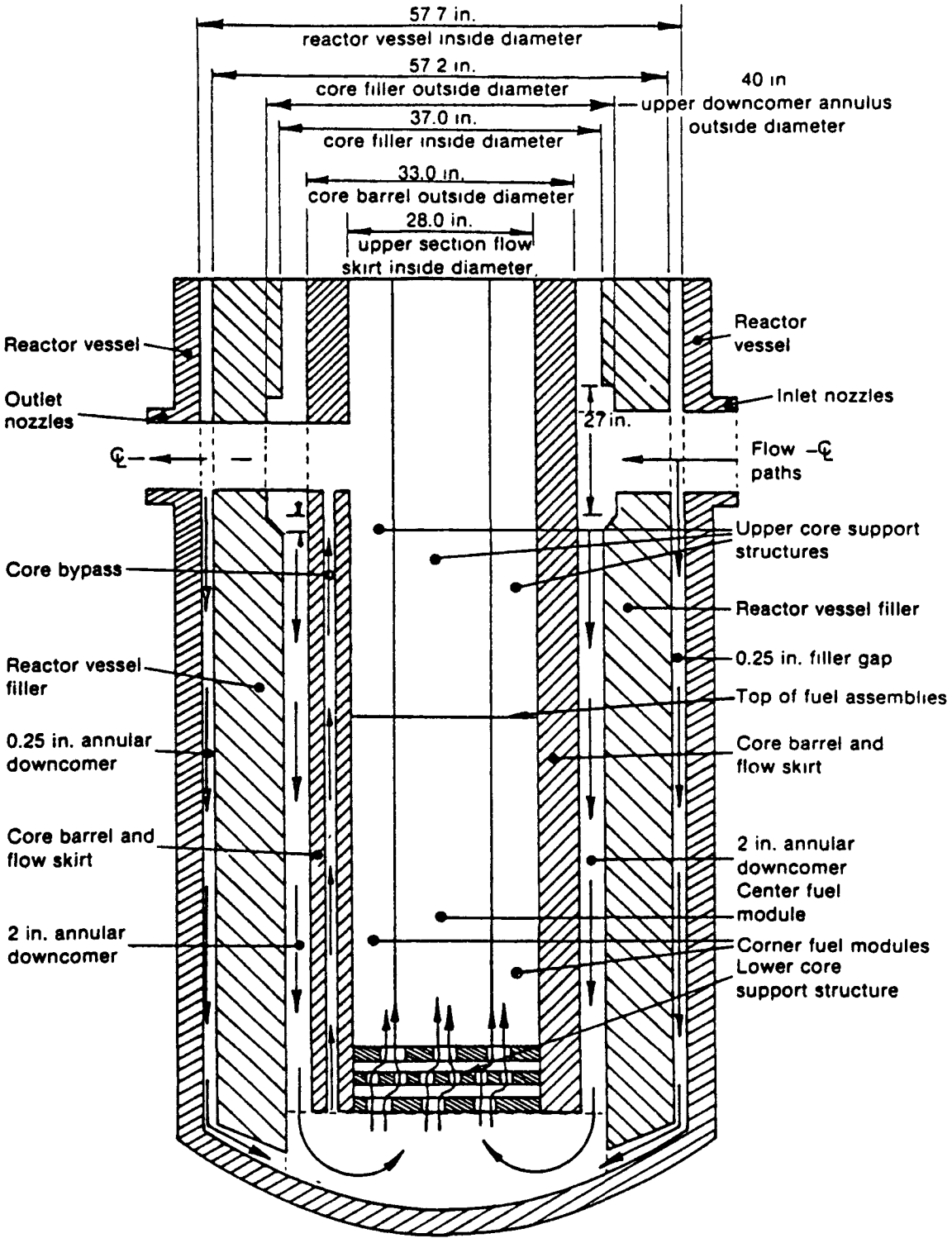

Figure 4

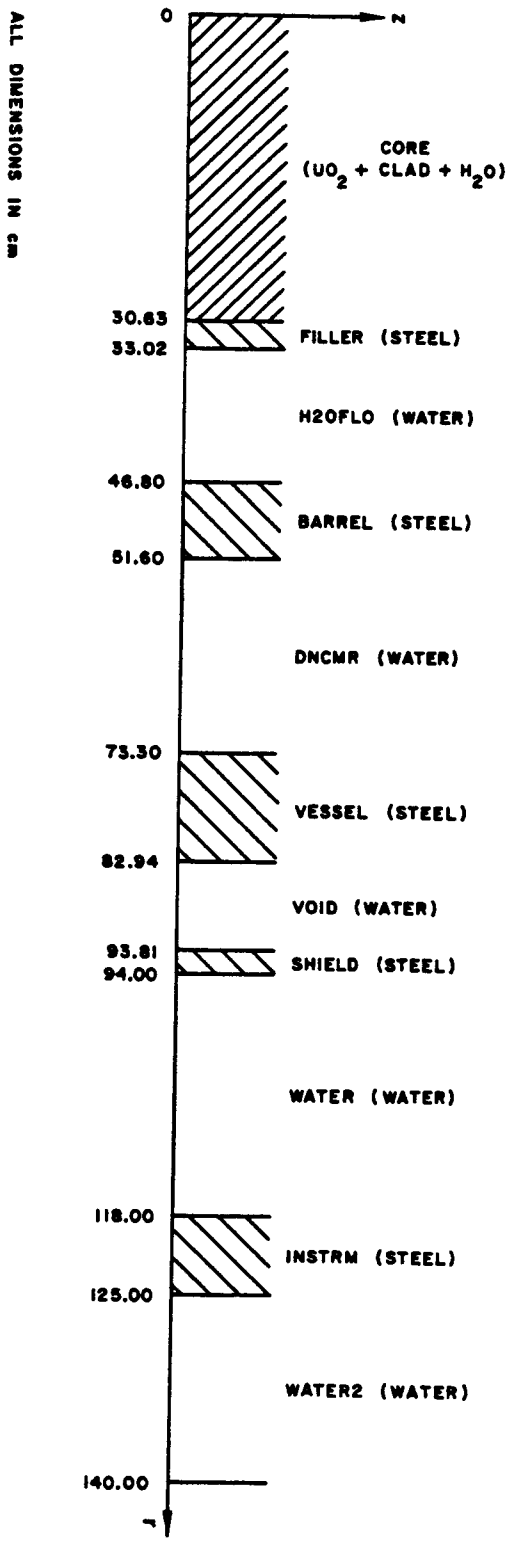

One-Dimensional Model for Mock-PWR Geometry

Figure 5

Mapping Scheme

ORIGEN Group Structure into BUGLE Group Structure

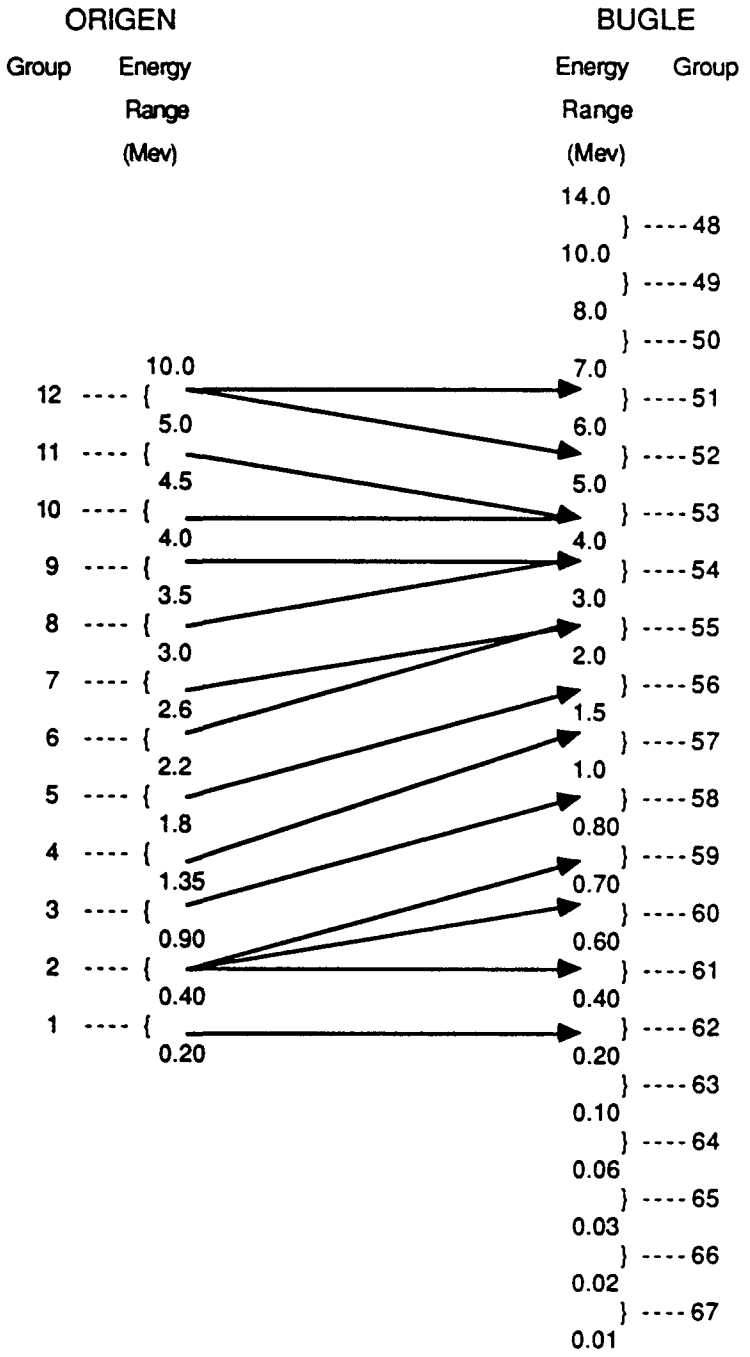

Figure 6

Mapping Scheme

Gamma-Ray Group Structure to Photoneutron Group Structure

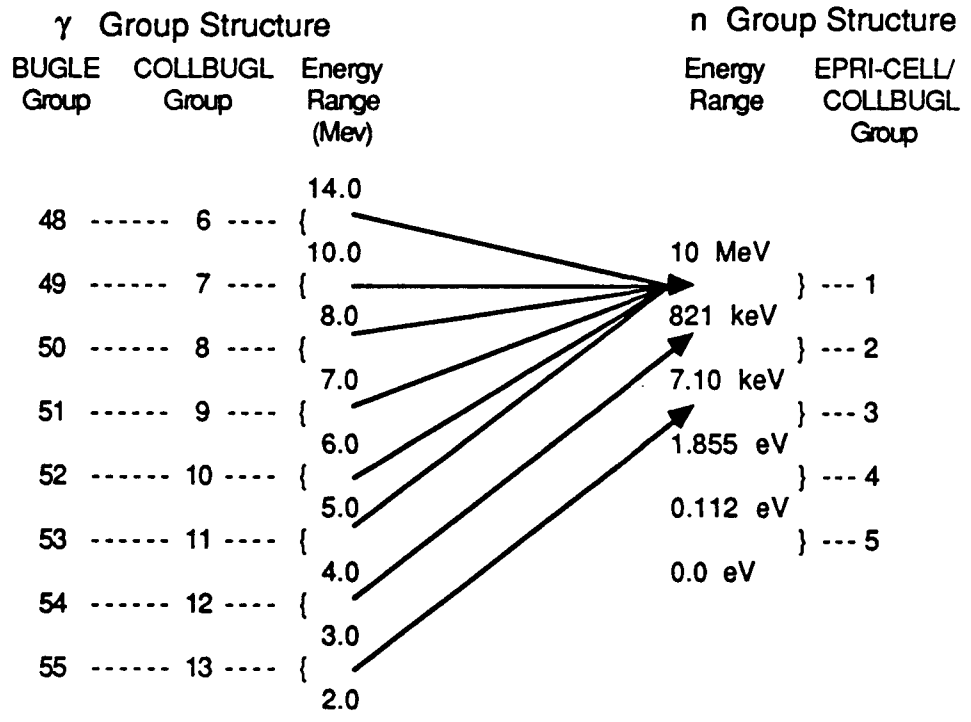

Figure 7

Cross Section Dataset Generation

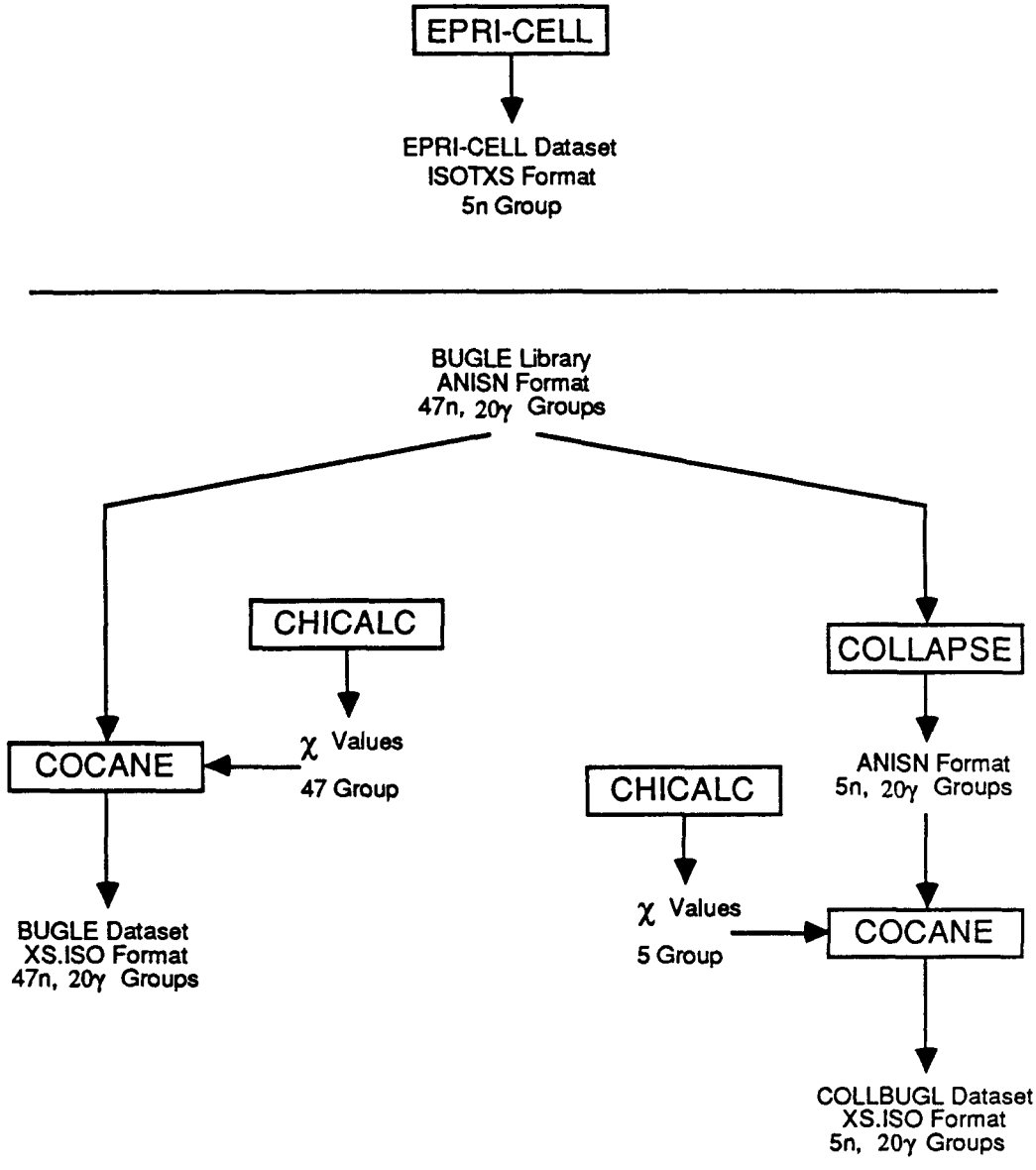

Figure 8

Calculations Flow Chart

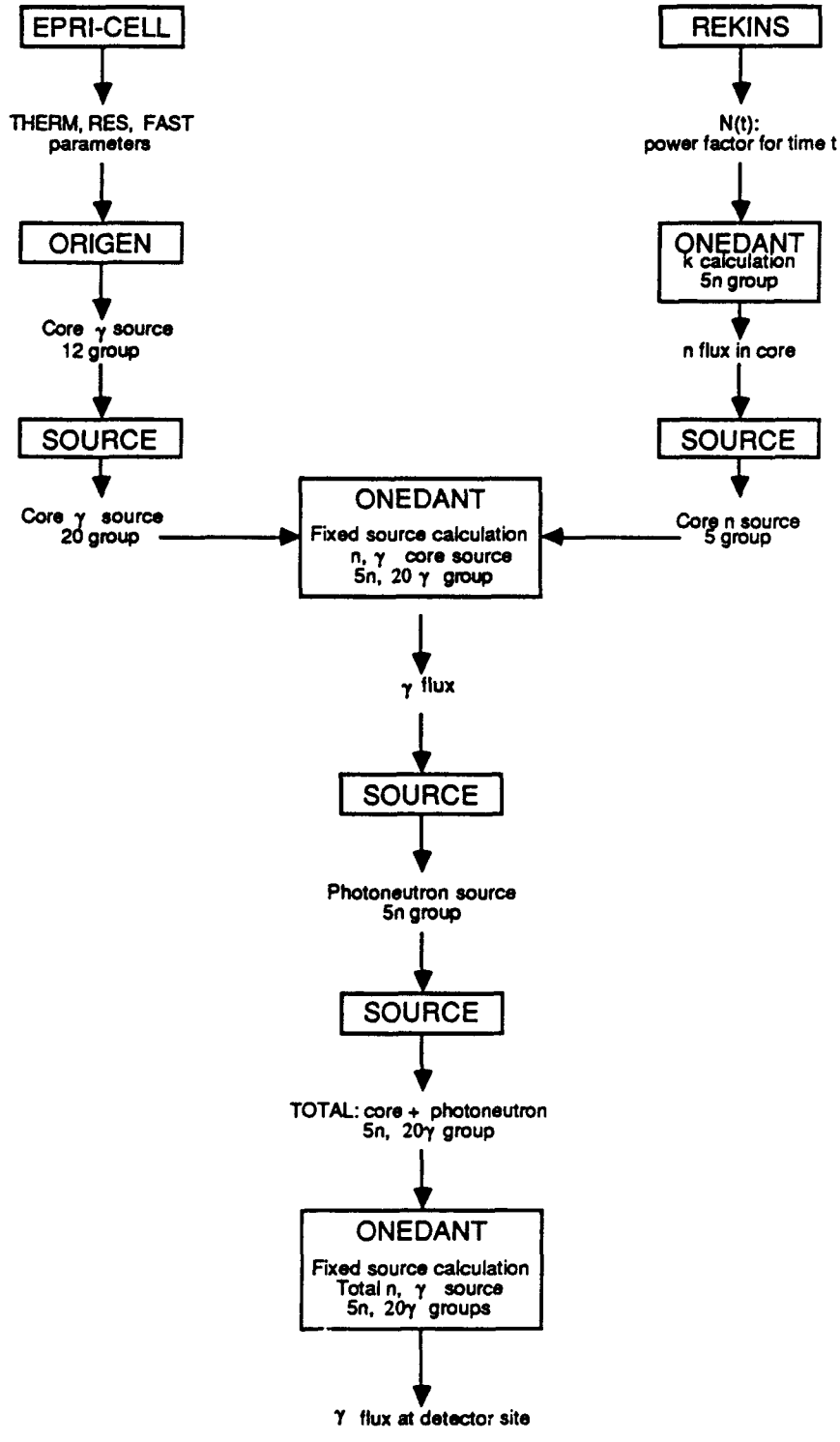

Figure 9

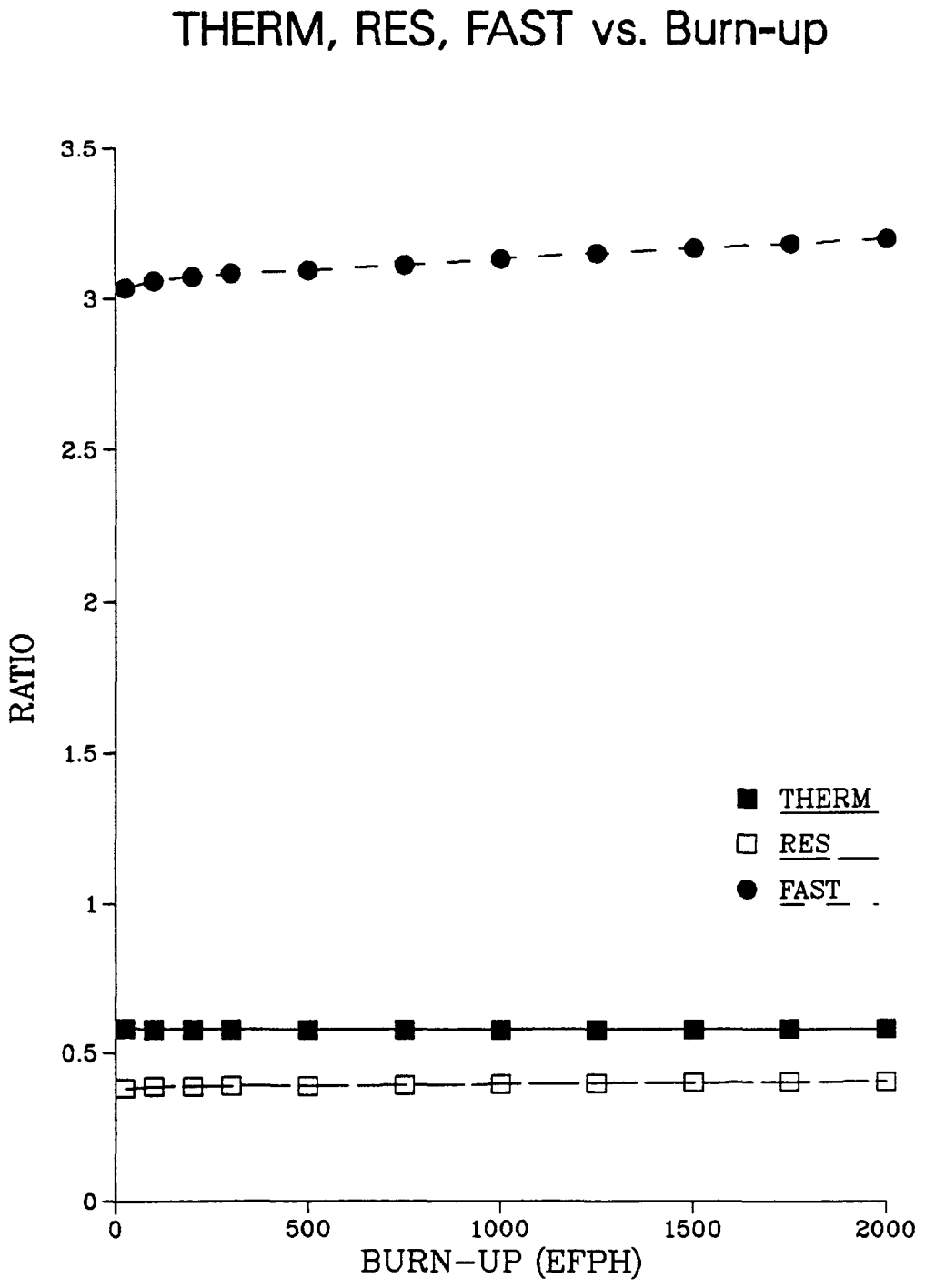
THERM, RES, FAST vs. Burn-up
RATIO
3.5
3
2.5
2
1.5
1
0.5
0
0
500
1000
1500
2000
BURN-UP (EFPH)
THERM
RES
FAST

Figure 10

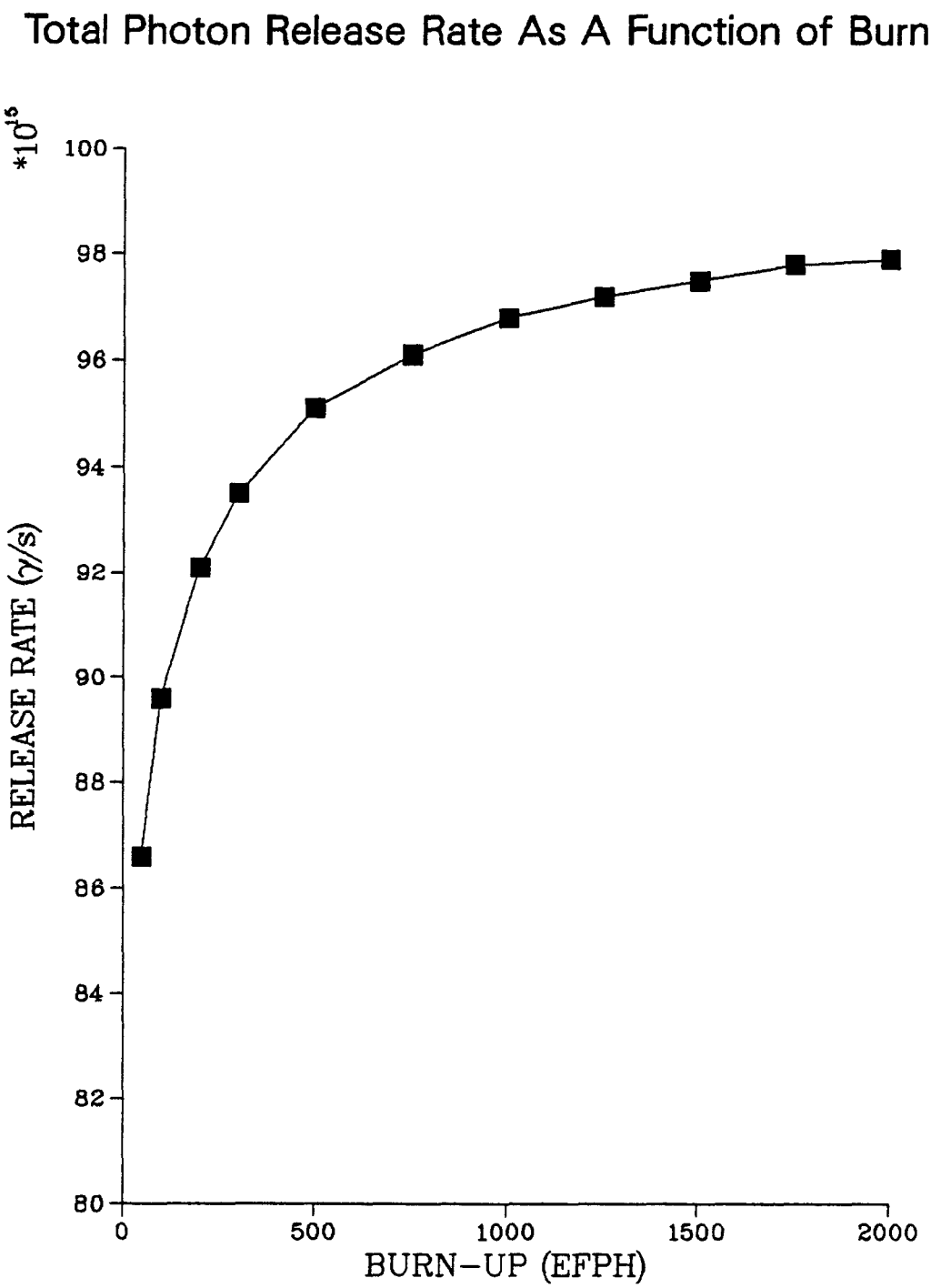
Total Photon Release Rate As A Function of Burn-up
*10^15
100
98
96
94
92
90
88
86
84
82
80
RELEASE RATE (γ/s)
0
500
1000
1500
2000
BURN-UP (EFPH)

Figure 11

High Energy Photon Release Rate As A Function Of Burn-up

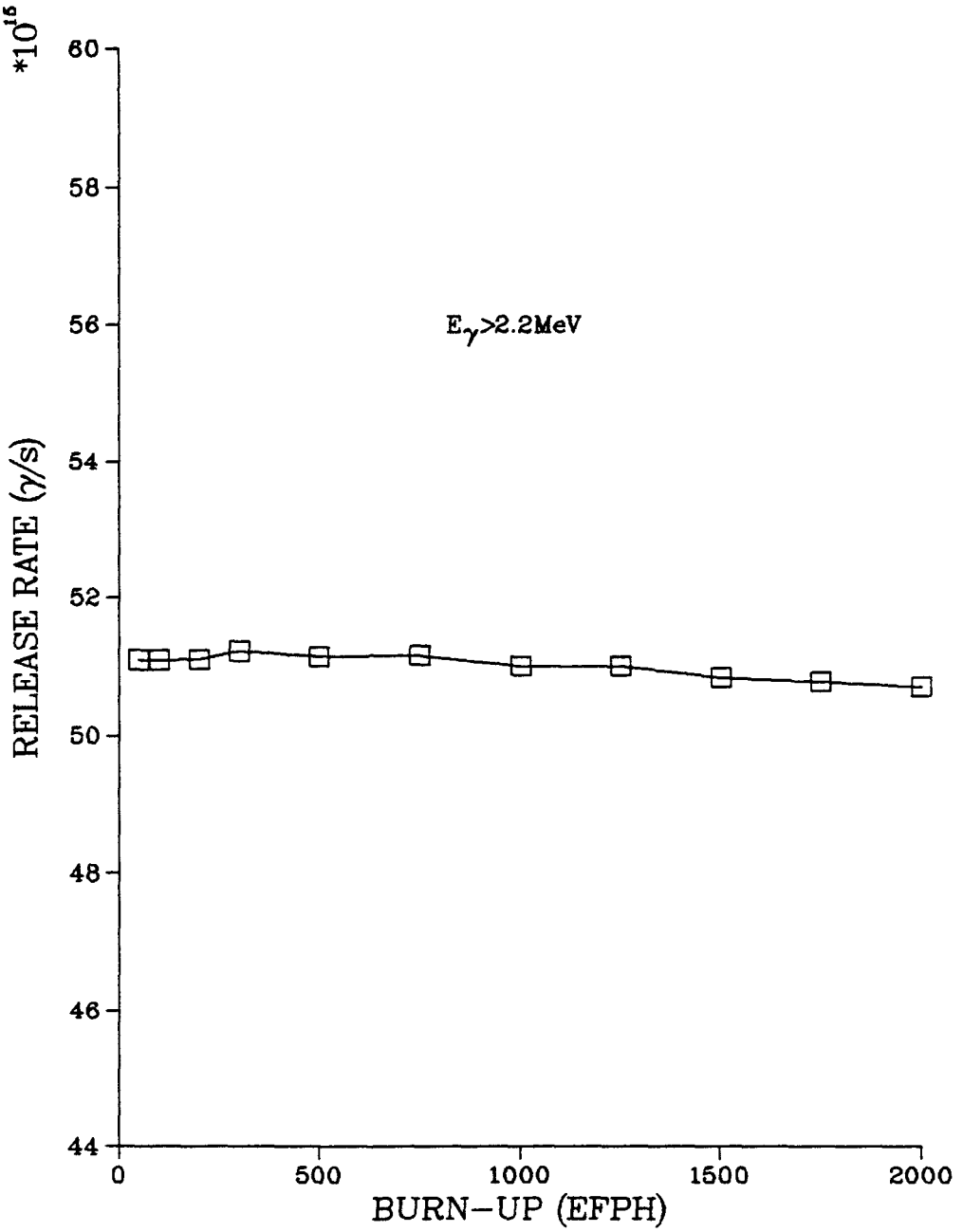

Figure 12

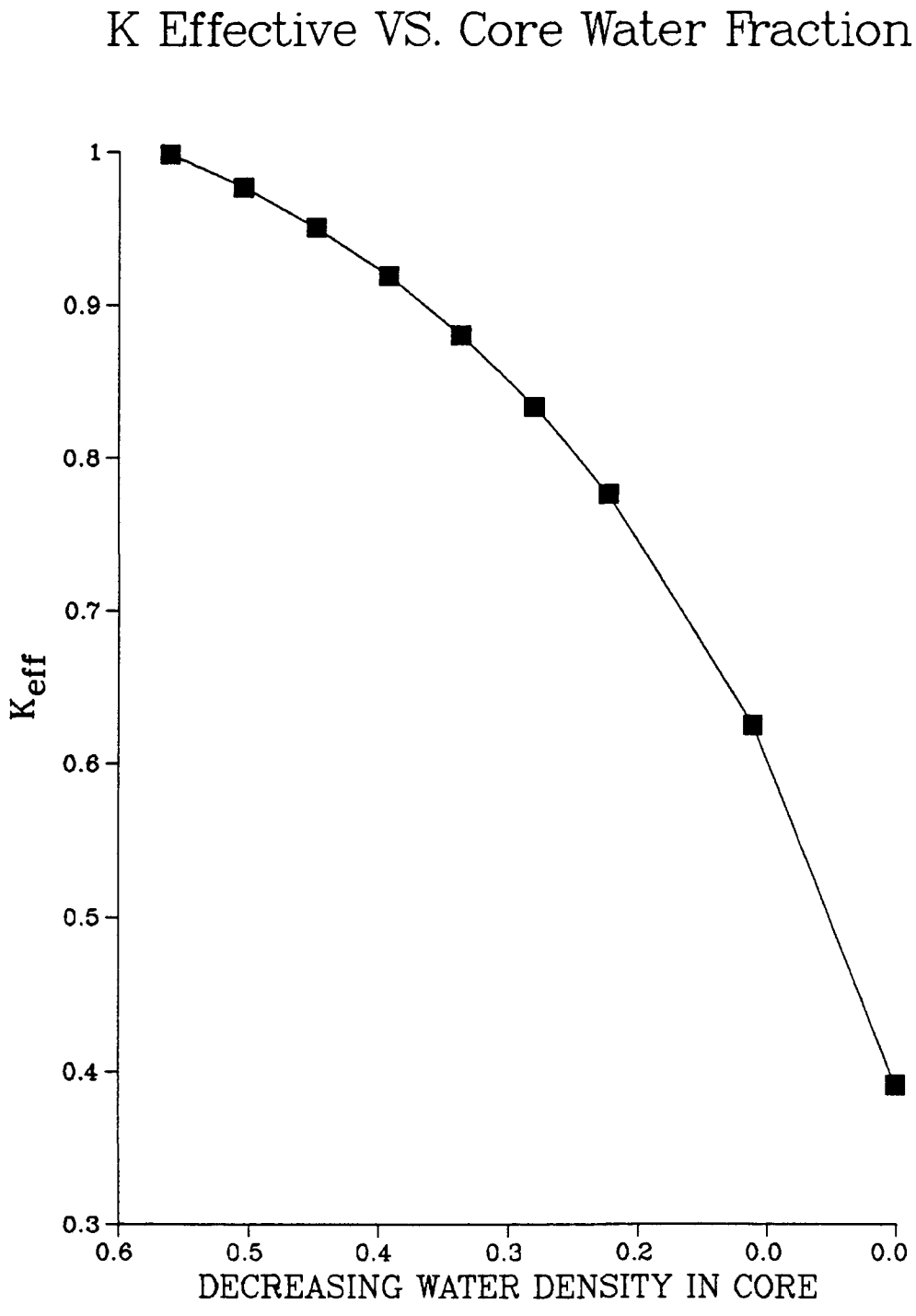
K Effective VS. Core Water Fraction
1
0.9
0.8
0.7
0.6
0.5
0.4
0.3
Keff
0.6
0.5
0.4
0.3
0.2
0.0
0.0
DECREASING WATER DENSITY IN CORE

Figure 13

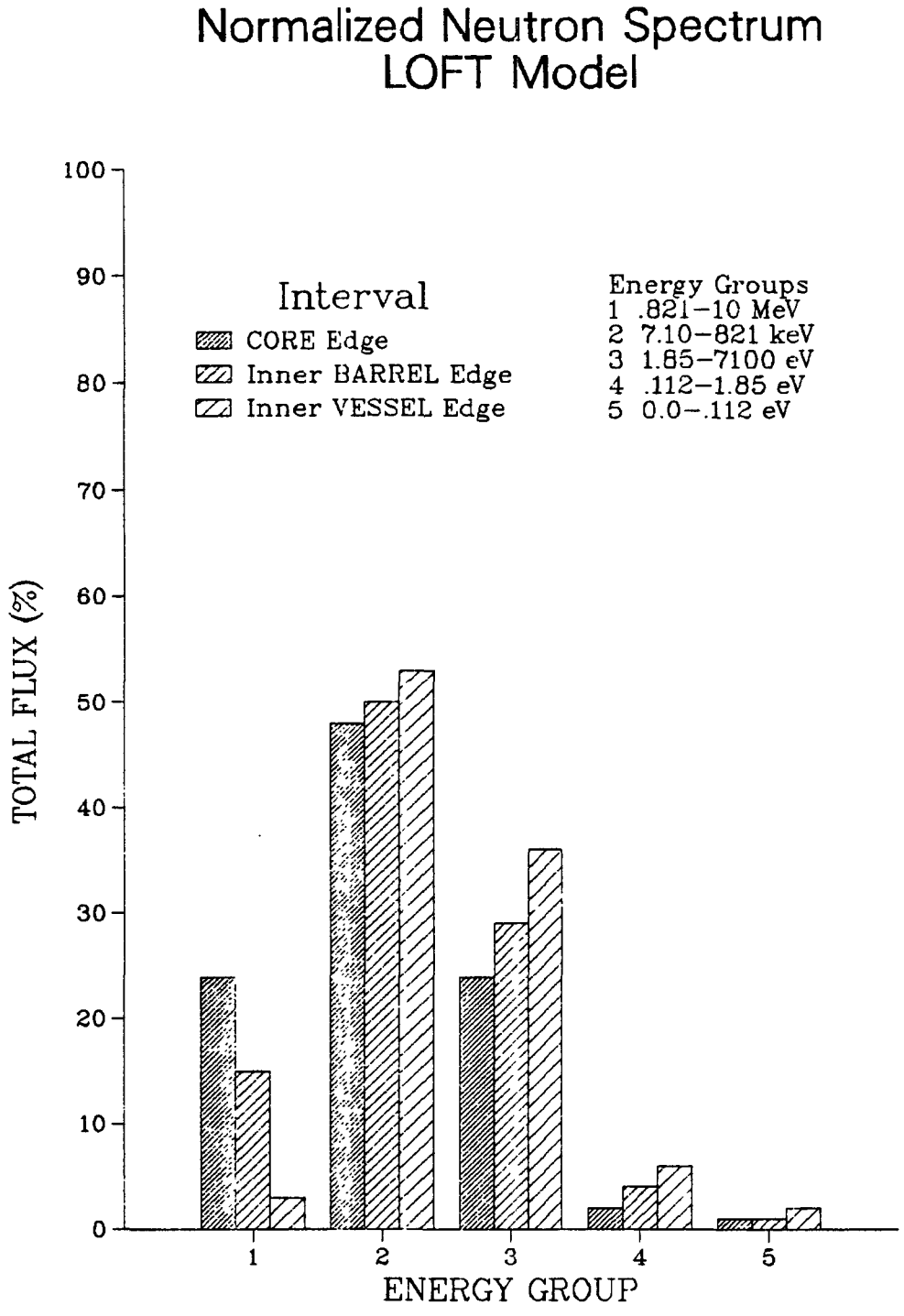
Normalized Neutron Spectrum
LOFT Model
Interval
CORE Edge
Inner BARREL Edge
Inner VESSEL Edge
Energy Groups
1 .821–10 MeV
2 7.10–821 keV
3 1.85–7100 eV
4 .112–1.85 eV
5 0.0–.112 eV
TOTAL FLUX (%)
100
90
80
70
60
50
40
30
20
10
0
1
2
3
4
5
ENERGY GROUP

Figure 14

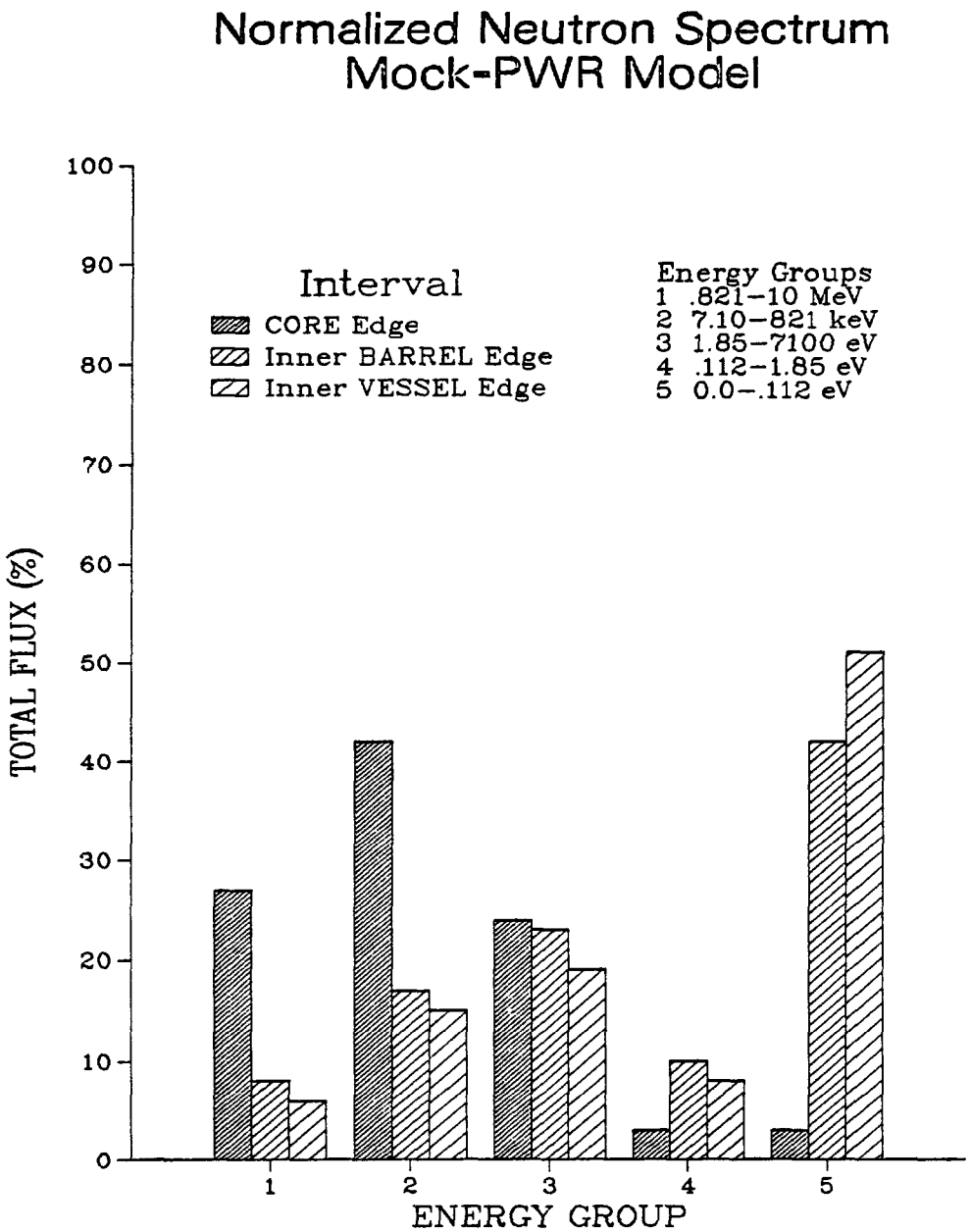
Normalized Neutron Spectrum
Mock-PWR Model
Interval
CORE Edge
Inner BARREL Edge
Inner VESSEL Edge
Energy Groups
1 .821–10 MeV
2 7.10–821 keV
3 1.85–7100 eV
4 .112–1.85 eV
5 0.0–.112 eV
TOTAL FLUX (%)
100
90
80
70
60
50
40
30
20
10
0
1
2
3
4
5
ENERGY GROUP

Figure 15

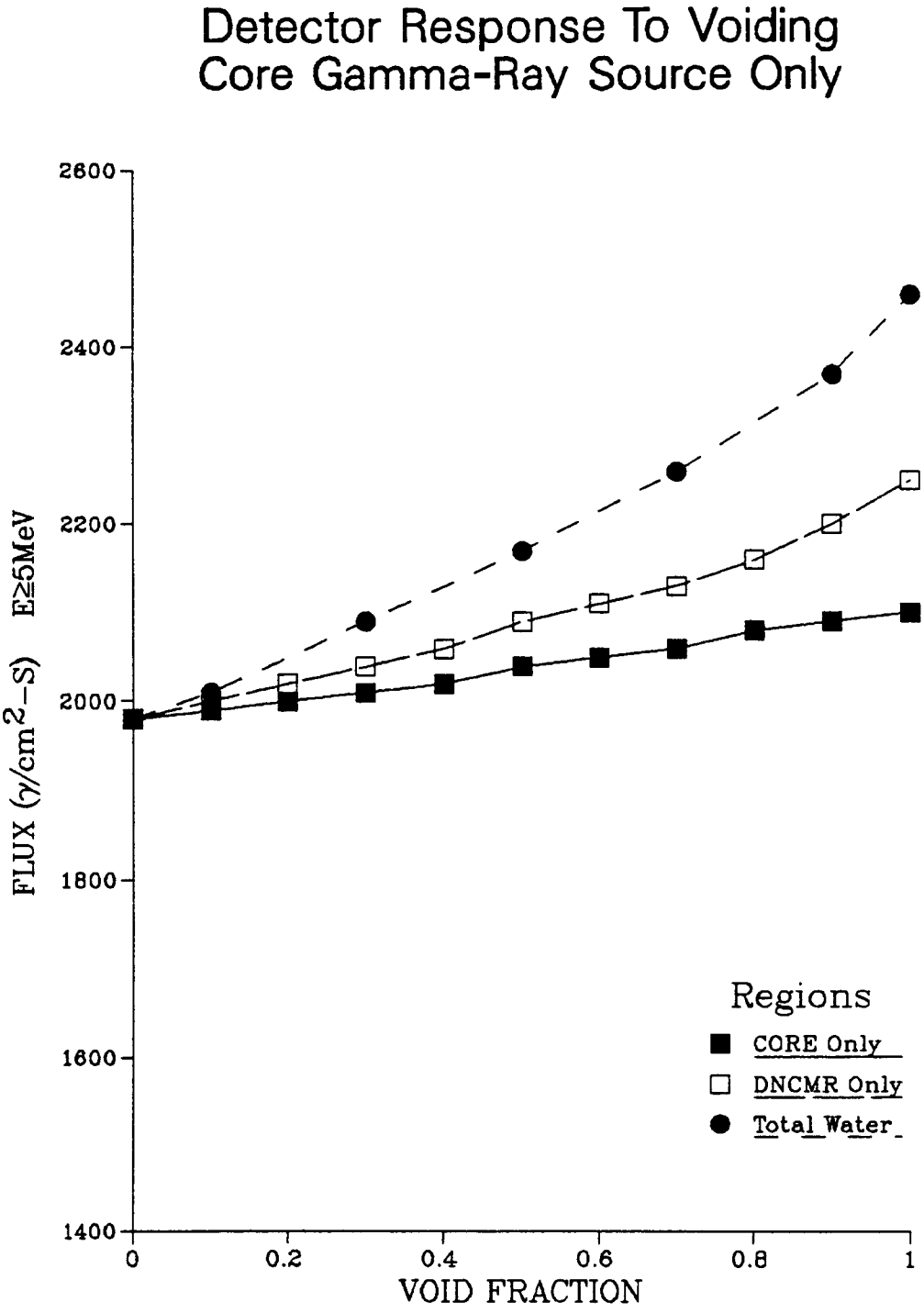
Detector Response To Voiding
Core Gamma-Ray Source Only
FLUX (γ/cm2-S) E≥5MeV
2600
2400
2200
2000
1800
1600
1400
0
0.2
0.4
0.6
0.8
1
VOID FRACTION
Regions
CORE Only
DNCMR Only
Total Water

Figure 16

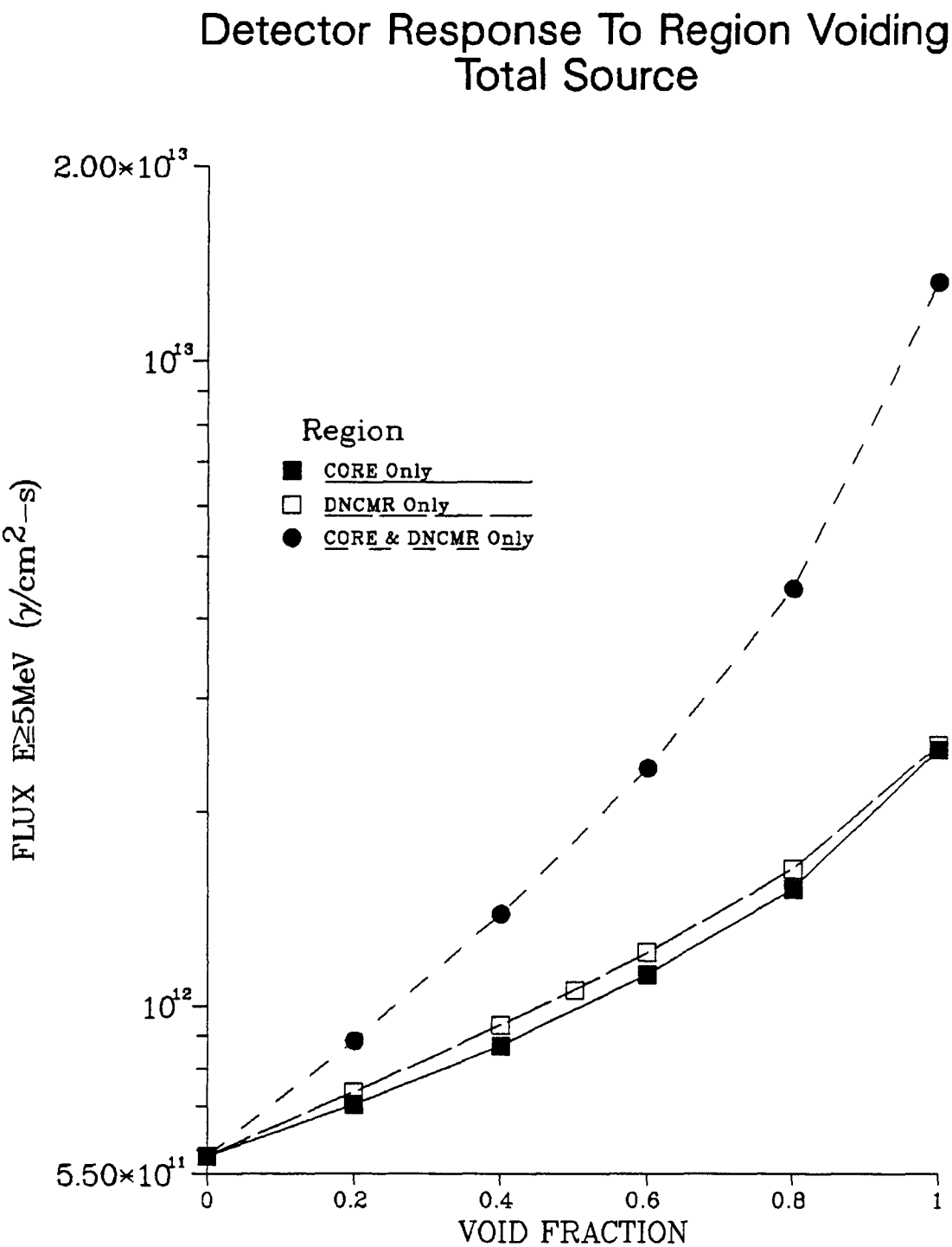
Detector Response To Region Voiding
Total Source
2.00×10^13
10^13
10^12
5.50×10^11
FLUX E≥5MeV (γ/cm^2-s)
Region
CORE Only
DNCMR Only
CORE & DNCMR Only
0
0.2
0.4
0.6
0.8
1
VOID FRACTION

Figure 17

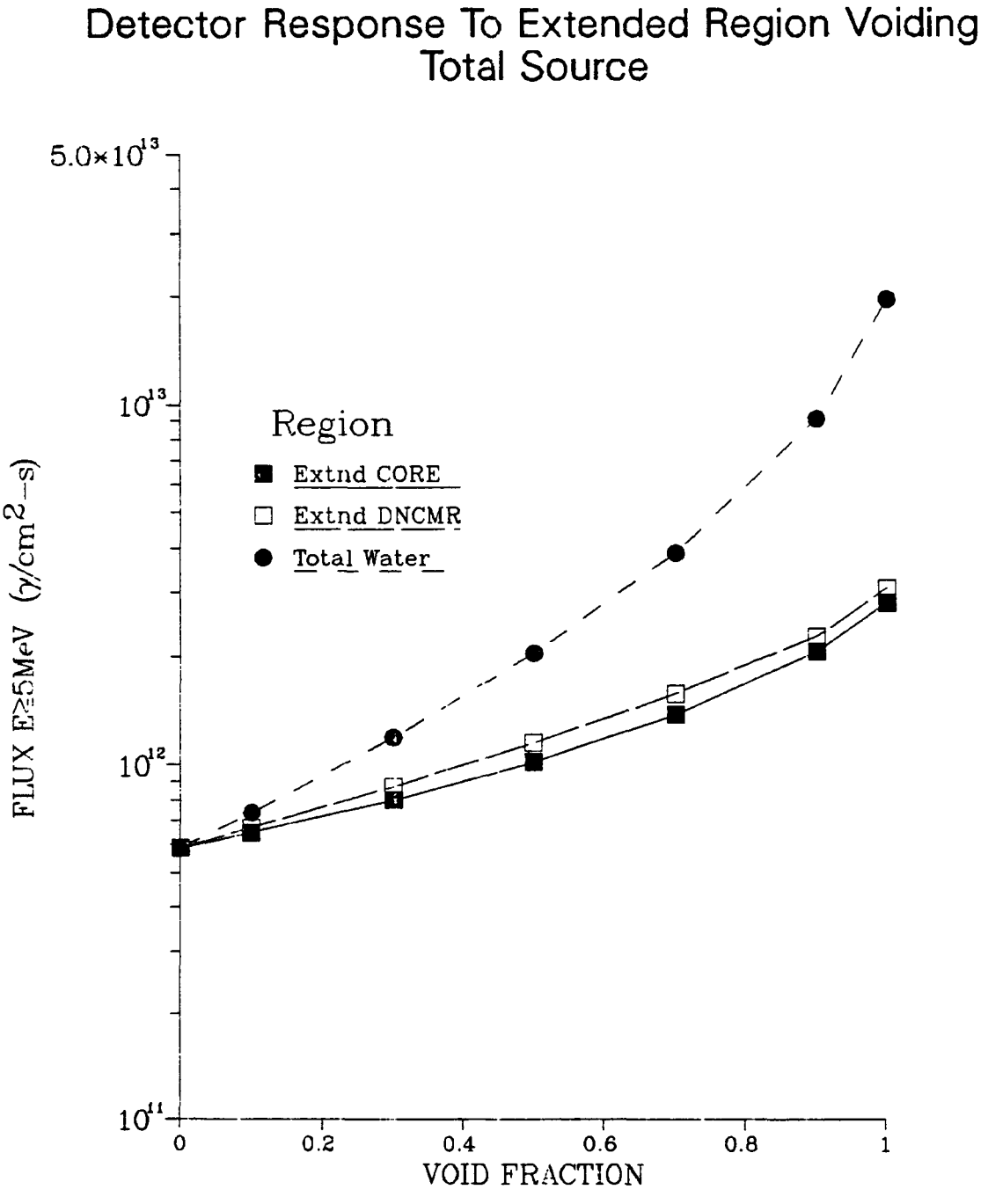
Detector Response To Extended Region Voiding
Total Source
5.0×10^13
10^13
10^12
10^11
FLUX E≥5MeV (γ/cm^2-s)
Region
Extnd CORE
Extnd DNCMR
Total Water
0
0.2
0.4
0.6
0.8
1
VOID FRACTION

Figure 18

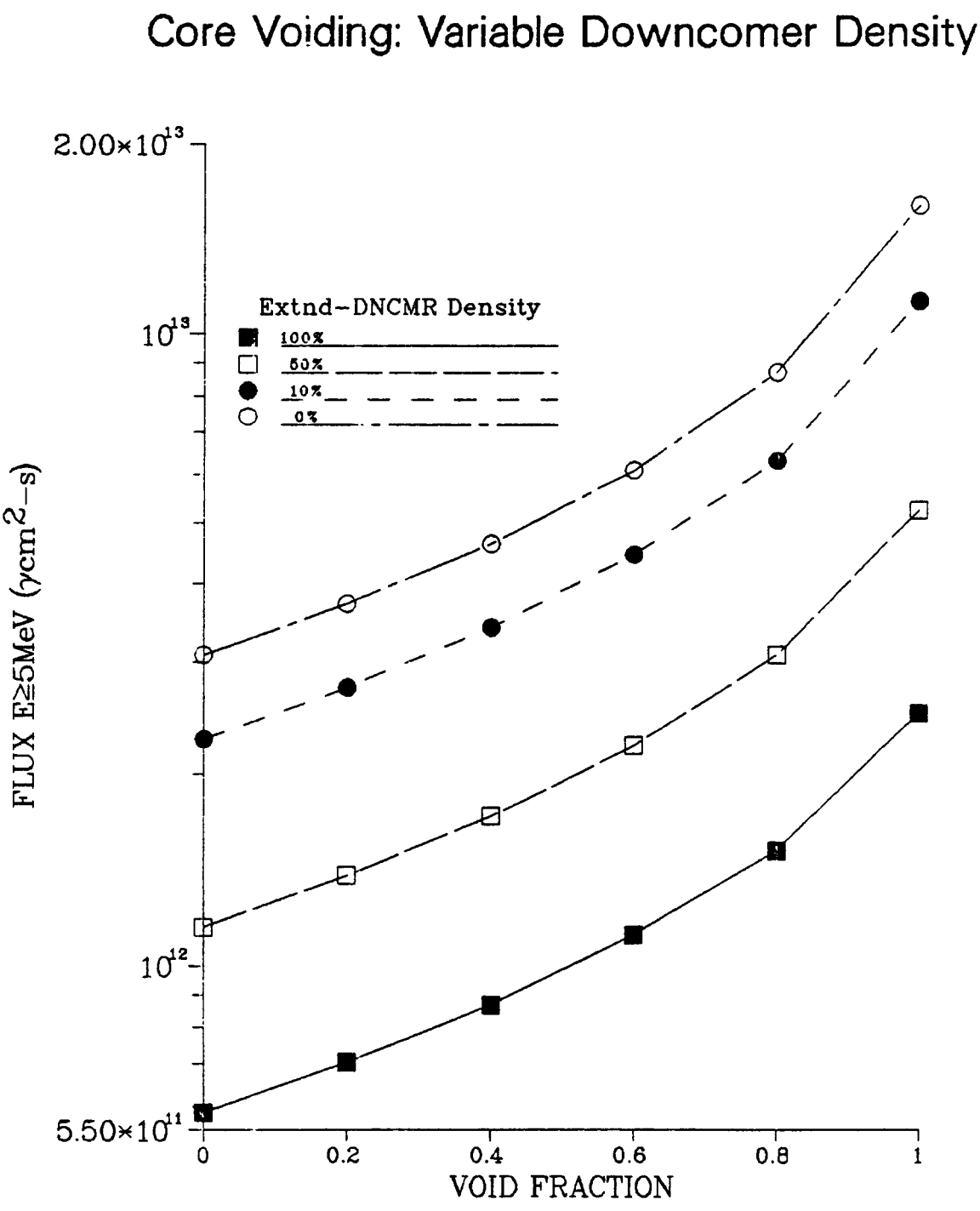
Core Voiding: Variable Downcomer Density
2.00×10^13
10^13
10^12
5.50×10^11
FLUX E≥5MeV (γcm^2-s)
Extnd-DNCMR Density
100%
50%
10%
0%
0
0.2
0.4
0.6
0.8
1
VOID FRACTION

Figure 19

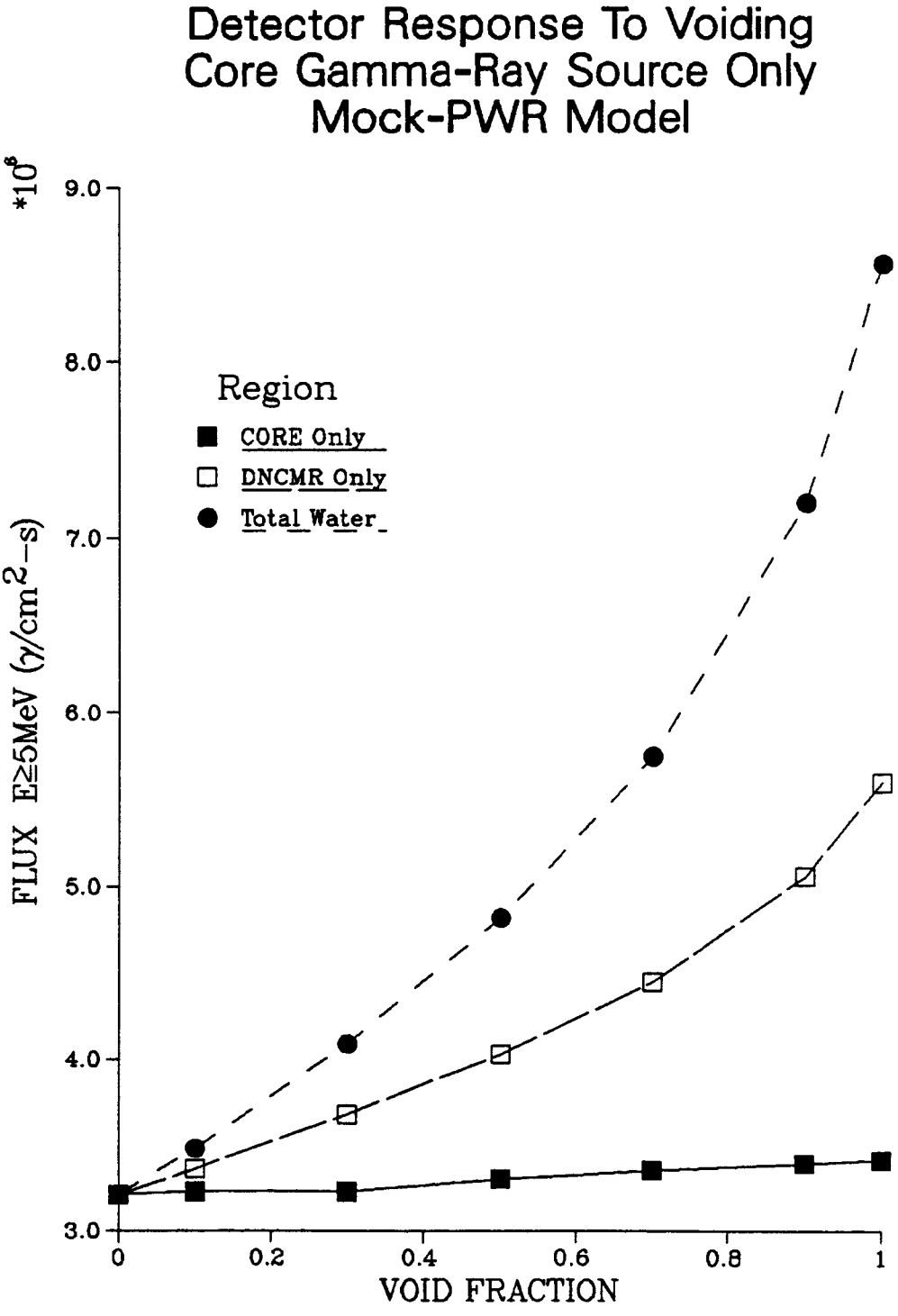
Detector Response To Voiding
Core Gamma-Ray Source Only
Mock-PWR Model
*10⁶
9.0
8.0
7.0
6.0
5.0
4.0
3.0
FLUX E≥5MeV (γ/cm²-s)
Region
CORE Only
DNCMR Only
Total Water
0
0.2
0.4
0.6
0.8
1
VOID FRACTION

Figure 20

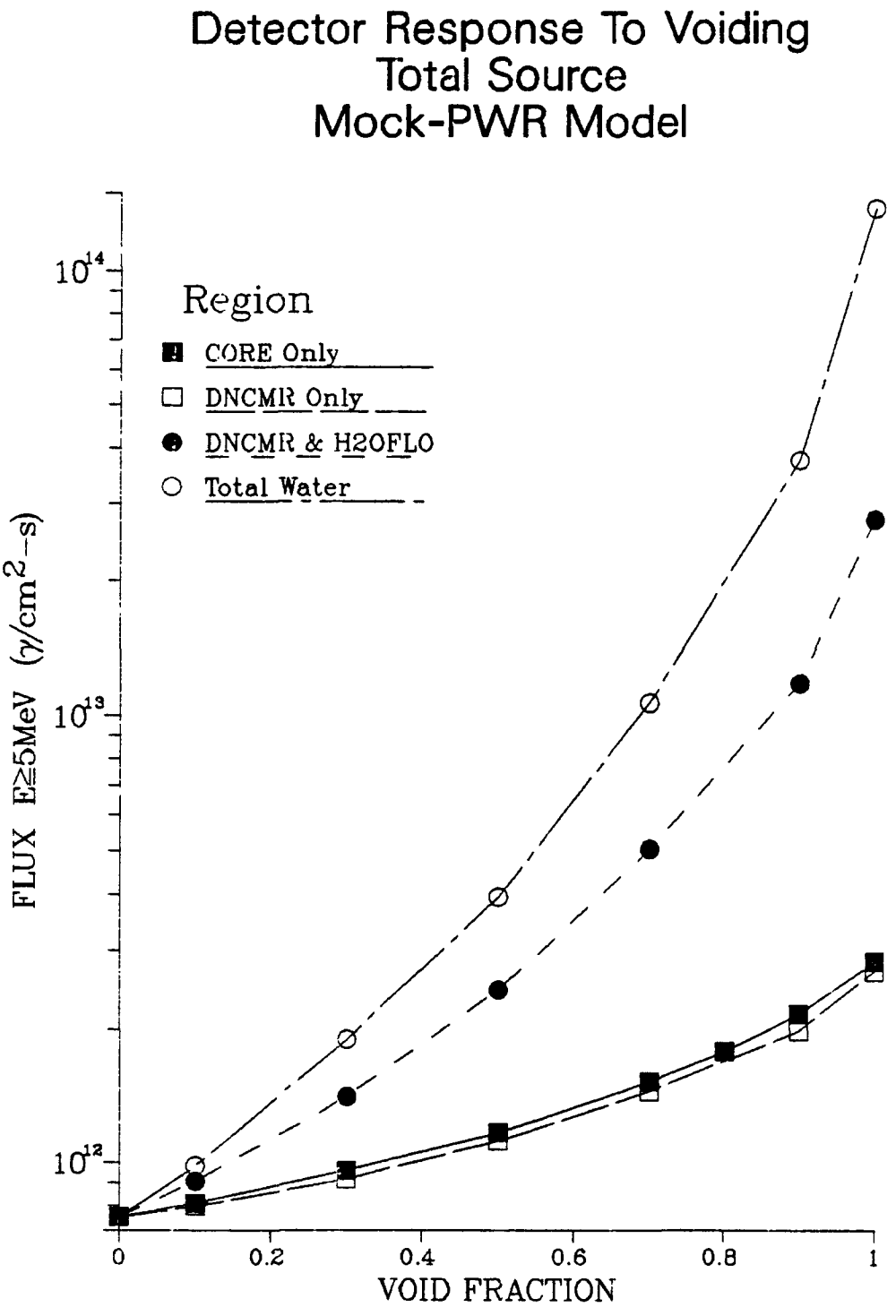
Detector Response To Voiding
Total Source
Mock-PWR Model
Region
CORE Only
DNCMR Only
DNCMR & H2OFLO
Total Water
FLUX E≥5MeV (γ/cm²-s)
10¹⁴
10¹³
10¹²
0
0.2
0.4
0.6
0.8
1
VOID FRACTION

Figure 21

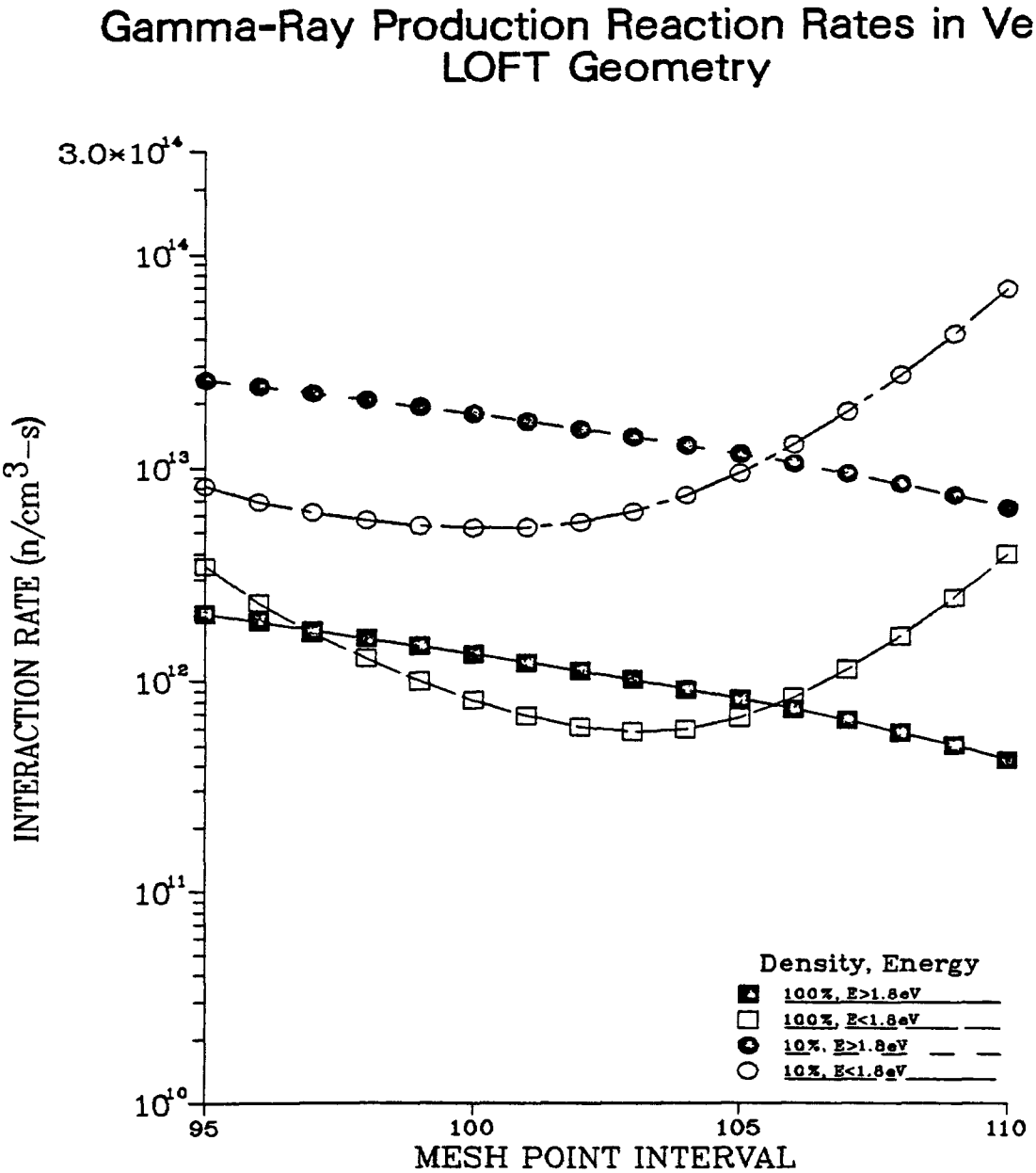
Gamma-Ray Production Reaction Rates in Vessel
LOFT Geometry
INTERACTION RATE (n/cm3-s)
3.0×10^14
10^14
10^13
10^12
10^11
10^10
95
100
105
110
MESH POINT INTERVAL
Density, Energy
100%, E>1.8eV
100%, E<1.8eV
10%, E>1.8eV
10%, E<1.8eV

Figure 22

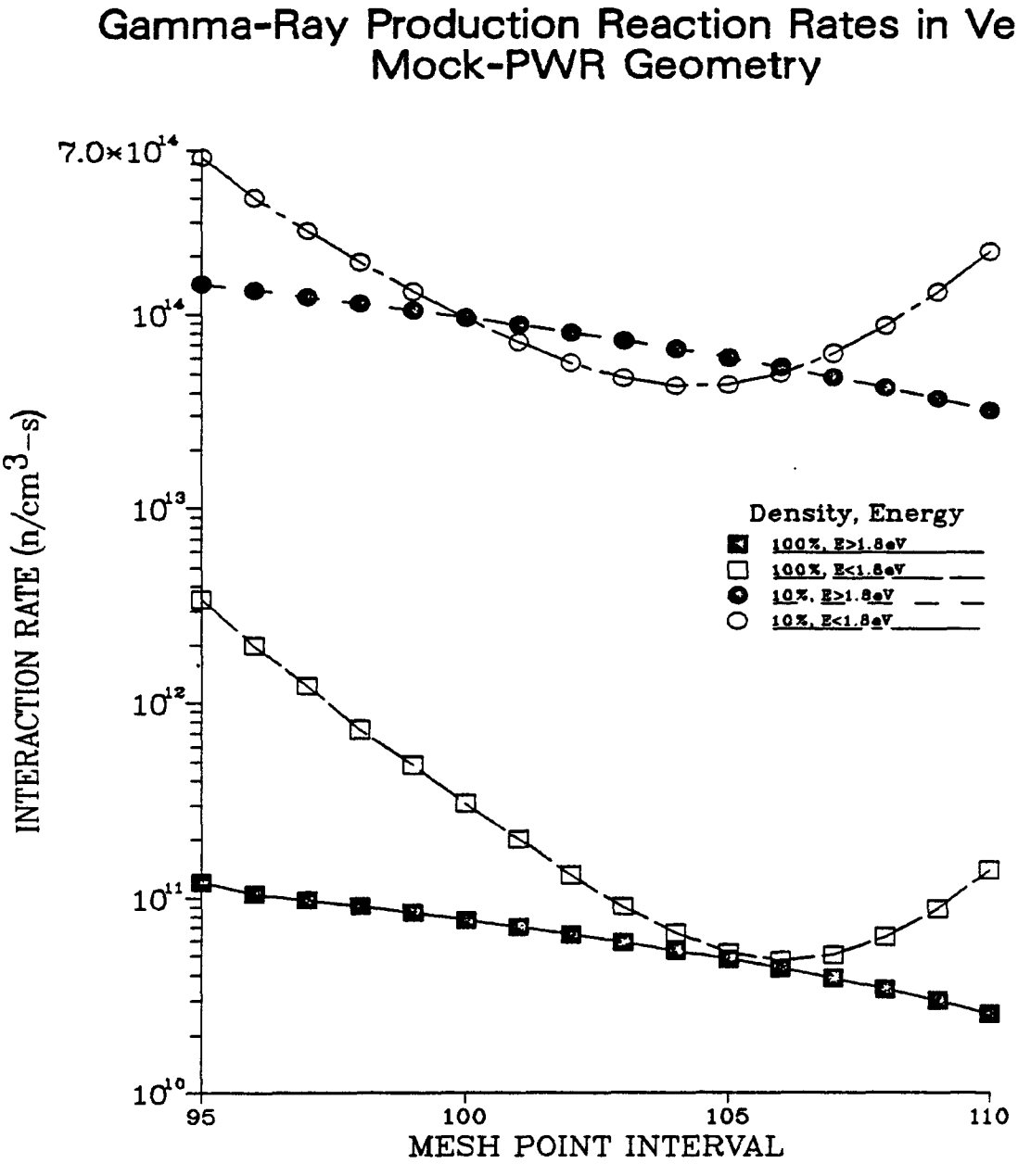
Gamma-Ray Production Reaction Rates in Vessel
Mock-PWR Geometry
7.0×10^14
10^14
10^13
10^12
10^11
10^10
INTERACTION RATE (n/cm^3-s)
95
100
105
110
MESH POINT INTERVAL
Density, Energy
100%, E>1.8eV
100%, E<1.8eV
10%, E>1.8eV
10%, E<1.8eV

Figure 23

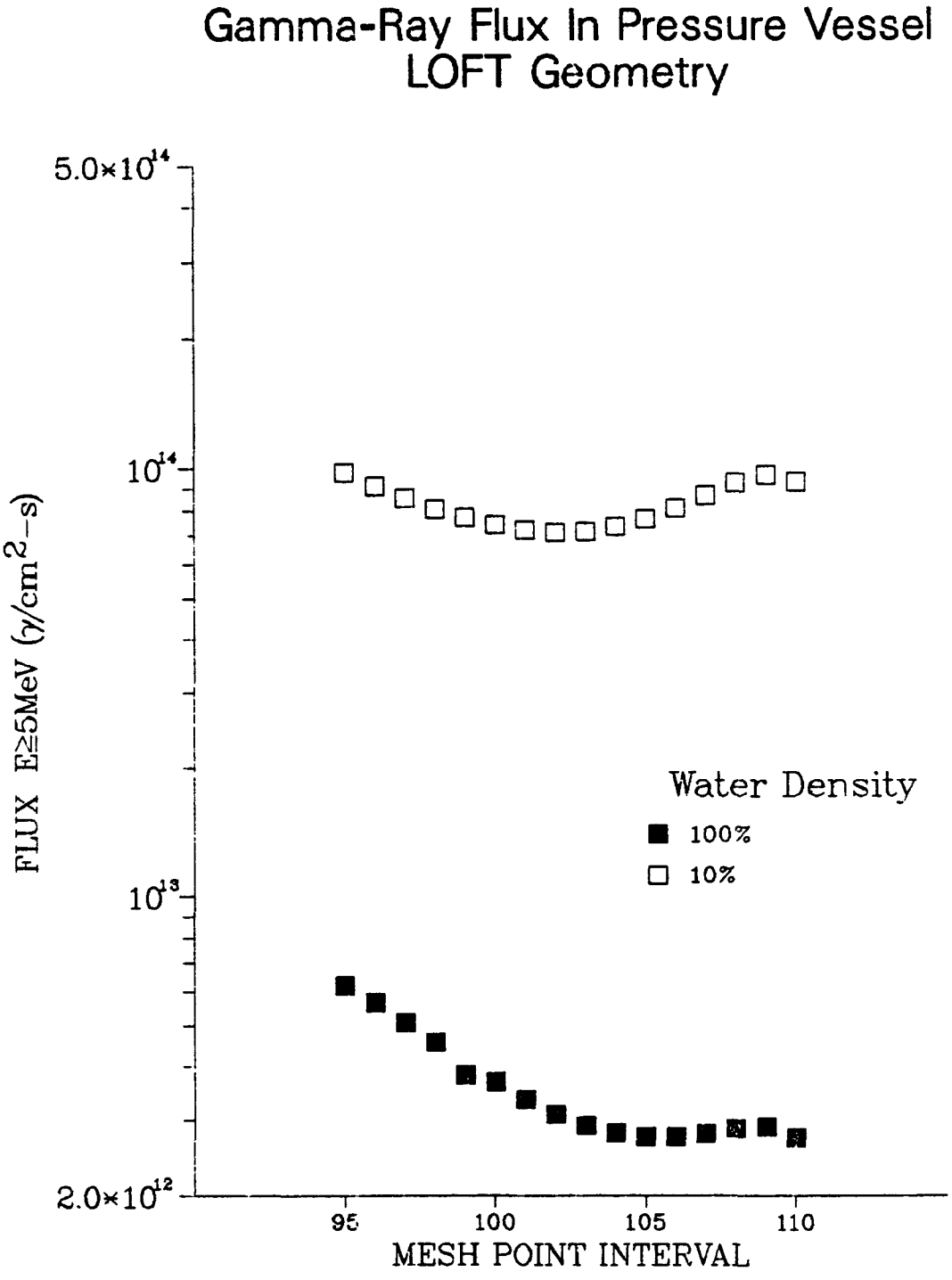
Gamma-Ray Flux In Pressure Vessel
LOFT Geometry
5.0×10^14
10^14
10^13
2.0×10^12
FLUX E≥5MeV (γ/cm^2-s)
Water Density
100%
10%
95
100
105
110
MESH POINT INTERVAL

Figure 24

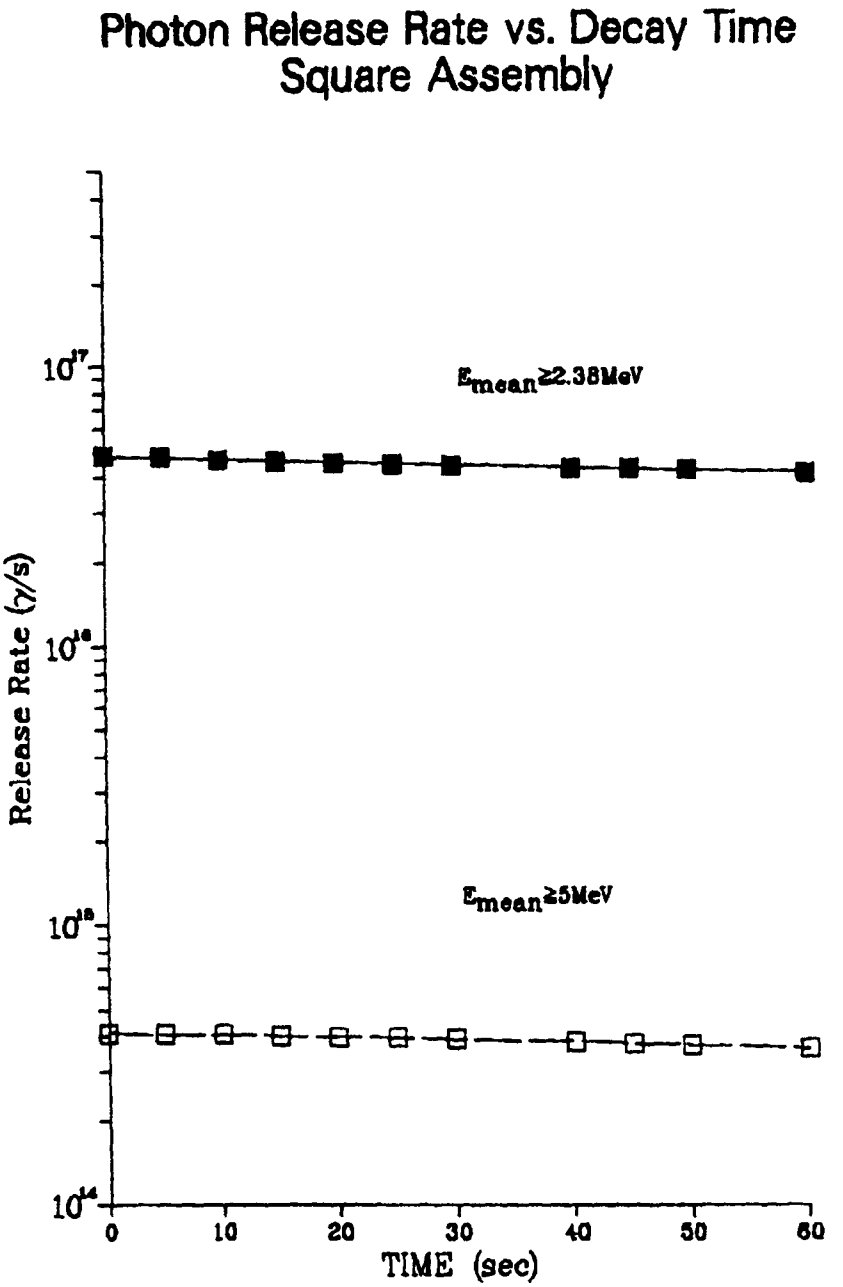
Photon Release Rate vs. Decay Time
Square Assembly
$E_{mean} \geq 2.38 MeV$
$E_{mean} \geq 5 MeV$
Release Rate (γ/s)
10^{17}
10^{16}
10^{15}
10^{14}
0
10
20
30
40
50
60
TIME (sec)

Figure 25

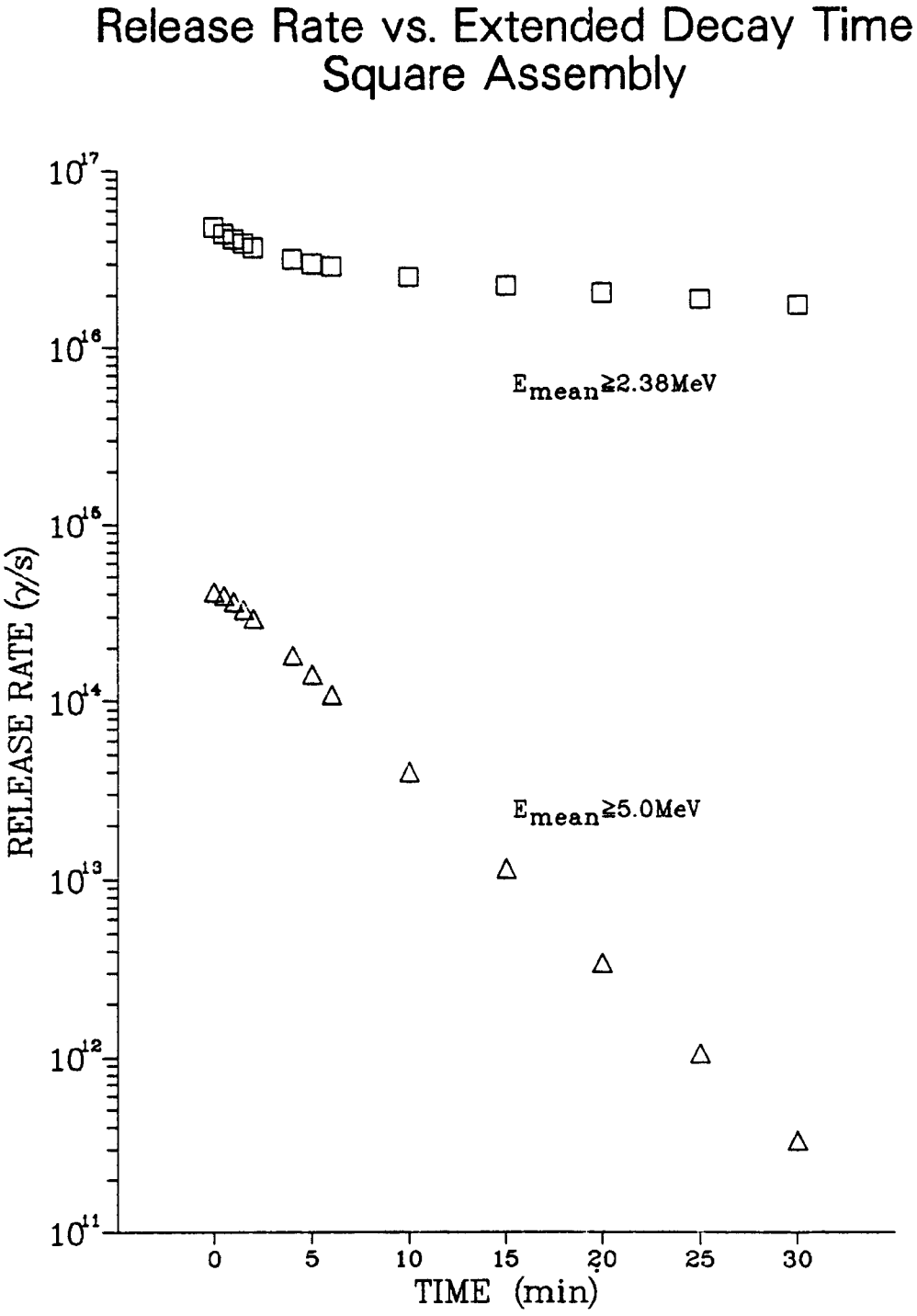
Release Rate vs. Extended Decay Time
Square Assembly
RELEASE RATE (γ/s)
10^{17}
10^{16}
10^{15}
10^{14}
10^{13}
10^{12}
10^{11}
$E_{mean} \geq 2.38 MeV$
$E_{mean} \geq 5.0 MeV$
0
5
10
15
20
25
30
TIME (min)

Figure 26

Post-Shutdown Volumetric Delayed Neutron Source

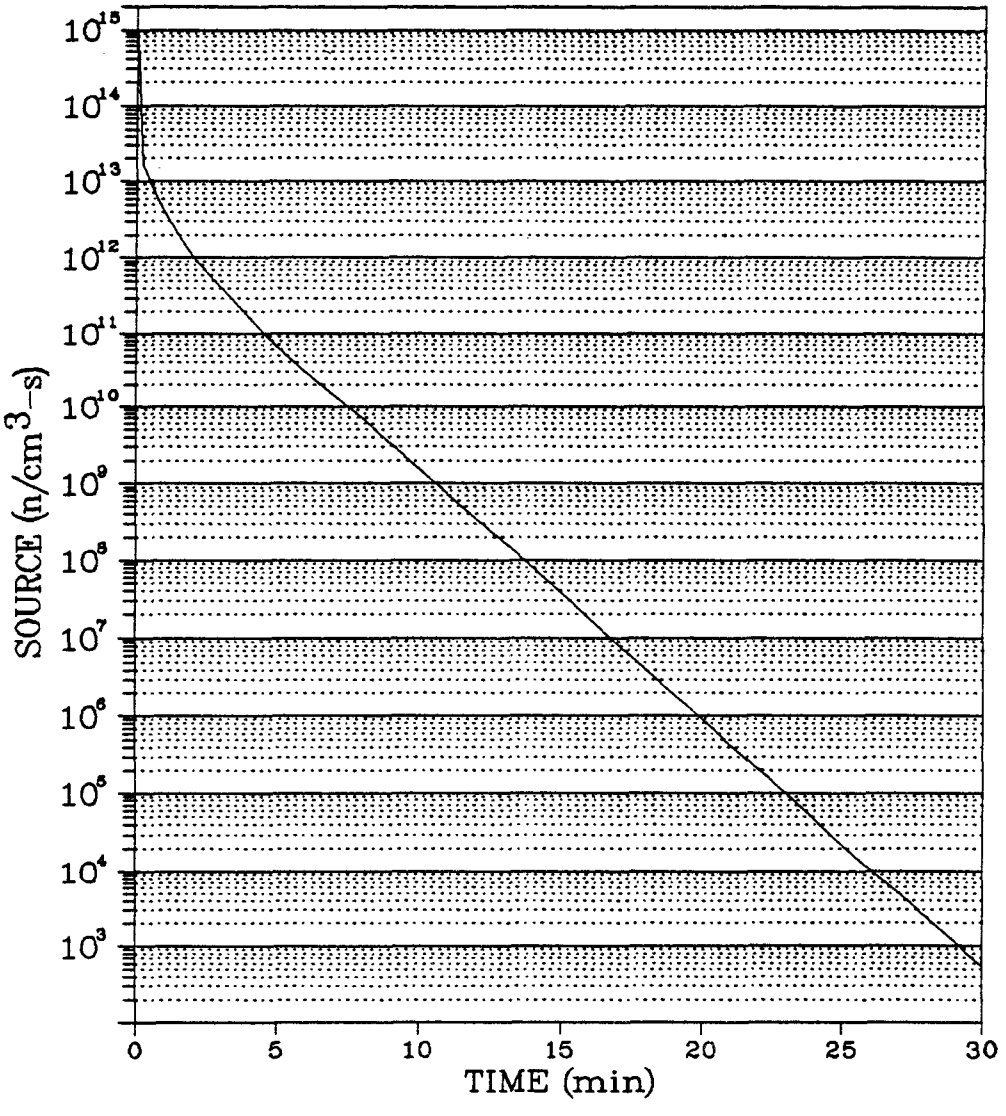

Figure 27

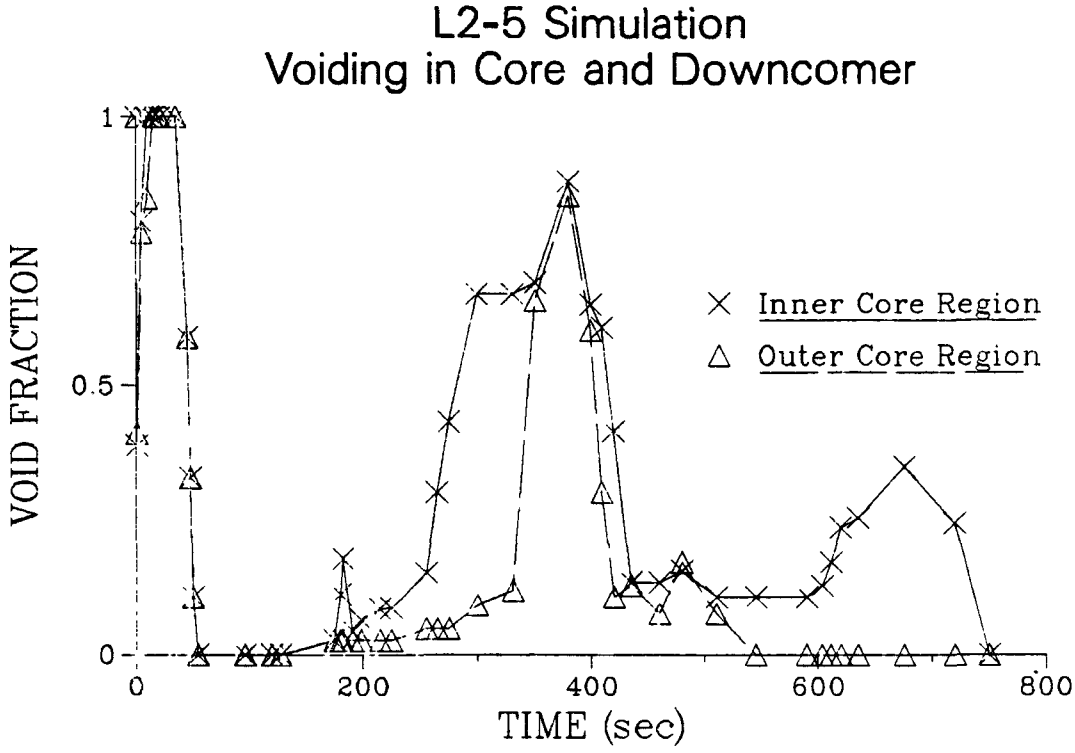
L2-5 Simulation
Voiding in Core and Downcomer
VOID FRACTION
1
0.5
0
0
200
400
600
800
TIME (sec)
Inner Core Region
Outer Core Region

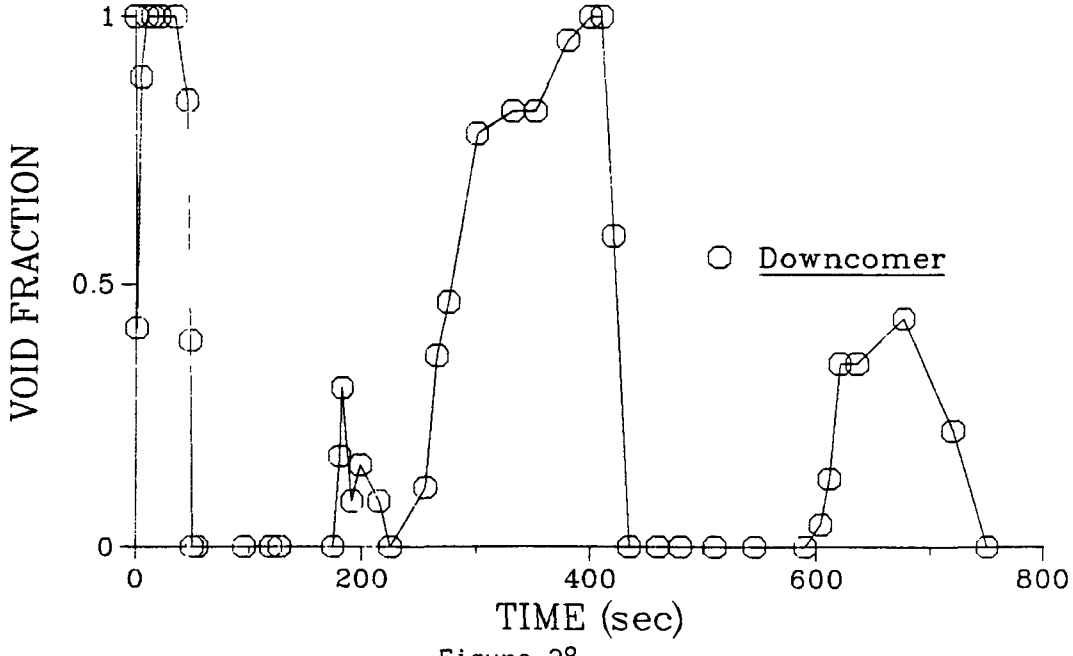
VOID FRACTION
1
0.5
0
0
200
400
600
800
TIME (sec)
Downcomer

Figure 28

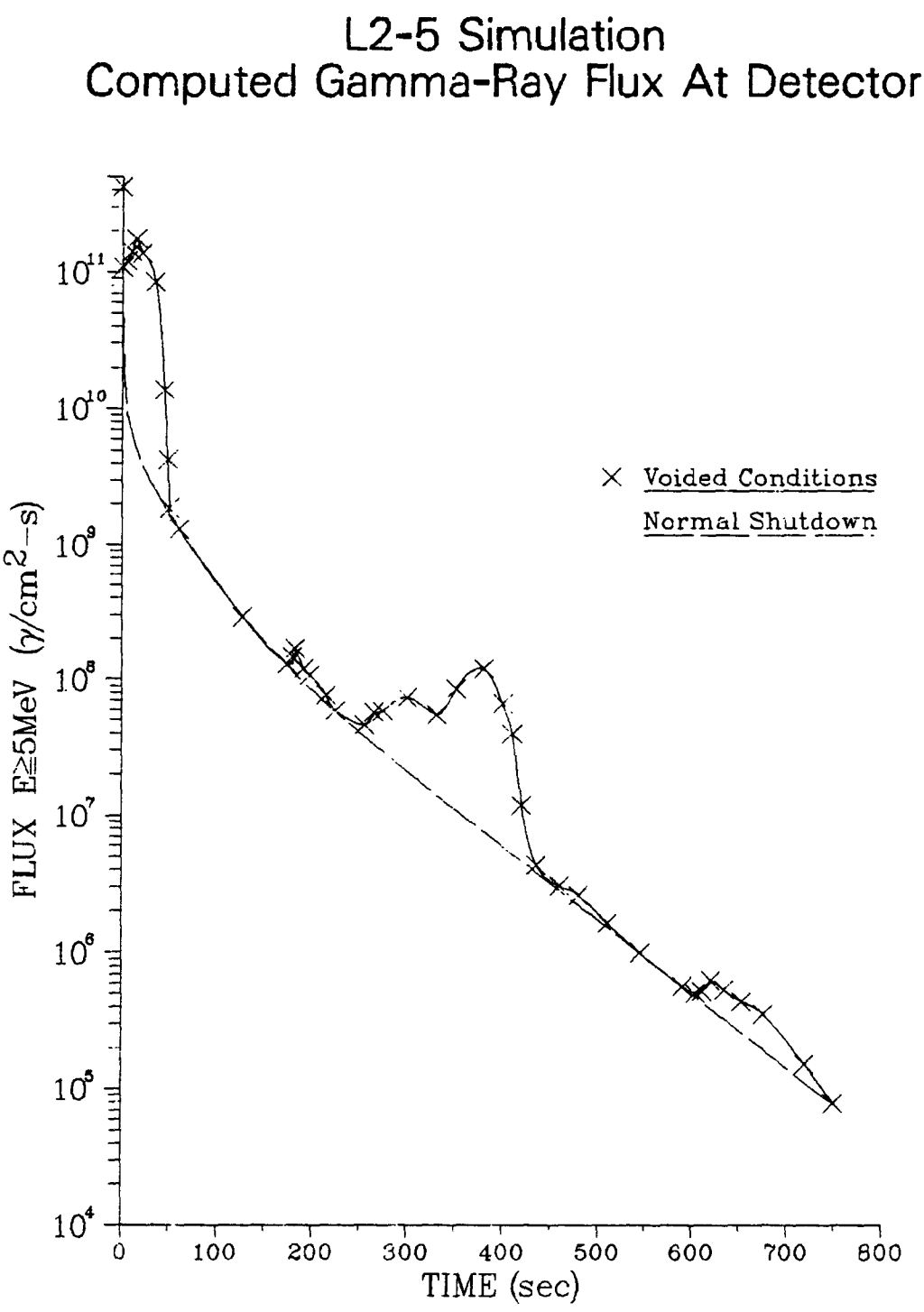
L2-5 Simulation
Computed Gamma-Ray Flux At Detector
FLUX E≥5MeV (γ/cm²-s)
10¹¹
10¹⁰
10⁹
10⁸
10⁷
10⁶
10⁵
10⁴
0
100
200
300
400
500
600
700
800
TIME (sec)
Voided Conditions
Normal Shutdown

Figure 29

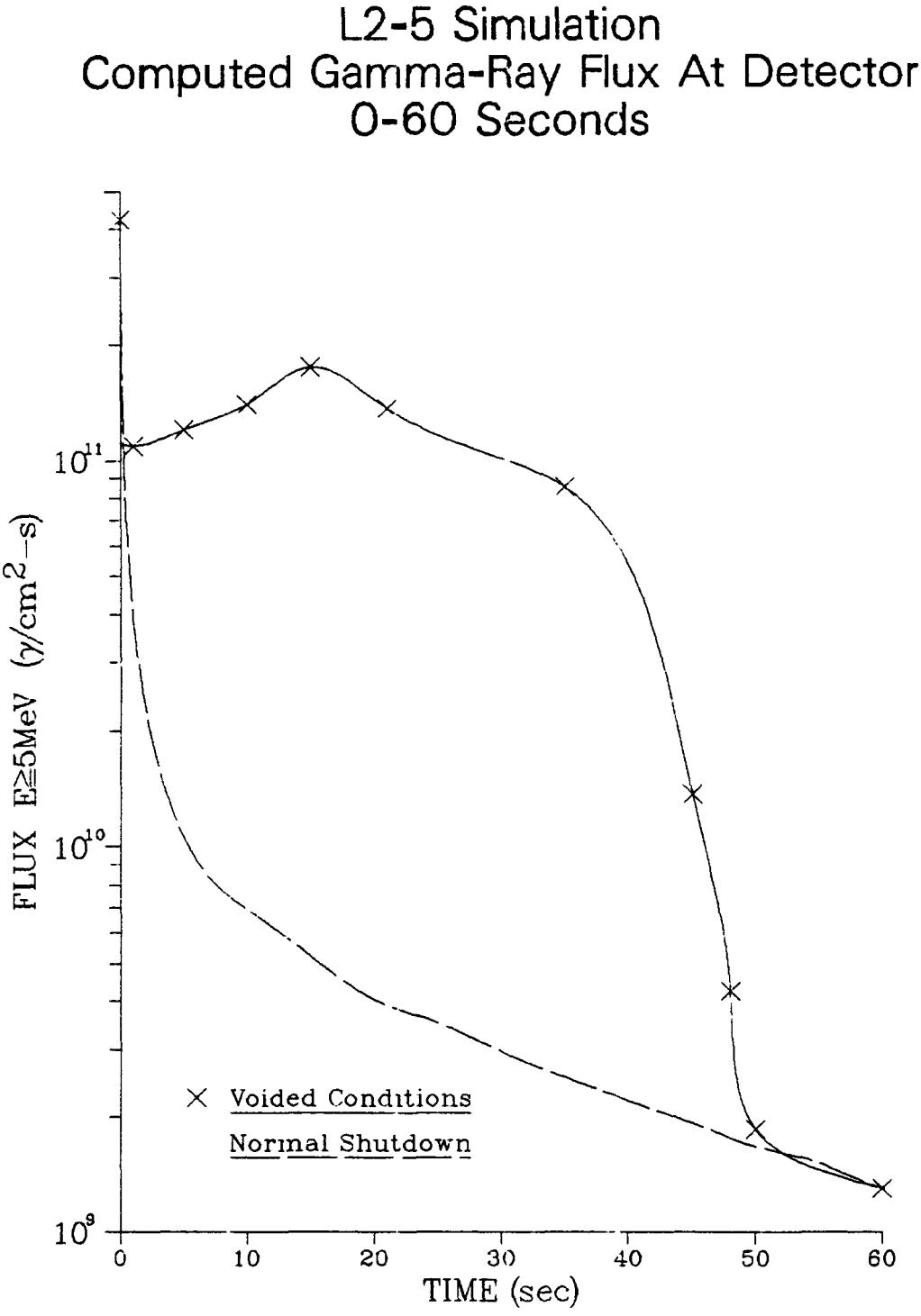
L2-5 Simulation
Computed Gamma-Ray Flux At Detector
0-60 Seconds
FLUX E≥5MeV (γ/cm²-s)
10¹¹
10¹⁰
10⁹
0
10
20
30
40
50
60
TIME (sec)
Voided Conditions
Normal Shutdown

Figure 30

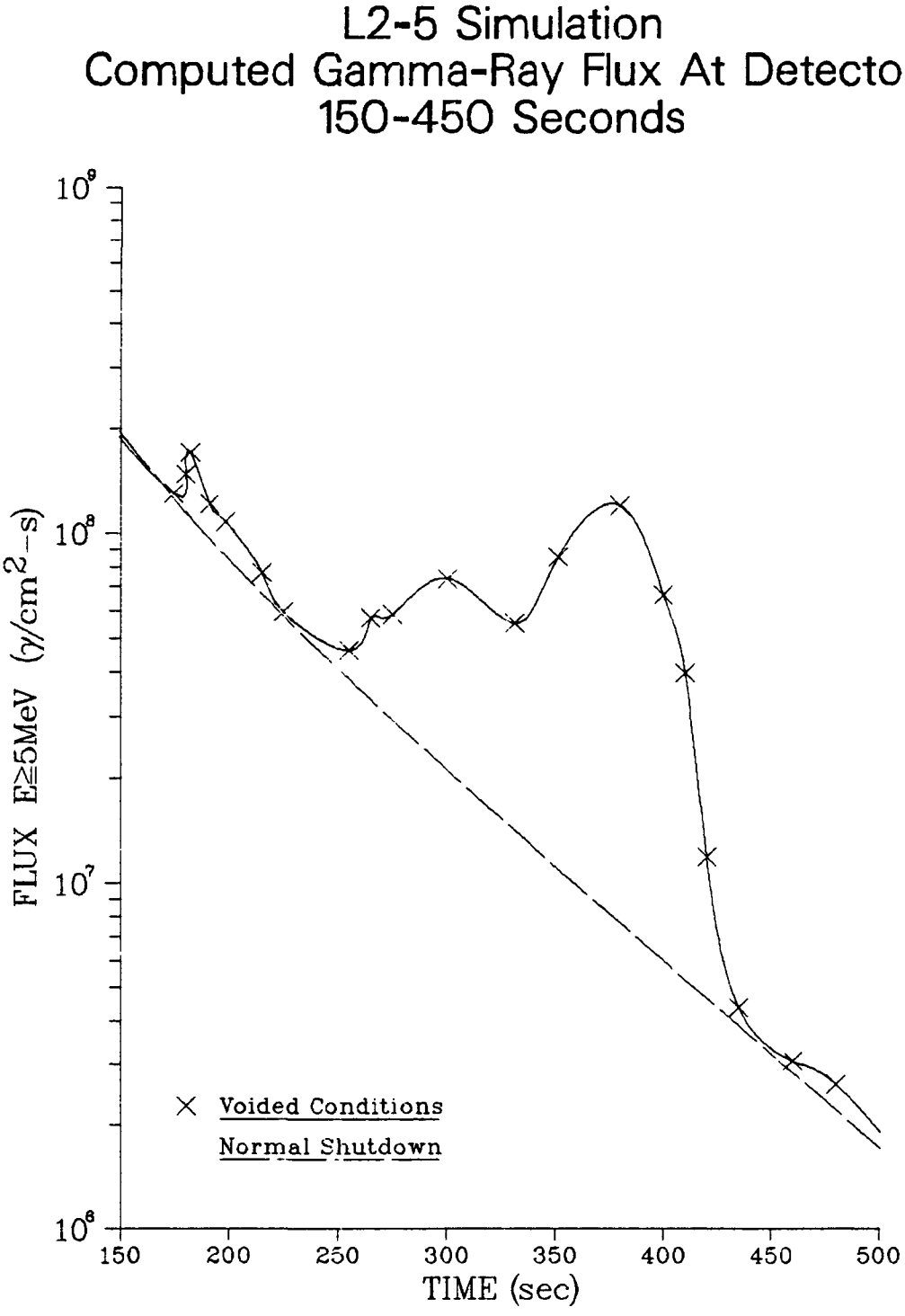
L2-5 Simulation
Computed Gamma-Ray Flux At Detector
150-450 Seconds
FLUX E≥5MeV (γ/cm²-s)
10⁹
10⁸
10⁷
10⁶
150
200
250
300
350
400
450
500
TIME (sec)
Voided Conditions
Normal Shutdown

Figure 31

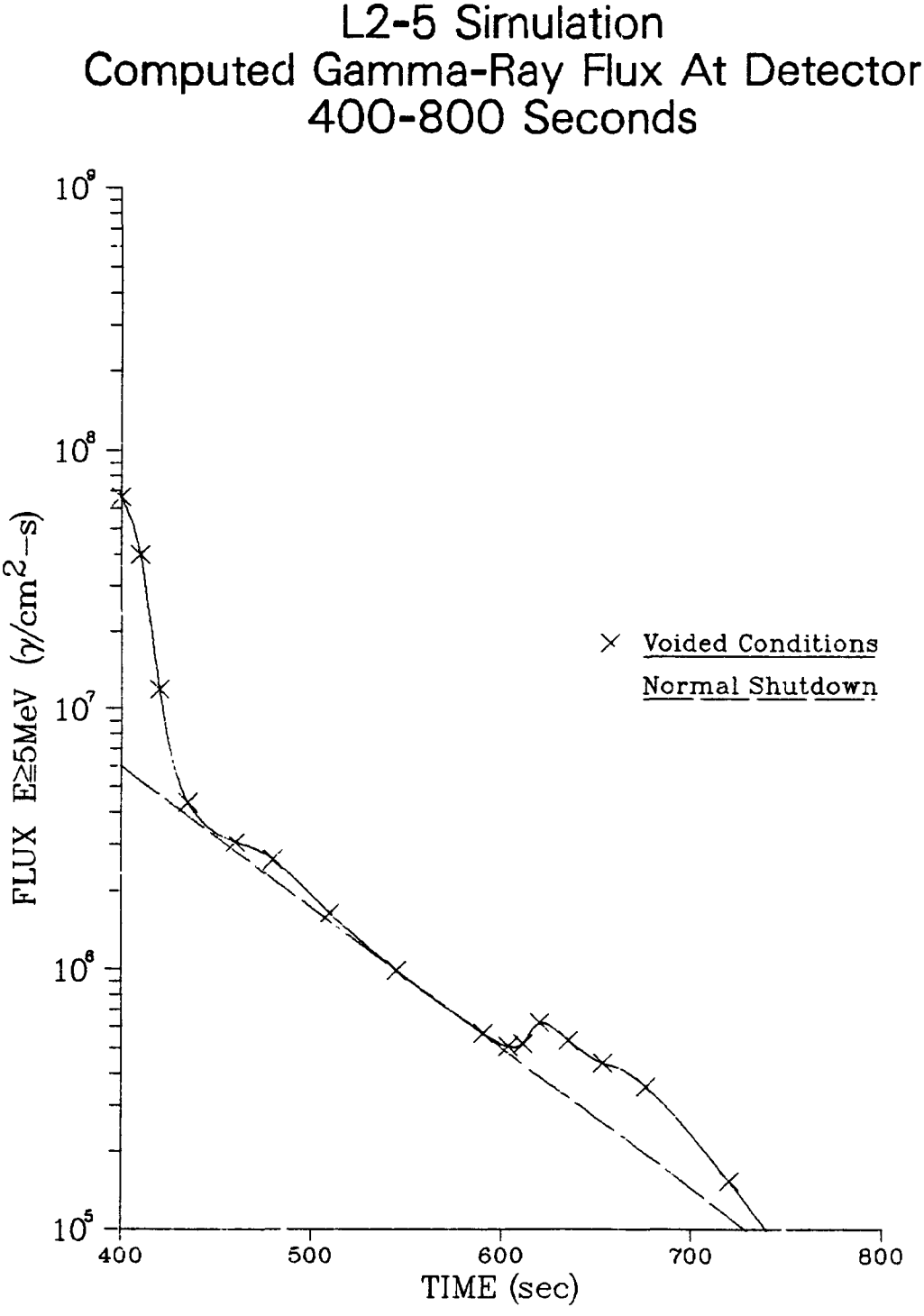
L2-5 Simulation
Computed Gamma-Ray Flux At Detector
400-800 Seconds
FLUX E≥5MeV (γ/cm²-s)
10⁹
10⁸
10⁷
10⁶
10⁵
400
500
600
700
800
TIME (sec)
× Voided Conditions
Normal Shutdown

Figure 32

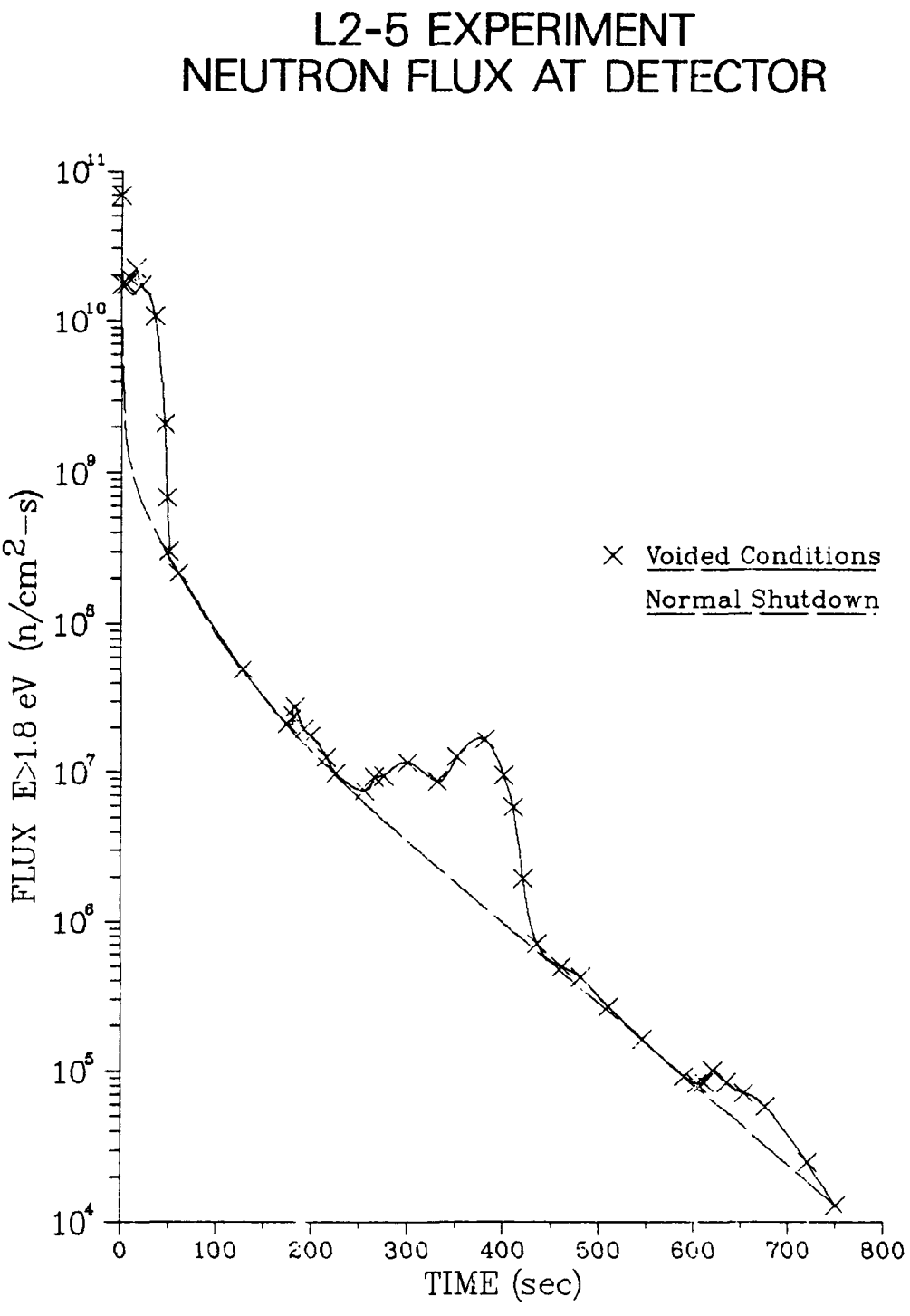
L2-5 EXPERIMENT
NEUTRON FLUX AT DETECTOR
FLUX E>1.8 eV (n/cm2-s)
10^11
10^10
10^9
10^8
10^7
10^6
10^5
10^4
0
100
200
300
400
500
600
700
800
TIME (sec)
Voided Conditions
Normal Shutdown

Figure 33

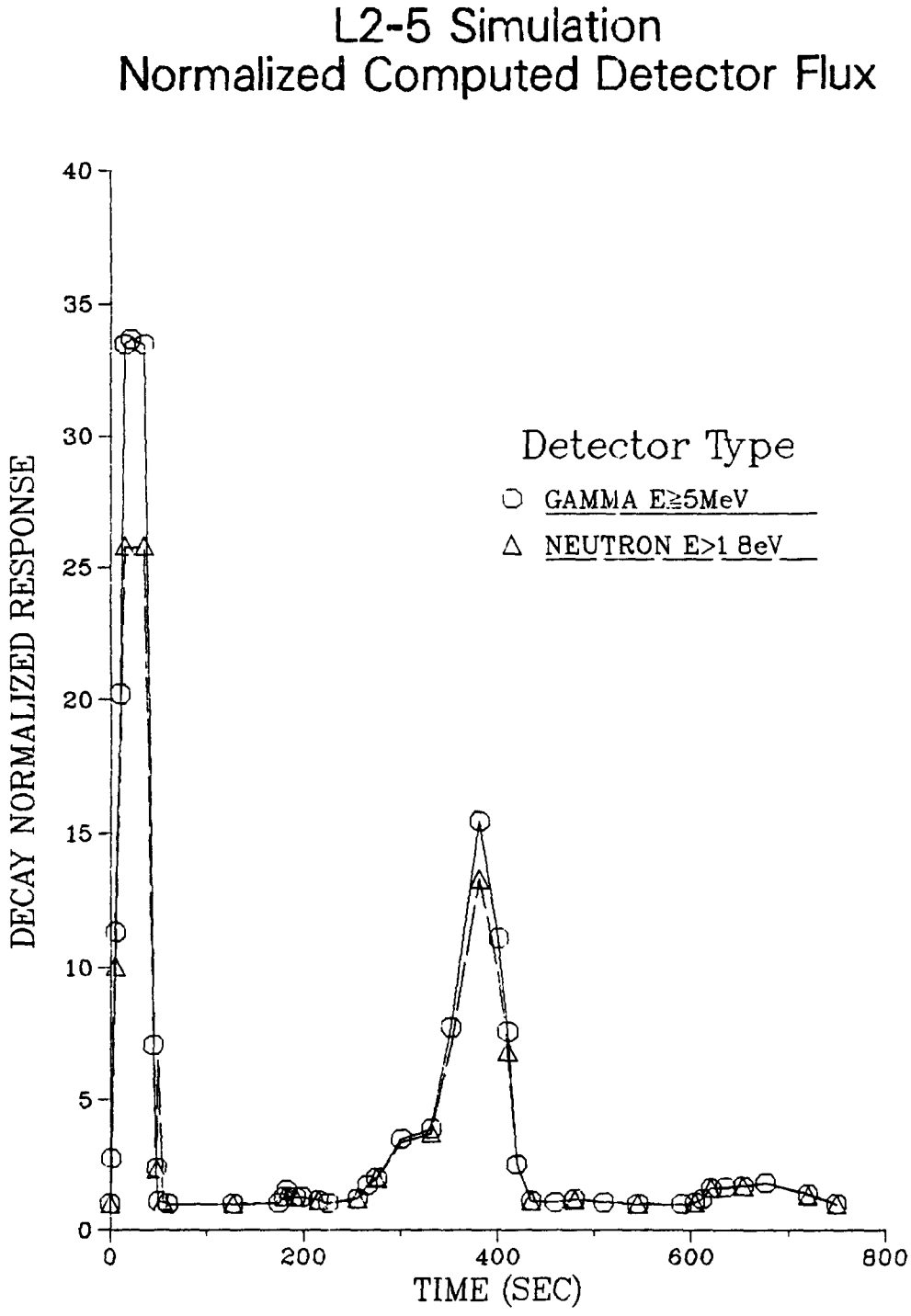
L2-5 Simulation
Normalized Computed Detector Flux
DECAY NORMALIZED RESPONSE
TIME (SEC)
Detector Type
GAMMA E≥5MeV
NEUTRON E>1 8eV
0
5
10
15
20
25
30
35
40
0
200
400
600
800

Figure 34

LOFT Intermediate-Range Detector Normalized Response

L2-5 Experiment

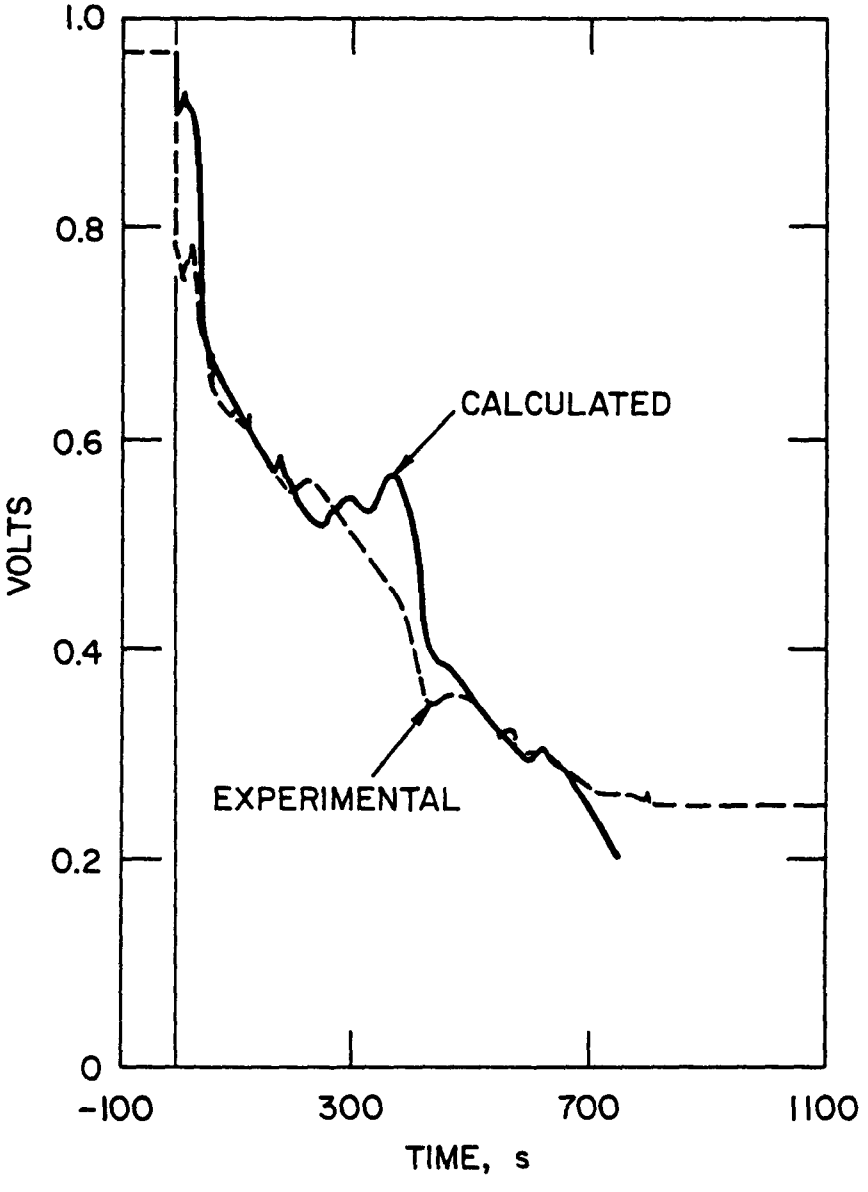

Figure 35

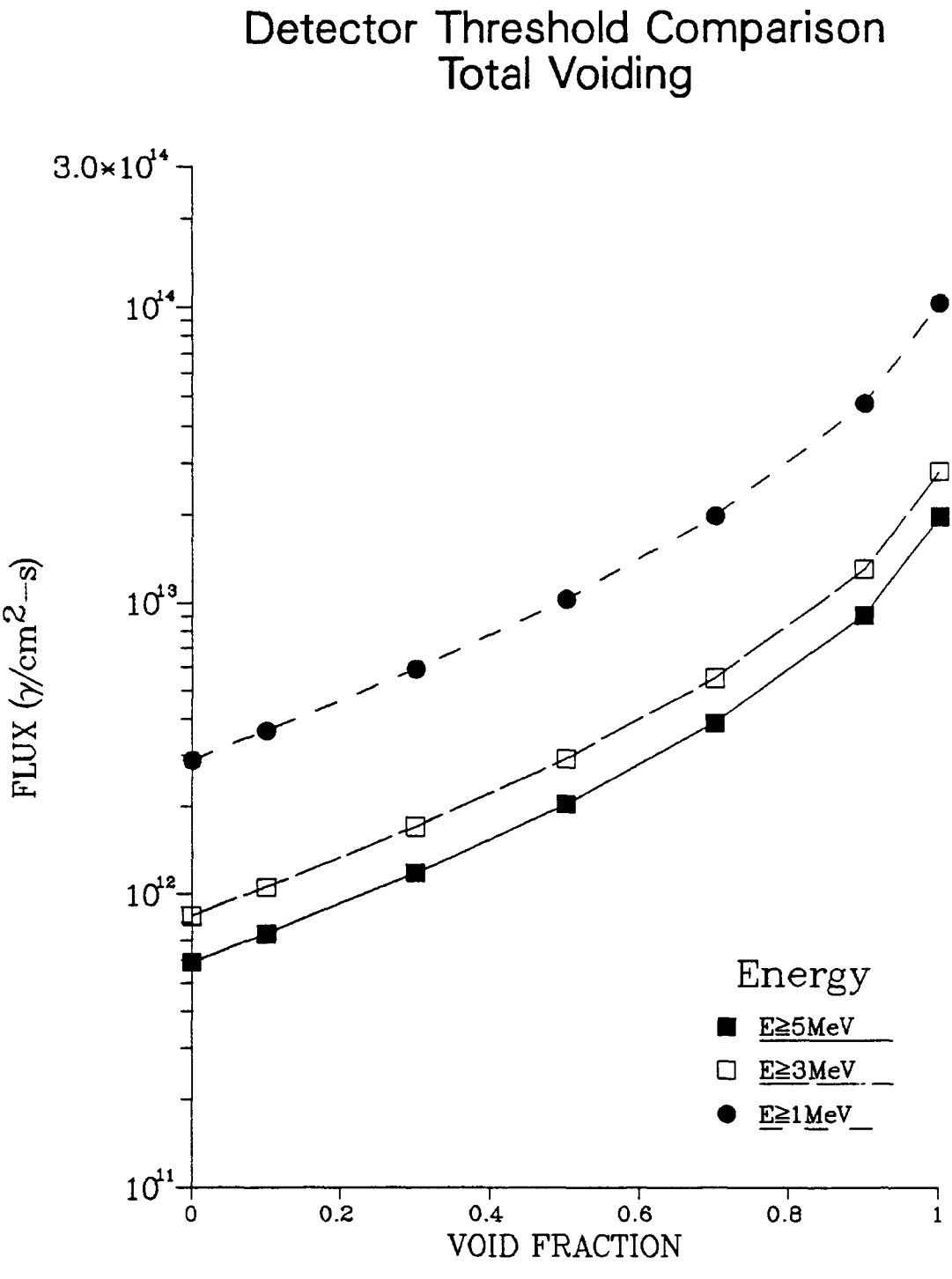
Detector Threshold Comparison
Total Voiding
3.0×10^14
10^14
10^13
10^12
10^11
FLUX (γ/cm^2-s)
0
0.2
0.4
0.6
0.8
1
VOID FRACTION
Energy
E≥5MeV
E≥3MeV
E≥1MeV

Figure 36

LIST OF TABLES

Table 1. Simulated Bubbles Calculations
Gamma Flux at Detector Site

Energy	Flux (γ/cm^2-sec)	
	1 Bubble/1 Water	1 Water/1 Bubble
$E_\gamma \geq 5$ MeV	1.040×10^{12}	1.021×10^{12}
$E_\gamma \geq 3$ MeV	1.500×10^{12}	1.470×10^{12}
	5 Bubbles/5 Water	5 Water/5 Bubbles
$E_\gamma \geq 5$ MeV	1.027×10^{12}	1.032×10^{12}
$E_\gamma \geq 3$ MeV	1.482×10^{12}	1.488×10^{12}
	10 Bubbles/10 Water	10 Water/10 Bubbles
$E_\gamma \geq 5$ MeV	1.028×10^{12}	1.031×10^{12}
$E_\gamma \geq 3$ MeV	1.481×10^{12}	1.490×10^{12}
	Flux (γ/cm^2-sec)	
	Homogeneous Voiding 50% Density	
$E_\gamma \geq 5$ MeV	1.059×10^{12}	
$E_\gamma \geq 3$ MeV	1.522×10^{12}	

Table 2. Simulated Bubbles Calculations
Neutron Flux at Detector Site

Energy	Flux (n/cm^2-sec)	
	1 Bubble/1 Water	1 Water/1 Bubble
Group 1	1.378×10^{10}	1.336×10^{10}
Group 5	2.944×10^{11}	2.870×10^{11}
	5 Bubbles/5 Water	5 Water/5 Bubbles
Group 1	1.359×10^{10}	1.350×10^{10}
Group 5	2.908×10^{11}	2.892×10^{11}
	10 Bubbles/10 Water	10 Water/10 Bubbles
Group 1	1.357×10^{10}	1.352×10^{10}
Group 5	2.905×10^{11}	2.896×10^{11}
	Flux (n/cm^2-sec)	
	Homogeneous Voiding 50% Density	
Group 1	1.628×10^{10}	
Group 5	3.733×10^{11}	

Table 3. Neutron Flux Values

Neutron Source (5 Group Neutron Calculation, EPRI-CELL Cross Sections)		
Energy	Flux (n/cm^2-sec)	
	Core Edge	Vessel Inner Edge
$E_n > 1.8$ eV	2.08×10^{16}	8.29×10^{13}
$E_n < 1.8$ eV	1.51×10^{15}	5.92×10^{12}

Neutron Source (25 Group n-γ Calculation, COLLBUGL Cross Sections)		
Energy	Flux (n/cm^2-sec)	
	Core Edge	Vessel Inner Edge
$E_n > 1.8$ eV	2.05×10^{16}	1.75×10^{14}
$E_n < 1.8$ eV	6.29×10^{14}	1.54×10^{13}

Neutron + Gamma Source (25 Group n-γ Calculation, COLLBUGL Cross Sections)		
Energy	Flux (n/cm^2-sec)	
	Core Edge	Vessel Inner Edge
$E_n > 1.8$ eV	2.05×10^{16}	1.75×10^{14}
$E_n < 1.8$ eV	6.29×10^{14}	1.54×10^{13}

Table 4. Gamma-Ray Flux Values

Gamma Source
(67 Group γ Calculation, BUGLE Cross Sections)

Energy	Flux (γ/cm^2-sec)		
	Core Edge	Vessel Inner Edge	Detector Site
$E_\gamma \geq 5$ MeV	1.46×10^{10}	9.64×10^{4}	1.98×10^{3}
$E_\gamma \geq 3$ MeV	5.59×10^{11}	1.67×10^{6}	2.77×10^{4}
$E_\gamma \geq 2$ MeV	1.73×10^{12}	2.53×10^{6}	3.74×10^{4}

Neutron Source
(25 Group n-γ Calculation, COLLBUGL Cross Sections)

Energy	Flux (γ/cm^2-sec)		
	Core Edge	Vessel Inner Edge	Detector Site
$E_\gamma \geq 5$ MeV	2.46×10^{14}	6.21×10^{12}	5.87×10^{11}
$E_\gamma \geq 3$ MeV	9.04×10^{14}	8.79×10^{12}	8.45×10^{11}
$E_\gamma \geq 2$ MeV	2.29×10^{15}	1.08×10^{13}	2.12×10^{12}

Neutron + Gamma Source
(25 Group n-γ Calculation, COLLBUGL Cross Sections)

Energy	Flux (γ/cm^2-sec)		
	Core Edge	Vessel Inner Edge	Detector Site
$E_\gamma \geq 5$ MeV	2.46×10^{14}	6.21×10^{12}	5.87×10^{11}
$E_\gamma \geq 3$ MeV	9.04×10^{14}	8.79×10^{12}	8.45×10^{11}
$E_\gamma \geq 2$ MeV	2.29×10^{15}	1.08×10^{13}	2.12×10^{12}

Table 5. Photoneutron Generated Flux Values
photoneutron source only; n-γ coupled calculation; t=0

	Flux (particle/cm^2-sec)		
	Core Edge	Vessel Inner Edge	Detector Site
Neutron:			
E_n > 1.83 eV	3.41×10^8	6.36×10^6	3.98×10^3
E_n > 1.83 eV	1.87×10^7	5.51×10^5	8.83×10^3
Gamma-Ray:			
$E_\gamma \geq 5$ MeV	6.53×10^6	2.19×10^5	2.15×10^4
$E_\gamma \geq 3$ MeV	2.47×10^7	3.10×10^5	3.09×10^4
$E_\gamma \geq 2$ MeV	6.36×10^7	3.82×10^5	7.82×10^4

Table 6. Mock-PWR Geometry
Neutron Flux Values

Neutron Source (5 Group Neutron Calculation, EPRI-CELL Cross Sections)		
Energy	Flux (n/cm^2-sec)	
	Core Edge	Vessel Inner Edge
E_n > 1.8 eV	1.80×10^{16}	2.72×10^{12}
E_n < 1.8 eV	1.56×10^{15}	3.82×10^{11}

Neutron Source (25 Group n-γ Calculation, COLLBUGL Cross Sections)		
Energy	Flux (n/cm^2-sec)	
	Core Edge	Vessel Inner Edge
E_n > 1.8 eV	1.58×10^{16}	5.29×10^{12}
E_n < 1.8 eV	1.09×10^{15}	7.62×10^{12}

Neutron + Gamma Source (25 Group n-γ Calculation, COLLBUGL Cross Sections)		
Energy	Flux (n/cm^2-sec)	
	Core Edge	Vessel Inner Edge
E_n > 1.8 eV	1.58×10^{16}	5.29×10^{12}
E_n < 1.8 eV	1.09×10^{15}	7.62×10^{12}

Table 7. Mock-PWR Geometry
Gamma-Ray Flux Values

Gamma Source
(67 Group γ Calculation, BUGLE Cross Sections)

Energy	Flux (γ/cm^2-sec)		
	Core Edge	Vessel Inner Edge	Detector Site
$E_\gamma \geq 5$ MeV	1.50×10^{10}	1.58×10^{8}	3.21×10^{6}
$E_\gamma \geq 3$ MeV	5.71×10^{11}	4.53×10^{9}	6.73×10^{7}
$E_\gamma \geq 2$ MeV	1.77×10^{12}	1.02×10^{10}	1.17×10^{8}

Neutron Source
(25 Group n-γ Calculation, COLLBUGL Cross Sections)

Energy	Flux (γ/cm^2-sec)		
	Core Edge	Vessel Inner Edge	Detector Site
$E_\gamma \geq 5$ MeV	5.20×10^{14}	3.13×10^{15}	7.52×10^{11}
$E_\gamma \geq 3$ MeV	1.21×10^{15}	4.94×10^{13}	1.30×10^{12}
$E_\gamma \geq 2$ MeV	2.72×10^{15}	9.66×10^{13}	1.99×10^{12}

Neutron + Gamma Source
(25 Group n-γ Calculation, COLLBUGL Cross Sections)

Energy	Flux (γ/cm^2-sec)		
	Core Edge	Vessel Inner Edge	Detector Site
$E_\gamma \geq 5$ MeV	5.20×10^{14}	3.13×10^{15}	7.52×10^{11}
$E_\gamma \geq 3$ MeV	1.21×10^{15}	4.94×10^{13}	1.30×10^{12}
$E_\gamma \geq 2$ MeV	2.72×10^{15}	9.66×10^{13}	1.99×10^{12}

Table 8. Increase Factors Comparison

Region Voiding	COLLBUGL		EPRI-CELL
	Int. 105 $E_{thermal}$	Int. 156 $E_{\gamma} > 5$ MeV	Int. 105 $E_{thermal}$
CORE	4.2	4.3	4.6
CORE+H2OFLO	4.8	4.8	5.3
DNCMR	4.4	4.3	5.2
DNCMR+H2OGAP	5.3	5.2	5.3
H2OFLO	1.1	1.1	1.1
H2OGAP	1.2	1.2	1.01
CORE+DNCMR	22.9	22.5	30.9
Total Water	34.0	33.4	38.1

Table 9. Flux Contributions t = 20 Minutes

Description	Total Flux (n/cm²-sec)	Flux Source	
		Core Neutrons	Photoneutrons
Neutrons			
Core Edge: (Int. 19)			
E_n > 1.8 eV	1.452×10^7	99.6%	0.4%
E_n < 1.8 eV	4.493×10^5	98.9%	1.1%
Vessel Edge: (Int. 95)			
E_n > 1.8 eV	1.236×10^5	99.9%	0.1%
E_n < 1.8 eV	1.091×10^4	99.9%	0.1%

Description	Total Flux (γ/cm²-sec)	Flux Source		
		Core γ	Core n-γ	Photoneutron n-γ
Gamma-Rays				
Core Edge: (Int. 19)				
$E_\gamma \geq 5$ MeV	1.225×10^8	100%	<0.01%	<0.01%
$E_\gamma \geq 2$ MeV	7.170×10^{11}	100%	<0.01%	<0.01%
Downcomer: (Int. 49)				
$E_\gamma \geq 5$ MeV	2.584×10^6	80.7%	19.3%	<0.01%
$E_\gamma \geq 2$ MeV	8.590×10^9	74.8%	25.2%	<0.01%
Detector Site: (Int. 156)				
$E_\gamma \geq 5$ MeV	442.8	3.7%	96.3%	<0.01%
$E_\gamma \geq 3$ MeV	9.505×10^3	34.8%	65.2%	<0.01%
$E_\gamma \geq 1$ MeV	6.172×10^4	14.2%	85.8%	<0.01%

Table 10. Flux Contributions t = 30 Minutes

Neutrons			
		Flux Source	
Description	Total Flux (n/cm²-sec)	Core Neutrons	Photoneutrons
Core Edge: (Int. 19)			
E_n > 1.8 eV	5.928×10^4	14.5%	85.5%
E_n < 1.8 eV	4.432×10^3	6.0%	94.0%
Vessel Edge: (Int. 95)			
E_n > 1.8 eV	1.557×10^2	47.2%	53.2%
E_n < 1.8 eV	1.459×10^1	44.4%	55.9%

Gamma-Rays

		Flux Source		
Description	Total Flux (γ/cm²-sec)	Core γ	Core n-γ	Photoneutron n-γ
Core Edge: (Int. 19)				
$E_\gamma \geq 5$ MeV	1.198×10^7	99.9%	<0.01%	<0.01%
$E_\gamma \geq 2$ MeV	6.052×10^{11}	99.9%	<0.01%	<0.01%
Downcomer: (Int. 49)				
$E_\gamma \geq 5$ MeV	2.227×10^5	98.9%	0.1%	<0.3%
$E_\gamma \geq 2$ MeV	7.010×10^9	99.9%	0.01%	<0.01%
Detector Site: (Int. 156)				
$E_\gamma \geq 5$ MeV	3.445×10^0	83.8%	7.6%	8.5%
$E_\gamma \geq 3$ MeV	7.005×10^3	99.6%	<0.01%	<0.01%
$E_\gamma \geq 1$ MeV	3.278×10^4	100.0%	<0.01%	<0.01%

Table 11

ORIGEN Results for L2-5 Simulation

Center Assembly

PHOTON SPECTRUM AS A FUNCTION OF TIME FOR FISSION PRODUCTS

POST IRRADIATION DECAY TEN STEPS FROM SHUTDOWN TO 54.0 SEC
POWER= 11.30 MW, BURNUP= 32.MWD, FLUX= 5.14E+13 N**2-SEC

TWELVE GROUP PHOTON RELEASE RATES, PHOTONS/SEC
BASIS = CENTER FUEL ASSEMBLY-ENRICHMENT 4.0%

EMEAN		TIME AFTER DISCHARGE									
(MEV)	INITIAL	1.SEC	5.SEC	10.SEC	15.SEC	21.SEC	35.SEC	45.SEC	48.SEC	50.SEC	54.SEC
3.00E-01	2.74E+17	2.72E+17	2.67E+17	2.61E+17	2.55E+17	2.48E+17	2.36E+17	2.29E+17	2.27E+17	2.26E+17	2.24E+17
6.30E-01	4.94E+17	4.92E+17	4.86E+17	4.79E+17	4.73E+17	4.67E+17	4.58E+17	4.53E+17	4.51E+17	4.50E+17	4.49E+17
1.10E+00	2.53E+17	2.50E+17	2.42E+17	2.34E+17	2.29E+17	2.24E+17	2.18E+17	2.14E+17	2.13E+17	2.12E+17	2.11E+17
1.55E+00	1.31E+17	1.30E+17	1.26E+17	1.22E+17	1.19E+17	1.15E+17	1.08E+17	1.04E+17	1.03E+17	1.03E+17	1.01E+17
1.99E+00	2.81E+16	2.79E+16	2.75E+16	2.71E+16	2.68E+16	2.64E+16	2.53E+16	2.54E+16	2.53E+16	2.53E+16	2.51E+16
2.38E+00	3.39E+16	3.38E+16	3.36E+16	3.33E+16	3.30E+16	3.27E+16	3.21E+16	3.16E+16	3.15E+16	3.14E+16	3.13E+16
2.75E+00	1.62E+16	1.60E+16	1.55E+16	1.50E+16	1.45E+16	1.39E+16	1.28E+16	1.21E+16	1.20E+16	1.18E+16	1.16E+16
3.25E+00	1.25E+16	1.25E+16	1.24E+16	1.24E+16	1.23E+16	1.23E+16	1.22E+16	1.20E+16	1.20E+16	1.20E+16	1.19E+16
3.70E+00	1.89E+15	1.89E+15	1.87E+15	1.85E+15	1.82E+15	1.79E+15	1.72E+15	1.66E+15	1.65E+15	1.64E+15	1.62E+15
4.22E+00	5.63E+15	5.62E+15	5.58E+15	5.50E+15	5.42E+15	5.31E+15	5.05E+15	4.86E+15	4.80E+15	4.76E+15	4.69E+15
4.70E+00	2.62E+15	2.60E+15	2.54E+15	2.45E+15	2.36E+15	2.25E+15	1.99E+15	1.83E+15	1.78E+15	1.75E+15	1.70E+15
5.25E+00	6.48E+14	6.48E+14	6.46E+14	6.42E+14	6.38E+14	6.31E+14	6.13E+14	5.97E+14	5.92E+14	5.89E+14	5.82E+14
TOTAL	1.25E+18	1.25E+18	1.22E+18	1.19E+18	1.17E+18	1.15E+18	1.11E+18	1.09E+18	1.08E+18	1.08E+18	1.07E+18

POST IRRADIATION DECAY TEN STEPS FROM 054.0 SEC TO 225.0 SEC
POWER= 11.30 MW, BURNUP= 32.MWD, FLUX= 5.14E+13 N**2-SEC

TWELVE GROUP PHOTON RELEASE RATES, PHOTONS/SEC
BASIS = CENTER FUEL ASSEMBLY-ENRICHMENT 4.0%

EMEAN		TIME AFTER DISCHARGE									
(MEV)	INITIAL	96.SEC	119.SEC	127.SEC	174.SEC	180.SEC	182.SEC	191.SEC	193.SEC	215.SEC	225.SEC
3.00E-01	2.24E+17	2.06E+17	1.99E+17	1.97E+17	1.86E+17	1.85E+17	1.85E+17	1.83E+17	1.82E+17	1.79E+17	1.77E+17
6.30E-01	4.49E+17	4.33E+17	4.26E+17	4.23E+17	4.12E+17	4.10E+17	4.10E+17	4.08E+17	4.08E+17	4.03E+17	4.01E+17
1.10E+00	2.11E+17	2.00E+17	1.95E+17	1.93E+17	1.85E+17	1.84E+17	1.84E+17	1.83E+17	1.82E+17	1.80E+17	1.78E+17
1.55E+00	1.01E+17	8.94E+16	8.44E+16	8.29E+16	7.56E+16	7.48E+16	7.45E+16	7.34E+16	7.32E+16	7.08E+16	6.98E+16
1.99E+00	2.51E+16	2.41E+16	2.36E+16	2.35E+16	2.28E+16	2.27E+16	2.26E+16	2.25E+16	2.25E+16	2.22E+16	2.21E+16
2.38E+00	3.13E+16	2.99E+16	2.93E+16	2.91E+16	2.83E+16	2.82E+16	2.81E+16	2.80E+16	2.80E+16	2.77E+16	2.75E+16
2.75E+00	1.16E+16	9.86E+15	9.16E+15	8.96E+15	8.02E+15	7.93E+15	7.89E+15	7.76E+15	7.73E+15	7.45E+15	7.33E+15
3.25E+00	1.19E+16	1.14E+16	1.11E+16	1.10E+16	1.04E+16	1.03E+16	1.03E+16	1.02E+16	1.02E+16	9.95E+15	9.85E+15
3.70E+00	1.62E+15	1.43E+15	1.34E+15	1.31E+15	1.17E+15	1.16E+15	1.15E+15	1.13E+15	1.12E+15	1.07E+15	1.05E+15
4.22E+00	4.69E+15	3.93E+15	3.54E+15	3.42E+15	2.78E+15	2.70E+15	2.68E+15	2.57E+15	2.55E+15	2.31E+15	2.21E+15
4.70E+00	1.70E+15	1.21E+15	1.01E+15	9.50E+14	6.82E+14	6.55E+14	6.46E+14	6.08E+14	6.00E+14	5.22E+14	4.91E+14
5.25E+00	5.82E+14	5.07E+14	4.64E+14	4.50E+14	3.74E+14	3.65E+14	3.61E+14	3.48E+14	3.45E+14	3.16E+14	3.03E+14
TOTAL	1.07E+18	1.01E+18	9.83E+17	9.75E+17	9.33E+17	9.29E+17	9.27E+17	9.20E+17	9.19E+17	9.04E+17	8.97E+17

POST IRRADIATION DECAY TEN STEPS FROM 225.0 SEC TO 420.0 SEC
POWER= 11.30 MW, BURNUP= 32.MWD, FLUX= 5.14E+13 N**2-SEC

TWELVE GROUP PHOTON RELEASE RATES, PHOTONS/SEC
BASIS = CENTER FUEL ASSEMBLY-ENRICHMENT 4.0%

EMEAN		TIME AFTER DISCHARGE									
(MEV)	INITIAL	255.SEC	265.SEC	275.SEC	300.SEC	331.SEC	351.SEC	380.SEC	400.SEC	410.SEC	420.SEC
3.00E-01	1.77E+17	1.73E+17	1.72E+17	1.70E+17	1.67E+17	1.64E+17	1.62E+17	1.59E+17	1.57E+17	1.56E+17	1.55E+17
6.30E-01	4.01E+17	3.96E+17	3.94E+17	3.92E+17	3.88E+17	3.84E+17	3.81E+17	3.77E+17	3.75E+17	3.73E+17	3.72E+17
1.10E+00	1.78E+17	1.75E+17	1.73E+17	1.72E+17	1.70E+17	1.66E+17	1.64E+17	1.62E+17	1.60E+17	1.59E+17	1.58E+17
1.55E+00	6.93E+16	6.71E+16	6.63E+16	6.56E+16	6.39E+16	6.20E+16	6.09E+16	5.95E+16	5.87E+16	5.83E+16	5.79E+16
1.99E+00	2.21E+16	2.17E+16	2.16E+16	2.15E+16	2.13E+16	2.10E+16	2.08E+16	2.05E+16	2.04E+16	2.03E+16	2.02E+16
2.38E+00	2.75E+16	2.72E+16	2.71E+16	2.70E+16	2.67E+16	2.64E+16	2.63E+16	2.60E+16	2.59E+16	2.58E+16	2.57E+16
2.75E+00	7.33E+15	7.03E+15	6.94E+15	6.86E+15	6.66E+15	6.46E+15	6.34E+15	6.19E+15	6.09E+15	6.05E+15	6.00E+15
3.25E+00	9.85E+15	9.56E+15	9.46E+15	9.37E+15	9.15E+15	8.90E+15	8.75E+15	8.54E+15	8.40E+15	8.33E+15	8.26E+15
3.70E+00	1.05E+15	9.96E+14	9.73E+14	9.61E+14	9.22E+14	8.78E+14	8.53E+14	8.19E+14	7.97E+14	7.87E+14	7.77E+14
4.22E+00	2.21E+15	1.94E+15	1.86E+15	1.78E+15	1.60E+15	1.40E+15	1.28E+15	1.13E+15	1.04E+15	9.98E+14	9.56E+14
4.70E+00	4.91E+14	4.11E+14	3.83E+14	3.67E+14	3.20E+14	2.72E+14	2.45E+14	2.13E+14	1.93E+14	1.84E+14	1.76E+14
5.25E+00	3.03E+14	2.67E+14	2.56E+14	2.46E+14	2.22E+14	1.95E+14	1.79E+14	1.58E+14	1.46E+14	1.40E+14	1.34E+14
TOTAL	8.97E+17	8.30E+17	8.74E+17	8.69E+17	8.56E+17	8.42E+17	8.33E+17	8.21E+17	8.13E+17	8.09E+17	8.06E+17

Table 11 (Cont'd)

PHOTON SPECTRUM AS A FUNCTION OF TIME FOR FISSION PRODUCTS

POST IRRADIATION DECAY TEN STEPS FROM 420.0 SEC TO 620.0 SEC
POWER= 11.30 MW, BURNUP= 32.MWD, FLUX= 5.14E+13 N**2-SEC

TWELVE GROUP PHOTON RELEASE RATES, PHOTONS/SEC
BASIS = CENTER FUEL ASSEMBLY-ENRICHMENT 4.0%

EMEAN		TIME AFTER DISCHARGE									
(MEV)	INITIAL	435.SEC	460.SEC	480.SEC	510.SEC	545.SEC	590.SEC	600.SEC	604.SEC	611.SEC	620.SEC
3.00E-01	1.55E+17	1.54E+17	1.52E+17	1.50E+17	1.48E+17	1.45E+17	1.42E+17	1.42E+17	1.41E+17	1.41E+17	1.40E+17
6.30E-01	3.72E+17	3.70E+17	3.68E+17	3.65E+17	3.62E+17	3.59E+17	3.54E+17	3.53E+17	3.53E+17	3.52E+17	3.51E+17
1.10E+00	1.58E+17	1.57E+17	1.55E+17	1.53E+17	1.51E+17	1.48E+17	1.45E+17	1.44E+17	1.44E+17	1.43E+17	1.43E+17
1.55E+00	5.79E+16	5.73E+16	5.64E+16	5.58E+16	5.49E+16	5.39E+16	5.28E+16	5.26E+16	5.25E+16	5.23E+16	5.21E+16
1.99E+00	2.02E+16	2.01E+16	1.99E+16	1.97E+16	1.95E+16	1.92E+16	1.89E+16	1.89E+16	1.88E+16	1.88E+16	1.87E+16
2.38E+00	2.57E+16	2.56E+16	2.54E+16	2.53E+16	2.51E+16	2.48E+16	2.45E+16	2.45E+16	2.44E+16	2.44E+16	2.43E+16
2.75E+00	6.00E+15	5.94E+15	5.84E+15	5.76E+15	5.66E+15	5.54E+15	5.41E+15	5.38E+15	5.37E+15	5.35E+15	5.32E+15
3.25E+00	8.26E+15	8.17E+15	8.01E+15	7.90E+15	7.73E+15	7.54E+15	7.32E+15	7.27E+15	7.25E+15	7.22E+15	7.18E+15
3.70E+00	7.77E+14	7.63E+14	7.40E+14	7.24E+14	7.00E+14	6.75E+14	6.46E+14	6.40E+14	6.38E+14	6.34E+14	6.28E+14
4.22E+00	9.56E+14	8.97E+14	8.08E+14	7.42E+14	6.54E+14	5.65E+14	4.68E+14	4.49E+14	4.42E+14	4.29E+14	4.13E+14
4.70E+00	1.76E+14	1.64E+14	1.46E+14	1.34E+14	1.17E+14	1.00E+14	8.27E+13	7.92E+13	7.80E+13	7.55E+13	7.27E+13
5.25E+00	1.34E+14	1.26E+14	1.13E+14	1.04E+14	9.20E+13	7.95E+13	6.59E+13	6.32E+13	6.23E+13	6.04E+13	5.82E+13
TOTAL	8.06E+17	8.00E+17	7.91E+17	7.85E+17	7.75E+17	7.64E+17	7.52E+17	7.49E+17	7.48E+17	7.46E+17	7.43E+17

POST IRRADIATION DECAY SIX STEPS FROM 620.0 SEC TO 900.0 SEC
POWER= 11.30 MW, BURNUP= 32.MWD, FLUX= 5.14E+13 N**2-SEC

TWELVE GROUP PHOTON RELEASE RATES, PHOTONS/SEC
BASIS = CENTER FUEL ASSEMBLY-ENRICHMENT 4.0%

EMEAN		TIME AFTER DISCHARGE					
(MEV)	INITIAL	635.SEC	653.SEC	676.SEC	720.SEC	750.SEC	900.SEC
3.00E-01	1.40E+17	1.39E+17	1.38E+17	1.37E+17	1.34E+17	1.33E+17	1.25E+17
6.30E-01	3.51E+17	3.50E+17	3.48E+17	3.47E+17	3.43E+17	3.41E+17	3.30E+17
1.10E+00	1.43E+17	1.42E+17	1.40E+17	1.39E+17	1.36E+17	1.34E+17	1.26E+17
1.55E+00	5.21E+16	5.18E+16	5.14E+16	5.10E+16	5.02E+16	4.96E+16	4.73E+16
1.99E+00	1.87E+16	1.86E+16	1.85E+16	1.84E+16	1.81E+16	1.79E+16	1.71E+16
2.38E+00	2.43E+16	2.42E+16	2.41E+16	2.40E+16	2.37E+16	2.35E+16	2.27E+16
2.75E+00	5.32E+15	5.28E+15	5.24E+15	5.18E+15	5.07E+15	5.00E+15	4.69E+15
3.25E+00	7.18E+15	7.11E+15	7.03E+15	6.93E+15	6.75E+15	6.63E+15	6.09E+15
3.70E+00	6.28E+14	6.20E+14	6.10E+14	5.98E+14	5.77E+14	5.63E+14	5.05E+14
4.22E+00	4.13E+14	3.88E+14	3.60E+14	3.27E+14	2.73E+14	2.41E+14	1.30E+14
4.70E+00	7.27E+13	6.82E+13	6.31E+13	5.74E+13	4.77E+13	4.21E+13	2.26E+13
5.25E+00	5.82E+13	5.47E+13	5.07E+13	4.61E+13	3.84E+13	3.39E+13	1.83E+13
TOTAL	7.43E+17	7.39E+17	7.35E+17	7.29E+17	7.18E+17	7.11E+17	6.79E+17

Table 12

ORIGEN Results for L2-5 Simulation

Square Assembly

PHOTON SPECTRUM AS A FUNCTION OF TIME FOR FISSION PRODUCTS

POST IRRADIATION DECAY TEN STEPS FROM SHUTDOWN TO 54.0 SEC
POWER= 7.35 MW, BURNUP= 280.MWD, FLUX= 3.35E+13 N**2-SEC

TWELVE GROUP PHOTON RELEASE RATES, PHOTONS/SEC
BASIS = SQUARE FUEL ASSEMBLY-ENRICHMENT 4.0%

EMEAN		TIME AFTER DISCHARGE									
(MEV)	INITIAL	1.SEC	5.SEC	10.SEC	15.SEC	21.SEC	35.SEC	45.SEC	48.SEC	50.SEC	54.SEC
3.00E-01	2.00E+17	1.99E+17	1.96E+17	1.92E+17	1.88E+17	1.84E+17	1.76E+17	1.71E+17	1.70E+17	1.69E+17	1.68E+17
6.30E-01	3.74E+17	3.73E+17	3.69E+17	3.64E+17	3.61E+17	3.57E+17	3.51E+17	3.48E+17	3.47E+17	3.46E+17	3.45E+17
1.10E+00	1.68E+17	1.66E+17	1.61E+17	1.56E+17	1.53E+17	1.50E+17	1.45E+17	1.43E+17	1.42E+17	1.42E+17	1.41E+17
1.55E+00	9.71E+16	9.64E+16	9.39E+16	9.12E+16	8.89E+16	8.67E+16	8.24E+16	7.98E+16	7.91E+16	7.87E+16	7.78E+16
1.99E+00	1.83E+16	1.83E+16	1.80E+16	1.77E+16	1.75E+16	1.73E+16	1.69E+16	1.66E+16	1.66E+16	1.65E+16	1.64E+16
2.33E+00	2.23E+16	2.23E+16	2.21E+16	2.19E+16	2.18E+16	2.16E+16	2.11E+16	2.09E+16	2.08E+16	2.07E+16	2.06E+16
2.75E+00	1.03E+16	1.03E+16	9.96E+15	9.60E+15	9.27E+15	8.91E+15	8.20E+15	7.78E+15	7.66E+15	7.59E+15	7.45E+15
3.25E+00	8.39E+15	8.38E+15	8.35E+15	8.33E+15	8.30E+15	8.27E+15	8.18E+15	8.11E+15	8.08E+15	8.07E+15	8.03E+15
3.70E+00	1.21E+15	1.20E+15	1.19E+15	1.18E+15	1.16E+15	1.14E+15	1.09E+15	1.06E+15	1.05E+15	1.04E+15	1.03E+15
4.22E+00	3.59E+15	3.57E+15	3.54E+15	3.50E+15	3.44E+15	3.38E+15	3.21E+15	3.09E+15	3.05E+15	3.03E+15	2.98E+15
4.70E+00	1.67E+15	1.65E+15	1.62E+15	1.56E+15	1.50E+15	1.43E+15	1.27E+15	1.16E+15	1.13E+15	1.12E+15	1.08E+15
5.25E+00	4.12E+14	4.12E+14	4.10E+14	4.08E+14	4.05E+14	4.01E+14	3.89E+14	3.79E+14	3.76E+14	3.74E+14	3.70E+14
TOTAL	9.06E+17	9.01E+17	8.85E+17	8.67E+17	8.53E+17	8.39E+17	8.15E+17	8.01E+17	7.97E+17	7.95E+17	7.90E+17

POST IRRADIATION DECAY TEN STEPS FROM 054.0 SEC TO 225.0 SEC
POWER= 7.35 MW, BURNUP= 280.MWD, FLUX= 3.35E+13 N**2-SEC

TWELVE GROUP PHOTON RELEASE RATES, PHOTONS/SEC
BASIS = SQUARE FUEL ASSEMBLY-ENRICHMENT 4.0%

EMEAN		TIME AFTER DISCHARGE									
(MEV)	INITIAL	96.SEC	119.SEC	127.SEC	174.SEC	180.SEC	182.SEC	191.SEC	193.SEC	215.SEC	225.SEC
3.00E-01	1.68E+17	1.56E+17	1.52E+17	1.50E+17	1.43E+17	1.43E+17	1.42E+17	1.41E+17	1.41E+17	1.39E+17	1.38E+17
6.30E-01	3.45E+17	3.35E+17	3.30E+17	3.29E+17	3.21E+17	3.20E+17	3.20E+17	3.19E+17	3.18E+17	3.15E+17	3.14E+17
1.10E+00	1.41E+17	1.34E+17	1.31E+17	1.30E+17	1.25E+17	1.24E+17	1.24E+17	1.23E+17	1.23E+17	1.21E+17	1.20E+17
1.55E+00	7.78E+16	7.02E+16	6.70E+16	6.60E+16	6.13E+16	6.08E+16	6.07E+16	6.00E+16	5.98E+16	5.83E+16	5.76E+16
1.99E+00	1.64E+16	1.58E+16	1.55E+16	1.54E+16	1.49E+16	1.49E+16	1.48E+16	1.48E+16	1.47E+16	1.46E+16	1.45E+16
2.33E+00	2.06E+16	1.98E+16	1.94E+16	1.93E+16	1.87E+16	1.86E+16	1.86E+16	1.85E+16	1.85E+16	1.83E+16	1.82E+16
2.75E+00	7.45E+15	6.32E+15	5.87E+15	5.74E+15	5.14E+15	5.08E+15	5.06E+15	4.97E+15	4.95E+15	4.77E+15	4.70E+15
3.25E+00	8.03E+15	7.68E+15	7.48E+15	7.42E+15	7.05E+15	7.00E+15	6.98E+15	6.92E+15	6.90E+15	6.75E+15	6.68E+15
3.70E+00	1.03E+15	9.10E+14	8.54E+14	8.36E+14	7.47E+14	7.37E+14	7.33E+14	7.19E+14	7.16E+14	6.84E+14	6.71E+14
4.22E+00	2.98E+15	2.50E+15	2.25E+15	2.17E+15	1.76E+15	1.72E+15	1.70E+15	1.63E+15	1.62E+15	1.47E+15	1.41E+15
4.70E+00	1.08E+15	7.69E+14	6.41E+14	6.04E+14	4.33E+14	4.16E+14	4.10E+14	3.87E+14	3.81E+14	3.32E+14	3.12E+14
5.25E+00	3.70E+14	3.22E+14	2.95E+14	2.86E+14	2.37E+14	2.32E+14	2.30E+14	2.21E+14	2.19E+14	2.01E+14	1.92E+14
TOTAL	7.90E+17	7.49E+17	7.32E+17	7.26E+17	6.99E+17	6.96E+17	6.95E+17	6.91E+17	6.90E+17	6.80E+17	6.76E+17

POST IRRADIATION DECAY TEN STEPS FROM 225.0 SEC TO 420.0 SEC
POWER= 7.35 MW, BURNUP= 280.MWD, FLUX= 3.35E+13 N**2-SEC

TWELVE GROUP PHOTON RELEASE RATES, PHOTONS/SEC
BASIS = SQUARE FUEL ASSEMBLY-ENRICHMENT 4.0%

EMEAN		TIME AFTER DISCHARGE									
(MEV)	INITIAL	255.SEC	265.SEC	275.SEC	300.SEC	331.SEC	351.SEC	380.SEC	400.SEC	410.SEC	420.SEC
3.00E-01	1.38E+17	1.35E+17	1.34E+17	1.33E+17	1.31E+17	1.29E+17	1.27E+17	1.25E+17	1.24E+17	1.24E+17	1.23E+17
6.30E-01	3.14E+17	3.11E+17	3.10E+17	3.08E+17	3.06E+17	3.03E+17	3.01E+17	2.98E+17	2.97E+17	2.96E+17	2.95E+17
1.10E+00	1.20E+17	1.18E+17	1.17E+17	1.16E+17	1.14E+17	1.12E+17	1.11E+17	1.09E+17	1.08E+17	1.08E+17	1.07E+17
1.55E+00	5.76E+16	5.59E+16	5.54E+16	5.49E+16	5.38E+16	5.26E+16	5.19E+16	5.10E+16	5.04E+16	5.02E+16	4.99E+16
1.99E+00	1.45E+16	1.43E+16	1.42E+16	1.41E+16	1.39E+16	1.38E+16	1.36E+16	1.35E+16	1.34E+16	1.33E+16	1.33E+16
2.33E+00	1.82E+16	1.80E+16	1.79E+16	1.79E+16	1.77E+16	1.75E+16	1.74E+16	1.73E+16	1.72E+16	1.71E+16	1.71E+16
2.75E+00	4.70E+15	4.50E+15	4.44E+15	4.39E+15	4.27E+15	4.14E+15	4.06E+15	3.96E+15	3.90E+15	3.87E+15	3.84E+15
3.25E+00	6.68E+15	6.49E+15	6.43E+15	6.37E+15	6.22E+15	6.06E+15	5.96E+15	5.82E+15	5.72E+15	5.68E+15	5.63E+15
3.70E+00	6.71E+14	6.34E+14	6.23E+14	6.12E+14	5.87E+14	5.59E+14	5.43E+14	5.21E+14	5.08E+14	5.01E+14	4.95E+14
4.22E+00	1.41E+15	1.23E+15	1.18E+15	1.13E+15	1.01E+15	8.83E+14	8.15E+14	7.20E+14	6.61E+14	6.34E+14	6.08E+14
4.70E+00	3.12E+14	2.61E+14	2.46E+14	2.33E+14	2.03E+14	1.73E+14	1.56E+14	1.35E+14	1.23E+14	1.17E+14	1.12E+14
5.25E+00	1.92E+14	1.70E+14	1.63E+14	1.56E+14	1.41E+14	1.24E+14	1.14E+14	1.01E+14	9.26E+13	8.88E+13	8.52E+13
TOTAL	6.76E+17	6.64E+17	6.61E+17	6.57E+17	6.49E+17	6.40E+17	6.34E+17	6.26E+17	6.21E+17	6.19E+17	6.16E+17

Table 12 (Cont'd)

PHOTON SPECTRUM AS A FUNCTION OF TIME FOR FISSION PRODUCTS

POST IRRADIATION DECAY TEN STEPS FROM 420.0 SEC TO 620.0 SEC
POWER= 7.35 MW, BURNUP= 280.MWD, FLUX= 3.35E+13 N**2-SEC

TWELVE GROUP PHOTON RELEASE RATES, PHOTONS/SEC
BASIS = SQUARE FUEL ASSEMBLY-ENRICHMENT 4.0%

EMEAN		TIME AFTER DISCHARGE									
(MEV)	INITIAL	435.SEC	460.SEC	480.SEC	510.SEC	545.SEC	590.SEC	600.SEC	604.SEC	611.SEC	620.SEC
3.00E-01	1.23E+17	1.22E+17	1.21E+17	1.20E+17	1.18E+17	1.17E+17	1.15E+17	1.14E+17	1.14E+17	1.14E+17	1.13E+17
6.30E-01	2.95E+17	2.94E+17	2.92E+17	2.91E+17	2.88E+17	2.86E+17	2.83E+17	2.83E+17	2.82E+17	2.82E+17	2.81E+17
1.10E+00	1.07E+17	1.06E+17	1.05E+17	1.04E+17	1.02E+17	1.00E+17	9.84E+16	9.79E+16	9.77E+16	9.74E+16	9.70E+16
1.55E+00	4.99E+16	4.96E+16	4.90E+16	4.86E+16	4.80E+16	4.74E+16	4.66E+16	4.65E+16	4.64E+16	4.63E+16	4.62E+16
1.99E+00	1.33E+16	1.32E+16	1.30E+16	1.29E+16	1.28E+16	1.26E+16	1.24E+16	1.24E+16	1.24E+16	1.24E+16	1.23E+16
2.38E+00	1.71E+16	1.70E+16	1.69E+16	1.68E+16	1.66E+16	1.65E+16	1.63E+16	1.63E+16	1.62E+16	1.62E+16	1.62E+16
2.75E+00	3.84E+15	3.80E+15	3.74E+15	3.69E+15	3.62E+15	3.55E+15	3.46E+15	3.45E+15	3.44E+15	3.43E+15	3.41E+15
3.25E+00	5.63E+15	5.57E+15	5.47E+15	5.39E+15	5.28E+15	5.15E+15	5.00E+15	4.97E+15	4.95E+15	4.93E+15	4.90E+15
3.70E+00	4.95E+14	4.86E+14	4.72E+14	4.61E+14	4.46E+14	4.30E+14	4.12E+14	4.08E+14	4.06E+14	4.04E+14	4.00E+14
4.22E+00	6.08E+14	5.70E+14	5.13E+14	4.72E+14	4.16E+14	3.59E+14	2.97E+14	2.85E+14	2.81E+14	2.72E+14	2.62E+14
4.70E+00	1.12E+14	1.04E+14	9.30E+13	8.50E+13	7.43E+13	6.38E+13	5.25E+13	5.03E+13	4.96E+13	4.80E+13	4.62E+13
5.25E+00	8.52E+13	8.00E+13	7.20E+13	6.63E+13	5.85E+13	5.05E+13	4.19E+13	4.02E+13	3.96E+13	3.84E+13	3.70E+13
TOTAL	6.16E+17	6.13E+17	6.07E+17	6.03E+17	5.96E+17	5.89E+17	5.81E+17	5.79E+17	5.78E+17	5.77E+17	5.75E+17

POST IRRADIATION DECAY SIX STEPS FROM 620.0 SEC TO 900.0 SEC
POWER= 7.35 MW, BURNUP= 280.MWD, FLUX= 3.35E+13 N**2-SEC

TWELVE GROUP PHOTON RELEASE RATES, PHOTONS/SEC
BASIS = SQUARE FUEL ASSEMBLY-ENRICHMENT 4.0%

EMEAN		TIME AFTER DISCHARGE					
(MEV)	INITIAL	635.SEC	653.SEC	676.SEC	720.SEC	750.SEC	900.SEC
3.00E-01	1.13E+17	1.13E+17	1.12E+17	1.11E+17	1.09E+17	1.08E+17	1.03E+17
6.30E-01	2.81E+17	2.80E+17	2.79E+17	2.78E+17	2.76E+17	2.74E+17	2.67E+17
1.10E+00	9.70E+16	9.63E+16	9.55E+16	9.46E+16	9.27E+16	9.15E+16	8.59E+16
1.55E+00	4.62E+16	4.60E+16	4.57E+16	4.54E+16	4.49E+16	4.46E+16	4.31E+16
1.99E+00	1.23E+16	1.23E+16	1.22E+16	1.21E+16	1.19E+16	1.18E+16	1.13E+16
2.38E+00	1.62E+16	1.61E+16	1.60E+16	1.59E+16	1.58E+16	1.57E+16	1.51E+16
2.75E+00	3.41E+15	3.30E+15	3.35E+15	3.32E+15	3.25E+15	3.20E+15	3.00E+15
3.25E+00	4.90E+15	4.86E+15	4.80E+15	4.73E+15	4.61E+15	4.53E+15	4.16E+15
3.70E+00	4.00E+14	3.95E+14	3.89E+14	3.81E+14	3.68E+14	3.59E+14	3.22E+14
4.22E+00	2.62E+14	2.47E+14	2.28E+14	2.08E+14	1.73E+14	1.53E+14	8.25E+13
4.70E+00	4.62E+13	4.34E+13	4.01E+13	3.65E+13	3.03E+13	2.68E+13	1.44E+13
5.25E+00	3.70E+13	3.47E+13	3.22E+13	2.93E+13	2.44E+13	2.16E+13	1.16E+13
TOTAL	5.75E+17	5.73E+17	5.70E+17	5.66E+17	5.59E+17	5.54E+17	5.33E+17

Table 13

ORIGEN Results for L2-5 Simulation

Triangle Assembly

PHOTON SPECTRUM AS A FUNCTION OF TIME FOR FISSION PRODUCTS

POST IRRADIATION DECAY TEN STEPS FROM SHUTDOWN TO 54.0 SEC
POWER= 2.35 MW, BURNUP= 89.MWD, FLUX= 3.12E+13 N**2-SEC

TWELVE GROUP PHOTON RELEASE RATES, PHOTONS/SEC
BASIS = TRIANGLE FUEL ASSEMBLY-ENRICHMENT 4.0%

EMEAN		TIME AFTER DISCHARGE									
(MEV)	INITIAL	1.SEC	5.SEC	10.SEC	15.SEC	21.SEC	35.SEC	45.SEC	48.SEC	50.SEC	54.SEC
3.00E-01	6.40E+16	6.37E+16	6.27E+16	6.14E+16	6.01E+16	5.87E+16	5.62E+16	5.48E+16	5.44E+16	5.42E+16	5.37E+16
6.30E-01	1.20E+17	1.19E+17	1.18E+17	1.17E+17	1.15E+17	1.14E+17	1.12E+17	1.11E+17	1.11E+17	1.11E+17	1.10E+17
1.10E+00	5.37E+16	5.32E+16	5.14E+16	4.99E+16	4.88E+16	4.79E+16	4.65E+16	4.58E+16	4.56E+16	4.54E+16	4.51E+16
1.55E+00	3.11E+16	3.08E+16	3.00E+16	2.92E+16	2.84E+16	2.77E+16	2.63E+16	2.55E+16	2.53E+16	2.52E+16	2.49E+16
1.99E+00	5.86E+15	5.84E+15	5.76E+15	5.67E+15	5.60E+15	5.53E+15	5.40E+15	5.32E+15	5.30E+15	5.29E+15	5.26E+15
2.33E+00	7.13E+15	7.12E+15	7.07E+15	7.02E+15	6.97E+15	6.90E+15	6.77E+15	6.68E+15	6.65E+15	6.64E+15	6.60E+15
2.75E+00	3.31E+15	3.29E+15	3.19E+15	3.07E+15	2.97E+15	2.85E+15	2.62E+15	2.49E+15	2.45E+15	2.43E+15	2.38E+15
3.25E+00	2.68E+15	2.67E+15	2.66E+15	2.66E+15	2.65E+15	2.64E+15	2.61E+15	2.59E+15	2.58E+15	2.57E+15	2.56E+15
3.70E+00	3.86E+14	3.85E+14	3.82E+14	3.77E+14	3.72E+14	3.65E+14	3.50E+14	3.39E+14	3.36E+14	3.34E+14	3.30E+14
4.22E+00	1.15E+15	1.15E+15	1.14E+15	1.12E+15	1.10E+15	1.08E+15	1.03E+15	9.89E+14	9.77E+14	9.70E+14	9.54E+14
4.70E+00	5.33E+14	5.31E+14	5.18E+14	5.00E+14	4.81E+14	4.57E+14	4.06E+14	3.73E+14	3.64E+14	3.57E+14	3.46E+14
5.25E+00	1.32E+14	1.32E+14	1.31E+14	1.31E+14	1.30E+14	1.28E+14	1.25E+14	1.22E+14	1.21E+14	1.20E+14	1.18E+14
TOTAL	2.90E+17	2.88E+17	2.83E+17	2.77E+17	2.73E+17	2.68E+17	2.61E+17	2.56E+17	2.55E+17	2.54E+17	2.53E+17

POST IRRADIATION DECAY TEN STEPS FROM 054.0 SEC TO 225.0 SEC
POWER= 2.35 MW, BURNUP= 89.MWD, FLUX= 3.12E+13 N**2-SEC

TWELVE GROUP PHOTON RELEASE RATES, PHOTONS/SEC
BASIS = TRIANGLE FUEL ASSEMBLY-ENRICHMENT 4.0%

EMEAN		TIME AFTER DISCHARGE									
(MEV)	INITIAL	96.SEC	119.SEC	127.SEC	174.SEC	180.SEC	182.SEC	191.SEC	193.SEC	215.SEC	225.SEC
3.00E-01	5.37E+16	5.00E+16	4.85E+16	4.81E+16	4.58E+16	4.56E+16	4.55E+16	4.52E+16	4.51E+16	4.43E+16	4.40E+16
6.30E-01	1.10E+17	1.07E+17	1.06E+17	1.05E+17	1.03E+17	1.02E+17	1.02E+17	1.02E+17	1.02E+17	1.01E+17	1.00E+17
1.10E+00	4.51E+16	4.29E+16	4.18E+16	4.15E+16	3.99E+16	3.97E+16	3.96E+16	3.93E+16	3.93E+16	3.87E+16	3.84E+16
1.55E+00	2.49E+16	2.25E+16	2.14E+16	2.11E+16	1.96E+16	1.95E+16	1.94E+16	1.92E+16	1.91E+16	1.86E+16	1.84E+16
1.99E+00	5.26E+15	5.05E+15	4.95E+15	4.92E+15	4.77E+15	4.75E+15	4.75E+15	4.72E+15	4.71E+15	4.66E+15	4.63E+15
2.33E+00	6.60E+15	6.32E+15	6.20E+15	6.17E+15	5.99E+15	5.97E+15	5.96E+15	5.93E+15	5.93E+15	5.86E+15	5.84E+15
2.75E+00	2.38E+15	2.02E+15	1.88E+15	1.84E+15	1.64E+15	1.63E+15	1.62E+15	1.59E+15	1.58E+15	1.53E+15	1.50E+15
3.25E+00	2.56E+15	2.45E+15	2.39E+15	2.36E+15	2.25E+15	2.23E+15	2.23E+15	2.21E+15	2.20E+15	2.15E+15	2.13E+15
3.70E+00	3.30E+14	2.92E+14	2.73E+14	2.68E+14	2.39E+14	2.36E+14	2.35E+14	2.30E+14	2.29E+14	2.19E+14	2.15E+14
4.22E+00	9.54E+14	7.99E+14	7.21E+14	6.95E+14	5.65E+14	5.50E+14	5.45E+14	5.23E+14	5.18E+14	4.71E+14	4.51E+14
4.70E+00	3.46E+14	2.46E+14	2.05E+14	1.93E+14	1.39E+14	1.33E+14	1.31E+14	1.24E+14	1.22E+14	1.06E+14	9.99E+13
5.25E+00	1.18E+14	1.03E+14	9.45E+13	9.16E+13	7.60E+13	7.42E+13	7.36E+13	7.09E+13	7.03E+13	6.43E+13	6.16E+13
TOTAL	2.53E+17	2.40E+17	2.34E+17	2.32E+17	2.24E+17	2.23E+17	2.22E+17	2.21E+17	2.21E+17	2.18E+17	2.16E+17

POST IRRADIATION DECAY TEN STEPS FROM 225.0 SEC TO 420.0 SEC
POWER= 2.35 MW, BURNUP= 89.MWD, FLUX= 3.12E+13 N**2-SEC

TWELVE GROUP PHOTON RELEASE RATES, PHOTONS/SEC
BASIS = TRIANGLE FUEL ASSEMBLY-ENRICHMENT 4.0%

EMEAN		TIME AFTER DISCHARGE									
(MEV)	INITIAL	255.SEC	265.SEC	275.SEC	300.SEC	331.SEC	351.SEC	380.SEC	400.SEC	410.SEC	420.SEC
3.00E-01	4.40E+16	4.31E+16	4.28E+16	4.26E+16	4.19E+16	4.12E+16	4.08E+16	4.02E+16	3.98E+16	3.96E+16	3.94E+16
6.30E-01	1.00E+17	9.93E+16	9.90E+16	9.86E+16	9.78E+16	9.68E+16	9.62E+16	9.54E+16	9.49E+16	9.46E+16	9.44E+16
1.10E+00	3.84E+16	3.76E+16	3.74E+16	3.71E+16	3.66E+16	3.59E+16	3.55E+16	3.50E+16	3.46E+16	3.44E+16	3.42E+16
1.55E+00	1.84E+16	1.79E+16	1.77E+16	1.76E+16	1.72E+16	1.68E+16	1.65E+16	1.63E+16	1.61E+16	1.60E+16	1.60E+16
1.99E+00	4.63E+15	4.56E+15	4.54E+15	4.51E+15	4.46E+15	4.40E+15	4.36E+15	4.31E+15	4.27E+15	4.26E+15	4.24E+15
2.33E+00	5.84E+15	5.76E+15	5.74E+15	5.72E+15	5.67E+15	5.61E+15	5.57E+15	5.52E+15	5.49E+15	5.47E+15	5.46E+15
2.75E+00	1.50E+15	1.44E+15	1.42E+15	1.41E+15	1.37E+15	1.32E+15	1.30E+15	1.27E+15	1.25E+15	1.24E+15	1.23E+15
3.25E+00	2.13E+15	2.07E+15	2.05E+15	2.03E+15	1.98E+15	1.93E+15	1.90E+15	1.85E+15	1.82E+15	1.81E+15	1.80E+15
3.70E+00	2.15E+14	2.03E+14	1.99E+14	1.96E+14	1.88E+14	1.79E+14	1.74E+14	1.67E+14	1.63E+14	1.61E+14	1.59E+14
4.22E+00	4.51E+14	3.95E+14	3.78E+14	3.62E+14	3.25E+14	2.84E+14	2.61E+14	2.31E+14	2.12E+14	2.03E+14	1.95E+14
4.70E+00	9.99E+13	8.36E+13	7.89E+13	7.46E+13	6.51E+13	5.53E+13	4.99E+13	4.33E+13	3.93E+13	3.75E+13	3.58E+13
5.25E+00	6.16E+13	5.44E+13	5.22E+13	5.01E+13	4.51E+13	3.96E+13	3.64E+13	3.22E+13	2.97E+13	2.84E+13	2.73E+13
TOTAL	2.16E+17	2.12E+17	2.11E+17	2.10E+17	2.08E+17	2.05E+17	2.03E+17	2.00E+17	1.99E+17	1.98E+17	1.97E+17

Table 13 (Cont'd)

PHOTON SPECTRUM AS A FUNCTION OF TIME FOR FISSION PRODUCTS

POST IRRADIATION DECAY TEN STEPS FROM 420.0 SEC TO 620.0 SEC
POWER= 2.35 MW, BURNUP= 89.MWD, FLUX= 3.12E+13 N**2-SEC

TWELVE GROUP PHOTON RELEASE RATES, PHOTONS/SEC
BASIS = TRIANGLE FUEL ASSEMBLY-ENRICHMENT 4.0%

EMEAN		TIME AFTER DISCHARGE									
(MEV)	INITIAL	435.SEC	460.SEC	480.SEC	510.SEC	545.SEC	590.SEC	600.SEC	604.SEC	611.SEC	620.SEC
3.00E-01	3.94E+16	3.91E+16	3.87E+16	3.84E+16	3.79E+16	3.73E+16	3.67E+16	3.66E+16	3.65E+16	3.64E+16	3.63E+16
6.30E-01	9.44E+16	9.40E+16	9.34E+16	9.29E+16	9.22E+16	9.15E+16	9.05E+16	9.03E+16	9.03E+16	9.01E+16	9.00E+16
1.10E+00	3.42E+16	3.40E+16	3.35E+16	3.32E+16	3.27E+16	3.21E+16	3.15E+16	3.13E+16	3.13E+16	3.11E+16	3.10E+16
1.55E+00	1.60E+16	1.58E+16	1.57E+16	1.55E+16	1.53E+16	1.51E+16	1.49E+16	1.49E+16	1.48E+16	1.48E+16	1.48E+16
1.99E+00	4.24E+15	4.21E+15	4.17E+15	4.14E+15	4.10E+15	4.04E+15	3.98E+15	3.97E+15	3.96E+15	3.95E+15	3.94E+15
2.38E+00	5.46E+15	5.43E+15	5.40E+15	5.37E+15	5.32E+15	5.28E+15	5.21E+15	5.20E+15	5.20E+15	5.19E+15	5.17E+15
2.75E+00	1.23E+15	1.22E+15	1.20E+15	1.18E+15	1.16E+15	1.14E+15	1.11E+15	1.10E+15	1.10E+15	1.10E+15	1.09E+15
3.25E+00	1.80E+15	1.78E+15	1.74E+15	1.72E+15	1.68E+15	1.64E+15	1.59E+15	1.58E+15	1.58E+15	1.57E+15	1.56E+15
3.70E+00	1.59E+14	1.56E+14	1.51E+14	1.48E+14	1.43E+14	1.38E+14	1.32E+14	1.31E+14	1.30E+14	1.29E+14	1.23E+14
4.22E+00	1.95E+14	1.83E+14	1.64E+14	1.51E+14	1.33E+14	1.15E+14	9.53E+13	9.14E+13	9.00E+13	8.72E+13	8.41E+13
4.70E+00	3.53E+13	3.34E+13	2.98E+13	2.72E+13	2.38E+13	2.04E+13	1.68E+13	1.61E+13	1.59E+13	1.54E+13	1.48E+13
5.25E+00	2.73E+13	2.56E+13	2.31E+13	2.12E+13	1.87E+13	1.62E+13	1.34E+13	1.29E+13	1.27E+13	1.23E+13	1.18E+13
TOTAL	1.97E+17	1.96E+17	1.94E+17	1.93E+17	1.91E+17	1.88E+17	1.86E+17	1.85E+17	1.85E+17	1.85E+17	1.84E+17

POST IRRADIATION DECAY SIX STEPS FROM 620.0 SEC TO 900.0 SEC
POWER= 2.35 MW, BURNUP= 89.MWD, FLUX= 3.12E+13 N**2-SEC

TWELVE GROUP PHOTON RELEASE RATES, PHOTONS/SEC
BASIS = TRIANGLE FUEL ASSEMBLY-ENRICHMENT 4.0%

EMEAN		TIME AFTER DISCHARGE					
(MEV)	INITIAL	635.SEC	653.SEC	676.SEC	720.SEC	750.SEC	900.SEC
3.00E-01	3.63E+16	3.61E+16	3.58E+16	3.56E+16	3.50E+16	3.47E+16	3.30E+16
6.30E-01	9.00E+16	8.97E+16	8.93E+16	8.39E+16	8.81E+16	8.76E+16	8.53E+16
1.10E+00	3.10E+16	3.08E+16	3.05E+16	3.02E+16	2.96E+16	2.93E+16	2.75E+16
1.55E+00	1.48E+16	1.47E+16	1.46E+16	1.45E+16	1.44E+16	1.43E+16	1.38E+16
1.99E+00	3.94E+15	3.92E+15	3.90E+15	3.87E+15	3.81E+15	3.78E+15	3.61E+15
2.38E+00	5.17E+15	5.15E+15	5.13E+15	5.10E+15	5.05E+15	5.01E+15	4.83E+15
2.75E+00	1.09E+15	1.08E+15	1.07E+15	1.06E+15	1.04E+15	1.03E+15	9.61E+14
3.25E+00	1.56E+15	1.55E+15	1.53E+15	1.51E+15	1.47E+15	1.44E+15	1.33E+15
3.70E+00	1.28E+14	1.27E+14	1.24E+14	1.22E+14	1.18E+14	1.15E+14	1.03E+14
4.22E+00	8.41E+13	7.90E+13	7.32E+13	6.66E+13	5.55E+13	4.90E+13	2.64E+13
4.70E+00	1.40E+13	1.39E+13	1.29E+13	1.17E+13	9.71E+12	8.57E+12	4.61E+12
5.25E+00	1.18E+13	1.11E+13	1.03E+13	9.39E+12	7.82E+12	6.91E+12	3.73E+12
TOTAL	1.84E+17	1.83E+17	1.82E+17	1.81E+17	1.79E+17	1.77E+17	1.70E+17

Table 14. L2-5 Simulation: Voided Shutdown Region Volume Fractions

Time (sec)	Inner Core Vol. Fract.	Outer Core Vol. Fract.	H2OFLO Vol. Fract.	DNCMR Vol. Fract.	H2OGAP Vol. Fract
1.0	0.343	0.330	0.590	0.583	0.583
5.0	0.109	0.121	0.220	0.113	0.113
10.0	0.000	0.085	0.150	0.000	0.000
15.0	0.000	0.000	0.000	0.000	0.000
21.0	0.000	0.000	0.000	0.000	0.000
35.0	0.000	0.000	0.000	0.000	0.000
45.0	0.231	0.231	0.410	0.156	0.156
48.0	0.377	0.377	0.672	0.607	0.607
50.0	0.501	0.501	0.893	1.000	1.000
54.0	0.561	0.561	1.000	1.000	1.000
60.0	0.561	0.561	1.000	1.000	1.000
95.6	0.561	0.561	1.000	1.000	1.000
119.2	0.561	0.561	1.000	1.000	1.000
127.2	0.561	0.561	1.000	1.000	1.000
174.2	0.546	0.546	0.973	1.000	1.000
180.0	0.498	0.546	0.973	0.826	0.826
182.1	0.461	0.546	0.973	0.693	0.695
191.1	0.537	0.546	0.973	0.913	0.913
198.3	0.525	0.546	0.973	0.843	0.843
215.0	0.513	0.546	0.973	0.913	0.913
225.0	0.512	0.546	0.973	1.000	1.000
255.0	0.476	0.534	0.952	0.887	0.887
265.0	0.392	0.534	0.952	0.635	0.635
275.0	0.318	0.534	0.952	0.533	0.533
300.0	0.185	0.509	0.908	0.219	0.219
331.0	0.185	0.494	0.881	0.176	0.176
351.0	0.173	0.192	0.342	0.176	0.176
380.0	0.067	0.082	0.147	0.044	0.044
400.0	0.349	0.223	0.398	0.000	0.000
410.0	0.220	0.392	0.698	0.000	0.000
420.0	0.328	0.501	0.893	0.408	0.408
435.0	0.486	0.488	0.871	1.000	1.000
460.0	0.486	0.518	0.924	1.000	1.000
480.0	0.474	0.464	0.828	1.000	1.000
510.0	0.501	0.518	0.924	1.000	1.000
545.0	0.501	0.561	1.000	1.000	1.000
590.0	0.501	0.561	1.000	1.000	1.000
603.6	0.489	0.561	1.000	0.957	0.957
611.1	0.465	0.561	1.000	0.870	0.870
620.0	0.428	0.561	1.000	0.650	0.650
635.0	0.419	0.561	1.000	0.650	0.650
653.0	0.392	0.561	1.000	0.607	0.607
676.0	0.365	0.561	1.000	0.564	0.564
720.0	0.424	0.561	1.000	0.779	0.779
750.0	0.561	0.561	1.000	1.000	1.000

Table 15. Voiding Sensitivity Ratios
Gamma-Ray Detector Response E>5MeV

	n-γ Production Source Sensitivity Ratio	
Voiding Region	LOFT Geometry	Mock-PWR Geometry
CORE	-1.01	-0.76
extended - CORE	-1.28	--
DNCMR	-1.02	-0.60
extended - DNCMR	-1.38	-2.06
Total Water Regions	-2.54	-3.06

	Core γ-Ray Source Sensitivity Ratio	
Voiding Region	LOFT Geometry	Mock-PWR Geometry
CORE	-0.05	-0.06
DNCMR	-0.10	-0.47
Total Water Regions	-0.15	-0.84

$$\text{Sensitivity Ratio} = \frac{\Delta\phi/\phi_o}{\Delta\rho/\rho_o}$$

Table 16. Two-Dimensional Effects

Comparison of high-energy (E≥5MeV) gamma-ray flux (γ/cm^2-sec) at detector site from homogeneous voiding of the downcomer and from combining full water and complete void results.

80% homogeneous density	0.80 (100% density) + 0.20 (0% density
7.37×10^{11}	9.78×10^{11}
60% homogeneous density	0.60 (100% density) + 0.40 (0% density)
9.34×10^{11}	1.37×10^{12}
50% homogeneous density	0.50 (100% density) + 0.50 (0% density)
1.06×10^{12}	1.56×10^{12}
40% homogeneous density	40 (100% density) + 0.60 (0% density)
1.21×10^{12}	1.76×10^{12}
20% homogeneous density	0.20 (100% density) + 0.80 (0% density)
1.63×10^{12}	2.15×10^{12}

Table 17. Neutron and Gamma-Ray Response Comparison

Steady State: t=0 seconds			
Radiation Detected	Energy Range	Detector Flux at Operating Densities (ϕ_0)	Voiding Sensitivity Ratio
Neutron	E > 1.8 eV	9.62×10^{10} n/cm^2-sec	13.6
γ-ray	E > 5 MeV	5.87×10^{11} γ/cm^2-sec	16.1
γ-ray	E > 1 MeV	2.88×10^{12} γ/cm^2-sec	17.1

Post Shutdown: t=30 minutes			
Radiation Detected	Energy Range	Detector Flux at Operating Densities (ϕ_0)	Voiding Sensitivity Ratio
Neutron	E > 1.8 eV	5.98×10^{-2} n/cm^2-sec	10.5
γ-ray	E > 5 MeV	3.44×10^{0} γ/cm^2-sec	1.6
γ-ray	E > 1 MeV	3.23×10^{4} γ/cm^2-sec	1.03

APPENDIX

Code and Program Descriptions

A.1 EPRI-CELL CODE

Code Description

EPRI-CELL is a cell depletion code which calculates both flux and cross sections for a specified reactor composition. The code has been used to calculate ORIGEN input factors THERM, RES, and FAST for the LOFT research reactor core. For a detailed explanation of the three parameters, refer to the ORIGEN code description in the next section of the Appendix. The cross section generation capability of EPRI-CELL has also been used to produce a neutron cross section datafile.

EPRI-CELL is a proprietary code, originally developed by the Electric Power Research Institute (EPRI), and subsequently modified at Argonne National Lab (ANL). The primary reference for this section is the EPRI-CELL manual and code description [1A]. The ANL version has retained the basic structure of the original EPRI-CELL code, with changes instituted primarily to increase the accuracy of the data libraries and the flexibility of input and output control. The code was originally designed for light water reactor applications, performing cylindrical pin calculations of neutron spectra with space, energy, and burn-up dependence. Thus, the code is well suited to model the Loss of Fluid Test Reactor (LOFT), a scaled-down version of a pressurized water reactor.

The code unites modified versions of the following three previously existing codes, as described by their manual titles: "GAM-1: A consistent P_1 multigroup code for the calculation of fast neutron spectra and multigroup constants" [2A]; "THERMOS: A thermalization transport theory code for reactor lattice calculations" [3A]; and "CINDER: A one-point depletion and fission product program" [4A].

The resonance integrals are calculated in the modified GAM module by interpolating between values which are tabulated as a function of temperature and the fictitious excess potential scattering cross section. The tabulated resonance integrals assume single isolated resonant absorbers, ignoring interactions which can deplete the available resonance energy neutron population. The interpolation method employs the results of the resonance equivalence theorems, which express the fuel escape probability in a fractional form known as Wigner's rational approximation. This rational expression reproduces the

correct asymptotic values for small and large fuel lumps. The Bell Factor, a constant calculated assuming isolated fuel lumps, is introduced to improve the accuracy for realistic reactor lump sizes. To account for non-isolated fuel lumps and resulting shadowing effects, the Dancoff Factor is incorporated into the rational expression. The Dancoff Factor is a lattice parameter and is therefore specified by the user to accurately reflect the reactor geometry being modeled. The effect of other resonant nuclides and of resonant scatterers is approximated with an additive term adjusting the excess potential scattering cross section. Because the added term is a function of the resonance integral which is itself a function of the excess potential scattering cross section, an iterative process is performed with the initial cross section guess for each isotope provided in the input.

The thermal fluxes are calculated in the THERMOS module using thermal scattering kernels with a 35 thermal energy group structure. The time dependent isotopic concentrations are calculated in the CINDER module, using depletion chains for heavy metal fuel isotopes, including transuranics, and using fission product decay chains. The code assumes a constant flux for the duration of the user specified timestep. The fission products, except samarium-149 and xenon-133, which change rapidly in time with both build-up and decay, are treated as one lumped fission product for the epithermal energy range and another lumped fission product for the thermal energy range calculations. The negative reactivity effect of fission product poisoning is accounted for by lumped macroscopic absorption cross sections. The three modules are linked with source and leakage term calculations and data transfer processes which assure spectrum consistency over the complete energy range and material composition.

The use of a one fuel pin cell calculation to determine the fuel assembly, and hence the core neutron spectrum, is an obvious approximation. The neglect of control rods and leakage inherently assumes an infinite fuel pin lattice configuration. This assumption is very reasonable for a large reactor, but for smaller research reactors such as LOFT, leakage effects are more significant, with a resulting flux depression in a greater fraction of the whole core. This effect, however, was neglected.

The cross section libraries for EPRI-CELL, developed and updated by Argonne Applied Physics personnel, are based on ENDFB data, and are checked

against other cross section generation codes. Calculations are carried out with a fine group structure defined by the 68 group (62 fast, 6 slow) GAM library and the 35 thermal group library in the THERMOS module. The code collapses the cross sections and the results into a 5 neutron broad group structure. (See Table 1Aa.) The collapsing scheme employs the computed fluxes, which are normalized to the input power. The generated cross sections reflect the composition and geometry of the particular model and therefore well represent the system.

One ANL modification to the code allows the user to extract the cross section data in an ISOTXS format datafile which is compatible with transport codes. The user can specify the group structure by choosing the energy boundaries from the GAM and THERMOS libraries [5A]. Although the option allows for flexibility in the number of groups, a maximum 5 group structure can be transferred into ISOTXS format and structures with less than 5 groups have been found to be unreliable when compared to those from other cross section generation codes [6A].

Input Description

The input consists in general of the cell composition, the cell geometry, and the isotope resonance data. A sample input file is provided at the end of this discussion.

Standard atomic weights and densities were used to calculate the number densities of the uranium dioxide (UO_2) fuel, the zircaloy-IV (Zr-4) cladding and the water (H_2O) moderator. The UO_2 fuel number densities were calculated using 93% of theoretical density and 4.0 wt.% enrichment. The thermal expansion of water at operating temperatures was taken into account with the density fraction factor, DENFRC. The Zr-4 material cross sections provided in the EPRI-CELL library were compared to a constructed Zr-4 material cross section set. The Zr-4 was mixed approximating component atom density fractions with ASTM standard weight fractions. The resulting output showed no significant difference (less than 0.8% change in the flux and macroscopic cross sections) between the two input compositions. The library zircaloy-4 was chosen for the remainder of the calculations.

The code cannot successfully process a void region. Therefore, to account for the pellet-clad gap, the cladding material and gap void region

were homogenized, resulting in a volume fraction, VOLFRC, for the clad zone which is less than unity. Thermal expansion of the clad was also taken into account with the density fraction variable DENFRAC.

The cross sections are listed in the library for several values of temperature. The TEMPID for the material cross sections were chosen as close to operating temperatures as was available. The material temperature is also an input parameter, TEMP(I), which is designed, according to the manual, to further adjust calculations for actual material operating temperatures. A comparison study was done to see the effect of changing the TEMP(I) array. The TEMP(I) values appear to have no effect on the calculational results.

The cell geometry is cylindrical, with dimensions determined from the LOFT System and Test Description [7A] values for the fuel pellet and fuel rod. The cell boundary was calculated for an equivalent volume cell for a box with sides of length equal to the rod pitch. The unit cell volume fractions were then compared to values given in the Final Safety Analysis Report (FSAR) for the LOFT reactor [8A]. The calculated unit cell volume fractions correlated with the cold temperature (69°F) volume fractions. Assuming that the rod pitch is constant with thermal expansion, the unit cell boundary was unchanged and new fuel and clad dimensions were calculated using the hot (540°F) unit cell volume fractions. The spectrum results of both geometries was evaluated (see Results Section 4.1.1), but the cold conditions geometry was primarily used as the basis of comparison for the sensitivity study.

The equal volume spacing option, OPTION(6), was chosen to divide the zones into equal volume regions and not by the default process of division by equal radial distances. This was chosen for convenience since compositions are entered and listed in volume densities, and initially, region homogenized densities are equal within a zone. The optimum number of fuel regions to account for the changing radial flux within the fuel, was determined by comparing the infinite multiplication factor, k_∞, between output runs of varying numbers of regions. Calculations show that there is no significant change in k_∞ for 6, 8, and 10 regions at high burn-up. Thus, 6 regions provides enough mesh intervals to eliminate mathematical instabilities arising from the fuel center flux depression and the effect of uneven burn-up between regions.

The resonance data for each resonant isotope involves two calculated values: The Dancoff Factor, and the excess potential scattering cross

section, both of which were calculated using the formulas provided in the EPRI-CELL manual. The Dancoff Factor calculational method presented, employs the methodology developed by Sauer, and assumes a uniform lattice [1A]. The calculations were done using the actual clad volume and the homogenized unit cell clad volume, with the resulting difference in THERM, RES, and FAST less than 0.2%. Because the Dancoff Factor is dependent upon the fuel pin geometry, calculations were repeated for the hot unit cell geometry. The excess potential scattering term was calculated using an ANL revised table of $\lambda\sigma_p$ values for resonant nuclides and resonance neutron scattering isotopes.

To help determine the range of values for THERM, RES, and FAST, several input parameters were varied. The boron (isotopes B-10 and B-11) concentration in the moderator was entered for an approximate operating concentration (668 ppm) and for a trace amount (10^{-20} g-atoms) which does not affect the interaction rate. The fuel burn-up for LOFT is measured in units of effective full power hours (EFPH). The calculations were performed with full power operation for intervals over the range of the lifetime of the core (2000 EFPH). The results for a given time interval at a particular burn-up, called a burn step, will vary according to the calculational history of the burn-up. Thus the resulting amount of depletion, and fission activity for a given burn step of one run of the code may be different for the same burn step in another run with different previous calculated time intervals leading to the burn step. In particular, a burn step which is preceded with a history of many small time intervals will show a greater fission activity, and thus, for example, a higher fission product poisoning, than a burn step preceded by fewer, longer time intervals. The smallest first time interval for any run was set at 25 EFPH to allow for samarium-149 and xenon-133 equilibrium.

The ISOTXS options were enabled for the cross section generation run. The standard 5 group structure was modified using the LBGNF and IGTH variables to produce the structure given in Table 1A. The HISONM array was used to name the isotopes so that the first four identifying letters are the same as that used by the program COCANE. (See Utility Programs description Section A.4.1.) The fifth position of the isotope name was designated by the code with the number 1, signifying that the data was generated in the first burn step. The cross sections do not vary much over the lifetime of the core, so that using fresh fuel cross sections is appropriate. The input file for the ISOTXS generation run is given following this discussion.

EPRI-CELL: Sample Input Data File

```
GEN XSECT:  TRACE BORON IN MOD, EQUIVALENT CELL
UO2 ZR-4BH2O
FU-1FU-2FU-3FU-4FU-5FU-6FU-7FU-8CLADMOD MOD MOD
FUELCLAD MOD
 &INFREE
 NCOM=3,ID=24,
 NUCLID(1)=4040,10010,50100,50110,60120,80160,
  140000,240000,250550,260000,280000,420960,
 922340,922354,922361,922384,932371,942380,942394,942402,942411,942421,
 999998,999999,
 TEMPID(1)=598,556,2*564,296,564,6*293,10*1110,2*0,
 PUREDN(1,1)=5*0,.045466,6*0,1*1.0E-20,9.21027E-4,1.0E-20,.021818,8*1.0E-20,
 PUREDN(1,2)=.043084,3*0,1.0E-20,0,6*1.0E-20,12*0,
 PUREDN(1,3)=0,.06685793,2*1.00E-20,0,.03342904,18*0,
 VOLFRC(1,1)=1.0,   VOLFRC(2,2)=.874555,   VOLFRC(3,3)=1.0,
 DENFRC(1,1)=1.0,   DENFRC(2,2)=.994325,  DENFRC(3,3)=.705297,
 ISPEC=9,PHITYP=0.0,IEDIT(1)=3*1,POWR=195.34,
 TEMP(1)=300.0,293.,293.0,
 OPTION(11)=0,   OPTION(12)=1,
 OPTION(6)=1,1,1,
 OPTION(12)=1,
 OPTION(24)=1,
 NTS=2,          TIMSTP(1)=25.,50.,
 ZONEPT(1)=6,1,3,
 ZONETK(1)=.463472,.071091,.272239,
 ZONECT(1)=1,0,0,
 NUCRE=7,IDRES(1)=922354,922361,922384,942394,942402,942411,942421,
 RES(1,1)=300.,0.92,0.263013,224.100,8.403E-4,
 RES(1,2)=300.,0.92,0.263013,1.90240E19,1.0E-20,
 RES(1,3)=300.,0.92,0.263013,7.4408,1.98983E-2,
 RES(1,4)=300.,0.92,0.263013,1.90240E19,1.0E-20,
 RES(1,5)=300.,0.92,0.263013,1.902400E19,1.0E-20,
 RES(1,6)=300.,0.92,0.263013,1.902400E19,1.0E-20,
 RES(1,7)=300.,0.92,0.263013,1.902400E19,1.0E-20,
 ISOSTP=1,
 OLDISO=0,
 LBGNF(1)=1,11,30,63,
 IGTH(1)=  9*5, 26*4,
 HISONM(1)='ZIRC','H-H-','B-10','B-11','C-12','O-16',
  'SISI','CRCR','MN55','FEFE','NINI','MO96',
  'U234','U235','U236','U238','NP27','PU28','PU29','PU20','PU21','PU22',
 &END
```

A.2 ORIGEN CODE

Code Description

ORIGEN, the Isotope Generation and Depletion Code, was developed at the Oak Ridge National Laboratory (ORNL) for calculating compositions and activities of reactor materials after a specified irradiation history. The input requires specification of the material composition, the irradiation and decay time intervals, and the neutron spectrum parameters. Included in the output is the composition of each nuclide during and after the irradiation period, the photon production for specified time intervals during the decay period, and the neutron generation from spontaneous fission and alpha decay. The primary reference for this section is the ORIGEN code manual Sections 2 and 3 [9A].

ORIGEN is a point depletion code which solves the general equations for nuclear transmutation and decay to determine the composition and radioactivity of specified isotopes. The composition as a function of time is determined by:

$$\frac{dx_i}{dt} = \sum \ell_{ij}\lambda_j x_i + \phi_{av}\sum f_{ik}\sigma_k x_k - (\lambda_i + \phi_{av}\sigma_i)x_i \qquad (A.2.1)$$

where

x_i = concentration of nuclide i

i = 1,2,...,N; N = total number of nuclides

λ_i = radioactive disintegration constant for nuclide i

σ_i = spectrum averaged neutron absorption cross section for nuclide i

ℓ_{ij} = fraction of nuclide i produced from decay or fission of nuclide j

f_{ij} = fraction of nuclide i produced from neutron absorption by nuclide j

ϕ_{av} = position averaged and energy averaged neutron flux

The first two terms give the rate of production of nuclide i from radioactive decay and neutron absorption respectively, and the last term gives the rate of destruction of nuclide i from the same two processes. The assumption of a slowly varying neutron flux over the time interval allows for the approxima-

tion of setting the flux equal to a predetermined constant over the calculational timestep. Therefore, the problem is simplified to a homogeneous set of simultaneous first order ordinary differential equations with constant coefficients. In matrix notation, Eq. (1) is written in the form:

$$\dot{X}(t) = A\,X(t) \tag{A.2.2}$$

with the solution given as

$$X(t) = X(0)\,\exp\,(At) \tag{A.2.3}$$

where

$X(0)$ = vector of initial atom densities

A = transition matrix constructed from nuclear library decay data

The ORIGEN code accounts for a changing neutron flux as a result of fuel depletion with burn-up. An expression for the averaged neutron flux as a function of time is derived to calculate the constant value, ϕ_{av}, used in the transition matrix. The equation is derived for a specified power level from the following relation, for any time t, between the instantaneous flux and the fission cross section, which is calculated from the fuel composition:

$$P = 3.20 \times 10^{-17}\ \Sigma\phi \tag{A.2.4}$$

where

P = specific power (MW/unit fuel)

Σ = macroscopic fission cross section (cm^2/unit fuel)

ϕ = instantaneous neutron flux (n/cm^2-sec)

The constant gives the energy released in MW/fission, assuming the average energy release of 200 MeV per fission event. At the initiation of the computations for a time interval, the fuel composition and hence the macroscopic fission cross section, is known, and the power is specified in the input. Therefore, the initial flux, $\phi(0)$, is known. The expression for the average flux as a function of time is arrived at by solving Eq. (4) for the flux,

expanding in a Taylor's series about the initial interval time t=0, for changing cross section, $\Sigma(t)$, integrating over the interval and dividing by the total interval time.

$$\phi_{av} = \phi(0)\left[1 - \frac{t}{2}\frac{\dot{\Sigma}(0)}{\dot{\Sigma}(0)} + \frac{t^2}{6}\left(\frac{2\dot{\Sigma}(0)^2 - \Sigma(0)\ddot{\Sigma}(0)}{\Sigma(0)^2}\right) + \ldots\right] \qquad (A.2.5)$$

The derivatives for the macroscopic cross section are calculated from the composition matrix. Evaluating Eq. (3) at t=0 gives $\dot{X}(0) = A\,X(0)$, and differentiating Eq. (3) and evaluating at t=0 gives $\ddot{X}(0) = A\,\dot{X}(0)$, where X(0) is a matrix of known initial isotope compositions for the time interval. Thus, the average neutron flux for an interval is determined from the initial conditions for that time interval.

The Nuclear Data Library is divided into three groups categorized by material type: cladding and structural materials (or light elements), actinide elements and their daughters, and fission products. The ORIGEN output is also organized in this manner. Some overlap may occur, especially isotopes that may be both a structural material and a fission product, in which the isotope is listed twice. Within each category, there is data which is isotope specific and independent of the reactor spectrum, and there is neutron capture data for four reactor spectra (HTGR, LWR, LMFBR, MSBR). Appropriately, the LWR spectra data was used (variable IT=2) and thus the following discussion refers only to this particular case.

The reactor independent data includes the isotope decay constant and the fraction of transitions which are by beta decay, alpha emission, positron emission, etc. Also included is the amount of energy released as recoverable heat in radioactive decay, and the fraction of this energy which is associated with γ-ray radiation. The reactor-dependent neutron interaction cross sections include thermal neutron absorption cross sections, infinite dilution resonance integrals, thermal and fast fission cross sections, and high energy neutron absorption reaction cross sections, where appropriate for each category. Also included are the fission yields for every fission product from each of the five fissionable actinides. All of the above mentioned data can be read by invoking the Nuclear Data Library edit option.

The spectrum averaged neutron absorption cross sections (σ_i in Eq. (1)) are calculated by weighting the contributions from the fast ($E \geq 1$ MeV), resonance (1 MeV $< E <$ .5 eV), and thermal ($E \leq$ .5 eV) energy regions. The weight factors are referred to as the neutron spectrum parameters THERM, RES and FAST. For the light elements, the total effective neutron cross section is given as

$$\text{TOCAP} = \text{SIGTH} \times \text{THERM} + \text{RITH} \times \text{RES} + \text{SIGMEV} \times \text{FAST} \qquad \text{(A.2.6)}$$

where SIGTH is the theoretical (2200 m/sec) thermal neutron cross section, RITH is the infinite dilution resonance integral for epithermal neutron absorption given as

$$\int_{.5}^{\infty} \frac{1}{E} \sigma_t(E)dE \qquad \text{(A.2.7)}$$

and SIGMEV is the fission spectrum averaged cross section for reactions with a 1 MeV energy threshold. The three group averaged neutron absorption cross sections are taken directly from the Nuclear Data Library. For the actinides, the effective neutron cross section is

$$\begin{aligned}\text{TOCAP} = (\text{SIGNG}+\text{SIGF})\times\text{THERM} &+ (\text{RING}+\text{RIF})\times\text{RES} \\ &+ (\text{SIGFF}+\text{SIGN2N}+\text{SIGN3N})\times\text{FAST}\end{aligned} \qquad \text{(A.2.8)}$$

where SIGNG and SIGF are the theoretical thermal (n,γ) and (n,fiss) cross sections; RING and RIF are the resonance integrals for (n,γ) and (n,fiss) reactions; SIGFF, SIGN2N, and SIGN3N are fission spectrum averaged (n,fiss), (n,2n), and (n,3n) cross sections, which are all read from the data library. The total effective cross section for the fission products is given as

$$\text{TOCAP} = \text{SIGNG} \times \text{THERM} + \text{RING} \times \text{RES} \qquad \text{(A.2.9)}$$

where SIGNG is the theoretical thermal (n,γ) cross section, and RING is the resonance integral for (n,γ) reactions, also taken from the data library. The resonance integrals assume a 1/E dependence for the neutron spectrum in the resonance region. The high energy spectrum dependence is well approximated by the fission spectrum.

The three weight factors are defined so that the total neutron cross section TOCAP, is an effective thermal neutron cross section. THERM is a measure of the ratio of the actual reactor thermal spectrum to the theoretical thermal spectrum. RES is the ratio of resonance flux per unit lethergy to the thermal flux. FAST is the ratio of the fast flux per fission neutron to the thermal flux. The result of multiplying the total effective neutron absorption cross section times a thermal flux is that the thermal flux cancels in the nonthermal energy terms to leave a sum of effective thermal, resonant, and fast interaction rates ($\sigma \times \phi$). Therefore, ϕ_{av} is calculated as an effective thermal flux and $\phi_{av} \times \sigma_i$ is an effective interaction rate. The methods of calculating the neutron spectrum parameters is given below in the Input Description.

The nuclear properties of the spontaneous fission reaction and alpha particle interactions are programmed directly into the code. The photon spectrum used for spontaneous fission is the sum of the prompt gamma-ray and the equilibrium fission product photon spectra. This photon source is included in the tables of photon production from the decay of the actinide isotopes. The average number of neutrons, ν, produced in spontaneous fission is calculated using the following linear formula for isotopes of mass A=238 to A=244:

$$\nu = 2.84 + 0.1225\ (A - 244) \qquad \text{(A.2.10)}$$

The energy dependence of the spontaneous neutron spectrum is not calculated, thus only the total neutron production is provided. High-energy alpha particles are emitted during the alpha decay of such isotopes as ^{238}Pu, ^{242}Cm, and ^{244}Cm found in spent fuel. These alpha particles are able to interact with neighboring oxygen atoms via (α,n) reactions. The number of neutrons produced per alpha disintegration is calculated from

$$\frac{\text{neutrons}}{\alpha \text{ disintegration}} = 1.0 \times 10^{-10} (E_\alpha)^{3.65} \qquad \text{(A.2.11)}$$

where E_α is the alpha particle energy in MeV.

Input Description

The ORIGEN code input consists of the compositions of the materials which comprise the system, the irradiation history, the decay time intervals, and

the neutron spectrum parameters. A sample input file used for the L2-5 simulation is provided following this discussion.

The material compositions are entered by isotope in gram-atoms per unit of fuel. The fuel assembly was used as the unit of fuel. The LOFT reactor has three types of fuel assemblies: the peripheral square assembly, the peripheral triangular assembly, and the removable center square assembly (see Fig. 1A). The calculations for the center square assembly used the configuration of the peripheral square assembly. A structural difference between the peripheral square and the center square assemblies is the material used for the support grids: that of stainless steel in the first and zircaloy in the latter. Because the structural materials provide a negligible contribution to the photon release rate in the energies of interest, it was assumed that the support grid material change would not affect the photon source term.

Another structural difference is that the peripheral assembly contains control rods, whereas the center assembly is instrumented. Both the control rod poisons and the instruments were neglected in the EPRI-CELL spectrum calculations (see Appendix discussion Section A.1) and in the present γ-ray source term calculations. The instrumentation should have a negligible effect on the spectrum. Neglecting the control rod poisons does not affect the burn history calculations since the reactor is run with the rods essentially out of the core. The poison material nuclides are low-energy gamma-ray emitters, and thus are not of interest. These assumptions would affect the calculations in the amount of stainless steel that is neglected in the instrumentation, and the control rod cladding, which is small in comparison with the rest of the assembly. The material composition of the peripheral assemblies was taken from the Final Safety Analysis Report, Revision 1 [8A], for the LOFT reactor, and from the System and Test Description, NUREG/CR-0247 [7A].

The burn-up and irradiation history used for the experimental calculations was a flat power distribution for 200 effective full power hours (EFPH) of operation. The irradiation history for the source term calculations was modeled by 885 EFPH for the peripherals and 39 EFPH for the center assembly at the initiation of experiment L2-5, and the addition of 28 EFPH acquired during the test. An average power distribution of 22.6% total power in the center module, 14.7% total power in each square assembly and 4.7% total power in each triangular assembly was used [10A].

The neutron spectrum parameters THERM, RES, and FAST were calculated using the flux and cross section data generated by the EPRI-CELL code. The following methods of calculating the parameters were obtained from Refs. [9A] and [11A].

The thermal weight factor adjusts standard 2200 m/sec tabulated cross sections to account for the spectrum deviance from thermal temperatures (.0253 eV). In this energy range, the cross section is assumed to be Maxwell-Boltzmann and to vary inversely with the speed. To determine the effective thermal speed specific to the reactor configuration and resulting neutron spectrum, the absorption cross section for ^{10}B is used, because of its nearly ideal Maxwell-Boltzmann behavior at low energies. EPRI-CELL calculates spectrum averaged broad group microscopic cross sections with an upper energy cut-off limit of .625 eV for the thermal group, Group 5. (See Table 1A.) Therefore, the ratio of inverse spectrum averaged effective thermal speed, to inverse theoretical thermal speed (2200 m/sec) is nearly equal to the ratio of the EPRI-CELL calculated absorption cross section to the tabulated 2200 m/sec absorption cross section. Thus,

$$\text{THERM} = \frac{1/v_{th}(\text{eff.})}{1/v_{th}(\text{theo.})} \approx \frac{\sigma_5(^{10}B)}{\sigma_{2200}(^{10}B)} \qquad \text{(A.2.12)}$$

with σ_a (2200) = 3836 barns.

The RES weight factor multiplies the resonance integral to calculate the resonant region contribution to the effective total cross section and therefore to the interaction rate. The resonance integral is the sum of lethargy-weighted effective cross sections over the resonance energy region. The resonance weight factor is the ratio of the resonant flux per unit lethargy to the thermal flux. The EPRI-CELL broad group structure used in the flux calculations is given in Table 1A. Thus,

$$\text{RES} = \frac{\phi_{res}/\Delta u}{\phi_{th}} = \frac{\sum \phi_i/\Delta u}{\phi_5} \qquad \text{(A.2.13)}$$

where the sum is over the three EPRI-CELL resonance groups, and Δu is the unit change in lethargy over this energy region. Given the definition of lethargy, u, as:

$$u = \ln \frac{E_0}{E} \qquad (E_0 = 10 \text{ MeV reference energy}), \tag{A.2.14}$$

Δu can be calculated as follows:

Δu = u (lower energy) - u (upper energy)

$$= \ln \frac{10x10^6}{.625} - \ln \frac{10x10^6}{8.21x10^5} \tag{A.2.15}$$

$\Delta u = 14.0883$

The fast weight factor multiplies a fission-spectrum-averaged, or neutron-number weighted cross section for those reactions with a threshold energy above 1 MeV. As with RES, the FAST factor is then the ratio of the fast flux per fast neutron, to the thermal flux. Thus,

$$FAST = \frac{\phi_{fast}/x_1}{\phi_{th}} = \frac{\phi_1/x_1}{\phi_5} \tag{A.2.16}$$

where x_1, the fraction of fast neutrons produced per fission, is the number of neutrons in this energy interval referenced to a total of 1 neutron. The fission spectrum χ values for each group are included, along with the fluxes, in the EPRI-CELL macroscopic output edit.

The nuclear data changes in the input deck are recommended corrections to the nuclear data library for the actinides [11A].

The decay time intervals for the general study were chosen to determine the source terms at various times during the L2-5 transient when core voiding occurred and for an extended time up to 30 minutes. For the L2-5 simulation

calculations, the specified decay intervals were designated to correspond in time with the available void data [12A].

ORIGEN: Sample Input Data File

```
     NUCLEAR DATA LIBRARY FOR PWR                                                -2
   0.57599   0.39705   3.13524   1.0E-25 40185 1 0 017
902320491233049223204922330492234049223504922360492238049323704942380494239O4
9424004942410494242049524104952430496242O4
     7.97529      0.16468      0.03346          0.0
   155.47845      1.08853      0.00903          0.0
   7.4309E+1    1.2061E+2    2.6633E-2          0.0
    46.90497    383.90151      0.01865          0.0
   176.34072      3.25455      0.00267          0.0
   7.2513E+1    3.1346E+2    2.2267E-2          0.0
   6.7497E+1    1.3944E+0    1.5879E-2          0.0
   6.4239E+0    7.1895E-1    3.7512E-3          0.0
   1.3357E+2    3.7163E+0    6.8231E-3          0.0
   2.2536E+2    1.6900E+1    1.0656E-3          0.0
   4.4940E+2    7.7625E+2    5.0821E-3          0.0
   1.0605E+3    4.3000E+0    2.7439E-3          0.0
   2.3168E+2    8.4040E+2    4.6632E-2          0.0
   6.9973E+2    3.2431E+0    1.1866E-2          0.0
   8.9383E+2    1.0202E+1          0.0          0.0
   3.3611E+2    2.5405E+0          0.0          0.0
   1.2941E+2    9.1530E+0    3.4296E-3          0.0
   10   10    0    0    0    0    1    0    0    2    0    0    0
          110        010        010        010        010
          110        010        010        010        010
          110        010        010        010        010
LOFT  L2-5   BURNUP: 0-500 EFPH  (SQUARE ASSEMB)
  7.350  7.350   7.350   7.350   7.350   7.350  7.350   7.350   7.350   7.350
    10.0    20.0    40.0    60.0   100.0   150.0   200.0   300.0   400.0   500.0
SQUARE FUEL ASSEMBLY-ENRICHMENT 4.0%    3600.0 HRS
     1.E-3     1.E-3     1.E-3     1.E-3     1.E-3     1.0       1.0
010010 2911.95 010020 .4368559                                                  1
030070 .007478                                                                  1
050100 .33542  050110 1.37592                                                  1
080160 3161.70 080170 1.17266 080180 6.46545                                    1
060120 1.94201 070140 208.087 090190 1.04E-04130270 3.01842                     4
140280 14.2491 150310 .577484 160320 .397299 170350 8.88E-05                    4
220480 3.06043 240520 187.369 250550 13.5315 260560 465.889                     4
270590 2.76386 280590 204.110 290630 .768969 400910 490.113                     4
410930 4.38301 420960 5.09328 501190 5.56537 731810 2.33996                     4
922340 .048820 922350 34.5433 922380 821.9857                                   2

    6    6    0    0   10    0    1    0    0    3    0    0    0
LOFT  L2-5   BURNUP: 500-885+28 EFPH  (SQUARE ASSEMB)
  7.350  7.350   7.350   7.350   7.350   7.350
   600.0    700.0  800.0   850.0   885.0   913.0
SQUARE FUEL ASSEMBLY-ENRICHMENT 4.0%    3600.0 HRS     500.0
    0   10    0    0    6    0    1    0    0    3    0    0    0
  POST IRRADIATION DECAY  TEN STEPS FROM SHUTDOWN TO 54.0 SEC
     1.0      5.0     10.0     15.0     21.0     35.0     45.0     48.0     50.0     54.0
SQUARE FUEL ASSEMBLY-ENRICHMENT 4.0%        1.0SEC       0.0
    0   10    0    0   10    0    1    0    0    3    0    0    0
  POST IRRADIATION DECAY  TEN STEPS FROM 054.0 SEC TO 225.0 SEC
    95.6    119.2    127.2    174.0    180.0    182.1    191.1    193.3    215.0    225.0
SQUARE FUEL ASSEMBLY-ENRICHMENT 4.0%        1.0SEC      54.0
    0   10    0    0   10    0    1    0    0    3    0    0    0
  POST IRRADIATION DECAY TEN STEPS FROM 225.0 SEC TO 420.0 SEC
   255.0    265.0    275.0    300.0    331.0    351.0    380.0    400.0    410.0    420.0
SQUARE FUEL ASSEMBLY-ENRICHMENT 4.0%        1.0SEC     225.0
    0   10    0    0   10    0    1    0    0    3    0    0    0
  POST IRRADIATION DECAY TEN STEPS FROM 420.0 SEC TO 620.0 SEC

   435.0    460.0    480.0    510.0    545.0    590.0    600.0    603.6    611.1    620.0
SQUARE FUEL ASSEMBLY-ENRICHMENT 4.0%        1.0SEC     420.0
    0    6    0    0   10    0    1    0    0    3    0    0    0
  POST IRRADIATION DECAY SIX STEPS FROM 620.0 SEC TO 900.0 SEC
   635.0    653.3    676.0    720.0    750.0    900.0
SQUARE FUEL ASSEMBLY-ENRICHMENT 4.0%        1.0SEC     620.0
```

A.3 ONEDANT CODE

Code Description

The One-Dimensional Diffusion-Accelerated Neutral-Particle Transport Code, ONEDANT, was developed at the Los Alamos National Laboratory (LANL) to solve the one-dimensional multigroup Boltzmann transport equation. The program was written as a modular code with separate input, solver, and edit modules. The Argonne National Laboratory (ANL) version has been incorporated into a larger multi-code package, referred to as the Argonne Reactor Code (ARC) System. The ONEDANT code package has been revised at Argonne to respond to various specific needs, and to ease the adaptation to the data management of the ARC system. The basic code information can be found in the 1982 updated version of the user's manual [13A]. Information on ANL revisions and the use of the ONEDANT code through the ARC system can be found in a series of internal memos [14A].

The ONEDANT code solves the following one-dimensional, time independent, inhomogeneous form of the Boltzmann equation:

$$\begin{aligned}\nabla\cdot\Omega\ \psi(r,E,\Omega) + \Sigma(r,E)\psi(r,E,\Omega) = {} & \int\int dE'd\Omega'\ \Sigma_s(r,E',E,\Omega\to\Omega')\ \psi(r,E',\Omega') \\ & + 1/4\pi \int\int dE'\ d\Omega'\ \chi(r,E'\to E)\nu\Sigma_f(r,E')\ \psi(r,E',\Omega') \\ & + Q(r,E,\Omega) \qquad (A.3.1)\end{aligned}$$

where $\psi(r,E,\Omega)$ is the particle flux density; $\Sigma(r,E)$ is the macroscopic total cross section; $\Sigma_s(r,E',E,\Omega\to\Omega')$ is the macroscopic scattering transfer probability for energy E' to E through angle $\Omega\cdot\Omega$; $\Sigma_f(r,E')$ is the macroscopic fission cross section; ν is the number of particles emitted istropically $(1/4\pi)$ per fission; $\chi(r,E'\to E)$ is the fraction of neutrons in energy interval dE about E released from fissions resulting from the absorption of neutrons with energy dE' about E'; and $Q(r,E,\Omega)$ is the source rate density from particles emitted which are independent of the flux, ψ. For fixed source calculations, χ is set to zero for all energies, and Q is the nonzero fixed source. Modifying Eq. (1) gives

$$\nabla\cdot\Omega\ \psi(r,E,\Omega) + \Sigma(r,E)\psi(r,E,\Omega) = \int\int dE'd\Omega'\ \Sigma_s(r,E',E,\Omega\rightarrow\Omega')\ \psi(r,E',\Omega) + Q(r,E,\Omega) \qquad (A.3.2)$$

The homogeneous case sets Q=0 and inserts the eigenvalue factor into the fission source term to produce the equation

$$\nabla\cdot\Omega\ \psi(r,E,\Omega) + \Sigma(r,E)\psi(r,E,\Omega) = \int\int dE'd\Omega'\ \Sigma_s(r,E'\rightarrow E,\Omega\cdot\Omega')\ \psi(r,E',\Omega') + 1/(4\pi\ k_{eff})\ \int\int dE'd\Omega'\ \chi(r,E'\rightarrow E)\nu\Sigma_f(r,E')\ \psi(r,E',\Omega') \qquad (A.3.3)$$

The above differentio-integral equations in continuous variables are converted for computer use to algebraic expressions for discrete points with the following methods. The divergence operator in the geometrical leakage term is determined according to the specified geometry of the problem, with the resulting derivatives computed by finite differences. The scattering source term and the inhomogeneous source term are expanded by polynomial functions using the spherical harmonics expressions. The order of the Legendre polynomials is specified by the user with the variable ISCT. The multigroup approximation is employed for the discretization of the energy variable, E. The discrete ordinates method is used to discretize the angular direction variable, Ω, into a set of quadrature points each associated with a quadrature weight or coordinate. The quadrature directions are determined by the order of the quadrature and the geometry of the problem, both specified in the input. The spatial variable is partitioned into the user specified fine mesh intervals, with the discretization accomplished under the diamond-difference scheme.

The transport equation is solved through a two-step iterative procedure. The iterations are accelerated with diffusion theory calculations to reduce running time and thus cost. For a fixed source calculation without fission sources or upscattering, an initial diffusion calculation is performed to determine the group fluxes. Next a series of inner-iterations are performed consisting of, for each group consecutively: a transport calculation generating angular fluxes, a correction to the group source terms, and then an effective diffusion calculation based on the new source to determine the group scalar fluxes. The iterations continue for each group until convergence of the mesh point scalar fluxes is achieved.

The eigenvalue problem is solved using an initial multigroup diffusion calculation with an assumed flat fission source distribution to generate group scalar fluxes. These scalar flux values are then used to calculate the fission source rate distribution. These two calculations are repeated in this diffusion sub-outer iteration until the scalar fluxes and the source term have converged. Next, an inner-iteration series of calculations is performed to adjust the scalar fluxes. For each group, a set of angular fluxes are determined which are then used to generate effective diffusion coefficients. Using these coefficients, a diffusion calculation is performed to calculate the group scalar fluxes at each mesh point interval. After establishing convergence of this new set of group scalar fluxes, the final product of the inner-iteration process, a fission source rate is calculated as the initial guess for the diffusion sub-outer iteration. The sequence of inner-iterations followed by a diffusion sub-outer iteration is considered an outer iteration. The outer iteration procedure is then repeated until full convergence of the fluxes and source terms is achieved.

Input Description

The input and output data management is handled by several modules in the ARC system. The input file is designed to identify each module being accessed and the functions which it is to perform. The modules which process the data input, transform the given information into a form useable by ONEDANT. The output was sometimes processed by the DIF3D edit module, in addition to the built-in ONEDANT edit options. Two sample input decks to run ONEDANT as a k calculation and as a fixed source problem, are given at the end of this discussion.

The material compositions and geometry are processed by the NIP3 module. The core is a homogeneous mixture of UO_2 fuel, zircaloy cladding, and water moderator. The core material number densities are the same as those used in the EPRI-CELL calculations. (See Appendix Section A-1.) The stainless steel, and low carbon steel compositions were determined directly from the number density table describing the material compositions used in the LWR Benchmark problems in the BUGLE package [15A]. (See Table 2A.) The geometry configuration for the flow paths and the reactor vessel was developed primarily from Fig. 78 of the System and Test Description [7A] (Figure 4),

which gives details of the core and reactor vessel dimensions. The computational model for LOFT developed by PSU [7A], was used as a guideline for dimensions beyond the vessel. The core radius was determined using the equivalent core diameter of 24.12 inches.

The cylindrical geometry option was chosen with a reflective boundary condition at the core centerline, r=0 cm, and a vacuum boundary condition at the outermost edge of the geometry model, r=140 cm. The buckling height option was invoked in ONEDANT by assigning the parameter BHGT=169.324 cm. This value was determined by adding a calculated extrapolation distance to the 5.5 ft. (167.64 cm) active core height. The extrapolation distance was calculated from the following expression which assumes a planar free surface boundary [17A]:

$$d = .71 \times \lambda_{tr} \qquad (A.3.4)$$

where the transport mean free path is defined as $\lambda_{tr} = 1/\Sigma_{tr}$ with Σ_{tr} equal to the macroscopic transport cross section. For a one-dimensional cylindrical calculation in the axial direction, the boundary is a finite planar surface. The free surface assumption is not appropriate for the core since there exists a considerable amount of steel which acts as a reflector, but is more reasonable for areas outside the core in which there exists water, a steel container, and then air. The value of Σ_{tr} for the core was calculated using the core number densities and the thermal σ_{tr} values from the EPRI-CELL output. The actual buckling term is calculated by the ONEDANT program.

The Legendre polynomial order was determined by the order of the cross section set involved. The EPRI-CELL cross sections are derived with a P_0 scattering order, and the BUGLE, and thus the COLLBUGL cross sections were generated with P_3 scattering order.

The angular quadrature order, S_N, was chosen to optimize accuracy while minimizing computer processing time and cost. A comparison calculation of 4th order and of 8th order quadrature showed essentially no difference in the flux output. Therefore, the calculations were performed with S_4 quadrature. The standard Gaussian angular quadrature coefficients are provided by the code with the option IQUAD=1. For several voided region calculations, the problem failed to converge using the standard quadrature set. For these calculations,

the double Gaussian angular quadrature set of coefficients, also provided in the code, were used with option IQUAD=4.

The cross section dataset is converted from XS.ISO format to ISOTXS format by the ARC module HMG4C for input into ONEDANT. The cross section data library is assigned in the job control language of the input deck. For the coupled n-γ dataset, the variable LNG was set to the last neutron group. This organizes the output edits only and does not affect the calculational process.

The ONEDANT flux output from a k calculation problem is normalized to one fission event. The output was routed through the DIF3D edits to change the normalization to a user specified power rating in watts. For fixed source calculations, the source is generated with a normalized flux and therefore is itself normalized to a specific power rating. Thus, the fixed source ONEDANT output flux does not require renormalization. The isotropic components of the flux are entered into a file, referred to as the RTFLUX file, and when requested in the job control language, the file is saved on a user specified permanent file.

Some modifications to the input deck are required to run a fixed source problem. The source datafile is assigned to the FIXSRC file in the job control language. The source option variable, INSORS, alerts the ONEDANT code to the existence of a fixed source file and where to find the data. The chi vector array must be set to zero, or else the program processes a multiplying fission source which upon each iteration, causes the flux values to increase.

General program control input which is independent of the specific problem, was taken on recommendation from ANL personnel. This includes storage allocation and iteration control criteria.

ONEDANT: Input File for k Calculation

```
1.     //KCALC JOB (,F89305),USER=B89305,CLASS=W,MSGCLASS=W,
2.     //  REGION=2000K,TIME=10
3.     //*MAIN ORG=RADS12,LINES=49
4.     //*FORMAT PR,DDNAME=,DEST=3800
5.     // EXEC ARCSP021,PATH=LASL,
6.     // ISOTXS='B89305.XSECT.ECELL.ISOTXS',
7.     // ISODSP=SHR
7.1    //FT10F001 DD DUMMY
7.11   //FT26F001 DD DSN=B89305.ONEDANT.GEODST,
7.12   //   DISP=SHR,UNIT=ALLPERM,VOL=SER=,SPACE=(TRK,(1,1),RLSE),
7.13   //   DCB=(RECFM=VBS,LRECL=X,BLKSIZE=6136)
7.2    //FT30F001 DD DSN=B89305.ONEDANT.RTFLUX.KCALC,
7.3    //   DISP=SHR,UNIT=ALLPERM,VOL=SER=,SPACE=(TRK,(4,2),RLSE),
7.4    //   DCB=(RECFM=VBS,LRECL=X,BLKSIZE=6136)
7.7    //SYSUDUMP DD DUMMY
8.     //SYSIN DD *
9.     BLOCK=OLD
10.    DATASET=ISOTXS
11.    BLOCK=STP021
12.    DATASET=A.DIF3D
13.    01    KCALC: T=0SECS, EPRI-CELL XSECTNS
14.    02     15000120000     0
15.    03        0     0     0          -2     0
16.    04        1     0     1    00     0    00
17.    05
18.    06
19.    DATASET=A.HMG4C
20.    01    KCALC: T=0SECS, EPRI-CELL XSECTNS
21.    02    120000     0     0     0     0     1     0     0
22.    DATASET=A.NIP3
23.    01    KCALC: T=0SECS, EPRI-CELL XSECTNS
24.    02               0     1 20000     0120000
25.    03              20
26.    04               3     2
27.    06    CORE                    30.63
28.    06    FILLER                  35.56
28.2   06    SKIRT                  37.782
28.3   06    H2OFLO                  38.10
28.4   06    BARREL                  41.91
29.    06    DNCMR                   46.99
30.    06    VESFIL                  72.64
31.    06    H2OGAP                 73.279
32.    06    VESSEL                  82.94
33.    06    VOID                    93.81
34.    06    SHIELD                  94.00
35.    06    WATER                  118.00
36.    06    INSTRM                 125.00
37.    06    WATER2                 140.00
38.    09        X     7 20.0           5 27.8           2 29.38
39.    09        X     4 30.63         13 35.56          6 37.7820
39.5   09        X     1 38.10         10 41.91         17 46.99
40.    09        X     5 50.0          17 70.0           5 72.64
41.    09        X     2 73.279        16 82.94         20 93.81
41.5   09        X     1 94.00          6 96.00          3 98.00
42.    09        X    15 118.00         5 125.00        10 140.00
43.    13         U02    U2351 9.21030E-04 U2381 2.18118E-02 O-161 4.54657E-02
43.5   13         CLAD   ZIRC1 4.29863E-02
44.    13         AGUA   H-H-1 4.71551E-02 O-161 2.35775E-02
45.    13         LCS1   C-121 8.67000E-04 SISI1 4.96000E-04 CRCR1 1.54000E-04
```

```
45.2    13          LCS2   MN551 1.12000E-03 FEFE1 8.20000E-02 NINI1 5.95000E-04
45.4    13          LCSMAT MO961 2.71000E-04 LCS1  1.0         LCS2   1.0
45.5    13          SST    CRCR1 1.74000E-02 MN551 1.52000E-03 NINI1 8.51000E-03
45.7    13          SSMAT  FEFE1 5.81000E-02 SST   1.0
46.     13          NADA   H-H-1 .000001
47.     14          NUKE   UO2     .330      CLAD    .095      AGUA    .561
48.     14          SS     SSMAT  1.0
48.5    14          SS1    SSMAT  1.0
49.     14          H2O1   AGUA   1.0
50.     14          SS2    SSMAT  1.0
51.     14          H2O2   AGUA   1.0
54.     14          SS3    SSMAT  1.0
55.     14          H2O3   AGUA   1.0
55.2    14          LCS    LCSMAT 1.0
55.3    14          ZERO   NADA   .001
56.     14          SS4    SSMAT  1.0
57.     14          H2O4   AGUA   1.0
57.1    14          SS5    SSMAT  1.0
57.2    14          H2O5   AGUA   1.0
58.     15    NUKE  CORE
59.     15    SS    FILLER
59.4    15    SS1   SKIRT
59.5    15    H2O1  H2OFLO
59.6    15    SS2   BARREL
60.     15    H2O2  DNCMR
61.     15    SS3   VESFIL
62.     15    H2O3  H2OGAP
63.     15    LCS   VESSEL
64.     15    ZERO  VOID
65.     15    SS4   SHIELD
66.     15    H2O4  WATER
67.     15    SS5   INSTRM
68.     15    H2O5  WATER2
69.     NOSORT=A.1DANT
70.          1
71.     KCALC: T=0SECS, EPRI-CELL XSECTNS
72.      IGEOM=2,    NGROUP= 5,  ISN=4,      NISO=22,
73.      MT=14,      NZONE=14,   IM=21,      IT=170,
74.      IDIMEN=1,
75.      MAXLCM=130000,          MAXSCM=50000,   T
76.     LIB=ISOTXS, I2LP1=-1,   T
77.     ASSIGN=MATLS, T
78.      IEVT=1,       ISCT=0,     ITH=0,
79.      IBL=1,        IBR=0,
80.      CHI= 7.38659E-01, 2.61057E-01, 2.77385E-04,         0.0,         0.0
89.      FLUXP=0,    XSECTP=1,   FISSRP=0,   GEOMP=1,    ANGP=0,
90.      INFLUX=0,   IQUAD=1,    NORM=0,     BHGT=169.324,
90.5     EPSI=.0001, EPSO=.0001,
91.      IITL=50,    OITM=20,    T
92.      PTED=1,     ZNED=1,                 T
93.     BLOCK=STP021
94.     REMOVE=A.1DANT
95.     DATASET=A.0IF3D
96.     01    KCALC: T=0SECS, EPRI-CELL XSECTNS
97.     02
98.     03          0     0     0          -2     0
99.     04          0     0     0    01   011    11   001
100.    05
101.    06                                                  50.0E+06
102.    /*
```

ONEDANT: Input File for Fixed Source Calculation

```
1.      //L25 JOB (,F89305),USER=B89305,CLASS=W,MSGCLASS=W,
2.      //  REGION=2000K,TIME=10
3.      //*MAIN ORG=RADS12,LINES=49
4.      //*FORMAT PR,DDNAME=,DEST=3800
5.      // EXEC ARCSP021,PATH=LASL,
6.      // XSISO='B89305.XSECT.COLLBUGL.XSISO1',
7.      // XSISO2='B89305.XSECT.COLLBUGL.XSISO2'
7.1     //FT10F001 DD DUMMY
7.2     //FT32F001 DD DSN=B89305.ONEDANT.FIXSRC.L25SORC,DISP=SHR
7.9     //SYSUDUMP DD DUMMY
8.      //SYSIN DD *
9.      BLOCK=OLD
10.     DATASET=XS.ISO
10.5    DATASET=FIXSRC
11.     BLOCK=STF021
12.     DATASET=A.DIF3D
13.     01      L2-5 NORMAL SHUTDOWN: T=1 SEC
14.     02     15000120000     0
15.     03         0     0     0          -2     0
16.     04         1     0     1    00     0    00
17.     05
18.     06
19.     DATASET=A.HMG4C
20.     01      L2-5 NORMAL SHUTDOWN: T=1 SEC
21.     02    120000     0     0     0     0     1     0     0
22.     DATASET=A.NIP3
23.     01      L2-5 NORMAL SHUTDOWN: T=1 SEC
24.     02               0     1 20000     0120000
25.     03              20
26.     04               3     2
26.5    06    CORE1                    12.07
27.     06    CORE2                    30.63
27.5    06    FILLER                   35.56
28.     06    SKIRT                   37.782
28.5    06    H2OFLO                   38.10
29.     06    BARREL                   41.91
29.5    06    DNCMR                    46.99
30.     06    VESFIL                   72.64
30.5    06    H2OGAP                  73.279
31.     06    VESSEL                   82.94
31.5    06    VOID                     93.81
32.     06    SHIELD                   94.00
32.5    06    WATER                   118.00
33.     06    INSTRM                  125.00
33.5    06    WATER2                  140.00
33.9    09        X     5 12.07
34.     09        X     3 20.0           4 27.8           2 29.38
34.5    09        X     4 30.63         13 35.56          6 37.7820
35.     09        X     1 38.10         10 41.91         17 46.99
35.5    09        X     5 50.0          17 70.0           5 72.64
36.     09        X     2 73.279        16 82.94         20 93.81
36.5    09        X     1 94.00          6 96.00          3 98.00
37.     09        X    15 118.00         5 125.00        10 140.00
37.5    13         U02   U-2351 9.21030E-04U-2381 2.18118E-020-0--1 4.54657E-02
38.     13         CLAD  ZRZR-1 4.29863E-02
38.5    13         AGUA1 H-H--1 4.71551E-020-0--1 2.35775E-02
38.6    13         AGUA  H-H--6 4.71551E-020-0--6 2.35775E-02
39.     13         LCS1  C-C--9 8.67000E-04SISI-9 4.96000E-04CRCR-9 1.54000E-04
39.5    13         LCS2  MNMN-9 1.12000E-03FEFE-9 8.20000E-02NINI-9 5.95000E-04
```

```
40.     13          LCSMATHOMO-9 2.71000E-04 LCS1  1.0        LCS2   1.0
40.5    13          SST5  CRCR-5 1.74000E-02NMN-5 1.52000E-03NINI-5 8.51000E-03
41.     13          SSM5  FEFE-5 5.81000E-02 SST5  1.0
41.3    13          SST13 CRCR13 1.74000E-02MNMN13 1.52000E-03NINI13 8.51000E-03
41.4    13          SSM13 FEFE13 5.81000E-02 SST13 1.0
41.5    13          NADA  H-H--6 .000001
42.     14          NUKE1 UO2     .330      CLAD    .095      AGUA1   .561
42.1    14          NUKE2 UO2     .330      CLAD    .095      AGUA1   .561
42.5    14          SS    SSM5    1.0
43.     14          SS1   SSM5    1.0
43.5    14          H2O1  AGUA    1.0
44.     14          SS2   SSM5    1.0
44.5    14          H2O2  AGUA    1.0
45.     14          SS3   SSM5    1.0
45.5    14          H2O3  AGUA    1.0
46.     14          LCS   LCSMAT  1.0
46.5    14          ZERO  NADA    .001
47.     14          SS4   SSM13   1.0
47.5    14          H2O4  AGUA    1.0
48.     14          SS5   SSM13   1.0
48.5    14          H2O5  AGUA    1.0
49.     15     NUKE1 CORE1
49.2    15     NUKE2 CORE2
49.5    15     SS    FILLER
50.     15     SS1   SKIRT
50.5    15     H2O1  H2OFLO
51.     15     SS2   BARREL
51.5    15     H2O2  DNCMR
52.     15     SS3   VESFIL
52.5    15     H2O3  H2OGAP
53.     15     LCS   VESSEL
53.5    15     ZERO  VOID
54.     15     SS4   SHIELD
54.5    15     H2O4  WATER
55.     15     SS5   INSTRM
55.5    15     H2O5  WATER2
69.     NOSORT=A.1DANT
70.         1
71.       L2-5 NORMAL SHUTDOWN: T=1 SEC
72.      IGEOM=2,     NGROUP=25,  ISN=4,       NISO=23,
73.      MT=15,       NZONE=15,   IM=22,       IT=170,
74.      IDIMEN=1,
75.      MAXLCM=130000,           MAXSCM=50000,   T
76.     LIB=ISOTXS, LNG=5,   T
77.     ASSIGN=MATLS, T
78.      IEVT=0,       ISCT=3,     ITH=0,
79.      IBL=1,        IBR=0,
80.      CHI= 0.0,          0.0,          0.0,        , 0.0,          F 0.0,
89.      FLUXP=1,     XSECTP=0,   FISSRP=0,   GEOMP=1,     ANGP=0,
90.      INFLUX=0,    IQUAD=1,    INSORS=1,   NORM=0,      BHGT=169.324,
91.      EPSI=.0001, EPSO=.0001, IITL=50,    OITM=20,     T
92.      PTED=1,      ZNED=1,                 T
102.    /*
103.    /* END OF FILE
```

A.4 UTILITY PROGRAMS

The utility programs were used primarily for cross section datafile management and for fixed source file generation. Most of the programs are either direct modified versions, or written based on programs which originated in the Applied Physics Division (AP) of the Argonne National Laboratory. The coding for each utility program is given following the text description.

A.4.1 COCANE

COCANE is a utility program in the AP Division written to transfer cross section datasets from ANISN format to XS.ISO format suitable for use with the transport code ONEDANT [18A]. This program was used to transfer the Oak Ridge cross section dataset BUGLE into an equivalent XS.ISO dataset. The program was later revised to include a more flexible isotope naming process [19A], because the original version required a specified format which was in use at the time the program was written. This newer version was used to transfer the collapsed BUGLE cross section set.

The input data includes group energy boundaries, spectrum chi values, and the isotope identification. The revised version of COCANE also requires data input of energy per capture (ECAP), energy per fission (EFISS), isotope mass, and cross section temperature. These last input values were automatically assigned in the older version. For consistency, the values put in for the revised version data were taken from the original version. The naming format used was similar to the original format, keeping the first four isotope identification letters, and assigning the region number over which the isotope cross sections were collapsed to the fifth and sixth positions. The original format used the sixth position as a temperature specification. The temperature data is not used by ONEDANT and therefore is not relevant to the calculations. The energy per capture and energy per fission are used by ONEDANT to determine power values for the regions and are not pertinent to flux calculations.

A.4.2 COLLAPSE

The COLLAPSE program transforms a cross section dataset in ANISN format to another ANISN format dataset with an input specified group structure of

equal or fewer number of groups [18A]. The program used in the calculations was jointly modified to handle higher order scattering [20A]. COLLAPSE was applied to the 67 group (47 neutron, 20 gamma-ray) BUGLE cross section dataset to create a 25 group (5 neutron, 20 gamma-ray) cross section set.

The program employs a flux-volume weighting scheme to produce broad group cross sections which are averaged over the spatial and energy variables. The theoretical development which can be found in many basic reactor theory texts, gives the following expression for the broad group cross section:

$$\sigma_G(E) = \frac{\int_{E_1}^{E_2} \sigma(E)\ \phi(E,t)\ dE}{\int_{E_1}^{E_2} \phi(E,t)\ dE} \qquad (A.4.1)$$

where

$$\phi(E,t) = \frac{\int_V \phi(r,E,t)\ d^3r}{\int_V d^3r}\ ,$$

group G = (E_1,E_2), and V = volume of region. For descrete numerical points, this becomes

$$\sigma_G = \frac{\sum_{g\epsilon G} \sigma_g \phi_g}{\sum_{g\epsilon G} \phi_g} \qquad (A.4.2)$$

where

$$\phi_g = \frac{\sum_i \phi_g(i)\ V_i}{\sum_i V_i}$$

is the region averaged flux,

V_i = volume of interval i

$\sum_i V_i = V_R$ the region volume

G - broad group
g - fine group

Substituting for ϕ_g in Eq. (A.4.2), cancelling the common factor of the region volume and rearranging gives

$$\sigma_G = \sum_{g\epsilon G} \sigma_g \frac{(\sum_i \phi_g(i)\, V_i)}{\sum_g (\sum_i \phi_g(i)\, V_i)} \qquad (A.4.3)$$

an expression for the broad group cross section in terms of the fine group cross section multiplying a weight factor. In the COLLAPSE program, the weight factor appears as

$$\frac{\text{PHIVLF}}{\text{PHIVOL}} \qquad (A.4.4)$$

where

$$\text{PHIVLF} = \sum_i \phi_g(i)\, V_i$$
$$\text{PHIVOL} = \sum_g \text{PHIVLF}$$

For any collapsing scheme, some factors are preserved at the expense of others. In this method, it is the volume averaged reaction rates that are conserved for a given region. This can be shown by first substituting the expression for ϕ_g in Eq. (A.4.2), and cancelling the region volume.

$$\sigma_G = \frac{\sum_{g\epsilon G} \sigma_g \sum_i \phi_g(i)\, V_i}{\sum_{g\epsilon G} \sum_i \phi_g(i)\, V_i} \qquad (A.4.5)$$

Then noting the following expression for the broad group flux for a particular interval, i.

$$\phi_G(i) = \sum_{g\epsilon G} \phi_g(i) \qquad (A.4.6)$$

Substitute Eq. (A.4.6) into (A.4.5), and rearrange to find

$$\sigma_G \phi_G = \sum_{g \varepsilon G} \sigma_g \phi_g \qquad (A.4.7)$$

where

$$\phi_G = \frac{\sum_i \phi_G(i) V_i}{\sum_i V_i}$$

is the volume averaged broad group flux, and

$$\phi_g = \frac{\sum_i \phi_g(i) V_i}{\sum_i V_i}$$

is the volume averaged fine group flux. Subsituting the flux expressions into Eq. (A.4.7), gives the following equation showing the equivalence of the volume averaged reaction rates for the original (g) and collapsed group (G) structures:

$$\sigma_G \sum_i \phi_G(i) V_i = \sum_g \sigma_g \left(\sum_i \phi_g(i) V_i\right) \qquad (A.4.8)$$

The input data simply requires specification of the broad group structure, and the collapsing region. The flexibility of the program allows for collapsing a given isotope over multiple regions, thereby increasing the accuracy of a given cross section set in that region. This was done for several isotopes including those in water for the CORE and DNCMR regions. A datafile of the fine group flux spectrum is required for use in the flux weighting scheme.

A.4.3 SOURCE

The series of SOURCE programs, NSORC, GSORC, PHN, and MIX, were written to create fixed source input files, FIXSRC, for the transport code ONEDANT. The programs are nearly the same with minor modifications added to take care of different cases as was needed. A single program with all of the options available was not written.

The SOURCE.NSORC program generates the core neutron source by modifying flux values with a multiplication factor to obtain reaction rates. The flux file, RTFLUX, is generated during the ONEDANT k calculation, by the DIF3D module edits which normalizes the values to a user specified power. The program multiplies the core neutron flux values by the user input product $\nu\Sigma_f$, where Σ_f is the macroscopic fission cross section for the core composition, ν is the average number of neutrons released per fission. For a given interval i, the interaction rates, $\nu\Sigma_f$ are summed to determine the total fission neutron source, and then multiplied by χ_g, the fraction of fission neutrons emitted into group g. These values are listed in the principle cross section edit of ONEDANT as χ and $\nu\Sigma_f$ for each group. The total product $\chi(\sum\nu\Sigma_f\phi)$ with units of n/cm^3, becomes the volumetric source terms in the created FIXSRC file.

The core γ-ray source FIXSRC file was created with the SOURCE.GSORC program. The ORIGEN output provides the photon release rate (γ/sec) in a 12 group energy structure. Initially, the total core volumetric photon release rate is calculated and converted to the 20 group BUGLE structure. The group volumetric γ-ray source values are simply arranged by the program into the created FIXSRC datafile for each mesh interval in the core.

The SOURCE.PHN program was used to produce a fixed source file for photoneutron production. The γ-ray flux input file (RTFLUX) was generated by either a gamma-ray only or a coupled n-γ ONEDANT calculation. As with the neutron source, the flux values are multiplied by the product $N\sigma_{(\gamma,n)}$ to generate an interaction rate. The number density, N, is the estimated deuterium density in the water region of interest, and $\sigma_{(\gamma,n)}$ is the microscopic cross section for a photon of energy, E, in the range E_1 to E_2 to produce a neutron of energy, E', between E_1' and E_2'. The photoneutron energy was determined with Eq. 2.5. (See Section 2.) The interaction rates for photoneutron production into a given energy interval are converted to the 5 group neutron group structure, and entered by interval into the FIXSRC file format.

The SOURCE.MIX program, as its name implies, creates a new FIXSRC file by adding two existing FIXSRC files or by combining an existing FIXSRC file and a method of source creation described above. This was used to create the core neutron and γ-ray source-input file, and to combine the core and photoneutron sources into a total fixed source file.

A.4.4 CHICALC

The prompt neutron spectrum or $\chi(E)$ values are not included in the ANISN format cross section sets and are required for the XS.ISO format datasets. The $\chi(E)$ values were calculated using the following formula [17A]:

$$\chi(E) = .453\ e^{-1.036E}\ \sinh\ (2.29E)^{1/2} \tag{A.4.9}$$

with the energy given in MeV. The short program, CHICALC, was written to integrate the above function over the group energy intervals specified in the input.

A.4.5 REKINS

The REKINS program was developed and modified by numerous people to solve the following standard reactor kinetics equations under various transient conditions:

$$\frac{dn}{dt} = \frac{n}{\ell^*}(dk-\beta) + \Sigma\ \lambda_i c_i \tag{A.4.10}$$

$$\frac{dc_i}{dt} = \frac{n}{\ell^*}(\beta_i) - \lambda_i c_i$$

where n is the neutron density at time t, with n_0 the initial value, c_i is the delayed neutron precursor densities, ℓ^* is the neutron mean lifetime, and dk is the fractional change in effective multiplication factor given as

$$dk = \frac{k_{eff} - 1}{k_{eff}} \approx k_{eff} - 1 \tag{A.4.11}$$

Because the program has been pieced together and modified for very specific purposes, and there exists a minimal amount of documentation, the input file has been built up to contain a large amount of fixed data which is necessary

to correctly run the program, but is not relevant to the current problem. The data of interest is in the first two lines and lines 45-50 of the input data file.

The program was used to run a simple problem of a linear insertion of reactivity over a specified time interval, after which the neutron population decays. The delayed neutron group fractions, β_i, for the 6 delayed neutron groups are specified in line 1. The corresponding decay constants are given in line 2. The delayed neutron group values for LOFT were taken from the System and Test Description [7A]. The 6 data lines (45-50) are used to define the current problem. This input includes the prompt neutron lifetime, the specification of the time interval over which k_{eff} changes, and the following linear equation which governs the change:

$$\text{TTMK} = \text{TTMKA} + \text{TTMKB} \times \text{time} \tag{A.4.12}$$

where TTMK is the change in the multiplication factor, k, at a given time t, in units of mk/sec, TTMKA is a constant insertion of reactivity, set to 0 in this case, and TTMKB is the slope given as

$$\text{TTMKB} = \frac{k_f - k_0}{t_{int}} \tag{A.4.13}$$

where k_f is the shutdown k, k_0 is the initial k, and t_{int} is the total interval time over which reactivity is inserted.

The input data file also includes the initial power and other factors relating to the power, but these parameters along with the output associated with them were not used. All of the trip switches were disabled. The iteration criteria used were the standard values passed on in the sample data file.

The mean neutron lifetime was taken from the System and Test Description. The reactivity data was calculated using the integral control rod worth for a given rod insertion depth curve and the curve for rod drop time as a function of rod insertion depth [7A]. Initial k was assumed to be 1.0.

Only the first three output data columns were used: time in seconds, percent of initial neutron population initially set as 100, and k-effective.

The fraction, N was used to determine the neutron power or scaled neutron flux for a given time t after shutdown.

COCANE: Program and Input Data

```
1.    //COCANE JOB (,F89305),USER=B89305,CLASS=W,MSGCLASS=W,
2.    //  REGION=500K,TIME=5
3.    //*MAIN ORG=RADS12,LINES=49
4.    // EXEC FTXCLG
5.    //FTX.SYSIN DD *
6.    C*****************************************************
7.    C     COCANE: PROGRAM TO TRANSFER ISOTOPE CROSS SECTION DATA
8.    C             FROM ANISN FORMAT TO XS.ISO FORMAT
9.    C             NEW XS.ISO DATA FILES ARE CREATED EITHER AS A NEW
10.   C             DATASET OR AS A MODIFICATION OF EXISTING DATA FILES
11.   C
12.         IMPLICIT REAL*8 (A-H,O-Z)
13.         REAL*4 A
14.         REAL*8 ISONAM
15.         COMMON /L4/ A(20000),LOCA(500),N10,N11,N12,N13,N14,NGRP,NTRAN,
16.        1NEX,NHT,NGG,NTT,NAB,NFS,NNF,N2N,NGM,NNP,NALF,NISO,MAXUP,
17.        2MAXDN,MAXORD,LREC,LOR1
18.         COMMON /L8/ RNAME(500),ISONAM(500),TEMP(500),TNAME(500),
19.        1AMASS(500),CHI(10,100),CHISO(10,100),E(100),U(100),VEL(100),
20.        2SS(200),EFISS,ECAPT
21.   C
22.   C     ASSIGN I/O VALUES
23.   C           10  ANISN XSECT DATASET
24.   C           11  EXISTING XS.ISO FILE 1
25.   C           12  EXISTING XS.ISO FILE 2
26.   C           13  GENERATED XS.ISO FILE 1
27.   C           14  GENERATED XS.ISO FILE 2
28.   C
29.         N10=10
30.         N11=11
31.         N12=12
32.         N13=13
33.         N14=14
34.      10 FORMAT(12I6)
35.      11 FORMAT(1H ,12I6)
36.      12 FORMAT(6D12.6)
37.      13 FORMAT(1H ,6(3X,D13.6))
38.      14 FORMAT(A6,A6,I6,I6)
39.   C
40.   C     INPUT: BASIC INFORMATION  CARD 1 AND CARD 2
41.   C     CARD 1    (FORMAT 12I6)
42.   C           NGRP=  NUMBER OF GROUPS
43.   C           NTRAN= NUMBER OF MATERIALS BEING TRANSFERED
44.   C           NEX=   EXISTING XS.ISO FLAG (0/1: OLD EXISTS/NEW)
45.   C           NHT=   NUMBER OF POSITIONS PRECEDING SCATTERING XSECTNS
46.   C           NGG=   POSITION OF SELF-SCATTER XSECTN
47.   C           NTT=   POSITION OF TRANSPORT/TOTAL XSECTN
48.   C     CARD 2    (FORMAT 12I6)
49.   C           NAB=   POSITION OF ABSORPTION XSECTN
50.   C           NFS=   POSITION OF FISSION XSECTN
51.   C           N2N=   POSITION OF THE (N-2N) XSECTN
52.   C           NGM=   POSITION OF THE (N-GAMMA) XSECTN
53.   C           NNP=   POSITION OF THE (N-P) XSECTN
54.   C           NALF=  POSITION OF THE (N-ALPHA) XSECTN
55.   C
56.         READ(5,10)NGRP,NTRAN,NEX,NHT,NGG,NTT
57.         WRITE(6,11)NGRP,NTRAN,NEX,NHT,NGG,NTT
58.         READ(5,10)NAB,NFS,N2N,NGM,NNP,NALF
59.         WRITE(6,11)NAB,NFS,N2N,NGM,NNP,NALF
60.         NNF=NAB+1
61.         NGRP1=NGRP+1
62.         NIS=0
63.         MAXUP=0
64.         MAXDN=0
65.         MAXORD=0
66.         IPREC=0
67.         IF(NEX.GT.0)GO TO 450
```

```
68.      C
69.      C     READ EXISTING XS.ISO--FILE 1
70.      C
71.           READ(N11)NGROUP,NISO,MAXUP,MAXDN,MAXORD,IPREC
72.           NISO1=NISO+1
73.           READ(N11)(ISONAM(I),I=1,NISO),(LOCA(I),I=1,NISO1),
74.          1(TEMP(I),I=1,NISO),(TNAME(I),I=1,NISO),(AMASS(I),I=1,NISO)
75.           NGP1=NGROUP+1
76.           READ(N11)ICHI,(E(I),I=1,NGP1),(U(I),I=1,NGP1),(VEL(I),I=1,NGROUP)
77.           IF(ICHI.NE.0)READ(N11)((CHI(I,J),I=1,ICHI),J=1,NGROUP)
78.      C
79.      C     READ EXISTING XS.ISO--FILE 2
80.      C
81.           DO 400 N=1,NISO
82.           NIS=NIS+1
83.           NIS1=NIS+1
84.           READ(N12)RNAME(N)
85.           WRITE(N14)RNAME(N)
86.           READ(N12)JCHI,LIN,LEL,LN2N,EFISS,ECAPT
87.           WRITE(N14)JCHI,LIN,LEL,LN2N,EFISS,ECAPT
88.           MX=MAX0(LIN,LEL,LN2N)
89.           NX=MX-1
90.           IF(NX.GT.MAXORD)MAXORD=NX
91.           IF(JCHI.LE.0)GO TO 150
92.           READ(N12)((CHISO(I,J),I=1,JCHI),J=1,NGROUP)
93.           WRITE(N14)((CHISO(I,J),I=1,JCHI),J=1,NGROUP)
94.      150  CONTINUE
95.      C
96.      C     READ PRINCIPAL CROSS SECTIONS
97.      C
98.           NP=5
99.           IF(JCHI.NE.0)NP=7
100.          DO 175 K=1,NGROUP
101.          READ(N12)KK,(SS(I),I=1,NP)
102.          WRITE(N14)KK,(SS(J),J=1,NP)
103.     175  CONTINUE
104.     C
105.     C     READ SCATTERING ARRAYS
106.     C
107.          DO 350 L=1,MX
108.          DO 325 K=1,NGROUP
109.          LSCAT=LIN+LEL+LN2N
110.          IF(LSCAT.EQ.0)GO TO 190
111.          READ(N12)LINUP,LINDN,LELUP,LELDN,LN2NUP,LN2NDN
112.          WRITE(N14)LINUP,LINDN,LELUP,LELDN,LN2NUP,LN2NDN
113.     190  CONTINUE
114.          NUP=MAX0(LINUP,LELUP,LN2NUP)
115.          NDN=MAX0(LINDN,LELDN,LN2NDN)
116.          IF(NUP.GT.MAXUP)MAXUP=NUP
117.          IF(NDN.GT.MAXDN)MAXDN=NDN
118.          IF(L.GT.LIN)GO TO 220
119.          MAX=LINUP+LINDN+1
120.          READ(N12)(SS(I),I=1,MAX)
121.          WRITE(N14)(SS(J),J=1,MAX)
122.     220  CONTINUE
123.          IF(L.GT.LEL)GO TO 240
124.          MAX=LELUP+LELDN+1
125.          READ(N12)(SS(I),I=1,MAX)
126.          WRITE(N14)(SS(J),J=1,MAX)
127.     240  CONTINUE
128.          IF(L.GT.LN2N)GO TO 260
129.          MAX=LN2NUP+LN2NDN+1
130.          READ(N12)(SS(I),I=1,MAX)
131.          WRITE(N14)(SS(J),J=1,MAX)
132.     260  CONTINUE
133.     325  CONTINUE
134.     350  CONTINUE
135.     400  CONTINUE
```

```
      LAST=LOCA(NISO1)
      GO TO 500
  450 CONTINUE
C
C     XS.ISO IS NEW--READ CHI AND ENERGY BOUNDARIES
C
      NISO=0
      LAST=0
      LOCA(1)=0
      MAXUP=0
      MAXDN=0
      MAXORD=0
      IPREC=0
C
C     INPUT: CHI AND ENERGY GROUP INFORMATION
C     CARD 3   (FORMAT 12I6)
C            ETOP= VALUE OF HIGHEST ENERGY BOUNDARY
C     CARD 4   (FORMAT 6E12.6)
C            ENERGY GROUP BOUNDARIES (NGRP + 1 VALUES)
C     CARD 5   (FORMAT 12I6)
C            ICHI= 0/1/N  NO CHI VALUES/CHI VECTOR/CHI MATRIX DIM=N
C     CARD 6   (FORMAT 6D12.6)
C            CHI VALUES LISTED FOR GROUP 1 TO NGRP
C            FOR EACH DIMENSION, ICHI
C
      READ(5,12)ETOP
      READ(5,12)(E(I),I=1,NGRP1)
      READ(5,10)ICHI
      READ(5,12)((CHI(I,J),I=1,ICHI),J=1,NGRP)
      DO 460 I=1,NGRP1
      U(I)=-DLOG(E(I)/ETOP)
      IF(I.GT.1)VEL(I-1)=2.2D+05*DSQRT((E(I)+E(I-1))/0.0508)
  460 CONTINUE
C
C     LOOP OVER ISOTOPES (MATERIALS) TO BE PLACED ON XS.ISO
C
  500 CONTINUE
      NEXT=1
      NISO=NISO+1
      NI=NISO+1
      WRITE(6,2001)
C
C     INPUT: ISOTOPE INFORMATION
C     CARD 7   (FORMAT 2A6,2I6)
C            XNAM   XS.ISO NAME
C            ENDNAM NAME ON ENDF/B DATSET
C            LSO    ISOTOPE NUMBER FOR THE ANISN DATASET
C                   NOTE: THIS IS NOT THE ANISN MATERIAL NUMBER
C            LORD   LEGENDRE ORDER
C                   NOTE: LSO=MATERIAL NUMBER (MOD (LORD+1))
C     CARD 8    (FORMAT 6D12.6)
C            TEM    ISOTOPE TEMPERATURE
C            AMAS   ATOMIC MASS
C            EFIS   ENERGY RELEASED PER FISSION (UNITS MEV)
C            ECAP   ENERGY RELEASED PER CAPTURE (N,GAMMA) (MEV)
C                      (UNITS OF MEV--WILL BE TRANSFERRED TO WATTS)
C
      DO 800 II=1,NTRAN
      READ(5,14)XNAM,ENDNAM,LSO,LORD
      LOR1=LORD+1
      READ(5,12)TEM,AMAS,EFIS,ECAP
      TEMP(NISO)=TEM
      TNAME(NISO)=ENDNAM
      AMASS(NISO)=AMAS
      EFISS=EFIS*1.60203E-13
      ECAPT=ECAP*1.60203E-13
      ISONAM(NISO)=XNAM
      RNAME(NISO)=XNAM
```

```
      550 CONTINUE
          IF(LSO.EQ.NEXT)GO TO 600
C
C     SKIP REMAINING RECORDS FOR THIS MATERIAL
C
          DO 575 L=1,LOR1
          READ(N10)K1,K2,K3,K4
          WRITE(6,11)K1,K2,K3,K4,LORD,LOR1,LSO
          READ(N10)
      575 CONTINUE
          NEXT=NEXT+1
          GO TO 550
      600 CONTINUE
C
C     ISOTOPE TO BE ADDED TO XS.ISO
C
          CALL FILE2
          NEXT=NEXT+1
          WRITE(6,2002)II,LSO,NISO,XNAM
     2001 FORMAT(1H1,5X,20HMATERIAL TRANSFERRED,5X,20HNUMBER ON ANISN TAPE,
         19X,16HNUMBER ON XS.ISO,11X,14HNAME ON XS.ISO)
     2002 FORMAT(1H ,3(20X,I5),19X,A6)
          LAST=LAST+LREC
          LOCA(NI)=LAST
          NISO=NISO+1
          NI=NISO+1
      800 CONTINUE
          END FILE N14
          NISO=NISO-1
          NISO1=NISO+1
C
C     WRITE FILE 1 OF XS.ISO
C
          NGROUP=NGRP
          WRITE(N13)NGROUP,NISO,MAXUP,MAXDN,MAXORD,IPREC
          WRITE(N13)(ISONAM(I),I=1,NISO),(LOCA(I),I=1,NISO1),
         1(TEMP(I),I=1,NISO),(TNAME(I),I=1,NISO),(AMASS(I),I=1,NISO)
          NGP1=NGROUP+1
          WRITE(N13)ICHI,(E(I),I=1,NGP1),(U(I),I=1,NGP1),(VEL(I),I=1,NGROUP)
          IF(ICHI.NE.0)WRITE(N13)((CHI(I,J),I=1,ICHI),J=1,NGROUP)
          END FILE N13
          STOP
          END
          SUBROUTINE FILE2
          IMPLICIT REAL*8 (A-H,O-Z)
          REAL*4 A
          REAL*8 ISONAM
          COMMON /L4/ A(20000),LOCA(500),N10,N11,N12,N13,N14,NGRP,NTRAN,
         1NEX,NHT,NGG,NTT,NAB,NFS,NNF,N2N,NGM,NNP,NALF,NISO,MAXUP,
         2MAXDN,MAXORD,LREC,LOR1
          COMMON /L8/ RNAME(500),ISONAM(500),TEMP(500),TNAME(500),
         1AMASS(500),CHI(10,100),CHISO(10,100),E(100),U(100),VEL(100),
         2SS(200),EFISS,ECAPT
       11 FORMAT(1H ,12I6)
          DO 500 L=1,LOR1
CC        LEN=200
CC        CALL RESET8(SS,LEN)
CC        LEN=20000
CC        CALL RESET4(A,LEN)
C
C     ZEROTH ORDER COMPONENT
C
          ZERO=0.0
          MAX=LOR1-1
          IF(MAX.GT.MAXORD)MAXORD=MAX
          LEL=0
          LN2N=0
          LIN=LOR1
```

```
      JCHI=0
      READ(N10)K1,K2,K3,K4
      LENGTH=K1*K2
      ITL=LENGTH/NGRP
      WRITE(6,11)K1,K2,K3,K4,MAX,LOR1,LENGTH,ITL
      READ(N10)(A(J),J=1,LENGTH)
      IF(L.GT.1)GO TO 100
      IF(A(NNF).NE.ZERO)JCHI=-1
      WRITE(N14)XNAM
      WRITE(N14)JCHI,LIN,LEL,LN2N,EFISS,ECAPT
      IF(JCHI.GT.0)WRITE(N14)((CHISO(I,J),I=1,JCHI),J=1,NGRP)
C
C     PRINCIPAL CROSS SECTIONS
C
      NP=7
      IF(JCHI.EQ.0)NP=5
      DO 75 N=1,NGRP
      LC=(N-1)*ITL
      DO 20 I=1,7
      SS(I)=0.0
   20 CONTINUE
      SS(1)=A(LC+NTT)
      SS(7)=A(LC+NNF)
      IF(NALF.GT.0)SS(3)=A(LC+NALF)
      IF(NNP.GT.0)SS(4)=A(LC+NNP)
      IF(NFS.GT.0)SS(6)=A(LC+NFS)
      IF(NGM.GT.0)GO TO 30
      SS(2)=A(LC+NAB)-SS(4)-SS(6)-SS(3)
      GO TO 40
   30 CONTINUE
      SS(2)=A(LC+NGM)
      IF(N2N.GT.0)SS(2)=SS(2)-A(LC+N2N)
   40 CONTINUE
      WRITE(N14)N,(SS(I),I=1,NP)
   75 CONTINUE
      LREC=NGRP+2
      IF(JCHI.GT.0)LREC=LREC+1
C
C     WRITE SCATTERING CROSS SECTIONS INTO INELASTIC ARRAY
C
  100 CONTINUE
      FL=FLOAT(L)
      F=1.0/(2.0*FL-1.0)
C        NOTE: THE 2L+1 FACTOR IS REMOVED FROM THE SCATTERING XSECTNS
      LELUP=0
      LELDN=0
      LN2NUP=0
      LN2NDN=0
C
C     DETERMINE LINUP AND LINDN FOR PRESENT GROUP
C
      DO 300 N=1,NGRP
      LC=(N-1)*ITL
      LINDN=ITL-NGG
      LL=LINDN
      IF(LL.EQ.0)GO TO 175
      DO 125 I=1,LL
      J=ITL-I+1
      IF(A(LC+J).NE.ZERO)GO TO 175
      LINDN=LINDN-1
  125 CONTINUE
  175 CONTINUE
      LC=LC+NHT
      LINUP=NGG-NHT-1
      LL=LINUP
      IF(LL.LE.0)GO TO 225
      DO 200 I=1,LL
      IF(A(LC+I).NE.ZERO)GO TO 225
```

```
339.            LINUP=LINUP-1
340.          200 CONTINUE
341.          225 CONTINUE
342.            NUMBER=LINDN+LINUP+1
343.            NSTART=NGG-LINUP+(N-1)*ITL-1
344.            DO 250 I=1,NUMBER
345.            SS(I)=F*A(NSTART+I)
346.          250 CONTINUE
347.            IF(LINUP.GT.MAXUP)MAXUP=LINUP
348.            IF(LINDN.GT.MAXDN)MAXDN=LINDN
349.        C
350.            WRITE(N14)LINUP,LINDN,LELUP,LELDN,LN2NUP,LN2NDN
351.            WRITE(N14)(SS(I),I=1,NUMBER)
352.          300 CONTINUE
353.            LREC=LREC+2*NGRP
354.          500 CONTINUE
355.            RETURN
356.            END
357.            SUBROUTINE RESET8(S,LEN)
358.            IMPLICIT REAL*8 (A-H,O-Z)
359.            DIMENSION S(LEN)
360.            DO 100 I=1,LEN
361.            S(I)=0.0
362.          100 CONTINUE
363.            RETURN
364.            END
365.            SUBROUTINE RESET4(S,LEN)
366.            DIMENSION S(LEN)
367.            DO 100 I=1,LEN
368.            S(I)=0.0
369.          100 CONTINUE
370.            RETURN
371.            END
372.        /*
373.        //GO.FT10F001 DD DSN=B89305.XSECT.COLLBUGL.ANISN,DISP=SHR
374.        //GO.FT13F001 DD DSN=B89305.XSECT.COLLBUGL.XSISO1,DISP=SHR,
375.        //  UNIT=ALLPERM,VOL=SER=,SPACE=(TRK,(1,1),RLSE),
376.        //  DCB=(RECFM=VBS,LRECL=X,BLKSIZE=6356)
377.        //GO.FT14F001 DD DSN=B89305.XSECT.COLLBUGL.XSISO2,DISP=SHR,
378.        //  UNIT=ALLPERM,VOL=SER=,SPACE=(TRK,(100,20),RLSE),
379.        //  DCB=(RECFM=VBS,LRECL=X,BLKSIZE=6356)
380.        //GO.SYSIN DD *
381.             25    23     1     3     4     3
382.              1     2     0     0     0     0
383.          1.73330E+07
387.          1.73330E+07 8.20850E+05 7.10170E+03 1.85540E+00 1.00000E-01 1.40000E+07
392.          1.00000E+07 8.00000E+06 7.00000E+06 6.00000E+06 5.00000E+06 4.00000E+06
393.          3.00000E+06 2.00000E+06 1.50000E+06 1.00000E+06 8.00000E+05 7.00000E+05
394.          6.00000E+05 4.00000E+05 2.00000E+05 1.00000E+05 6.00000E+04 3.00000E+04
395.          2.00000E+04 1.00000E+04
396.              1
403.          .754133E-00 .246777E-00 2.72315E-04 0.0         0.0         0.0
404.          0.0         0.0         0.0         0.0         0.0         0.0
405.          0.0         0.0         0.0         0.0         0.0         0.0
406.          0.0         0.0         0.0         0.0         0.0         0.0
408.          0.0
409.        H-H--1H    4     1     3
410.                500.0       1.0087          0.0         2.20
410.3       H-H--6H    4     2     3
410.4               500.0       1.0087          0.0         2.20
411.        B-B101B    4     3     3
412.                500.0      10.8110          0.0        10.01
413.        O-O--10-16 4     4     3
414.                600.0      15.9900          0.0         3.38
414.3       O-O--60-16 4     5     3
414.4               600.0      15.9900          0.0         3.38
```

```
415.     CRCR-5CR   4     6     3
416.           500.0     51.9960          0.0          9.29
416.3    CRCR-9CR   4     7     3
416.35         500.0     51.9960          0.0          9.29
416.4    CRCR13CR   4     8     3
416.45         500.0     51.9960          0.0          9.29
416.7    MNMN-5MN55 4     9     3
416.75         500.0     54.9380          0.0          6.80
417.     MNMN-9MN55 4    10     3
418.           500.0     54.9380          0.0          6.80
418.3    MNMN13MN55 4    11     3
418.4          500.0     54.9380          0.0          6.80
420.7    FEFE-5FE   4    12     3
420.75         500.0     55.8470          0.0          7.80
423.     FEFE-9FE   4    13     3
424.           500.0     55.8470          0.0          7.80
424.3    FEFE13FE   4    14     3
424.4          500.0     55.8470          0.0          7.80
425.     NINI-5NI   4    15     3
426.           500.0     58.7100          0.0          8.53
426.3    NINI-9NI   4    16     3
426.4          500.0     58.7100          0.0          8.53
426.5    NINI13NI   4    17     3
426.6          500.0     58.7100          0.0          8.53
427.     ZRZR-1ZR   4    18     3
428.          1000.0     91.2200          0.0          6.54
429.     U-2351U-235S    19     3
430.          1000.0    235.0400        192.90         6.54
431.     U-2381U-238S    20     3
432.          1000.0    238.0300        193.9          5.69
432.1    C-C--9C-12 4    21     3
432.2          500.0     12.0111          0.0          4.95
432.3    SISI-9SI   4    22     3
432.4          500.0     28.0860          0.0          8.50
434.1    MOMO-9MO   4    23     3
434.2          500.0     95.9400          0.0          8.79
449.     /*
450.     /* END OF FILE
```

COLLAPSE: Program and Input Data

```
1.    //COLLAFSE JOB (,F89305),USER=B89305,CLASS=W,MSGCLASS=W,
2.    //  REGION=1200K,TIME=6
3.    //*MAIN ORG=RADS12,LINES=49
3.5   //*FORMAT PR,DDNAME=,DEST=3800
4.    // EXEC FTXCLG
5.    //FTX.SYSIN DD *
6.    C     ****** PROGRAM COLLAFSE ******
7.    C
8.    C     COLLAPSE SPATIALLY COLLAPSES ISOTOPES OVER SPECIFIED REGIONS.  IT
9.    C     IS BASED ON COCOCO/COCOCO2 AND IS WRITTEN WITH THE VIEW OF BEING
10.   C     FOLLOWED BY COCANE TO CONVERT TO AN XS.ISO
11.   C
12.   C     MAXIMUM VALUES FOR VARIOUS PARAMETERS
13.   C
14.   C     NFGP     100
15.   C     NBGP     100
16.   C     NISH     200
17.   C     NISO     800
18.   C     NZONE     25
19.   C     JHT       10
20.   C     ITL      111
21.   C     MTL      111
22.   C
23.         REAL*8 STR(50,100),PHIVLF(200,100),PHIVOL(200,100)
24.         COMMON /IPAR/ NZNR(2000),IFGP(100),KUP(100),KDN(100),
25.        1ISN,ISC,NFL,IXX,JHT,NTT,NNF,NAB,NFS,N2N,NGM,NNP,NALF,NFGP,
26.        2NBGP,NISO,IGEOM,IGG,IDIF,NFLG,ITL,MGG,MTL,MUP,MDN,ISO,
27.        3KSCT,IGM,NPOS,IXSTR,MCUT,LENGTH,KMAT,NREG
28.         DATA STR/5000*0.0/,PHIVLF/20000*0.0/,PHIVOL/20000*0.0/
29.   C
30.   C     ASSIGN DEFAULT LOGICAL UNITS
31.   C     ISN--ORIGINAL (UNCOLLAPSED) ANISN/AMPX CROSS SECTION SET
32.   C     ISC--OUTPUT COLLAPSED ANISN/AMPXS CROSS SECTION SET
33.   C     NGE--GEODST (DIF3D/ONEDANT) GEOMETRY FILE
34.   C     NFL--RTFLUX (DIF3D/ONEDANT) FLUX FILE
35.   C     MXS--COMPXS (DIF3D) MACROSCOPIC CROSS SECTION SET--USED ONLY
36.   C               FOR TRAVELLI WEIGHTING OPTION
37.   C
38.         READ(5,10)ISN,ISC,NGE,NFL,MXS
39.         IF(ISN.LT.1)ISN=10
40.         IF(ISC.LT.1)ISC=11
41.         IF(NGE.LT.1)NGE=12
42.         IF(NFL.LT.1)NFL=13
43.         IF(MXS.LT.1)MXS=14
44.      10 FORMAT(12I6)
45.      11 FORMAT(1H ,12I6)
46.      12 FORMAT(6E12.5)
47.      13 FORMAT(1H ,6(3X,E13.6))
48.      14 FORMAT(1H )
49.   C
50.   C     ***** ASSIGN DEFAULT VALUES FOR CROSS SECTION POSITIONS
51.         KMAT=0
52.         JHT=8
53.         NTT=8
54.         NNF=7
55.         NAB=6
56.         NFS=5
57.         N2N=1
58.         NGM=2
```

```
      NNP=4
      NALF=3
CCCCCC SET UPSCATTERING CUTOFF AT LAST FAST BROAD GROUP
      MCUT=14
C
C
      READ(5,10)NFGP,NBGP,NISO,IGEOM,IDIF,NPOS,NFLG,IGG,MCUT
      IF(NPOS.LE.0)GO TO 100
      READ(5,10)JHT,NTT,NNF,NAB,NFS,N2N,NGM,NNP,NALF,IXSTR
  100 CONTINUE
      READ(5,10)(IFGP(I),I=1,NFGP)
      KSCT=JHT+1
      IDIF=IDIF+1
C
      CALL PSTN
      CALL EDIT
      CALL GEODST(PHIVLF,PHIVOL,NGE)
C
      IF(IDIF.LT.3)GO TO 120
C
      CALL COMPXS(STR,MXS)
      GO TO 140
C
  120 CONTINUE
  140 CONTINUE
      NEXT=0
      DO 800 N=1,NISO
      READ(5,10)IDAN,LORD,KREG,MULT
      LOR1=LORD+1
      IF (MULT.GT.0) GO TO 475
  400 CONTINUE
      NEXT=NEXT+1
      IF(IDAN.EQ.NEXT)GO TO 500
C
C     SKIP REMAINING RECORDS FOR THIS MATERIAL
C
      DO 450 L=1,LOR1
      READ(ISN)K1,K2,K3,K4
      WRITE(6,11)K1,K2,K3,K4,LORD,LOR1,IDAN
      READ(ISN)
  450 CONTINUE
      GO TO 400
  475 CONTINUE
C
C     REPOSITION POINTER FOR MATERIAL (MULT GT 0)
C
      REWIND ISN
      IF(IDAN.EQ.1) GO TO 500
      IDN=(IDAN-1)*4
  480 CONTINUE
      READ (ISN) K1,K2,K3,IDMAT
      READ (ISN)
      IF(IDMAT.EQ.IDN) GO TO 500
      GO TO 480
  500 CONTINUE
C
C     ISOTOPE (MATERIAL) IS TO BE COLLAPSED
C
      CALL CLPSE(PHIVLF,PHIVOL,LORD,KREG,MULT)
  800 CONTINUE
```

```
      STOP
      END
      SUBROUTINE EDIT
      COMMON /IPAR/ NZNR(2000),IFGP(100),KUP(100),KDN(100),
     1ISN,ISC,NFL,IXX,JHT,NTT,NNF,NAB,NFS,N2N,NGM,NNP,NALF,NFGP,
     2NBGP,NISO,IGEOM,IGG,IDIF,NFLG,ITL,MGG,MTL,MUP,MDN,ISO,
     3KSCT,IGM,NPOS,IXSTR,MCUT,LENGTH,KMAT,NREG
C
      WRITE(6,1000)
 1000 FORMAT(1H1,50X,'****** PROGRAM COLLAPSE ******'///)
C
      WRITE(6,1001)NFGP,NBGP,NISO
 1001 FORMAT(1X,'NFGP',I5,' NUMBER OF GROUPS ON INITIAL X-S SET',
     X      /1X,'NBGP',I5,' NUMBER OF GROUPS ON COLLAPSED X-S SET',
     X      /1X,'NISO',I5,' NUMBER OF ISOTOPES PLACED ON COLLAPSED SET')
C
      JDIF=IDIF-1
      WRITE(6,1002)IGEOM,IGG,NFL,NPOS,JDIF,NFLG
 1002 FORMAT(1X,'IGEOM',I4,' 1/2/3 PLANE/CYLINDRICAL/SPHERICAL GEOM.',
     X      /1X,'IGG',I6,' POSITION OF SELF-SCATTER ON INITIAL X-S SET',
     X      /1X,'NFL',I5,' LU-- ONEDANT/DIF3D RTFLUX DATASET',
     X      /1X,'NPOS',I5,' 0/1 STANDARD/INPUT X-S POSITIONS',
     X      /1X,'IDIF',I5,' 0/1/2/3 FLUX/INVERSE-FLUX/INVERSE-MACRO/TRAV
     XELLI  WEIGHTING FOR TRANSPORT X-S COLLAPSE',
     X      /1X,'NFLG',I5,' 0/1 INPUT/COMPXS MACRO TRANSPORT X-S'/)
C
      WRITE(6,1003)JHT,NTT,NNF,NAB,NFS,N2N,NGM,NNP,NALF
 1003 FORMAT(1X,'JHT',I6,' NUMBER OF POSITIONS PRECEDING SCATTER X-S',
     X      /1X,'NTT',I6,' POSITION OF TOTAL/TRANSPORT X-S',
     X      /1X,'NNF',I6,' POSITION OF NU*FISSION X-S',
     X      /1X,'NAB',I6,' POSITION OF ABSORPTION X-S',
     X      /1X,'NFS',I6,' POSITION OF FISSION X-S',
     X      /1X,'N2N',I6,' POSITION OF N-2N X-S',
     X      /1X,'NGM',I6,' POSITION OF RADIATIVE CAPTURE X-S',
     X      /1X,'NNP',I6,' POSITION OF N-PROTON X-S',
     X      /1X,'NALF',I5,' POSITION OF N-ALPHA X-S'/)
C
      WRITE(6,1004)MGG,MTL
 1004 FORMAT(1X,'MGG',I6,' POSITION OF SELF SCATTER ON COLLAPSED ANISN S
     XET',  /1X,'MTL',I6,' TABLE LENGTH OF COLLAPSED ANISN SET'///)
C
      RETURN
      END
      SUBROUTINE PSTN
      COMMON /IPAR/ NZNR(2000),IFGP(100),KUP(100),KDN(100),
     1ISN,ISC,NFL,IXX,JHT,NTT,NNF,NAB,NFS,N2N,NGM,NNP,NALF,NFGP,
     2NBGP,NISO,IGEOM,IGG,IDIF,NFLG,ITL,MGG,MTL,MUP,MDN,ISO,
     3KSCT,IGM,NPOS,IXSTR,MCUT,LENGTH,KMAT,NREG
C
C     COMPUTES THE NUMBER OF POSITIONS,MTL, AND THE POSITION OF
C     SELF-SCATTER IN THE COLLAPSED CROSS SECTION SET
C
      READ(ISN)K1,K2
      LENGTH=K1*K2
      ITL=LENGTH/NFGP
      BACKSPACE ISN
      MTL=ITL
      MGG=IGG
      MDN=MTL-MGG
      MUP=MTL-JHT-MDN-1
```

```
      C
            DO 130 IG=1,NFGP
            KUP(IG)=0
            KDN(IG)=0
            MG=IFGP(IG)
      CCCCC CHECK THE UPSCATTERING LIMIT
            IF(MG.LE.MCUT) GO TO 120
            IF(MUP.EQ.0) GO TO 120
            DO 115 J=1,MUP
            JG=IG+J
            IF(JG.GT.NFGP) GO TO 115
            NG=IFGP(JG)
            K=NG-MG
            IF(K.GT.KUP(IG)) KUP(IG)=K
          115 CONTINUE
          120 CONTINUE
      C
            MG=IFGP(IG)
            IF(MDN.EQ.0) GO TO 130
            DO 125 J=1,MDN
            JG=IG-J
            IF(JG.LE.0) GO TO 125
            NG=IFGP(JG)
            K=MG-NG
            IF(K.GT.KDN(IG)) KDN(IG)=K
          125 CONTINUE
          130 CONTINUE
      C
            MUP=0
            MDN=0
            DO 135 IG=1,NFGP
            IF(KUP(IG).GT.MUP) MUP=KUP(IG)
            IF(KDN(IG).GT.MDN) MDN=KDN(IG)
          135 CONTINUE
      C
            IGG=MGG
            MGG=JHT+MUP+1
            MTL=MGG+MDN
            RETURN
            END
            SUBROUTINE GEODST(PHIVLF,PHIVOL,NG)
            REAL*8 FL(200,100),XMESH(300),YMESH(300),ZMESH(300),HUSE(2),HNAME
            REAL*8 PHIVLF(200,100),PHIVOL(200,100)
            COMMON /IPAR/ NZNR(2000),IFGP(100),KUP(100),KDN(100),
           1ISN,ISC,NFL,IXX,JHT,NTT,NNF,NAB,NFS,NZN,NGM,NNP,NALF,NFGP,
           2NBGP,NISO,IGEOM,IGG,IDIF,NFLG,ITL,MGG,MTL,MUP,MDN,ISO,
           3KSCT,IGM,NPOS,IXSTR,MCUT,LENGTH,KMAT,NREG
            DIMENSION VOL(200,100,2),VOLR(2000),BSQ(2000),BNDC(2000),
           1BNCI(2000),XB(300),YB(300),ZB(300),XM(300),YM(300),ZM(300)
            DIMENSION MC(200,100),MR(200,100),IFINTS(300),JFINTS(300),
           1KFINTS(300),NZHBB(2000),NZC(2000),NGOP(5)
            DATA VOL/40000*0.0/,VOLR/2000*0.0/,BSQ/2000*0.0/,
           1BNDC/2000*0.0/,BNCI/2000*0.0/
            DATA XMESH/300*0.0/,YMESH/300*0.0/,ZMESH/300*0.0/,
           1XB/300*0.0/,YB/300*0.0/,ZB/300*0.0/,XM/300*0.0/,YM/300*0.0/,
           2ZM/300*0.0/
            DATA MC/20000*0/,MR/20000*0/,IFINTS/300*0/,JFINTS/300*0/,
           1KFINTS/300*0/,NZHBB/2000*0/,NZC/2000*0/,
           2NGOP/5*0/
      C
```

```
227.      C     READ GEODST FILE
228.      C
229.            READ (NG) HNAME,(HUSE(I),I=1,2),IVERS
230.            READ (NG) IGOM,NZONE,NREG,NZCL,NCINTI,NCINTJ,NCINTK,NINTI,NINTJ,
231.           1 NINTK,IMB1,IMB2,JMB1,JMB2,KMB1,KMB2,NBS,NBCS,NIBCS,NZHBB,NTRIAG,
232.           2 NRASS,NTHPT,(NGOP(I),I=1,4)
233.            NCBNDI=NCINTI+1
234.            IF (IGOM.GT.0.AND.IGOM.LE.3) READ (NG) (XMESH(I),I=1,NCBNDI),
235.           1 (IFINTS(J),J=1,NCINTI)
236.            NCBNDJ=NCINTJ+1
237.            IF (IGOM.GE.6.AND.IGOM.LE.11) READ (NG) (XMESH(I),I=1,NCBNDI),
238.           1 (YMESH(J),J=1,NCBNDJ),(IFINTS(K),K=1,NCINTI),(JFINTS(L),L=1,
239.           2 NCINTJ)
240.            NCBNDK=NCINTK+1
241.            IF (IGOM.GE.12) READ (NG) (XMESH(I),I=1,NCBNDI),(YMESH(J),J=1,
242.           1NCBNDJ),(ZMESH(K),K=1,NCBNDK),(IFINTS(L),L=1,NCINTI),(JFINTS(KK),
243.           2KK=1,NCINTJ),(KFINTS(N),N=1,NCINTK)
244.            IF (NZHBB.EQ.0) GO TO 110
245.            IF (IGOM.GT.0.OR.NBS.GT.0) READ (NG) (VOLR(N),N=1,NREG),(BSQ(N),
246.           1 N=1,NBS),(BNDC(N),N=1,NBCS),(BNCI(N),N=1,NIBCS),(NZHBB(N),N=1,
247.           2 NZHBB),(NZC(N),N=1,NZONE),(NZNR(N),N=1,NREG)
248.            GO TO 120
249.          110 CONTINUE
250.            IF (IGOM.GT.0.OR.NBS.GT.0) READ (NG) (VOLR(N),N=1,NREG),(BSQ(N),
251.           1 N=1,NBS),(BNDC(N),N=1,NBCS),(BNCI(N),N=1,NIBCS),(NZC(N),N=1,
252.           2 NZONE),(NZNR(N),N=1,NREG)
253.          120 CONTINUE
254.            IF(IGOM.LE.0.OR.NRASS.NE.0)GO TO 250
255.            DO 200 K=1,NINTK
256.            READ(NG)((MC(I,J),I=1,NCINTI),J=1,NCINTJ)
257.          200 CONTINUE
258.            GO TO 400
259.          250 CONTINUE
260.            IF(IGOM.LE.0.OR.NRASS.EQ.0)GO TO 400
261.            DO 350 K=1,NINTK
262.            READ(NG)((MC(I,J),I=1,NINTI),J=1,NINTJ)
263.          350 CONTINUE
264.          400 CONTINUE
265.      C
266.      C     COMPUTE MR ARRAY
267.      C
268.            IF(IGEOM.LT.4)GO TO 500
269.            J=0
270.            DO 460 J1=1,NCINTJ
271.            JJJ=JFINTS(J1)
272.            DO 450 J2=1,JJJ
273.            J=J+1
274.            I=0
275.            DO 440 I1=1,NCINTI
276.            III=IFINTS(I1)
277.            DO 430 I2=1,III
278.            I=I+1
279.            MR(I,J)=MC(I1,J1)
280.          430 CONTINUE
281.          440 CONTINUE
282.          450 CONTINUE
283.          460 CONTINUE
284.            GO TO 550
285.          500 CONTINUE
286.            I=0
```

```
      DO 520 I1=1,NCINTI
      III=IFINTS(I1)
      DO 510 I2=1,III
      I=I+1
      MR(I,1)=MC(I1,1)
  510 CONTINUE
  520 CONTINUE
  550 CONTINUE
C
C     COMPUTE MESH INTERVAL BOUNDARIES AND VOLUMES
C
      XB(1)=0.0
      J=1
      DO 580 I=1,NCINTI
      DELTAI=(XMESH(I+1)-XMESH(I))/FLOAT(IFINTS(I))
      KKK=IFINTS(I)
      DO 570 K=1,KKK
      J=J+1
      XM(J-1)=XB(J-1)+DELTAI/2.0
  570 XB(J)=XB(J-1)+DELTAI
  580 CONTINUE
      NINTIF=NINTI+1
      WRITE(6,3001)NINTIF
      WRITE(6,3005)
 3001 FORMAT(1H1,2X,'XB',I5,' X MESH INTERVAL BOUNDARIES')
 3002 FORMAT(1H1,2X,'YB',I5,' Y MESH INTERVAL BOUNDARIES')
 3003 FORMAT(1H1,2X,'ZB',I5,' Z MESH INTERVAL BOUNDARIES')
 3004 FORMAT(1H ,6(1X,I4,1X,1PD14.7))
 3005 FORMAT(1H )
      WRITE(6,3004)(I,XB(I),I=1,NINTIF)
      IF(IGEOM.LT.4)GO TO 670
      YB(1)=0.0
      J=1
      DO 630 I=1,NCINTJ
      DELTAJ=(YMESH(I+1)-YMESH(I))/FLOAT(JFINTS(I))
      KKK=JFINTS(I)
      DO 620 K=1,KKK
      J=J+1
      YM(J-1)=YB(J-1)+DELTAJ/2.0
  620 YB(J)=YB(J-1)+DELTAJ
  630 CONTINUE
      NINTJF=NINTJ+1
      WRITE (6,3002) NINTJF
      WRITE(6,3005)
      WRITE(6,3004)(J,YB(J),J=1,NINTJF)
      IF(IGEOM.LT.7)GO TO 670
      ZB(1)=0.0
      J=1
      DO 660 I=1,NCINTK
      DELTAK=(ZMESH(I+1)-ZMESH(I))/FLOAT(KFINTS(I))
      KKK=KFINTS(I)
      DO 650 K=1,KKK
      J=J+1
      ZM(J-1)=ZB(J-1)+DELTAK/2.0
  650 ZB(J)=ZB(J-1)+DELTAK
  660 CONTINUE
      NINTKF=NINTK+1
      WRITE(6,3003)NINTKF
      WRITE(6,3005)
      WRITE(6,3004)(K,ZB(K),K=1,NINTKF)
```

```
347.       670 CONTINUE
348.           PI=3.141592654
349.           IF(IGEOM.GT.1)GO TO 750
350.     C     SLAB
351.           DO 720 I=1,NINTI
352.           VOL(I,1,1)=XB(I+1)-XB(I)
353.       720 CONTINUE
354.           GO TO 2500
355.       750 CONTINUE
356.           IF(IGEOM.GT.2)GO TO 850
357.     C     CYLINDER
358.           DO 800 I=1,NINTI
359.           RI=XB(I)
360.           RO=XB(I+1)
361.           VOL(I,1,1)=PI*(RO*RO-RI*RI)
362.       800 CONTINUE
363.           GO TO 2500
364.       850 CONTINUE
365.           IF(IGEOM.GT.3)GO TO 950
366.     C     SPHERE
367.           DO 900 I=1,NINTI
368.           RI=XB(I)
369.           RO=XB(I+1)
370.           VOL(I,1,1)=(4.0*PI/3.0)*(RO*RO*RO-RI*RI*RI)
371.       900 CONTINUE
372.           GO TO 2500
373.       950 CONTINUE
374.           IF(IGEOM.GT.4)GO TO 1050
375.     C     XY
376.           DO 1000 J=1,NINTJ
377.           YL=YB(J)
378.           YU=YB(J+1)
379.           DO 980 I=1,NINTI
380.           XL=XB(I)
381.           XU=XB(I+1)
382.           VOL(I,J,1)=(XU-XL)*(YU-YL)
383.       980 CONTINUE
384.      1000 CONTINUE
385.           GO TO 2500
386.      1050 CONTINUE
387.           IF(IGEOM.GT.5)GO TO 1150
388.     C     RZ
389.           DO 1100 J=1,NINTJ
390.           ZL=YB(J)
391.           ZU=YB(J+1)
392.           DO 1080 I=1,NINTI
393.           RI=XB(I)
394.           RO=XB(I+1)
395.           VOL(I,J,1)=PI*(RO*RO-RI*RI)*(ZU-ZL)
396.      1080 CONTINUE
397.      1100 CONTINUE
398.           GO TO 2500
399.      1150 CONTINUE
400.           IF(IGEOM.GT.6)GO TO 1250
401.     C     R-THETA
402.           DO 1200 J=1,NINTJ
403.           THETA=YB(J+1)-YB(J)
404.           DO 1180 I=1,NINTI
405.           RI=XB(I)
406.           RO=XB(I+1)
```

```
      VOL(I,J,1)=PI*(RO*RO-RI*RI)*(THETA/(2.0*PI))
 1180 CONTINUE
 1200 CONTINUE
      GO TO 2500
 1250 CONTINUE
      IF(IGEOM.GT.7)GO TO 1350
C     XYZ
      DO 1310 K=1,NINTK
      ZL=ZB(K)
      ZU=ZB(K+1)
      DO 1290 J=1,NINTJ
      YL=YB(J)
      YU=YB(J+1)
      DO 1270 I=1,NINTI
      XL=XB(I)
      XU=XB(I+1)
      VOL(I,J,K)=(XU-XL)*(YU-YL)*(ZU-ZL)
 1270 CONTINUE
 1290 CONTINUE
 1310 CONTINUE
      GO TO 2500
 1350 CONTINUE
      IF(IGEOM.GT.8)GO TO 2500
C     R-THETA-Z
      DO 1410 K=1,NINTK
      ZL=ZB(K)
      ZU=ZB(K+1)
      DO 1390 J=1,NINTJ
      THETA=YB(J+1)-YB(J)
      DO 1370 I=1,NINTI
      RI=XB(I)
      RO=XB(I+1)
      VOL(I,J,K)=PI*(RO*RO-RI*RI)*(ZU-ZL)*(THETA/(2.0*PI))
 1370 CONTINUE
 1390 CONTINUE
 1410 CONTINUE
 2500 CONTINUE
C     READ RTFLUX FILE
      READ(NFL)HNAME,(HUSE(I),I=1,2),IVERS
      READ(NFL)NDIM,NGROUP,NINTI,NINTJ,NINTK,ITER,EFFK,POWER,NBLOK
      IF(NDIM.NE.1)GO TO 2600
      DO 2520 M=1,NBLOK
      JL=(M-1)*((NGROUP-1)/NBLOK+1)+1
      JUP=M*((NGROUP-1)/NBLOK+1)
      JU=MIND(NGROUP,JUP)
      READ(NFL)((FL(I,J),I=1,NINTI),J=JL,JU)
 2520 CONTINUE
C     INTEGRATE FLUX OVER VOLUME
      DO 2560 L=1,NGROUP
      DO 2540 I=1,NINTI
      NR=MR(I,1)
      PHIVLF(NR,L)=PHIVLF(NR,L)+FL(I,L)*VOL(I,1,1)
 2540 CONTINUE
 2560 CONTINUE
      GO TO 2700
 2600 CONTINUE
      IF(NDIM.LT.2)GO TO 2700
      DO 2670 L=1,NGROUP
      DO 2650 K=1,NINTK
      DO 2630 M=1,NBLOK
```

```
      JL=(M-1)*((NINTJ-1)/NBLOK+1)+1
      JUP=M*((NINTJ-1)/NBLOK+1)
      JU=MIN0(NINTJ,JUP)
      READ(NFL)((FL(I,J),I=1,NINTI),J=JL,JU)
 2630 CONTINUE
C     INTEGRATE FLUX OVER VOLUME
      DO 2645 J=1,NINTJ
      DO 2640 I=1,NINTI
      NR=MR(I,J)
      PHIVLF(NR,L)=PHIVLF(NR,L)+FL(I,J)*VOL(I,J,K)
 2640 CONTINUE
 2645 CONTINUE
 2650 CONTINUE
 2670 CONTINUE
 2700 CONTINUE
C     CORRECT FOR GROUPS WITH ZERO FLUX IN REGION
      DO 2750 IG=1,NGROUP
      DO 2740 NR=1,NREG
      IF(PHIVLF(NR,IG).GT.0.0)GO TO 2740
      PHIVLF(NR,IG)=1.0
 2740 CONTINUE
 2750 CONTINUE
C     INTEGRATE FLUX-VOLUME INTEGRAL TO BROAD GROUP STRUCTURE
      DO 2850 IFG=1,NGROUP
      IBG=IFGP(IFG)
      DO 2840 N=1,NREG
      PHIVOL(N,IBG)=PHIVOL(N,IBG)+PHIVLF(N,IFG)
 2840 CONTINUE
 2850 CONTINUE
      NFGP1=NFGP+1
      NBGP1=NBGP+1
      DO 2900 N=1,NREG
      WRITE(6,2901)(L,PHIVLF(N,L),L=1,NFGP1)
      WRITE(6,2901)(K,PHIVOL(N,K),K=1,NBGP1)
 2900 CONTINUE
 2901 FORMAT(1H ,6(I4,2X,D13.6))
      RETURN
      END
      SUBROUTINE CLPSE(PHIVLF,PHIVOL,LORD,KREG,MULT)
      REAL*8 PHIVLF(200,100),PHIVOL(200,100)
      DIMENSION A(10000),B(10000),W(100),FAKE(12)
      COMMON /IPAR/ NZNR(2000),IFGP(100),KUP(100),KDN(100),
     1ISN,ISC,NFL,IXX,JHT,NTT,NNF,NAB,NFS,N2N,NGM,NNP,NALF,NFGP,
     2NBGP,NISO,IGEOM,IGG,IDIF,NFLG,ITL,MGG,MTL,MUP,MDN,ISO,
     3KSCT,IGM,NPOS,IXSTR,MCUT,LENGTH,KMAT,NREG
      LOR1=LORD+1
      WRITE(6,13)PHIVLF(1,1),PHIVOL(1,1)
   13 FORMAT(1H ,6(3X,D13.6))
   11 FORMAT(1H ,12I6)
      DO 1000 L=1,LOR1
      LEG=L-1
      READ(ISN)K1,K2,K3,JMAT
      LENGTH=K1*K2
      ITL=LENGTH/NFGP
      KMAT=KMAT+1
      WRITE(ISC)MTL,NBGP,LEG,KMAT
      WRITE(6,11)K1,K2,K3,JMAT,MTL,NBGP,LEG,KMAT,KREG,MULT
      READ(ISN)(A(I),I=1,LENGTH)
      LCOL=MTL*NBGP
      DO 220 I=1,LCOL
```

```
527.           B(I)=0.0
528.         220 CONTINUE
529.       C
530.       C     CREATE MACROSCOPIC SIGMA-TRANSPORT WEIGHTING FACTORS
531.       C
532.           IF(IDIF.LT.3)GO TO 260
533.           IF(L.GT.1)GO TO 260
534.       CC  DO 230 IBG=1,NBGP
535.       CC230 W(IBG)=0.0
536.       CC  DO 250 I=1,NMSH
537.       CC  IF(KREG.NE.IZONE(I))GO TO 250
538.       CC  DO 240 IFINE=1,NFGP
539.       CC  IB=IFGP(IFINE)
540.       CC  W(IB)=W(IB)+FL(I,IFINE)*VOL(I,1,1)/MACTR(KREG,IFINE)
541.       CC240 CONTINUE
542.       CC250 CONTINUE
543.       C
544.       C     BEGIN CROSS SECTION COLLAPSE
545.       C
546.         260 CONTINUE
547.           DO 400 N=1,NREG
548.           IF(KREG.NE.N)GO TO 400
549.           DO 390 IG=1,NFGP
550.           IBG=IFGP(IG)
551.           F=1.0
552.           IF(FHIVOL(N,IBG).NE.0.0)F=PHIVLF(N,IG)/PHIVOL(N,IBG)
553.       C
554.       C     COLLAPSE NON-SCATTERING CROSS SECTIONS
555.       C
556.           DO 360 NP=1,JHT
557.           MP=(IBG-1)*MTL+NP
558.           IP=(IG -1)*ITL+NP
559.           IF(L.GT.1)GO TO 360
560.           IF(NP.NE.NTT)GO TO 280
561.       C
562.       C    TRANSPORT CROSS SECTION COLLAPSE OPTIONS
563.       C
564.           GO TO (280,300,320,340),IDIF
565.         280 B(MP)=B(MP) + F*A(IP)
566.           GO TO 360
567.         300 B(MP)=B(MP) + F/A(IP)
568.           GO TO 360
569.         320 CONTINUE
570.       CC  B(MP)=B(MP) + F*A(IP)*PHIVOL(N,IBG)/W(IBG)/MACTR(KREG,IG)
571.           GO TO 360
572.         340 CONTINUE
573.       CC  Q=PHIVOL(IBG,KREG)/W(IBG)/MACTR(KREG,IG)
574.       CC  B(MP)=B(MP) + F*A(IP)*(2.0*Q**2 - Q)
575.         360 CONTINUE
576.       C
577.       C     COLLAPSE SCATTERING CROSS SECTIONS
578.       C
579.           DO 380 NP=KSCT,ITL
580.           JG=NP+IG-IGG
581.           IF(JG.LE.0.OR.JG.GT.NFGP) GO TO 380
582.           JBG=IFGP(JG)
583.           IP=(JG -1)*ITL+NP
584.           MP=(JBG-1)*MTL+MGG+JBG-IBG
585.           B(MP)=B(MP)+F*A(IP)
586.         380 CONTINUE
```

```
587.       390 CONTINUE
588.     C
589.       400 CONTINUE
590.           IF(L.GT.1)GO TO 440
591.           IF(IDIF.NE.2)  GO TO 440
592.           DO 420 IB=1,NBGP
593.           MP=(IB-1)*MTL+NTT
594.           B(MP)=1.0/B(MP)
595.       420 CONTINUE
596.     C
597.       440 CONTINUE
598.           IF(IDIF.EQ.1) GO TO 520
599.           IF(L.GT.1)GO TO 520
600.     C
601.     C     ***** SELF-SCATTER X-S WILL BE MODIFIED SUCH THAT THE SUM OF THE
602.     C     ***** ABSORPTION AND SCATTER X-S EQUALS TRANSPORT/TOTAL X-S
603.     C
604.           IF(IXSTR.NE.1)GO TO 520
605.           MAX=MTL-JHT
606.           IUP=MGG-JHT-1
607.           DO 500 NGP=1,NBGP
608.           LOC=(NGP-1)*MTL
609.           SUM=B(LOC+NAB)
610.           DO 460 M=1,MAX
611.           MPOS=MGG-IUP+M-1
612.           MGP=NGP+MPOS-MGG
613.           IF(MGP.LT.1) GO TO 460
614.           IF(MGP.GT.NBGP) GO TO 480
615.           MSCT=(MGP-1)*MTL+MPOS
616.           SUM=SUM+B(MSCT)
617.       460 CONTINUE
618.       480 CONTINUE
619.           B(LOC+MGG)=B(LOC+MGG)+B(LOC+NTT)-SUM
620.       500 CONTINUE
621.     C
622.       520 CONTINUE
623.           WRITE(ISC)(B(I),I=1,LCOL)
624.      1000 CONTINUE
625.           RETURN
626.           END
627.           SUBROUTINE COMPXS(STR,MXS)
628.           IMPLICIT REAL*8 (A-H,O-Z)
629.           DIMENSION STR(50,100)
630.           DO 50 J=1,100
631.           DO 40 I=1,50
632.           STR(I,J)=1.0
633.        40 CONTINUE
634.        50 CONTINUE
635.           RETURN
636.           END
637.     /*
638.     //GO.FT10F001 DD DSN=B89305.XSECT.BUGLE.ANISN,DISP=SHR
639.     //GO.FT11F001 DD DSN=B89305.XSECT.COLLBUGL.ANISN,DISP=SHR,
640.     //  UNIT=FERN,VOL=SER=,SPACE=(TRK,(100,20),RLSE),
641.     //  DCB=(RECFM=VBS,LRECL=X,BLKSIZE=6356)
642.     //GO.FT12F001 DD DSN=B89305.ONEDANT.GEODST,DISP=SHR
643.     //GO.FT13F001 DD DSN=B89305.ONEDANT.RTFLUX.WEIGHT,DISP=SHR
644.     //GO.SYSIN DD *
645.         10    11    12    13    14
646.         67    25    23     2     0     1     0     4     0
```

```
647.          3     3     2     1     0     0     0     0     0     0
648.          1     1     1     1     1     1     1     1     1     1     1     1
648.2         1     1     1     1     1     1     1     2     2     2     2     2
648.4         2     2     2     2     2     2     2     2     2     3     3     3
648.6         3     3     3     3     3     3     3     4     4     4     5     6
648.8         7     8     9    10    11    12    13    14    15    16    17    18
649.         19    20    21    22    23    24    25
650.          1     3     1     0
650.5         1     3     6     1
651.          2     3     1     0
654.5         3     3     1     0
655.          3     3     6     1
655.5         4     3     5     0
656.          4     3     9     1
656.5         4     3    13     1
657.          5     3     5     0
657.5         5     3     9     1
658.          5     3    13     1
658.5         6     3     5     0
659.          6     3     9     1
659.5         6     3    13     1
660.          7     3     5     0
660.5         7     3     9     1
661.          7     3    13     1
661.5         8     3     1     0
662.          9     3     1     0
662.5        10     3     1     0
663.         11     3     9     0
663.5        12     3     9     0
664.         13     3     9     0
675.    /*
676.    /* END OF FILE
```

SOURCE: Sample Program and Input Data

```
1.    //SOURCE JOB ($,B89305),USER=B89305,CLASS=W,MSGCLASS=W,
2.    //  REGION=900K,TIME=6
3.    //*MAIN ORG=RADS12,LINES=49,CARDS=40
4.    //*FORMAT PR,DDNAME=,DEST=3800
5.    // EXEC FTXCLG,OBJROOM='(CYL,(4,4))'
6.    //FTX.SYSIN DD *
7.          IMPLICIT REAL*8 (A-H,O-Z)
8.          REAL*4  FA(500),EFFK,POWER,RR(200,70),Q(200,70)
9.          DIMENSION F(200,70),SIG(200,70),HUSE(2)
10.         DIMENSION IMIN(20),IMAX(20),JMIN(20),JMAX(20)
11.         DIMENSION K1(10),K2(10)
12.         DATA K1/10*0/,K2/10*0/
13.         DATA F/14000*0.0/,RR/14000*0.0/,SIG/14000*0.0/,Q/14000*0.0/
14.         DATA IMIN/20*0/,IMAX/20*0/,JMIN/20*0/,JMAX/20*0/
15.         DATA HFILE/'FIXSRC'/
16.   C*********************************************************
17.   C     ASSIGN I/O FILES
18.   C         10  RTFLUX FILE
19.   C         11  GEODST FILE
20.   C         12  FIXSRC FILE
21.   C*********************************************************
22.         NF=10
23.         NG=11
24.         NS=12
25.   C*********************************************************
26.   C    READ INPUT DATASET
27.   C     FIRST CARD
28.   C         FORMAT  12I6
29.   C         NPT     NUMBER OF MESH PTS (MAX 200 IN X )
30.   C         NGROUP  NUMBER OF GROUPS
31.   C         IGEOM   GEOMETRY FLAG (1/2/3 : X/XY/R)
32.   C         ICD     FLUX FORMAT FLAG (0/1 : RTFLUX/ANISN)
33.   C         INORM   NORMALIZATION FLAG (0/1 : N/Y)
34.   C         ISPEC   SPECIFY SOURCE INTERVALS FLAG (0/1:N/Y)
35.   C         NSPEC   SPECIFY GROUP INTERVALS FLAG (0/1:N/Y)
36.   C         ICARD   INPUT DATA FLAG (0/1/2:N/Y BY GRP,INT/Y BY GRP)
37.   C*********************************************************
38.         READ(5,80)NPT,NGROUP,IGEOM,ICD,INORM,ISPEC,NSPEC,ICARD
39.         WRITE(6,90)NPT,NGROUP,IGEOM,ICD,INORM,ISPEC,NSPEC,ICARD
40.   C*********************************************************
41.   C     SECOND CARD  IF INORM NOT ZERO
42.   C         RNORM    NORMALIZATION FACTOR
43.   C                  DEFAULT VALUE IS 1.0
44.   C*********************************************************
45.         IF(INORM.NE.0)READ(5,70)RNORM
46.         IF(INORM.NE.0)WRITE(6,75)RNORM
47.         IF(RNORM.EQ.0.0)RNORM=1.0
48.   C*********************************************************
49.   C     THIRD CARD   IF ISPEC NOT ZERO
50.   C                  IBEG    FIRST NONZERO SOURCE INTERVAL
51.   C                  IEND    LAST NONZERO SOURCE INTERVAL
52.   C                  DEFAULT VALUES:  IBEG=1, IEND=NPT
53.   C*********************************************************
54.         IF (ISPEC.NE.0) READ(5,80) IBEG,IEND
55.         IF (ISPEC.NE.0) WRITE(6,90) IBEG,IEND
56.         IF (IBEG.EQ.0) IBEG=1
57.         IF (IEND.EQ.0) IEND=NPT
58.   C*********************************************************
59.   C     FOURTH CARD  IF NSPEC NOT ZERO
```

```
C                 NBEG    FIRST NONZERO SOURCE GROUP
C                 NEND    LAST NONZERO SOURCE GROUP
C                 DEFAULT VALUES:  NBEG=1, NEND=NGROUP
C*************************************************************
      IF (NSPEC.NE.0) READ(5,80) NBEG,NEND
      IF (NSPEC.NE.0) WRITE(6,90) NBEG,NEND
      IF (NBEG.EQ.0) NBEG=1
      IF (NEND.EQ.0) NEND=NGROUP
C
      IF (ICARD.NE.0) GO TO 900
C*************************************************************
C     READ SIGMA VALUES FOR REACTION RATES
C          FORMAT 6D12.6
C          LIST BY GROUP 1-NGROUP
C*************************************************************
      READ(5,70)(SIG(1,K),K=NBEG,NEND)
      WRITE(6,75)(SIG(1,L),L=NBEG,NEND)
      IF(NPT.LT.2)GO TO 38
      DO 37 JT=2,NPT
      DO 35 KT=1,NGROUP
      SIG(JT,KT)=SIG(1,KT)
   35 CONTINUE
   37 CONTINUE
   38 CONTINUE
   70 FORMAT(6D12.6)
   75 FORMAT(1H ,6(3X,1PD13.6))
   80 FORMAT(12I6)
   90 FORMAT(1H ,12I6)
      IF(ICD.GT.0)GO TO 715
C*************************************************************
C
C     READ DIF3D RTFLUX FILE
C
C*************************************************************
      READ(NF)HNAME,(HUSE(I),I=1,2),IVERS
      READ(NF)NDIM,NGROUP,NINTI,NINTJ,NINTK,ITER,EFFK,POWER,NBLOK
      NG1=NGROUP+1
      IF(IGEOM.EQ.3)GO TO 700
      DO 400 NG=1,NGROUP
      DO 300 M=1,NBLOK
      JL=(M-1)*((NINTJ-1)/NBLOK+1)+1
      JUP=M*((NINTJ-1)/NBLOK+1)
      JU=MIN0(NINTJ,JUP)
      READ(NF)((F(I,J),I=1,NINTI),J=JL,JU)
  300 CONTINUE
      DO 390 NP=1,NPT
      IL=IMIN(NP)
      IU=IMAX(NP)
      JL=JMIN(NP)
      JU=JMAX(NP)
      DO 350 J=JL,JU
      DO 340 I=IL,IU
      RR(NP,NG)=RR(NP,NG)+F(I,J)*SIG(NP,NG)/RNORM
  340 CONTINUE
  350 CONTINUE
      RR(NP,NG1)=RR(NP,NG1)+RR(NP,NG)
  390 CONTINUE
  400 CONTINUE
      GO TO 405
  700 CONTINUE
```

```
120.            DO 710 M=1,NBLOK
121.            JL=(M-1)*((NGROUP-1)/NBLOK+1)+1
122.            JUP=M*((NGROUP-1)/NBLOK+1)
123.            JU=MIN0(NGROUP,JUP)
124.            READ(NF)((F(I,J),I=1,NINTI),J=JL,JU)
125.          710 CONTINUE
126.            GO TO 739
127.       C-------------------------------------------------------
128.       C
129.       C     READ ANISN FLUX FILE
130.       C
131.          715 CONTINUE
132.            READ(NF)IMA,IGMA
133.            DO 725 K=1,IGMA
134.            READ(NF)(FA(L),L=1,IMA)
135.            DO 720 LL=1,IMA
136.            F(LL,K)=FA(LL)
137.          720 CONTINUE
138.          725 CONTINUE
139.       C-------------------------------------------------------
140.          739 CONTINUE
141.       C*******************************************************
142.       C
143.       C     CALCULATE REACTION RATES
144.       C
145.       C*******************************************************
146.            DO 800 NG=NBEG,NEND
147.            DO 790 NP=IBEG,IEND
148.            RR(NP,NG)=F(NP,NG)*SIG(NP,NG)/RNORM
149.          790 CONTINUE
150.          800 CONTINUE
151.          405 CONTINUE
152.            GO TO 950
153.          900 CONTINUE
154.       C*******************************************************
155.       C
156.       C     READ SOURCE VALUES FROM CARDS (ICARD>0)
157.       C                   FORMAT 6D12.6
158.       C                   INPUT MESH PTS IBEG TO IEND FOR EACH GROUP
159.       C
160.       C*******************************************************
161.            DO 910 NG=NBEG,NEND
162.            IF (ICARD.EQ.1) READ (5,70)  (RR(NP,NG),NP=IBEG,IEND)
163.            IF (ICARD.EQ.1) GO TO 909
164.            IF (ICARD.EQ.2) READ (5,70)   RR(IBEG,NG)
165.            IBEG1= IBEG + 1
166.            DO 908 NP=IBEG1,IEND
167.          908 RR(NP,NG)=RR(IBEG,NG)
168.          909 CONTINUE
169.          910 CONTINUE
170.          950 CONTINUE
170.11     C*******************************************************
170.12     C
170.13     C     MODIFICATIONS FOR PHOTONEUTRON SOURCE DETERMINATION
170.14     C
170.15     C*******************************************************
170.5      C   READ INPUT
170.55          READ(5,80) NINT
170.6           WRITE(6,90) NINT
170.65          DO 100 N=1,NINT
```

```
170.7          READ(5,80) K1(N),K2(N)
170.75         WRITE(6,90) K1(N),K2(N)
170.8        100 CONTINUE
170.81     C   ADD GROUP VALUES, CONVERT TO NEUTRON STRUCTURE
170.82         DO 200 N=1,NINT
170.821        KF=K1(N)
170.822        KL=K2(N)
170.83         DO 202 K=KF,KL
170.84         Q(K,1) = RR(K,6)+RR(K,7)+RR(K,8)+RR(K,9)+RR(K,10)+RR(K,11)
170.85         Q(K,2) = RR(K,12)
170.86         Q(K,3) = RR(K,13)
170.87       202 CONTINUE
170.88       200 CONTINUE
171.       C*************************************************************
172.       C
173.       C      WRITE FIXSRC FILE
174.       C
175.       C*************************************************************
176.       C      OTH RECORD
177.              IVERS=1
178.              MULT=2
179.              HNAME=HFILE
180.              WRITE(NS) HNAME,(HUSE(I),I=1,2),IVERS
181.       C      1ST RECORD
182.              ITYPE= 0
183.              IDISTS=1
184.              NSCOMP=0
185.              NDCOMP=1
186.              NEDGI=0
187.              NEDGJ=0
188.              NEDGK=0
189.              IF (IGEOM.EQ.3) GO TO 500
190.       C      PUT IN 2D STUFF WHEN NEED IT
191.              GO TO 505
192.       500    CONTINUE
193.       C      1 DIM VALUES
194.              NDIM=1
195.              NINTI=NPT
196.              NINTJ=1
197.              NINTK=1
198.              NBLOK=0
199.       505    CONTINUE
200.              WRITE(NS) ITYPE,NDIM,NGROUP,NINTI,NINTJ,NINTK,IDISTS,NDCOMP,
201.             1NSCOMP,NEDGI,NEDGJ,NEDGK,NBLOK
201.1            WRITE (6,821)
201.2        821 FORMAT ('1THE FOLLOWING INFORMATION DESCRIBES THE PHOTONEUTRON
201.3           1REACTION RATE FROM THE GAMMA ACTIVITY')
202.             WRITE(6,789) NPT,NGROUP
203.       789   FORMAT (' NPT= ',I6,4X,'NGROUP= ',I6)
204.             IF (IBEG.EQ.1 .AND. IEND.EQ.NPT) GO TO 506
205.             WRITE (6,801) IBEG
206.       801   FORMAT (' FIRST NONZERO SOURCE INTERVAL IS ',I6)
207.             WRITE (6,802) IEND
208.       802   FORMAT (' LAST NONZERO SOURCE INTERVAL IS ',I6)
209.             WRITE (6,803)
210.       803   FORMAT (' ALL OTHER SOURCE INTERVAL VALUES ARE ZERO')
211.       506   CONTINUE
212.             IF (NBEG.EQ.1 .AND. NEND.EQ.NGROUP) GO TO 507
213.             WRITE (6,806) NBEG
214.       806   FORMAT (' FIRST NONZERO SOURCE GROUP IS ',I6)
```

```
215.            WRITE (6,807) NEND
216.       807  FORMAT (' LAST NONZERO SOURCE GROUP IS ',I6)
217.            WRITE (6,808)
218.       808  FORMAT (' ALL OTHER SOURCE GROUP VALUES ARE ZERO')
219.         507 CONTINUE
223.       C    PRINT OUT SAMPLE VALUES
224.            DO 874 J=NBEG,NEND
224.3           DO 875 N=1,NINT
224.35          KF=K1(N)
224.36          KL=K2(N)
224.4           DO 873 K=KF,KL
226.            WRITE(6,852) J,K,F(K,J),SIG(K,J),RR(K,J)
227.       852  FORMAT (' GROUP#=',I6,2X,'INTERVAL=',I6,2X,
228.           1'FLUX= ',1PD12.5,2X,'SIGMA= ',1PD12.5,2X,'REACTION RATE= ',
229.           21PD12.5)
230.       873  CONTINUE
230.5       875 CONTINUE
231.       874  CONTINUE
232.            IF (ICARD.EQ.0) GO TO 870
233.            WRITE (6,854)
234.       854  FORMAT (' NOTE: FOR VALUES READ BY CARDS FLUX = SIGMA = ZERO')
235.       870  CONTINUE
235.11          WRITE(6,881)
235.12     881  FORMAT('1THE FOLLOWING VALUES ARE WRITTEN TO THE FIXSRC FILE
235.13         1AS THE NEUTRON GROUP STRUCTURE PHOTONEUTRON SOURCE')
235.14          DO 303 J=1,NGROUP
235.15          WRITE(NS) (Q(K,J),K=1,NINTI)
235.16       303 CONTINUE
235.2      C    PRINT VALUES
235.3           DO 360 J=1,NGROUP
235.4           DO 370 K=1,NINTI
235.5           WRITE (6,351) J,K,Q(K,J)
235.6        351 FORMAT (' GROUP=',I6,2X,'INTERVAL=',I6,2X,'REACTION RATE=',
235.7           11PD12.5)
235.8        370 CONTINUE
235.9        360 CONTINUE
236.            STOP
237.            END
295.       //GO.FT10F001 DD DSN=B89305.ONEDANT.RTFLUX.CORE,DISP=SHR
299.       //GO.FT12F001 DD DSN=B89305.ONEDANT.FIXSRC.PHN1,
300.       //       DISP=SHR,UNIT=ALLPERM,SPACE=(TRK,(20,10),RLSE),
301.       //       VOL=SER=,DCB=(RECFM=VBS,LRECL=X,BLKSIZE=6136)
302.       //GO.SYSIN DD *
303.          170    25     3     0     0     0     1     0
303.2          6    13
303.4        4.64E-09    6.54E-09    8.02E-09    9.07E-09    9.92E-09    1.03E-08
303.5        9.71E-09    4.22E-09
303.6         1
303.7         1    18
305.       /*
306.       /* END OF FILE
```

CHICALC: Program

```
1.      //CHICALC JOB (,F89305),MSGCLASS=W
2.      // EXEC FTXCLG
3.      //SYSIN DD *
4.      C THIS IS A PROGRAM FOR CHI INTEGRATION
5.            EXTERNAL FUN
6.            DOUBLE PRECISION A1,B1,EP,FUN,ANC4,Y
7.      C
8.      C READ IN VALUES:
9.      C       K=NUMBER OF INTEGRATIONS (I6)
10.     C       EP=ERROR (D12.6)
11.     C       N=CONVERGENCE CRITERIA (I6)
12.     C
13.           READ (5,10) K,EP,N
14.     10    FORMAT (I6,D12.6,I6)
14.5          WRITE (6,15)
14.6    15    FORMAT (' LOWER LIMIT',4X,'UPPER LIMIT',4X,
14.7         *'EVALUATIONS',4X,'INTEGRAL VALUE')
15.           DO 50 J=1,K
16.     C
17.     C READ IN INTEGRATION LIMITS:
18.     C         A1=LOWER LIMIT (D12.6)
19.     C         B1=UPPER LIMIT (D12.6)
20.     C
21.           READ (5,20) A1,B1
22.     20    FORMAT (2D12.6)
23.           Y=ANC4(A1,B1,EP,M,N,FUN)
24.     50      WRITE (6,100) A1,B1,M,Y
25.     100   FORMAT (1X,D11.6,4X,D11.6,4X,I6,4X,D25.15)
27.           STOP
28.           END
29.     C  FUNCTION TO BE USED IN CHI EVALUATION
30.           DOUBLE PRECISION FUNCTION FUN(X)
31.           REAL*8 FUN,X
32.           FUN=.453*DEXP(-1.036*X) * DSINH((2.29*X)**.5)
33.           RETURN
34.           END
35.     //GO.SYSIN DD *
36.          6     1.0D-06     1
37.              .821        1.7D1
38.         7.10D-03          .821
39.        1.855D-06    7.10D-03
40.         .100D-06   1.855D-06
41.              0.0    .100D-06
42.              0.0        17.3
50.     /*
```

REKINS: Input Data File

```
1.    2.3955E-4 1.5897E-3 1.4228E-3 2.8673E-3 8.3478E-4 3.0498E-4     BETA FOR PWR
2.    0.0124000  0.030500   0.11100   0.30100   1.14000   3.01000   LAMDA  FOR PWR
3.    0.0      0.5       1.0         2.592E+60.0       0.0          RAMP
4.    0.0        0.0       0.0       0.0       0.0       0.0        TIME
5.    0.0        0.0       0.0       0.0       0.0       0.0
6.    0.0        0.0       0.0       0.0       0.0       0.0
7.    0.0        0.0       0.0       0.0       0.0       0.0
8.    0.0        0.0       0.0       0.0       0.0       0.0
9.    0.0      1.0       0.0       0.0       0.0       0.0          RAMP
10.   0.0        0.0       0.0       0.0       0.0       0.0        SHAPE
11.   0.0        0.0       0.0       0.0       0.0       0.0        FRACTION
12.   0.0        0.0       0.0       0.0       0.0       0.0
13.   0.0        0.0       0.0       0.0       0.0       0.0
14.   0.0        0.0       0.0       0.0       0.0       0.0
15.   0.0      0.285     0.323     0.355     0.385     0.410      SOR TIME
16.   0.430    0.450     0.497     0.520     0.558     0.580
17.   0.710    0.733     0.762     0.797     0.830     0.850
18.   0.870    0.930     1.730       1.0E+200.0       0.0
19.   0.0      0.0       0.0       0.0       0.0       0.0
20.   0.0      0.0       0.0       0.0       0.0       0.0
21.   0.0      0.0       0.002     0.007     0.016     0.032      SOR
22.   0.058    0.089     0.172     0.223     0.343     0.410      REACTIVTY
23.   0.796    0.846     0.888     0.923     0.940     0.950      FRACTION
24.   0.953    0.962     0.985     0.985     0.0       0.0
25.   0.0      0.0       0.0       0.0       0.0       0.0
26.   0.0      0.0       0.0       0.0       0.0       0.0
27.   4.0      11.0      19.0      29.0      39.0      49.0       LGRR(%/S)
28.   59.0     99.0      499.0       1.0E+200.0       0.0        LOG RATE
29.   0.0      0.0       0.0       0.0       0.0       0.0        TRIP 4%/S
30.     1.0E+201.0       0.475     0.35      0.3       0.25       LGRD
31.   0.20     0.16      0.055     0.055     0.0       0.0        TIME DELY
32.   0.0      0.0       0.0       0.0       0.0       0.0        SEC.
33.   2.5      4.0       5.0       10.0      15.0      20.0       LNRR
34.     1.0E+200.0       0.0       0.0       0.0       0.0
35.   0.0      0.0       0.0       0.0       0.0       0.0        LIN. RATE
36.     1.0E+202.4       1.5       0.65      0.47      0.37
37.   0.035    0.0       0.0       0.0       0.0       0.0        LNRD
38.   0.0      0.0       0.0       0.0       0.0       0.0
39.   1.3      1.31      1.35      1.45      1.5       1.6        LNPR
40.   5.3        1.0E+200.0       0.0       0.0       0.0        LINEAR
41.   0.0      0.0       0.0       0.0       0.0       0.0        POWER TRP
42.     1.0E+200.12      0.088     0.07      0.055     0.048      LNPD
43.   0.04     0.04      0.0       0.0       0.0       0.0
44.   0.0      0.0       0.0       0.0       0.0       0.0
45.            1 L2-5 SHUTDOWN   RAMP SCRAM OVER 1.90 SECONDS
46.     100.000        1.0     36.00   1.95E-5    0.3378        1.90            DAT  PWR
47.   3.0        1.0       0.0         -47.370     0.0       0.0                  K=0.91
48.   3.0        1.0       -117.45   0.0       .08       0.0
49.   3.0        3.0       3.0       4.0       2.5       1.3
50.    0.0001  1000.0    1.0         300.0   0.0       0.0
51.   1
52.  19          3.0
53.
54.
55.   /*
```

APPENDIX REFERENCES

1A. B. A. Zolotar, et al., "EPRI-CELL Code Description," Advanced Recycle Methodology Program System Documentation, Part II, Chapter 5 (Oct. 1975).

2A. G. D. Joanou and J. S. Dudek, "GAM-I: A Consistent P_1 Multigroup Code for the Calculation of Fast Neutron Spectra and Multigroup Constants," GA-1850 (June 1961).

3A. H. C. Honeck, "THERMOS: A Thermalization Transport Theory Code for Reactor Lattice Calculations," BNL-5826 (Sept. 1961).

4A. T. R. England, "CINDER: A One-Point Depletion and Fission Product Program," WAPD-TM-334 (Revised June 1964).

5A. C. G. Stenberg, ANL, unpublished information (1978).

6A. J. R. Deen, private communication (1985).

7A. D. L. Reeder, "LOFT System and Test Description (5.5-ft Nuclear Core 1 LOCES)," EG&G Idaho, NUREG/CR-0247, TREE-1208 (July 1978).

8A. "LOFT Integral Test System Final Safety Analysis Report Revision 1," EG&G Idaho, TID-28027/3 (Aug. 1977).

9A. M. J. Bell, "ORIGEN: The ORNL Isotope Generation and Depletion Code," ORNL-4628 (Revised Sept. 1979).

10A. W. Carpenter, private communication (1985).

11A. D. J. Malloy, private communication (1985).

12A. P. D. Bayless and J. M. Divine, "Experiment Data Report for LOFT Large Break Loss-of-Coolant Experiment L2-5," EG&G Idaho, NUREG/CR-2826, EGG-2210 (Aug. 1982).

13A. R. D. O'Dell, F. W. Brinkley, Jr., and D. R. Marr, "User's Manual for ONEDANT: A Code Package for One-Dimensional, Diffusion-Accelerated, Neutral Particle Transport," LA-9184-M (Revised Nov. 1982).

14A. C. H. Adams, ANL, unpublished information.

15A. R. W. Roussin, private communication.

16A. M. L. Gundy, "Application of the Adiabatic Spatially Dependent Reactor Kinetics Method to Voided Pressurized Water Reactors," Ph.D. Thesis Pennsylvania State University (1984).

17A. J. R. Lamarsh, Introduction to Nuclear Reactor Theory, Addison-Wesley Publishing Co. (1972).

18A. P. H. Kier, ANL, unpublished information (1978).

19A. R. M. Lell, private communication (1985).

20A. R. M. Lell, private communication (1985).

APPENDIX LIST OF FIGURES

LOFT Core Design

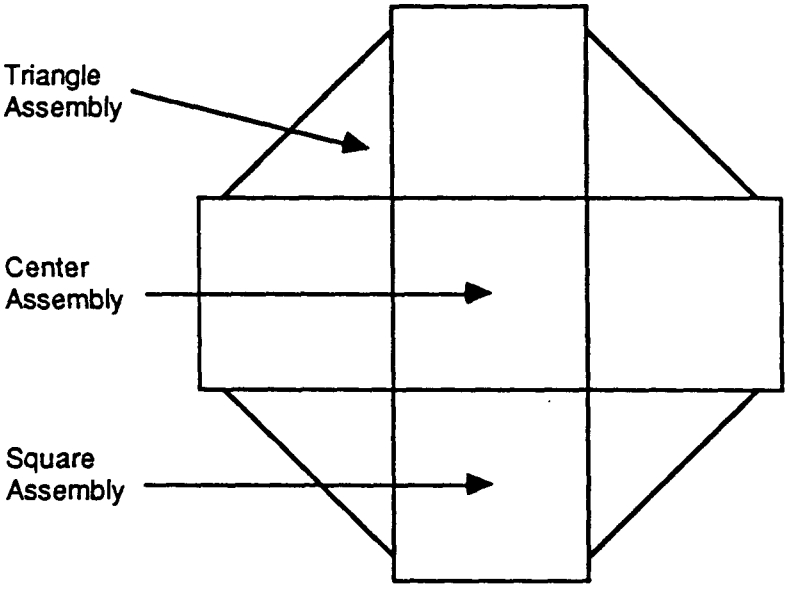

Power Distribution

Square	14.7%
Triangle	4.7%
Center	22.6%

Figure 1A

APPENDIX LIST OF TABLES

Table 1A. EPRI-CELL Energy Group Structure

Standard EPRI-CELL Broad Group Energy Structure

Group	Energy Range	Region
1	.821 - 10 MeV	Fast
2	5.53 - 821 keV	Resonance
3	1.855 - 5530 eV	Resonance
4	.625 - 1.855 eV	Resonance
5	0 - .625 eV	Thermal

Table 1Aa

Modified EPRI-CELL Broad Group Structure
for ISOTXS Generation

Group	Energy Range	Region
1	.821 - 10 MeV	Fast
2	7.10 - 821 keV	Resonance
3	1.855 - 7100 eV	Resonance
4	.112 - 1.855 eV	Resonance
5	0 - .112 eV	Thermal

Table 1Ab

Table 2A. LWR Benchmark Nuclear Densities
(BUGLE-80 Code Package)

LWR HOMOGENEOUS CORE		LOW CARBON STEEL A533B (7.86 g/cm^3)	
Hydrogen	2.68×10^{-2}	Carbon	8.67×10^{-4}
Boron-10	7.44×10^{-7}	Silicon	4.96×10^{-4}
Oxygen	2.51×10^{-2}	Chromium	1.54×10^{-4}
Chromium	6.86×10^{-5}	Manganese	1.12×10^{-3}
Manganese	5.98×10^{-6}	Iron	8.20×10^{-2}
Iron	2.29×10^{-4}	Nickel	5.95×10^{-4}
Nickel	3.36×10^{-5}	Molybdnum	2.71×10^{-4}
Zirconium	4.44×10^{-3}		
Uranium-235	2.05×10^{-4}		
Uranium-238	6.54×10^{-3}		
BORATED PRIMARY COOLANT		STAINLESS STEEL-304 (7.90 g/cm^3)	
Hydrogen	4.62×10^{-2}	Chromium	1.74×10^{-2}
Boron-10	1.28×10^{-6}	Manganese	1.52×10^{-3}
Oxygen	2.31×10^{-2}	Iron	5.81×10^{-2}
		Nickel	8.51×10^{-3}

Distribution for ANL-87-29

Internal:

C. E. Till
J. F. Marchaterre
A. J. Goldman
L. W. Deitrich
D. Rose
J. E. Cahalan
B. W. Spencer
J. M. Kramer
D. H. Cho
C. J. Mueller
T. Y. Wei
J. Deen
R. H. Sevy
J. E. Herceg
A. E. Klickman
C. E. Dickerman
L. Baker, Jr.
C. P. Tzanos
D. R. Pedersen
R. W. Seidensticker
Y. W. Chang
J. M. Kennedy
G. S. Stanford
R. Lell
E. A. Rhodes
T. H. Braid
R. C. Doerner
R. E. Boyar
A. DeVolpi (20)
D. Markoff (5)
D. Malloy
ANL Patent Dept.
ANL Contract File
ANL Libraries
TIS Files (3)

External:

DOE-TIC, for distribution per UC-78 (118)
Manager, Chicago Operations Office
Reactor Analysis and Safety Division Review Committee:
W. B. Behnke, Jr., Commonwealth Edison Co., Chicago, Ill. 60690
M. J. Ohanian, Univ. of Florida, Gainesville, Fla. 32611
R. L. Seale, Univ. of Arizona, Tucson, Ariz. 85721
J. S. Armijo, General Electric Company, San Jose, Calif. 95153-5354
T. J. Hirons, Los Alamos National Laboratory, Los Alamos, N. Mex. 87545
N. E. Todreas, Mass. Inst. of Technology, Cambridge, Mass. 02139
J. P. Adams, EG&G Idaho, Inc.
W. Carpenter, EG&G Idaho, Inc.
S. Prussin, Univ. of California-Berkeley
C. Williamson, Oak Ridge Associated Universities